ISSN: 1994-4691

# Промислова гідравліка і пневматика

Наукове фахове видання категорії Б

№ 1 (77)
2026

ПГП

**ISSN: 1994-4691**

*Асоціація спеціалістів*
*промислової гідравліки і пневматики*

*Наукове*
*фахове видання*
*категорії Б*

# Промислова гідравліка і пневматика

*Наукове фахове видання категорії Б*
*Наказ Міністерства освіти і науки України*
*№ 928 від 11.06.2026 р.*

*Журнал засновано у березні 2003 року*

*Засновник: Таврійський державний агротехнологічний університет імені Дмитра Моторного*

*Реєстрація суб'єкта у сфері друкованих медіа:*
*Рішення національної ради України з питань телебачення і радіомовлення*
*№ 532 від 13.03.2025 року*
*Ідентифікатор медіа: R 30-05942*

*Виходить 2 рази на рік*

**№ 1 (77)**
**2026**

*Scientific*
*Professional Publication*
*of Category B*

# Industrial Hydraulics Pneumatics

**WEB**: https://oj.tsatu.edu.ua **DOI**: 10.32782/1994-4691-2026-1-77

Видавничий дім
"Гельветика"
2026

Промислова гідравліка і пневматика: наукове фахове видання категорії Б. Запоріжжя: ТДАТУ, 2026. №1 (77). 200 с.

**ISSN 1994-4691**

**Кластер:** Механічна інженерія та машинобудування

**Спеціальності:** G8 Матеріалознавство, G9 Прикладна механіка, G11 Машинобудування (за спеціалізаціями), G12 Авіаційна та ракетно-космічна техніка

**Головний редактор**
Волошина А. А., *д-р техн. наук, професор*
*Таврійський державний агротехнологічний університет імені Дмитра Моторного, Україна*

**Заступники головного редактора**
Панченко А. І., *д-р техн. наук, професор*
*Таврійський державний агротехнологічний університет імені Дмитра Моторного, Україна*

**РЕДАКЦІЙНА КОЛЕГІЯ**
Абдуллоев М. А., *канд. техн. наук, доцент*
*Таджицький технічний університет імені академіка М. С. Осімі, Таджикистан*
Гловацький Ш, *д-р техн. наук, професор*
*Варшавський університет наук про життя, Польща*
Мудрик К, PhD, *д-р наук, професор*
*Сільськогосподарський університет у Кракові, Польща*
Гусак О. Г., *канд. техн. наук, професор*
*Сумський державний університет, Україна*
Гуцол Т. Д., *д-р техн. наук, професор*
*Сільськогосподарський університет у Кракові, Польща*
Козлов Л. Г., *д-р техн. наук, професор*
*Вінницький національний технічний університет, Україна*
Кондусь В. Ю., *канд. техн. наук, доцент*
*Сумський державний університет, Україна*
Самойчук К. О., *д-р техн. наук, професор*
*Таврійський державний агротехнологічний університет імені Дмитра Моторного, Україна*
Тітова О.А., *д-р пед. наук, професор*
*Інститут професійної освіти Національної академії педагогічних наук України*

**Editor in chief**
Voloshina A., *Dr. Sci. Tech., Professor*
*Dmytro Motornyi Tavria State Agrotechnological University, Ukraine*

**Deputy editors in chief**
Panchenko A., *Dr. Sci. Tech., Professor*
*Dmytro Motornyi Tavria State Agrotechnological University, Ukraine*

**EDITORIAL BOARD**
Abdullo M. A., *Cand. Sci. Tech., Associate Professor*
*Tajik Technical University named after academic M. S. Osimi, Tajikistan*
Głowacki, Sz., *Dr. Sci. Tech., Professor*
*Warsaw University of Life Sciences, Poland*
Mudryk K., *Dr. Sci. Tech., Professor*
*University of Agriculture in Krakow, Poland*
Gusak O., *Cand. Sci. Tech., Professor*
*Sumy State University, Ukraine*
Hutsol T., *Dr. Sci. Tech., Professor*
*University of Agriculture in Krakow, Poland*
Kozlov L., *Dr. Sci. Tech., Professor*
*Vinnytsia National Technical University, Ukraine*
Kondus V, *Cand. Sci. Tech, Associate Professor*
*Sumy State University, Ukraine*
Samoichuk K., *Dr. Sci. Tech., Professor*
*Dmytro Motornyi Tavria State Agrotechnological University, Ukraine*
Titova, O., *Dr. Ped. Tech., Professor*
*Institute of Vocational Education of the National Academy of Educational Sciences of Ukraine*

**ПРОМИСЛОВА ГІДРАВЛІКА І ПНЕВМАТИКА**

**Засновник**
Таврійський державний агротехнологічний університет імені Дмитра Моторного

*Заснований у 2003 році*
Включений до переліку фахових видань України категорії Б: Наказ Міністерства освіти і науки України № 928 від 11.06.2026 року
Реєстрація суб'єкта у сфері друкованих медіа: Рішення національної ради України з питань телебачення і радіомовлення № 532 від 13.03.2025 року
Ідентифікатор медіа: R 30-05942
Виходить 2 рази на рік

**Адреса редакції**
*Юридична*: 72312, Запорізька обл.
м. Мелітополь, пр. Б. Хмельницького, 18
*Фактична*: 69600, Запорізька обл.
м. Запоріжжя, вул. Жуковського, 66
https://oj.tsatu.edu.ua,

DOI: 10.32782/1994-4691-2026-1-77

**INDUSTRIAL HYDRAULICS AND PNEUMATICS**

**Founder**
Dmytro Motornyi Tavria State Agrotechnological University

*Founded in 2003*
Included in the list of professional publications of Ukraine of category B: Order of the Ministry of Education and Science of Ukraine No. 928 of June 11, 2026.
Registration of an entity in the field of print media: Decision of the National Council of Ukraine on Television and Radio Broadcasting No. 532 of March 13, 2025.
Media identifier: R 30-05942
Published 2 times a year

**Address of the Editorial office**
*Legal adress*: 72312, Zaporizhzhia region
Melitopol, 18, B. Khmelnitskyi Ave.
*Actual address*: 69600, Zaporizhzhia region
Zaporizhzhia, 66, Zhukovskyi Str.
https://oj.tsatu.edu.ua,

DOI: 10.32782/1994-4691-2026-1-77

***© Таврійський державний агротехнологічний університет імені Дмитра Моторного*, 2026**

# ЗМІСТ / CONTENTS

**Lukianov P. V., Pavlova K. S., Trofymenko M. K.** OPTIMAL PROPERTIES OF INCOMPRESSIBLE SWIRLING FLOW IN A RECTILINEAR CIRCULAR PIPE 5

**Лук'янов П. В., Павлова К. С., Трофименко М. К.** Оптимальні властивості нестисливої закрученої течії у прямолінійній круглій трубі

**Mingwei X.** IMPROVEMENT THE GLOBAL ENERGY EFFICIENCY OF HYDRAULIC SYSTEMS OF TECHNOLOGICAL EQUIPMENT 14

**Мінвей Щ.** Підвищення глобальної енергоефективності гідравлічних систем технологічного обладнання

**Panchenko A., Voloshina A., Panchenko I., Kholod I., Voloshin A.** DYNAMIC MODEL OF A HYDRAULIC DRIVE OF A MECHATRONIC SYSTEM WITH A PLANETARY HYDRAULIC MOTOR 37

**Панченко А. І., Волошина А. А., Панченко І. А., Холод І. М., Волошин А. А.** Динамічна модель гідравлічного приводу мехатронної системи з планетарним гідромотором

**Rogovyi A., Stryzhak M., Savenkov D., Dyomin D., Hasanov R.** FEASIBILITY ASSESSMENT OF A VORTEX TUBE FOR EXHAUST AIR ENERGY RECOVERY IN A PNEUMATIC CYLINDER 63

**Роговий А., Стрижак М., Савенков Д., Дьомін Д., Гасанов Р.** Обґрунтування можливості застосування вихорової труби для рекуперації енергії відпрацьованого повітря пневмоциліндра

**Skvorchevsky A.** QUANTITATIVE AND QUALITATIVE ANALYSIS OF THE GLOBAL HYDRAULIC MARKET DEVELOPMENT 73

**Скворчевський О.** Кількісний та якісний аналіз розвитку глобального ринку гідравлічного обладнання

**Stefanov V., Voronin M.** EFFECT OF FATTY ACID CONCENTRATION IN THE WORKING FLUID OF MACHINE HYDRAULIC DRIVES ON BOUNDARY LUBRICATING FILM FORMATION 82

**Стефанов В.О., Воронін М.О.** Вплив концентрації жирних кислот у робочій рідині гідроприводів машин на формування граничної мастильної плівки

**Strutynsky V.** COMPONENTS OF HYDRAULIC CONTROL SYSTEMS FOR WHEELLESS GROUND ROBOTIC COMPLEXES 92

**Струтинський В. Б.** Елементна база систем гідроавтоматики безколісних наземних роботизованих комплексів

**Syrotin O. A., Lozinskyi D. O.** CONTROL MODES OF A HYDRAULIC DRIVE WITH INDEPENDENT CONTROL OF FLOWS UNDER DIFFERENT LOAD CONDITIONS 121

**Сиротін О. А., Лозінський Д. О.** Режими керування в гідроприводі з незалежним керуванням потоками при різних умовах навантаження

**Trehubov V. O., Piontkevych O. V.** EXPERIMENTAL TEST BENCH FOR INVESTIGATING THE CHARACTERISTICS OF A HYDRAULIC DRIVE WITH AN ANTI-SLIP DEVICE 134

**Трегубов В. О., Піонткевич О. В.** Експериментальний випробувальний стенд для дослідження характеристик гідроприводу з антибуксувальним пристроєм

**Voronin S., Poletaev V.** SUBSTANTIATION OF THE METHOD FOR INCREASING THE EFFICIENCY AND RELIABILITY OF FLUID COUPLINGS IN MINE CONVEYOR DRIVES WHEN USING WATER EMULSIONS AS A OPERATING FLUID 144

**Воронін С. В., Полєтаєв В. В.** Обґрунтування методу підвищення ефективності та надійності гідромуфт приводів шахтних конвеєрів при застосуванні в якості робочої рідини водних емульсій

**Аврунін Г. А., Лебедик І. В., Підгорний М. В., Білан І. В., Мороз І. І.** ДИНАМІКА ГІДРОПРИВОДА ВСЮДИХОДА НА РЕЖИМАХ ТЯГОВО-ШВИДКІСНОЇ ХАРАКТЕРИСТИКИ 163

**Avrunin G., Lebedyk I., Podgorny M., Bilan I., Moroz I.** Dynamics of the hydraulic fluid power of all-wheel vehicles in the modes of traction-speed characteristics

**Волянський М. С., Лавріненко О. Т., Гуменюк Ю. О., Росамаха Ю. О.** АНАЛІЗ РОБОТИ ГІДРОМЕХАНІЧНИХ ТРАНСМІСІЙ FENDT VARIO ТА JOHN DEERE AUTOPOWR ТА ПОРІВНЯННЯ ЇХ ЕФЕКТИВНОСТІ 178

**Volianskyi M., Lavrinenko A., Humeniuk Y., Rosamakha Y.** Analysis of the operation of fendt vario and john deere autopowr hydromechanical transmissions and comparison of their efficiency

**Дмитрів В. Т., Великий Н.-Т.** ОБЧИСЛЮВАЛЬНИЙ ФАКТОРНИЙ ЕКСПЕРИМЕНТ ДОСЛІДЖЕННЯ ДИНАМІЧНИХ ХАРАКТЕРИСТИК РЕГУЛЯТОРА ТИСКУ ПНЕВМОСИСТЕМИ 189

**Dmytriv V., Velykyi N.-T.** Computational factorial experiment for investigating the dynamic characteristics of a pneumatic system pressure regulator

**DOI https://doi.org/10.32782/1994-4691-2026-1-77-1**
UDK 532, 531

# OPTIMAL PROPERTIES OF INCOMPRESSIBLE SWIRLING FLOW IN A RECTILINEAR CIRCULAR PIPE

# ОПТИМАЛЬНІ ВЛАСТИВОСТІ НЕСТИСЛИВОЇ ЗАКРУЧЕНОЇ ТЕЧІЇ У ПРЯМОЛІНІЙНІЙ КРУГЛІЙ ТРУБІ

P. V. Lukianov[1*], PhD, Senior Researcher ORCID: 0000-0002-5043-6182
K. S. Pavlova[1], PhD ORCID: 0000-0001-8818-4358
M. K. Trofymenko[1], student ORCID: 0009-0004-9750-4818

[1] *National University «Kyiv Aviation Institute», Kyiv, Ukraine*
*e-mail: Pavlo.Lukianov@npp.kai.edu.ua

**Abstract**. Swirling flows are frequently encountered in technical devices, particularly in hydraulic and pneumatic systems. Optimal performance of these devices cannot be achieved without a thorough understanding of the physics governing these flows—physics that, as it turns out, is characterized by optimality. It is precisely these optimality properties that prove useful in situations where existing models fail to accurately describe the flow on their own. This paper provides an overview of contemporary research and achievements regarding swirling flows and highlights the challenge of describing them adequately. Based on this, the study's objective is formulated: to consolidate and systematize existing knowledge while deriving new insights–specifically, the optimality properties of swirling flows. The results demonstrate that swirling flows in a rectilinear circular pipe possess optimality properties; for instance, a flow with extremal helicity exhibits zero helicity at every point. Swirling flow where the velocity field depends solely on the radial coordinate is also optimal. For laminar flow, this entails the property of maximum flow rate, whereas for turbulent flow, the condition of maximum vorticity is also satisfied. The obtained results are compared with existing theoretical and experimental data.

**Keywords**: swirling flow, rectilinear pipe, optimal properties.

## Introduction.

Swirling, or vortex, flows are widely encountered in nature and engineering. If the gas flow velocity does not exceed a Mach number of 0.2–0.3, such flows can be quantitatively treated as incompressible fluid flows. Modern flow classification [1] categorizes them into natural flows—formed without human intervention—and those generated through human intervention or, more broadly, by an external force. Understanding the nature (physics) of these flows is crucial for improving (optimizing) existing equipment and developing new technology that involves the generation of swirling flows.

To understand why a flow acquires a swirl in natural conditions, one must answer a single question: why? The answer is simple: such a flow must possess optimal properties—at least one. For instance, a swirling flow in a pipe containing a spiral insert exhibits the property of maximizing fluid rate [2]. However, this phenomenon (or property) does not manifest across the entire range of parameters [2]. It is associated, firstly, with a turbulent flow regime and, secondly, with the presence of a second phase (a small quantity of air bubbles). To entirely understand the physics of the phenomenon, it is necessary to recall the existence of the so-called inverse cascade of turbulent energy [3, 4]. For a long time, it was unclear why vortex flows in nature could persist for weeks or months. It was not clear where they derived the "fuel" to sustain themselves, given that turbulent energy dissipation occurs continuously within a vortex flow.

In the case of swirling flow—where the turbulent stress tensor loses its mirror symmetry—an inverse cascade of turbulent energy may occur; in simpler terms, this corresponds to flow domains characterized by negative turbulent viscosity. An inverse energy cascade is also possible in three-dimensional isotropic turbulence [5], freely decaying two-dimensional turbulence [6], and experimentally generated swirling turbulence [7]. Consequently, there arises the problem of describing swirling flow in a rectilinear circular pipe in terms of its optimality properties.

## Literature Review.

Since the inverse cascade of turbulent energy allows natural vortices to maintain a compact shape, swirling flows in pipes have been modeled based on the concept of compact vortices [11, 2, 9]. These studies essentially examine two types of swirling flows: helical flows [5] and flows with helical symmetry [2, 9]. In [8], the flow is termed "predominantly" Beltrami-Gromeka, as it is not helical throughout the entire domain: near a solid wall, viscous effects preclude the existence of such a flow. In this context, reference should be made to [10], which specifically analyzes the asymptotic behavior of swirling flow near the wall of a straight, circular-section pipe.

In this paper, the optimality of swirling flow in a rectilinear pipe of constant circular cross-section is examined using a unified approach based on the calculus of variations. Furthermore, the concept of swirling flow helicity—introduced by Moffatt [11] as a measure of extremality—is employed. Helicity is a physical quantity measurable in vortex tubes [12] and possesses the property of conservation [13]. Additionally, another property of helicity is demonstrated: swirling helical flows actually observed in nature and engineering exhibit an extremal helicity value. This value is zero. In light of this, an overview of recent research on the subject is presented.

A simplified model of helical vortex dynamics in the wake of an asymmetric rotor is examined in [14]. Models involving single and dual helical vortices are discussed in [15] and [16], respectively. Other studies focus on the interaction of helical vortex flow with other flows; for instance, the interaction between a helical vortex ring and a vortex line is analyzed in [17]. Issues regarding verification—specifically concerning the existence of such flows—are addressed in [18], which investigates the development of flow in the form of helical vortex pairs through both numerical and experimental methods. Studies concerning the breakdown of helical flow in helical tubes and helical rings are presented in [19]. Information on how axial flow affects the stability of a helical vortex tube can be found in [20]. Work [21] is devoted to the same topic of stability but focuses on the experimental realization (modeling and formation) of a helical vortex.

Helical vortex flows occur during the operation of a wind turbine. Theoretical research on this topic is presented in [22]. Work [23] is dedicated to the dynamics of helical vortices and vortex rings. Flow in the form of helical vortex pairs is examined in [24]. Issues regarding the stability and structure of the Zhukovsky model for the rotor wake are addressed in [25]. The topology of helical flows is studied in [26], while the internal structure of vortex rings and helical vortices is investigated in [27]. Helical vortices can exist in a state close to equilibrium while simultaneously evolving [28]. A stability analysis within the linear approximation is provided in [29].

## Research Methodology.

The aim of the study is to investigate the extremal properties of a steady swirling flow in a straight circular pipe.

This study is based on analytical methods, specifically the calculus of variations and the mathematical theory of fields.

This paper examines a class of incompressible fluid flows in which the velocity field satisfies the following relations:

$$V_r \equiv 0, \quad V_\theta = V_\theta(r), \quad V_z = V_z(r). \tag{1}$$

Essentially, two problems are considered. The first is the problem of a swirling flow with extremal helicity, and the second is a swirling flow with maximum vorticity and fluid flow rate.

## Results.

### Turbulent swirling flow with zero helicity

The first task is to identify, within class (1), the flow with extreme helicity:

$$J = \int_0^{2\pi}\int_0^{R}\left(rot\vec{V}\cdot\vec{V}\right)\cdot r dr d\varphi \to extr. \tag{2}$$

Turbulent stresses (or Reynolds stresses) for the flow described by (1). To understand the problem, let us present the Reynolds equations. Based on the general Reynolds equations, the form for (1) is as follows:

$$0 = \frac{d}{dr}\left(\tau_{r\theta}\right) + \frac{2}{r}\tau_{r\theta}, \tag{3}$$

$$0 = -\frac{dp}{dz} + \frac{1}{r}\frac{d}{dr}\left(\tau_{rz}\right). \tag{4}$$

Ordinary derivatives are used in equations (3)–(4). This is explained by relations (1) and the fact that the pressure is a function of the longitudinal coordinate only:

$$\frac{dp}{dz} = \Delta p = Const. \tag{5}$$

A distinctive feature of the Reynolds equations (3)–(4) is that they are expressed in terms of stresses, rather than in the conventional form involving velocity fluctuations. As will become evident, this allows for analytical solutions for the stresses. To this end, we employ the following form of equation (3):

$$\frac{d}{dr}\left(\tau_{rz}\right) = -\frac{2}{r}\tau_{r\theta}. \tag{6}$$

The general solution of equation (6) has the following form:

$$\tau_{r\theta} = \frac{Const}{r^2}. \tag{7}$$

Similarly, we use the following form of equation (4)

$$\frac{d}{dr}\left(r\tau_{rz}\right) = r\Delta p. \tag{8}$$

The general solution of equation (8) is

$$\tau_{rz} = \frac{1}{2}\Delta p r + \frac{Const}{r}. \tag{9}$$

As a result, analytical solutions (7) and (9) describing the Reynolds stresses for flow (1) have been obtained. Although these solutions exhibit a singularity at $r = 0$, they can still be used, since the flow is laminar near the axis ($r = 0$) and equations describing laminar flow should be employed there instead of equations (3)–(4).

**Determination of the averaged velocity field based on the helicity extremum condition.**

As it turns out, the condition of helicity extremum can determine the velocity field. Indeed, in accordance with condition (2), we find the components of the velocity curl:

$$\left(rot\vec{V}\right)_r \equiv 0, \quad \left(rot\vec{V}\right)_\theta = -\frac{dV_z}{dr}, \quad \left(rot\vec{V}\right)_z = \frac{1}{r}\frac{d\left(rV_\theta\right)}{dr}. \tag{10}$$

Substituting (10) into (2) yields:

$$J = \int_0^{2\pi}\int_0^{R}\left(V_z\frac{d\left(rV_\theta\right)}{dr} - rV_\theta\frac{dV_z}{dr}\right)drd\varphi \to extr\ . \tag{11}$$

Based on the form of the integrand in (11), we have:

$$\frac{\partial F}{\partial V_z} = \frac{d\left(rV_\theta\right)}{dr}, \quad \frac{\partial F}{\partial\left(\frac{dV_z}{dr}\right)} = -rV_\theta; \tag{12}$$

$$\frac{\partial F}{\partial V_\theta} = V_z, \quad \frac{\partial F}{\partial\left(\frac{dV_\theta}{dr}\right)} = rV_z. \tag{13}$$

The necessary condition for the extremum of functional (11) for the longitudinal component of the velocity is as follows

$$\frac{\partial F}{\partial V_z} - \frac{d}{dr}\left(\frac{\partial F}{\partial\left(\frac{dV_z}{dr}\right)}\right) = 0.$$

From this condition, the specific form follows.

$$V_z - \frac{d\left(rV_z\right)}{dr} = 0 \quad \Rightarrow \quad -r\frac{dV_z}{dr} = 0. \tag{14}$$

Similarly, for the rotational component of velocity

$$\frac{\partial F}{\partial V_\theta} - \frac{d}{dr}\left(\frac{\partial F}{\partial\left(\frac{dV_\theta}{dr}\right)}\right) = 0.$$

And therefore, the corresponding extremum condition is as follows:

$$\frac{d\left(rV_\theta\right)}{dr} - \frac{d\left(-rV_\theta\right)}{dr} = 0. \tag{15}$$

Equation (14) is equivalent to

$$-r\frac{dV_z}{dr}=0. \tag{16}$$

Its solution everywhere except ($r$=0) has the form:

$$V_z = Const. \tag{17}$$

From equation (15), we obtain:

$$V_\theta = \frac{Const}{r}. \tag{18}$$

Therefore, (17)-(18) is the desired solution. Since, according to (10),

$$\left(rot\vec{V}\right)_\theta = -\frac{dConst}{dr}\equiv 0,\ \left(rot\vec{V}\right)_z = \frac{1}{r}\frac{d\left(r\dfrac{Const}{r}\right)}{dr}\equiv 0$$

then (17)–(18) correspond to the minimum (zero) helicity of a swirling turbulent flow of class (1).

**Steady axisymmetric swirling flow**

Within the class of flows (1), let us identify a flow in which two extrema—a maximum of vorticity and a maximum of fluid discharge—are attained simultaneously.

$$J=\int_0^{2\pi}\int_0^R\left(rot\vec{V}\right)^2\cdot rdrd\varphi+\lambda\int_0^{2\pi}\int_0^R V_z\cdot rdrd\varphi\to extr. \tag{19}$$

For the flow described by (1), the components of the velocity curl (rotor) are given by expressions (10):

$$\left(rotV\right)_z=\frac{1}{r}\frac{\partial\left(rV_\theta\right)}{\partial r},\ \left(rotV\right)_\theta=-\frac{\partial V_z}{\partial r}.$$

Therefore, condition (19) takes the following form:

$$J=\int_0^{2\pi}\int_0^R\left[\left(\frac{\partial V_z}{\partial r}\right)^2+\left(\frac{1}{r}\frac{\partial\left(rV_\theta\right)}{\partial r}\right)^2\right]\cdot rdrd\varphi+\lambda\int_0^{2\pi}\int_0^R V_z\cdot rdrd\varphi\to extr. \tag{20}$$

Since the integrals in (20) have the same limits of integration, the overall integrand should be considered to be

$$F=\left[\left(\frac{\partial V_z}{\partial r}\right)^2+\left(\frac{1}{r}\frac{\partial\left(rV_\theta\right)}{\partial r}\right)^2\right]\cdot r+\lambda V_z\cdot r.$$

Analogously to formulas (12)–(13), we find the partial derivatives:

$$\frac{\partial F}{\partial V_\theta}=\frac{2V_\theta}{r}+2\frac{\partial V_\theta}{\partial r},\quad \frac{\partial F}{\partial\left(\dfrac{dV_\theta}{dr}\right)}=2V_\theta+2r\frac{dV_\theta}{dr}. \tag{21}$$

Substituting the expressions just obtained into the necessary condition for the extremum of the functional (20). Substituting (21) into (13) leads to the following equation:

$$\frac{d^2V_\theta}{dr^2}+\frac{1}{r}\frac{dV_\theta}{dr}-\frac{V_\theta}{r^2}=0. \tag{22}$$

Equation (22) is identical to the Navier-Stokes equation for the problem of fluid rotation when only the rotational velocity component is present and the velocity field depends solely on the radial coordinate. Recall that the general solution to (22) has the following form:

$$V_\theta = C_1 r + C_2 \frac{1}{r}.$$

It should be noted that this solution has components corresponding to both laminar and turbulent flow [30]. Let us use the second necessary condition for the extremum of functional (14).

Since

$$\frac{\partial F}{\partial V_z} = r\lambda(r); \qquad \frac{\partial F}{\partial\left(\frac{dV_z}{dr}\right)} = 2r\frac{dV_z}{dr},$$

then equation (14) takes the following explicit form:

$$r\lambda(r) - 2\frac{dV_z}{dr} - 2r\frac{d^2V_z}{dr^2} = 0. \tag{23}$$

The solution to equation (23) in the case of

$$\lambda(r) = 0$$

has the following form, well known for turbulent flow:

$$V_z = C_1 \ln r + C_2.$$

So, if we do not require the maximum flow rate condition from the flow, but only the maximum turbulence condition, then the flow is described by the well-known logarithmic law (this fact was first obtained earlier for ordinary flow in a pipe – without rotation; the corresponding article was submitted to the Journal of Turbulence). But in the case of satisfying the second extremity condition (maximum flow rate), the velocity field will be different. So, when

$$\lambda(r) = C_{lam} / r$$

the solution to equation (23) contains a solution well known in hydraulics:

$$V_z = C_{lam}\frac{r^2}{4} + C_1 \ln r + C_2. \tag{24}$$

For laminar flow in a circular pipe

$$C_1 = 0.$$

Note that for flow between concentric pipes, all three terms in (24) are non-zero. To understand the physics of the resulting solution, it should be treated as a piecewise continuous function: in the laminar flow region, the constant multiplying the logarithm is zero, whereas in the turbulent flow region, the logarithmic component must be included. Furthermore, other functions—such as Lagrange multipliers—may be specified if necessary to match an experimental profile.

## Conclusions.

Extremal properties of swirling flow—specifically helicity, vorticity, and flow rate—were investigated. The condition for extremal helicity allows for the derivation of the turbulent flow core (excluding the boundary layer) without recourse to the Boussinesq

hypothesis. Based on the derived analytical expression for the velocity field (which is also utilized in centrifugal pump theory), Reynolds stresses can be readily determined from the Reynolds equations. However, the principal conclusion drawn from this part of the study is that an optimal helical flow can possess only zero helicity—and this applies throughout the entire flow domain.

According to the generalized criterion of inertial stability [31], the velocity field in a turbulent flow must be such that the azimuthal velocity decreases more rapidly than the hyperbolic law dictates. Comparing equation (18) with this premise reveals that a real turbulent flow in a pipeline possesses an additional characteristic causing its velocity field to decay more sharply than a hyperbola. Such a vortex flow model is already known: the quasi-point vortex.

In addition to zero helicity, a swirling flow in a rectilinear circular pipe possesses two other optimal properties: maximum vorticity (or, more precisely, its square) and maximum fluid flow rate. It is the simultaneous application of these two conditions that yields well-known solutions corresponding to both laminar and turbulent incompressible fluid flows. In this context, the general solutions for azimuthal velocity satisfy the Navier-Stokes equations, while the longitudinal (axial) velocity satisfies an equation whose solution encompasses both laminar and turbulent flow By setting a particular integration constant to zero, it can be used separately for laminar and turbulent flows. Thus, both laminar and turbulent swirling flows in a rectilinear circular pipe are optimal.

Future research should focus on a more thorough investigation of the boundary layer in swirling flow and the identification of potential flow regions characterized by negative turbulent viscosity, which would further substantiate the optimal nature of swirling flow.

## References


1. Cengel Y.A., Cimbala J.M. Fluid Mechanics. Fundamentals and Applications. Mc Graw Hill Education. New York, 2018. 1024 p.
2. Lukianov P.V., Meshkov I, V. Helical flux structure and rate of fluid in curvilinear pipe with constant cross-section. *Promyslova Gygravlika I Pnevmatyka*, 2018. 2 (60). 5–22.
3. Lindborg E., Mohana A.V. A two-dimensional toy model for geophysical turbulence. *Physics of Fluids*, 2017. 29 (11). 111114. https://doi.org/10.1063/1.4985990
4. Oks D., Mininni P.D., Morio R., Pouquet A. Inverse cascade and stratified turbulence. *Physics of Fluids*, 2017. 29 (11). 111109. https://doi.org/10.1063/1.5001740
5. Biferale L., Meesascchio S., Toschi F. Inverse energy cascade in three-dimensional isotropic turbulence. *Physical Review Letters*, 2012. 108. 164501. https://doi.org/10.1103/PhysRevLett.108.164501
6. Mininni P.D. , Pouquet A. Inverse cascade behavior in freely decaying two-dimensional fluid turbulence. *Physical Review E*, 2013, 87. 033002. https://doi.org/10.1103/PhysRevE.87.033002
7. Compagne A., Gallet B., Moisy F., Cortel P.P. Direct and inverse energy cascades in a forced rotating turbulence experiment. *Physics of Fluids*, 2014. 26 (12). 125112. https://doi.org/10.1063/1.4904957
8. Lukianov P.V. Models of advanced screw (Beltrami-Gromeka) stationary compact vortex flows. *Promyslova Gygravlika I Pnevmatyka*, 2017. 4 (58). 17–24
9. Lukianov P.V. Stationary turbulent flow with helical symmetry of an incompressible fluid in a circular rectilinear pipe. *Promyslova Gygravlika I Pnevmatyka*, 2021. 1 (65). 27–36
10. Singh M.P., Simha P.C., Aggarwal M. Swirling flow in straight circular pipe. *ZAMM*. 1980. 60. 429–436
11. Moffat H.K., Tsinober A. Helicity in laminar and turbulent flow. *Annual Review of Fluid Mechanics*, 1992. 24. 281–312
12. Scheeler M.W., van Rees W.M., Kedia H., Kleckner D., Irwine W.T.M. Complete measurements of helicity and its dynamics in vortex tubes. *Science*, 2017. 357. 487–491. https://doi.org/10.1126/science.aam6897
13. Salman H. Helicity conservation and twisted Seifert surfaces for superfluid vortices. *Proceedings of the Royal Society*, 2017. A 473. 20160853. https://doi.org/10.1098/rspa.2016.0853

14. Abraham A., Castillo-Castellanos A., Leweke T. Simplified model foe helical vortex dynamics in the wake of an asymmetric rotor. *Flow*. 2023. 3E5. https://doi.org/10.1017/flo.2022.33

15. Fuentes O.V. Motion of helical vortex. *Journal of Fluid Mechanics*, 2018. 836. R1. https://doi.org/10.1017/jfm.2017.845

16. Fuentes O.V. Flow topology of helical vortices. *Journal of Fluid Mechanics*, 2018. 842. R2. https://doi.org/10.1017/jfm.2018.181

17. Bai W.K., Yang X., Zhu H., Gardiner S.A., Lin W.M., Yang T. Dynamics of helical vortex ring interacting with a vortex line. *Communications Physics.* 2025, 8 (183). https://doi.org/10.1038/s42005-025-02109-x

18. Mc Donough J.R., Ahmed S.M.R., Phan A.N., Harvey A.P. The development of helical vortex pair in oscillatory flows ÷A numerical and experimental study. *Chemical Engineering and Processing*. 2019. 143. 107588. https://doi.org/10.1016/j.cep.2019.107588

19. Ji L., van Rees W.M. Vortex bursting and associated twist dynamics on helical vortex tubes and vortex rings. *Journal of Fluid Mechanics*, 2024. 986. A34. https://doi.org/10.1017/jfm.2024.367

20. Hattory Y., Fukumoto Y. Effects of axial flow on the stability of helical vortex tube. *Physics of Fluids*, 2012. 24 (5). 054102. https://dx.doi.org/10.1063/1.4717769

21. Brynjall-Rahkola M., Hennigton D.S. Numerical realization of helical vortices: application to vortex instability. *Theoretical and Computational Fluid Dynamics*, 2020. 34. 1–20. https://doi.org/10.1007/s00162-019-00509-8

22. John I.H., Wood D.H., Vaz J.R.P. Helical vortex theory and blade element analysis of multi-bladed windmill. *Wind Energy*, 2023. 26 (2). 228–246. https://doi.org/10.1002/we.2796

23. Sonin E.B. Dynamics of helical vortices and helical-vortex rings. *Europhysics Letters*, 2012. 97 (4). 46002. https://doi.org/10.1209/0295-5075/97/46002

24. Duran Venegas E., Le Dizes S. Generalized helical vortex pairs. *Journal of Fluid Mechanics*, 2019. 865. 523-545. https://doi.org/10.1017/jfm.2019.65

25. Duran Venegas E., Rien P., Le Diezes S. Structure and stability of Joukowski's rotor wake model. *Journal of Fluid Mechanics*, 2021. 911 A6. https://doi.org/10.1017/jfm.2020.985

26. Andersen M., Brons M. Topology of helical fluid flows. *European Journal of Applied Mathematics*, 2011. 25 (3). 225–396. https://doi.org/10.1017/S0956792514000084

27. Blanco Rodrigues Le Diezes S., Selcuk C., Delbende L., Rossi M. Internal structure of vortex rings and helical vortices. *Journal of Fluid Mechanics*, 2015. 785. 219–247. https://doi.org/10.1017/jfm.2015.631

28. Selcuk S., Delbende L., Rossi M. Helical vortices quasiequilibrium states and their time evolution. *Physical Review Fluids*, 2017. 2. 0084701. https://doi.org/10.1103/PhysRevFluids.2.084701

29. Selcuk S.C., Delbende I., Rossi M. Helical vortices: linear stability analysis and nonlinear dynamics. *Fluid Dynamics Research*, 2017. 50 (1). 011411. https://doi.org/10.1088/1873-7005/aa73e3

30. Huisman S.G., van Gils D.P.M., Grossman S., Sun C., Lohse D. Ultimate turbulent Taylor-Couette flow. *Physical Review Letters*, 2012. 108. 024501. https://doi.org/10.1103/PhysRevLett.108.024501

31. Lukianov P.V. Inertial stability as a result of relation between transport and relative fluid rotation. *Research Bylletin of National Technical University of Ukraine "Kyiv Polytechnic Institute"*. 2014; 4(196):133-138. (in Ukrainian). Available at https://ela.kpi.ua/handle/123456789/9935

*Дата першого надходження статті до видання 28.09.2026*
*Дата прийняття статті до друку після рецензування 22.10.2026*
*Дата публікації (оприлюднення) статті 04.11.2026*
*Стаття поширюється на умовах ліцензії відкритого доступу(CC BY 4.0)*

# ОПТИМАЛЬНІ ВЛАСТИВОСТІ НЕСТИСЛИВОЇ ЗАКРУЧЕНОЇ ТЕЧІЇ У ПРЯМОЛІНІЙНІЙ КРУГЛІЙ ТРУБІ

**П. Лук'янов[1], К. Павлова[1], М. Трофименко[1]**
[1] *Національний університет «Київський авіаційний інститут»*

***Анотація***

Закручені течії часто зустрічаються у технічних пристроях, зокрема у гідравлічних та пневматичних. Досконала робота цих пристроїв не може бути досягнута без повного розуміння фізики цих течій. А вона, ця фізика, як виявляється, має оптимальний характер. Дійсно, адже ніхто, крім законів природи, не примушує воду текти у гірських струмках у вигляді закрученої течії (спостереження австрійського лісничого Віктора Шаубергера), а воду у ванні набувати закрутку. Раніше були проведені експериментальні дослідження у лабораторії. І ці дослідження дійсно виявили існування таких режимів турбулентної течії рідини у трубі із примусовою закруткою. Крім того, стало очевидним, що природа таких течій є дуже складною. Тому саме властивості оптимальності допомагають там, де існуючі моделі неспроможні самостійно впоратися із коректним описам течії. В роботі надано огляд сучасних робіт і досягнень щодо закручених течій, висвітлена проблема їх адекватного опису. На підставі цього сформульована мета даної роботи. Вона полягає у об'єднанні та систематизації вже відомого знання та отримання нового ÷ властивостей оптимальності закрученої течії. До цього вже були отримані такі результати, як відмінність ламінарної течії у примежовому шарі у випадках внутрішньої та зовнішньої задач. Також виявлено різницю між природою турбулентних течій у примежових шарах у круглій трубі та на плоский пластині. Звичайна розвинена турбулентна течія у круглій трубі має логарифмічний профіль, так само як і течія на плоскій пластині. Але якщо у першому випадку виконується умова максимального завихрення (точніше квадрату завихрення), то у другому випадку логарифмічний профіль є результатом виконання двох екстремумів ÷ максимуму квадрату виразу, що описує інерційну нестійкість, та мінімуму витрати рідини. Зазначені щойно ідеї та отримані за ними результати слугували основою для наведених у даній роботі досліджень. В результаті показано, що закручені течії у прямолінійній трубі кругового перерізу мають властивості оптимальності. Так течія із екстремальною спіральністю має рівну нулеві спіральність у кожній точці. Що стосується закрученої течії, у якої поле швидкості залежить лише від радіальної координати, то вона теж оптимальна. Для ламінарної течії – це властивість максимальної витрати, а для турбулентної течії додається ще максимальне значення квадрату завихрення. Отримані результати порівняються з вже відомими теоретичними та експериментальними даними.

***Ключові слова:*** закручена течія, прямолінійна труба, оптимальні властивості.

**DOI https://doi.org/10.32782/1994-4691-2026-1-77-2**
UDK 621.225

# IMPROVEMENT THE GLOBAL ENERGY EFFICIENCY OF HYDRAULIC SYSTEMS OF TECHNOLOGICAL EQUIPMENT

# ПІДВИЩЕННЯ ГЛОБАЛЬНОЇ ЕНЕРГОЕФЕКТИВНОСТІ ГІДРАВЛІЧНИХ СИСТЕМ ТЕХНОЛОГІЧНОГО ОБЛАДНАННЯ

Xu Mingwei[1*], PhD Student ORCID: 0009-0001-9165-1014

[1] *Ukrainian State University of Railway Transport, Kharkiv, Ukraine*
*e-mail: voronin.sergey@ukr.net

**Abstract**. This paper investigates multi-scale power losses and global energy-efficiency optimization in process machinery hydraulic systems. Power-loss mechanisms are analyzed at three levels: micro (components), meso (circuits), and macro (system), and a quantitative model accounting for their interactions is developed. A global energy-efficiency model is established, and a collaborative control strategy based on an improved adaptive genetic algorithm (IAGA) is proposed to optimize energy consumption and dynamic performance. Simulation and experimental results confirm that hydraulic pump volumetric losses, control valve throttling losses, and circuit coupling losses account for over 75% of total power losses. The proposed strategy improves system energy efficiency by 12%–18% and reduces dynamic response overshoot by more than 60%. The results provide a theoretical and practical basis for energy-efficient hydraulic system design and control.

**Keywords**: process machinery; hydraulic system; power loss; multi-scale mechanism; global energy efficiency; collaborative control.

## Introduction.

Process machinery is the core equipment of industrial production, covering fields such as metallurgical rolling mills, CNC machine tools, mining machinery, and injection molding machines. Its operational stability, efficiency, and energy consumption directly determine the quality, cost, and environmental performance of industrial production. Hydraulic transmission, as the core power transfer mode of process machinery, has become the preferred transmission scheme for most medium- and large-scale process machinery by virtue of its advantages of high-power density, fast response, precise positioning, and strong resistance to load impact, occupying an irreplaceable position in modern industrial production.

However, process machinery hydraulic systems exhibit significant power losses during energy conversion and transmission. Industrial field measurement data show that the energy efficiency of traditional process machinery hydraulic systems generally ranges between 45% and 60%, far lower than that of electrical drive systems, with a large amount of energy wasted in the form of heat and leakage [10, 14]. With the intensification of the global energy crisis and the advancement of the "dual carbon" goal, the pressure for energy conservation and emission reduction in the industrial sector is increasing. As high-energy-consuming equipment, improving the energy efficiency of the hydraulic systems of process machinery has become a key engineering problem to be solved urgently [1, 9].

Compared with ordinary hydraulic systems, process machinery hydraulic systems are characterized by complex and variable operating conditions (large load fluctuations, frequent start-stop, wide speed regulation range), the collaborative operation of multiple actuators, and the coupling of multiple circuits [3, 11]. Consequently, their power losses exhibit obvious multi-scale characteristics: at the micro level, friction and leakage losses exist inside components such as hydraulic pumps, cylinders, and control valves; at the meso level, uneven flow distribution and pressure interference among circuits give rise to coupling losses; and at

the macro level, overall system power matching imbalance causes redundant losses. The losses at different scales are coupled and mutually influential, making it difficult for traditional single-scale, single-component energy-saving control methods to achieve a significant improvement in the global energy efficiency of the system [4, 12, 14].

Therefore, an in-depth investigation of the multi-scale mechanism of power loss in process machinery hydraulic systems, the revelation of the coupling laws among losses at different scales, and the proposal of a global energy-efficiency collaborative control method that considers both multi-scale loss compensation and system dynamic performance can not only enrich the theoretical system of hydraulic system energy-efficiency optimization [2, 13].but also provide a practical and feasible technical solution for the energy-saving retrofit of process machinery hydraulic systems in industrial sites, reduce industrial energy consumption and environmental pollution, and promote the green and efficient upgrading of the process machinery industry. This has important theoretical significance and engineering application value [2, 3, 13].

## Literature Review.

In recent years, scholars at home and abroad have carried out extensive research on power loss and energy-efficiency optimization of hydraulic systems, forming a series of theoretical and technical achievements, mainly focusing on three aspects: loss mechanism analysis, energy-saving design of individual components, and control strategy optimization [5, 7, 10].

In the field of power-loss mechanism research, early foreign scholars focused mainly on the loss analysis of individual components, such as establishing leakage and friction models of hydraulic pumps to quantify volumetric and mechanical losses, and proposing loss-suppression methods based on component structure optimization [1, 14]. With the deepening of research, attention gradually shifted to the problem of loss coupling at the system level, and a "component–system" two-level loss analysis framework was proposed [11]. However, the boundaries of multi-scale losses were not clearly defined, and research on meso-scale circuit coupling losses remains relatively weak [14]. Domestic scholars, on the other hand, have focused more on the loss measurement and analysis of hydraulic systems at industrial sites, quantifying the loss distribution of hydraulic systems under different operating conditions by building experimental platforms, but most of this research remains at the macro level, lacking in-depth research on the coupling mechanism of multi-scale losses and making it difficult to reveal the essential causes of loss generation [3, 9].

In the field of energy-saving design of individual components, scholars at home and abroad have mainly focused on structural improvements to core components such as hydraulic pumps and control valves, such as replacing fixed-displacement pumps with variable-displacement pumps to achieve matching between flow and load by adjusting displacement, thereby reducing redundant losses; and developing low-leakage, low-friction hydraulic valves to reduce throttling and leakage losses [1, 4, 6]. In addition, the research and application of new energy-saving components (such as digital hydraulic valves and high-efficiency variable-displacement pumps) have provided new technical paths for energy saving at the component level. However, such methods target only individual components and do not consider the coupling relationships among components and circuits, making it difficult to achieve an improvement in the global energy efficiency of the system [4].

In the field of control strategy optimization, foreign research has mainly focused on the application of advanced control algorithms, such as fuzzy control, PID control, and model predictive control, to achieve precise control of flow and pressure in hydraulic systems and reduce throttling losses [5]. Domestic research has focused more on the engineering application of load-sensing control and variable-frequency speed-regulation technologies, which achieve matching between energy supply and load demand by dynamically adjusting system operating parameters [5, 9, 12]. However, most existing control strategies focus on

energy-efficiency optimization under a single operating condition or at a single scale, lacking collaborative consideration of multi-scale losses [12]. In the complex and variable operating scenarios of process machinery, it is difficult to balance system energy efficiency and dynamic performance, and the control effect is limited [12, 13, 15].

In summary, existing research still has three prominent problems [3]. First, the analysis of power-loss mechanisms lacks a multi-scale perspective, and the boundaries and coupling laws of losses at different scales have not been clearly defined, making it difficult to comprehensively reveal the essential causes of loss generation. Second, energy-efficiency control strategies lack global coordination, mostly targeting individual components or single operating conditions, and cannot achieve collaborative suppression of multi-scale losses [3, 11]. Third, the correlation between multi-scale loss models and energy-efficiency models is insufficient, making it difficult to provide precise theoretical support for global collaborative control [8, 13]. Therefore, carrying out research on the multi-scale mechanism of power loss and the global energy-efficiency collaborative control of process machinery hydraulic systems has become a research hotspot and difficulty in the field of hydraulic system energy saving [2, 10].

This paper carries out systematic research on the multi-scale mechanism of power loss and the global energy-efficiency improvement collaborative control of process machinery hydraulic systems [3]. The specific research content is as follows:

1. Multi-scale classification and mechanism analysis of power loss in process machinery hydraulic systems. The multi-scale classification criterion (micro, meso, macro) is defined, the causes and influencing factors of power loss at each scale are analyzed separately, quantitative models of power loss at each scale are established, and the coupling laws of multi-scale losses are revealed [4, 9, 11, 14].

2. Global energy-efficiency modeling of process machinery hydraulic systems. Based on the multi-scale power-loss model and the energy balance principle, a global energy-efficiency model covering "component–circuit–system" is constructed, and the relationship between multi-scale losses and system energy efficiency is established, providing a theoretical basis for energy-efficiency optimization control [2, 10].

3. Design of the global energy-efficiency collaborative control strategy. In view of the coupling characteristics of multi-scale losses, a control strategy integrating multi-scale loss compensation and global parameter collaborative optimization is proposed [13], and an improved adaptive genetic algorithm–based optimization controller is designed to achieve coordinated improvement of system energy consumption and dynamic performance.

4. Simulation and experimental verification. A simulation platform based on Simulink/SimHydraulics is built to verify the effectiveness of the multi-scale loss model and the collaborative control strategy; an experimental platform for the process machinery hydraulic system is constructed, and the practicability and reliability of the proposed method are further verified through measured data [2, 4].

The innovations of this paper are mainly reflected in the following three aspects:

1. A multi-scale classification criterion for power loss in process machinery hydraulic systems is proposed, and a "micro–meso–macro" three-level loss quantitative model is constructed, clarifying the coupling mechanism among losses at different scales. This breaks through the limitation of traditional single-scale loss analysis and can reveal the essential causes of loss generation more comprehensively and accurately [5, 7, 9].

2. A global energy-efficiency model covering multi-scale losses is established, directly correlating the losses at different scales with system energy efficiency. This solves the problem that traditional energy-efficiency models cannot reflect the influence of multi-scale coupling and provides precise theoretical support for global energy-efficiency optimization control [2].

3. A multi-scale collaborative global energy-efficiency improvement control strategy is proposed, integrating multi-scale loss compensation and parameter collaborative optimization,

and an improved adaptive genetic algorithm controller is designed [4, 6]. This achieves coordinated improvement of system energy efficiency and dynamic performance, solving the difficulty of balancing energy efficiency and dynamic performance in traditional control strategies [8,15].

## Research Methodology.

### Multi-Scale Mechanism Analysis of Power Loss in Process Machinery Hydraulic Systems

#### Multi-Scale Classification Criterion and Boundary Definition

Combining the structural characteristics and energy transfer laws of process machinery hydraulic systems, this paper divides power loss into three scales—micro, meso, and macro—and clarifies the boundaries and research objects of each scale to ensure the systematicness and pertinence of the multi-scale mechanism analysis [3, 9, 14].

1. Micro scale: The core components of the hydraulic system (hydraulic pump, cylinder, control valve, hydraulic motor, etc.) are taken as the research objects, focusing on power loss inside the components, mainly including friction loss, leakage loss, and throttling loss. The essential cause of these losses is the interaction among the internal structure, material properties, and operating parameters of the components [1, 7, 13].

2. Meso scale: A single circuit or the coupling part of multiple circuits of the hydraulic system is taken as the research object, focusing on power loss at the circuit level, mainly including uneven flow distribution loss, pressure interference loss, and pipeline friction (distributed) and local resistance losses. The essential cause of these losses is the insufficient cooperative matching among components [11, 13, 14].

3. Macro scale: The entire process machinery hydraulic system is taken as the research object, focusing on the power loss of the whole system, mainly including power matching imbalance loss, redundant power loss, and auxiliary system loss (e.g., cooling and filtration systems) [3, 10]. The essential cause of these losses is the mismatch between the overall system operating parameters and the process operating-condition requirements [2].

The three scales are interrelated and mutually coupled: micro component losses form the basis of meso circuit losses and macro system losses; meso circuit losses are the concentrated manifestation of micro component losses and simultaneously influence the distribution of macro system losses; macro system losses reflect the overall effect of multi-scale losses [1, 4, 10]. Together, the three scales determine the overall energy efficiency of the process machinery hydraulic system [11].

#### Micro-Scale Power-Loss Mechanism and Quantitative Model

Micro-scale power loss mainly originates from core components such as the hydraulic pump, cylinder, and control valve, whose loss types and mechanisms differ. They are analyzed separately and quantitative models are established below [2, 5, 14].

#### Power Loss of the Hydraulic Pump

As the power source of the hydraulic system, the power loss of the hydraulic pump mainly includes volumetric loss, mechanical loss, and hydraulic loss, among which volumetric and mechanical losses are the main forms (accounting for more than 90% of the total pump loss) [1, 14].

1. Volumetric loss. Due to internal clearances of the hydraulic pump (e.g., between the rotor and the stator, and between the vanes and the slots), part of the hydraulic oil leaks from the high-pressure chamber to the low-pressure chamber, causing flow loss and thereby producing volumetric loss [14]. According to the principles of fluid mechanics, the volumetric loss power can be expressed as:

$$P_{vol} = \Delta p_p \cdot Q_{leak} \quad (1)$$

where $P_{vol}$ is the volumetric loss power of the hydraulic pump (W); $\Delta p_p$ is the pressure difference between the inlet and outlet of the pump (Pa); and $Q_{leak}$ is the leakage flow ($m^3/s$).

The leakage flow is related to factors such as clearance size, pressure difference, and oil viscosity [6, 10]. For laminar leakage through an annular clearance, the calculation formula is:

$$Q_{leak} = \frac{\pi d h^3 \Delta p_p}{12 \mu L}(1 + 1.5\varepsilon^2) \quad (2)$$

where d is the mating surface diameter (m); h is the mating clearance (m); μ is the dynamic viscosity of the hydraulic oil (Pa·s); L is the mating surface length (m); and ε is the eccentricity ratio.

2. Mechanical loss. Owing to the friction between the moving parts inside the hydraulic pump (such as between the vanes and the slots, and between the rotor and the bearings), as well as the viscous friction of the hydraulic oil, part of the input power is consumed, producing mechanical loss [1, 5, 7]. The mechanical loss power can be expressed as:

$$P_{mech} = T_f \cdot \omega \quad (3)$$

where $P_{mech}$ is the mechanical loss power of the hydraulic pump (W); $T_f$ is the total friction torque (N·m); and ω is the angular velocity of the pump (rad/s).

The total friction torque comprises the solid friction torque and the viscous friction torque:

$$T_f = T_{solid} + T_{viscous} = fF_n r + \mu A \omega r \quad (4)$$

where $T_{solid}$ is the solid friction torque (N·m); $T_{viscous}$ is the viscous friction torque (N·m); f is the friction coefficient; $F_n$ is the normal force (N); r is the friction radius (m); and A is the viscous friction area ($m^2$).

The total micro-scale loss power of the hydraulic pump is the sum of the volumetric loss and the mechanical loss:

$$P_{pump} = P_{vol} + P_{mech}. \quad (5)$$

**Power Loss of the Control Valve**

The control valve is the control core of the hydraulic system, and its power loss is mainly throttling loss, i.e., when the hydraulic oil passes through the valve port, a pressure drop occurs due to the throttling effect, and part of the energy is converted into heat and lost [3,7,13]. According to the throttling principle, the throttling loss power can be expressed as:

$$P_{thr} = \Delta p_v \cdot Q_v \quad (6)$$

where $P_{thr}$ is the throttling loss power of the control valve (W); $\Delta p_v$ is the pressure difference across the valve port (Pa); and $Q_v$ is the flow through the valve port ($m^3/s$).

According to the thin-walled orifice flow formula, the flow through the valve port can be expressed as:

$$Q_v = C_d A_v \sqrt{\frac{2\Delta p_v}{\rho}} \quad (7)$$

where $C_d$ is the flow coefficient; $A_v$ is the orifice area of the valve port ($m^2$); and ρ is the density of the hydraulic oil ($kg/m^3$).

**Power Loss of the Hydraulic Cylinder**

As the actuator, the power loss of the hydraulic cylinder mainly includes leakage loss and friction loss, which are similar to those of the hydraulic pump but differ in mechanism [12].

1. Leakage loss. This is divided into internal leakage and external leakage. Internal leakage refers to the leakage of hydraulic oil from the rodless chamber to the rod chamber of

the cylinder, while external leakage refers to the leakage of hydraulic oil to the outside through the clearances between the cylinder body and the piston and between the piston rod and the seals. Internal leakage is the main form [2, 9, 11, 15]. The leakage loss power can be expressed as:

$$P_{cyl,leak} = \Delta p_c \cdot Q_{c,leak} \quad (8)$$

where $P_{cyl.leak}$ is the leakage loss power of the cylinder (W); $\Delta p_c$ is the pressure difference between the two chambers of the cylinder (Pa); and $Q_{c.leak}$ is the cylinder leakage flow ($m^3/s$).

2. Friction loss. Owing to the friction between the piston and the cylinder body and between the piston rod and the seals [13], part of the hydraulic energy is consumed. The friction loss power can be expressed as:

$$P_{cyl,fric} = F_{cf} \cdot v \quad (9)$$

where $P_{cyl.frec}$ is the friction loss power of the cylinder (W); $F_{cf}$ is the piston motion friction force (N); and v is the piston motion velocity (m/s).

The total micro-scale loss power of the hydraulic cylinder is:

$$P_{cyl} = P_{cyl,leak} + P_{cyl,fric} \quad (10)$$

**Meso-Scale Power-Loss Mechanism and Quantitative Model**

Meso-scale power loss mainly originates from the coupling and matching insufficiency at the circuit level [10]. The single-circuit resistance loss and the multi-circuit coupling loss are analyzed, and quantitative models are established in combination with the circuit characteristics of process machinery hydraulic systems (such as multi-actuator collaborative circuits and high/low-pressure circuits) [3].

**Pipeline Resistance Loss**

The hydraulic pipeline is the carrier of energy transfer. When hydraulic oil flows in the pipeline, it is subjected to distributed and local resistance, producing pipeline resistance loss [11, 12]. The loss power can be expressed as:

$$P_{pipe} = \Delta p_{pipe} \cdot Q_{pipe} \quad (11)$$

where $P_{pipe}$ is the pipeline resistance loss power (W); $\Delta p_{pipe}$ is the total pipeline pressure loss (Pa); and $Q_{pipe}$ is the flow in the pipeline ($m^3/s$).

The total pipeline pressure loss includes the distributed pressure loss and the local pressure loss:

$$\Delta p_{pipe} = \Delta p_{dis} + \Delta p_{loc} = \lambda \frac{L}{d} \frac{\rho v^2}{2} + \zeta \frac{\rho v^2}{2} \quad (12)$$

where $\Delta p_{dis}$ is the distributed pressure loss (Pa); $\Delta p_{loc}$ is the local pressure loss (Pa); $\lambda$ is the distributed resistance coefficient; L is the pipeline length (m); d is the pipeline inner diameter (m); v is the flow velocity of the hydraulic oil in the pipeline (m/s); and $\zeta$ is the local resistance coefficient (determined by local structures such as bends and joints).

**Multi-Circuit Coupling Loss**

Process machinery hydraulic systems mostly adopt a multi-actuator collaborative working mode (e.g., the feed circuit and the spindle circuit of machine tools, the screw-down circuit and the drive circuit of metallurgical rolling mills). There exist problems such as uneven flow distribution and pressure interference among circuits, resulting in coupling loss [13,14]. The coupling loss power can be expressed as:

$$P_{coup} = \sum_{i=1}^{n} \sum_{j=i+1}^{n} \Delta p_{ij} \cdot Q_{ij} \quad (13)$$

where $P_{coup}$ is the multi-circuit coupling loss power (W); n is the number of circuits; $\Delta p_{ij}$ is the pressure interference difference between circuit i and circuit j (Pa); and $Q_{ij}$ is the interference flow between the two circuits ($m^3/s$). Note that the interference flow here is defined strictly as the cross-circuit exchange flow beyond the designed flow distribution, so as to avoid double counting with the pipeline friction loss.

The total meso-scale loss power is the sum of the pipeline resistance loss and the multi-circuit coupling loss:

$$P_{meso} = P_{pipe} + P_{coup} \quad (14)$$

**Macro-Scale Power-Loss Mechanism and Quantitative Model**

Macro-scale power loss is mainly manifested as the power matching imbalance and redundant loss of the whole system. In view of the operating characteristics of process machinery (large load fluctuations, frequent start-stop), the power matching loss and the auxiliary system loss are analyzed, and quantitative models are established [7].

**Power Matching Loss**

The power matching loss refers to the redundant power loss caused by the mismatch between the output power of the hydraulic system and the load-demand power of the process. When the system output power is greater than the load-demand power, the redundant power is consumed in forms such as overflow and throttling; when the system output power is smaller than the load-demand power, the system cannot work normally and additional power must be consumed to compensate [9,13]. The power matching loss power can be expressed as:

$$P_{match} = P_{out} - P_{load} \quad (15)$$

where $P_{match}$ is the power matching loss power (W); $P_{out}$ is the output power of the hydraulic system (W); and $P_{load}$ is the process load-demand power (W).

The output power of the hydraulic system is the sum of the output powers of the individual components, while the load-demand power is determined by the process operating conditions and can be obtained by measurement or calculation from process parameters [10].

**Auxiliary System Loss**

The auxiliary systems of process machinery hydraulic systems (cooling, filtration, and lubrication systems) also consume a certain amount of power during operation, forming auxiliary system loss [1,2,8]. The loss power is mainly determined by the rated power and operating efficiency of the auxiliary equipment:

$$P_{aux} = \sum_{k=1}^{m} \frac{P_{k.rated}}{\eta_k} \quad (16)$$

where $P_{aux}$ is the auxiliary system loss power (W); m is the number of auxiliary devices; $P_{k.rated}$ is the rated power of the k-th auxiliary device (W); and $\eta_k$ is the operating efficiency of the k-th auxiliary device.

The total macro-scale loss power is the sum of the power matching loss and the auxiliary system loss:

$$P_{macro} = P_{match} + P_{aux} \quad (17)$$

**Analysis of the Coupling Law of Multi-Scale Losses**

The multi-scale losses of process machinery hydraulic systems are not independent of each other but exhibit significant coupling relationships [11]. The coupling law is mainly reflected in three aspects:

1. Coupling between micro component losses and meso circuit losses. The leakage and friction losses of micro components cause fluctuations in the flow and pressure of the circuit, which in turn aggravate the pipeline resistance loss and the multi-circuit coupling loss; conversely, the pressure interference and uneven flow distribution of meso circuits cause the

operating parameters of components to deviate from the optimal values, further increasing micro component losses. For example, the leakage loss of the hydraulic pump causes insufficient circuit flow; to satisfy the load demand, the control valve must increase the valve-port opening, resulting in increased throttling loss, while the intensified circuit pressure fluctuation increases the pipeline resistance loss [3, 7, 12, 14, 15].

2. Coupling between meso circuit losses and macro system losses. Meso circuit losses cause a decrease in the overall output power of the system [9]. To maintain normal system operation, the input power of the hydraulic pump must be increased, thereby increasing the macro power matching loss; conversely, macro power matching imbalance causes the pressure and flow of the circuit to be in a non-optimal state, aggravating meso circuit losses. For example, when the system power matching is insufficient, the hydraulic pump must operate at a high speed and high pressure for a long time, causing the circuit pressure to be too high and significantly increasing the pipeline resistance loss and the coupling loss [2, 5].

3. Indirect coupling between micro component losses and macro system losses. The accumulation of micro component losses leads to a decline in the overall system energy efficiency, which in turn aggravates the macro power matching loss; macro power matching imbalance causes components to operate in a harsh state for a long time, accelerating component wear and increasing micro losses [4]. For example, if the hydraulic pump operates at a high load for a long time, the friction between the vanes and the slots intensifies, the micro mechanical loss increases, and meanwhile the system energy efficiency decreases and the macro power matching loss further increases [1, 9].

Based on the above coupling law, the total system power loss is the sum of the losses at the three scales:

$$P_{total} = P_{micro} + P_{meso} + P_{macro} \quad (18)$$

where $P_{micro}$ is the total micro-scale loss power (W).

**Global Energy-Efficiency Modeling of Process Machinery Hydraulic Systems**

**Global Energy-Efficiency Definition and Evaluation Indicators**

The global energy efficiency of a process machinery hydraulic system is defined as the ratio of the effective output power to the input power over the entire working cycle, reflecting the efficiency of multi-scale energy conversion and transfer across "component–circuit–system":

$$\eta_{global} = \frac{P_{eff}}{P_{in}} \times 100\% \quad (19)$$

where $\eta_{global}$ is the global system energy efficiency (%); $P_{eff}$ is the effective output power of the system (W), i.e., the power used to drive the process load; and $P_{in}$ is the input power of the system (W), i.e., the input power of the hydraulic pump.

Combined with the multi-scale loss characteristics, the effective output power equals the system input power minus the total multi-scale loss power:

$$P_{eff} = P_{in} - P_{total} \quad (20)$$

To comprehensively evaluate the global energy efficiency, in addition to the global energy efficiency, the following auxiliary evaluation indicators are defined:

1. Micro energy efficiency: the ratio of the effective output power to the input power of a component, reflecting the energy conversion efficiency of the micro component [3];

2. Meso energy efficiency: the ratio of the effective output power to the input power of a circuit, reflecting the energy transfer efficiency at the circuit level [9];

3. Energy consumption reduction rate: the ratio of the difference between the total energy consumption after optimization and that before optimization to the total consumption before optimization, reflecting the effect of energy-efficiency optimization [11];

4. Dynamic performance indicators: including system response time and overshoot, used to evaluate the change in system dynamic performance during energy-efficiency optimization to ensure that the energy-efficiency improvement does not affect normal system operation [14].

**Establishment of the Global Energy-Efficiency Model**

Based on the multi-scale power-loss model and the energy balance principle, combined with the structural characteristics and operating-condition characteristics of process machinery hydraulic systems, a global energy-efficiency model covering "micro–meso–macro" is established [2, 13].

First, the micro component energy-efficiency model is established [10]. Taking the hydraulic pump, control valve, and cylinder as the core, their energy-efficiency models are established respectively:

$$\eta_{pump} = \frac{P_{pump,out}}{P_{pump,in}} \times 100\%, \quad (21)$$

$$\eta_{valve} = \frac{P_{valve,out}}{P_{valve,in}} \times 100\%, \quad (22)$$

$$\eta_{cyl} = \frac{P_{cyl,out}}{P_{cyl,in}} \times 100\%. \quad (23)$$

The total micro-scale energy efficiency is the weighted average of the energy efficiencies of the individual components, with the weights being the proportions of the input power of each component in the total micro-scale input power:

$$\eta_{micro} = \sum_{i=1}^{k} w_i \eta_i, \sum_{i=1}^{k} w_i = 1 \quad (24)$$

where k is the number of micro components; $w_i$ is the weight of the i-th component; and $\eta_i$ is the micro energy efficiency of the i-th component.

Second, the meso circuit energy-efficiency model is established. The meso circuit energy efficiency is the ratio of the effective output power of the circuit to the input power of the circuit [9]. Considering the pipeline resistance loss and the multi-circuit coupling loss, the model is:

$$\eta_{meso} = \frac{P_{circuit,eff}}{P_{circuit,in}} \times 100\% \quad (25)$$

where $\eta_{meso}$ is the meso circuit energy efficiency (%); $P_{circuit.eff}$ is the effective output power of the circuit (W); and $P_{circuit.in}$ is the input power of the circuit (W), equal to the sum of the output powers of the components.

Finally, the macro system global energy-efficiency model is established. The macro system input power is the input power of the hydraulic pump, and the effective output power is the load-demand power [14]. Combined with the multi-scale losses, the global energy-efficiency model is:

$$\eta_{global} = \frac{P_{in} - P_{total}}{P_{in}} \times 100 = \left(1 - \frac{P_{micro} + P_{meso} + P_{macro}}{P_{in}}\right) \times 100\%. \quad (26)$$

Substituting the micro, meso, and macro loss models into the above equation yields the relationship between the global energy efficiency and the parameters at each scale (such as component structural parameters, circuit parameters, and system operating parameters), providing a theoretical basis for subsequent energy-efficiency optimization control [3, 6, 11], as shown in Fig.1.

**Model Validation and Parameter Identification**

To ensure the accuracy and reliability of the global energy-efficiency model, parameter identification and experimental validation are carried out to adjust the model parameters so that the model output is consistent with the actual system [12].

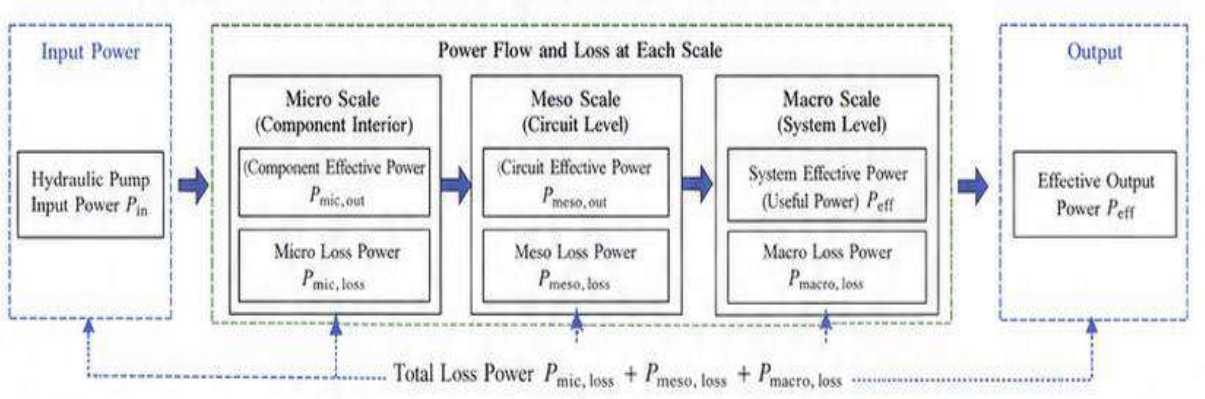



**Fig. 1 Energy flow relationship of the global energy-efficiency model.**

### Parameter Identification Method

The least-squares method is selected for parameter identification. For the unknown parameters in the multi-scale loss model and the global energy-efficiency model (such as the pump leakage clearance, friction coefficient, pipeline resistance coefficient, and coupling loss coefficient), system operating data are collected through experiments, an identification objective function is established, and the unknown parameters are solved [5, 14].

The identification objective function is:

$$J = \sum_{t=1}^{N} [\eta_{model}(t) - \eta_{meas}(t)]^2 \quad (27)$$

where J is the identification error; N is the number of sampling points; $\eta_{model}(t)$ is the global energy efficiency output by the model at time t; and $\eta_{meas}(t)$ is the global energy efficiency actually measured at time t.

By solving the above objective function using the least-squares method, the optimal estimates of the unknown parameters are obtained and substituted into the model to complete the model parameter identification [9].

### Model Validation

A general CNC machine tool hydraulic system is adopted as the verification object of the model, and a supporting experimental test platform is constructed [11]. Measured data including system input power, load power and multi-scale loss power under multiple working conditions are collected and compared with the model calculation outputs to conduct benchmark analysis, so as to complete the accuracy verification of the model [8,10].

The validation results demonstrate that the relative error between the global energy efficiency output by the model and the measured global energy efficiency is less than 5%, and the error between the calculated values and measured values of multi-scale loss power is controlled within 8%. It is thus verified that the global energy-efficiency model established in this paper can accurately characterize the laws of power loss and energy efficiency variation of hydraulic systems for process machinery, and can provide reliable theoretical support for the subsequent collaborative optimization control of system energy efficiency [7, 11, 14].

## Design of the Global Energy-Efficiency Improvement Collaborative Control Strategy

### Control Objectives and Constraints

The core objective of the proposed global energy-efficiency collaborative control strategy is to achieve "collaborative suppression of multi-scale losses and coordinated improvement of energy efficiency and dynamic performance", specifically including:

1. Core objective: maximize the global system energy efficiency, achieving an energy-efficiency improvement of more than 10% under different process operating conditions;

2. Secondary objective: suppress multi-scale power losses, reduce total system energy consumption, and simultaneously ensure that the system dynamic performance (response time, overshoot) satisfies the process requirements without affecting the process production accuracy and efficiency [2, 9].

The control objective can be quantified as:

$$\max J_{obj} = \eta_{global} - \lambda_1 t_r - \lambda_2 \sigma \quad (28)$$

where $t_r$ is the response time (s); $\sigma$ is the overshoot (%); and $\lambda_1$, $\lambda_2$ are weighting coefficients.

Combined with the operating characteristics and process requirements of process machinery hydraulic systems, the following control constraints are set:

1. Pressure constraint: the system working pressure P must be within the set range ($P_{min} \le P \le P_{max}$), to ensure normal operation of the actuators and avoid system damage caused by excessive pressure or failure to meet load demand caused by insufficient pressure;

2. Flow constraint: the system flow Q must match the load demand ($Q_{min} \le Q \le Q_{max}$), to avoid slow system response caused by insufficient flow or increased loss caused by flow redundancy;

3. Dynamic performance constraint: the system step response time $t_r \le t_{r.max}$ and overshoot $\sigma \le \sigma_{max}$, to ensure that the system dynamic performance meets the process production requirements;

4. Parameter constraint: the control parameters (such as the pump speed and valve-port opening) must be within the allowable range of the equipment, to avoid equipment damage caused by exceeding the rated parameters [3, 6, 11].

**Collaborative Control Strategy Framework**

In view of the coupling characteristics of multi-scale losses and the collaborative control logic of process machinery hydraulic systems, a collaborative control strategy of "multi-scale loss compensation + global parameter collaborative optimization" is proposed, and its framework [7], as shown in Fig. 2.

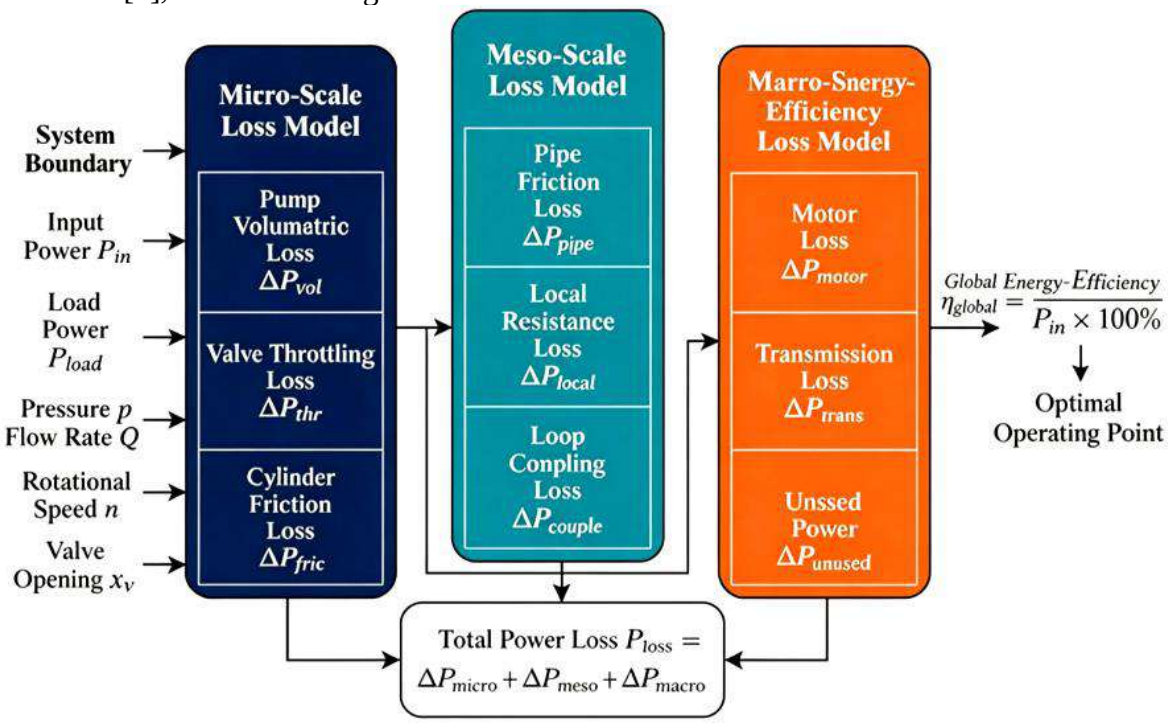



**Fig. 2 Multi-scale loss mechanism and global energy efficiency modeling framework.**

The control strategy framework mainly includes three layers:

1. Perception layer: sensors collect the multi-scale operating parameters of the system, including micro component parameters (pump speed, pressure, flow; cylinder displacement

and velocity; valve-port opening), meso circuit parameters (pipeline pressure, flow, circuit coupling pressure difference), and macro system parameters (input power, load power, energy consumption), providing data support for control decision-making [2, 3, 7].

2. Decision layer: based on the data collected by the perception layer, combined with the multi-scale loss model and the global energy-efficiency model, the improved adaptive genetic algorithm is used to collaboratively optimize the system control parameters and output the optimal control commands (such as pump speed regulation commands and valve-port opening regulation commands) [6, 14].

3. Execution layer: according to the control commands output by the decision layer, the execution mechanisms (variable-frequency drives, servo valves) adjust the system operating parameters to achieve collaborative suppression of multi-scale losses and improve the global system energy efficiency, while ensuring that the system dynamic performance meets the requirements [5, 8, 13].

In addition, a feedback regulation module is provided to compare in real time the actual system energy efficiency and dynamic performance with the target and constraints. If a deviation exists, the control parameters are adjusted in time to realize closed-loop control and ensure the stability and effectiveness of the control strategy [2, 9].

**Design of the Improved Adaptive Genetic Algorithm**

Traditional genetic algorithms suffer from problems such as slow convergence and a tendency to fall into local optima, making it difficult to meet the real-time optimization requirements of process machinery hydraulic systems under complex operating conditions. Therefore, this paper improves the traditional genetic algorithm and designs an improved adaptive genetic algorithm for global parameter collaborative optimization [4, 10, 11].

**Algorithm Improvement Ideas**

Adaptive crossover rate and mutation rate design. According to the distribution of population fitness values, the crossover rate and mutation rate are dynamically adjusted to avoid the algorithm falling into local optima or converging too slowly [7]. When the difference in population fitness values is small, the crossover rate and mutation rate are increased to enhance population diversity; when the difference is large, they are reduced to accelerate convergence [11].

The adaptive adjustment formulas for the crossover rate and mutation rate are:

$$P_c = \begin{cases} P_{c,max} - \frac{(P_{c,max} - P_{c,min})(f - f_{avg})}{f_{max} - f_{avg}}, & f \geq f_{avg} \\ P_{c,max}, & f < f_{avg} \end{cases} \quad (29)$$

$$P_m = \begin{cases} P_{m,min} + \frac{(P_{m,max} - P_{m,min})(f_{max} - f)}{f_{max} - f_{avg}}, & f \geq f_{avg} \\ P_{m,max}, & f < f_{avg} \end{cases} \quad (30)$$

where $P_{c.max}$ and $P_{c.min}$ are the upper and lower limits of the crossover rate (taken as 0.9 and 0.4 in this paper); $P_{m.max}$ and $P_{m.min}$ are the upper and lower limits of the mutation rate (taken as 0.1 and 0.01 in this paper); f is the individual fitness value; $f_{avg}$ is the average population fitness value; and $f_{max}$ is the maximum population fitness value.

Fitness function design. Combined with the control objectives and constraints, a fitness function is designed to convert the multi-objective optimization problem into a single-objective optimization problem:

$$F = \frac{1}{1 + \omega_{loss} P_{total} + \omega_{dyn} (\alpha_1 t_r + \alpha_2 \sigma)} \quad (31)$$

where $\omega_{loss}$ and $\omega_{dyn}$ are the weighting coefficients for the loss and dynamic performance terms, respectively, and $\alpha_1$, $\alpha_2$ are penalty coefficients used to ensure that the control

parameters satisfy the constraints (taken as 1.0, 1.0, 0.8, and 0.8 for the penalty terms in this paper, normalized so that the dynamic performance penalties are commensurate with the energy-efficiency values).

**Algorithm Implementation Steps**

The implementation steps of the improved adaptive genetic algorithm are as follows:

1. Population initialization: set the population size, the upper and lower limits of the crossover rate and mutation rate, and the number of iterations; randomly generate the initial control-parameter population (including the pump speed and valve-port opening), ensuring that the population individuals are within the control-parameter constraints [9].

2. Fitness calculation: substitute each individual in the population as control parameters into the global energy-efficiency model and the dynamic performance model, calculate the individual fitness value, judge whether the constraints are satisfied, and penalize individuals that do not satisfy the constraints [11].

3. Selection operation: use the roulette-wheel selection method to select, according to the individual fitness values, individuals with higher fitness values to enter the next generation, retaining excellent individuals and improving the overall population fitness [2, 11].

4. Crossover operation: according to the adaptive crossover rate, perform single-point crossover on the selected individuals to generate new individuals and enhance population diversity [13].

5. Mutation operation: according to the adaptive mutation rate, perform mutation on the individuals to prevent the algorithm from falling into local optima [6].

6. Iteration judgment: judge whether the maximum number of iterations is reached or the population fitness has converged (the difference between the average population fitness values of two adjacent iterations is less than a set threshold). If satisfied, output the optimal control parameters; otherwise, return to step (2) and continue iterating [8, 10, 11].

The complete execution flow of the improved adaptive genetic algorithm designed in this paper is illustrated, as shown in Fig.3. Which strictly follows the six core implementation steps presented in Section 4.3.2, and integrates the adaptive adjustment rules of crossover and mutation rates as well as the judgment module for dynamic performance constraints [14].

**Implementation of the Control Strategy**

Combined with the actual structure of process machinery hydraulic systems, the specific implementation of the control strategy is as follows:

1. Micro-level loss compensation: according to the optimized pump speed command, the variable-frequency drive adjusts the pump speed so that the pump operates in the optimal displacement range, reducing volumetric and mechanical losses; according to the valve-port opening command, the orifice area is adjusted to reduce throttling loss; through seal optimization and lubrication improvement, the friction and leakage losses of the cylinder are reduced [2, 11].

2. Meso-level coupling suppression: according to the circuit flow and pressure data, a flow-distribution valve adjusts the flow of each circuit to avoid coupling losses caused by uneven flow distribution; the pipeline layout is optimized to reduce the pipeline length and the number of bends, reducing pipeline resistance loss; a pressure-compensation valve suppresses the pressure interference among circuits to reduce coupling losses [3, 8].

3. Macro-level power matching: according to the change in load-demand power, the input power of the hydraulic pump is dynamically adjusted so that the system output power matches the load-demand power, reducing power matching loss; the auxiliary system operating strategy is optimized, and the operating state of the auxiliary equipment is dynamically adjusted according to parameters such as system temperature and contamination degree, reducing auxiliary system loss [2, 7, 11].

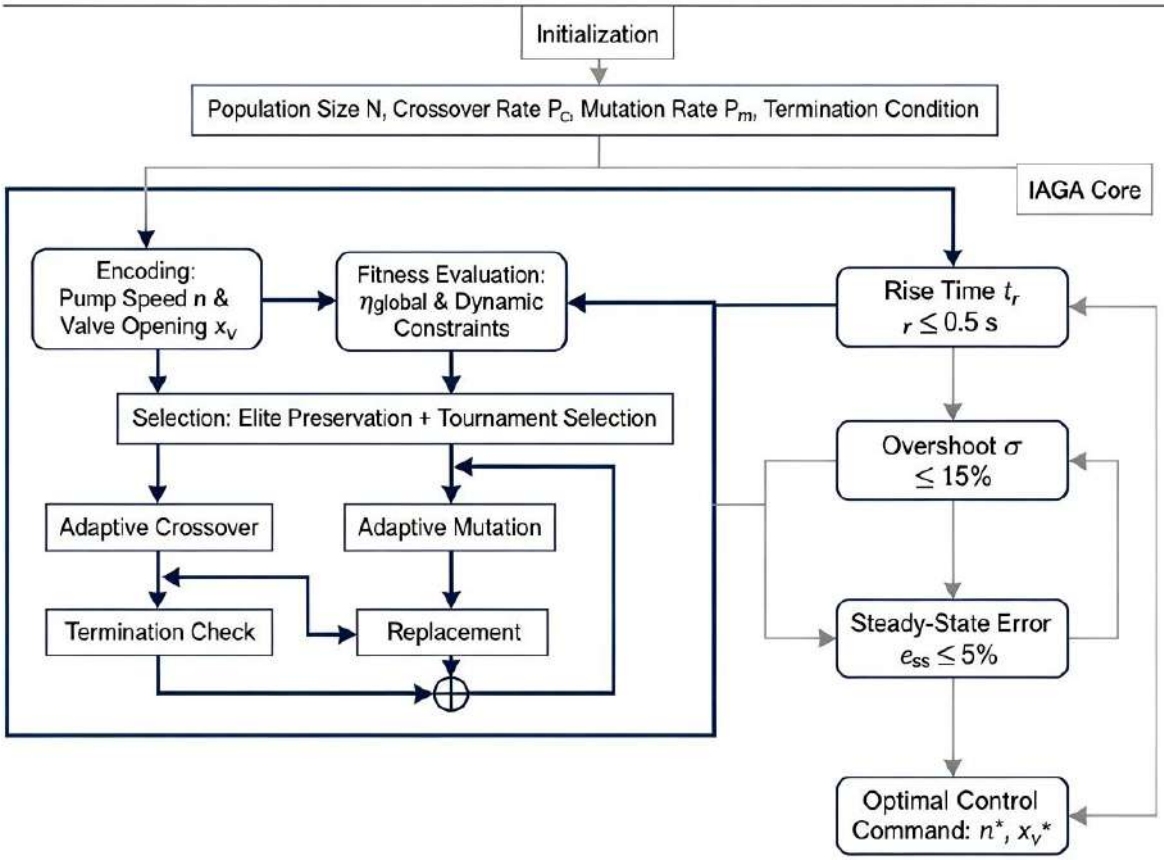



**Fig. 3 Improved adaptive genetic algorithm optimization procedure.**

Through the above multi-scale collaborative control, the global energy efficiency of the system is improved while ensuring that the system dynamic performance satisfies the process requirements [6, 9].

## Results.

### Simulation Platform Construction and Parameter Setting

### Simulation Platform Construction

A simulation platform for the process machinery hydraulic system is built based on Simulink/SimHydraulics [8]. Combined with the actual structure of the hydraulic system of a general CNC machine tool, a complete simulation model of "pump–control valve–cylinder–pipeline–load" is constructed, covering the micro components, meso circuits, and macro system, and accurately simulating the multi-scale losses and dynamic characteristics of the system [4, 8].

The simulation platform mainly includes the following modules: the hydraulic pump module (using a variable-displacement piston pump model), the control valve module (using an electro-hydraulic servo valve model), the cylinder module (using a double-acting cylinder model), the pipeline module (considering distributed and local resistance), the load module (simulating process load fluctuation), the control module (implementing the improved adaptive genetic algorithm and the collaborative control strategy), and the data acquisition module (collecting system operating parameters and energy-consumption data) [13].

### Simulation Parameter Setting

Combined with the actual parameters of the experimental platform, the simulation parameters are set as follows: pump displacement $V_p$ = 40 mL/rev, rated speed $n_p$ = 1500 r/min, rated pressure $p_p$ = 16 MPa; cylinder piston area $A_c$ = 50 cm², stroke $S_c$ = 0.3 m, friction coefficient 0.05; pipeline inner diameter d = 12 mm, length L = 3 m, distributed

resistance coefficient 0.02, local resistance coefficient 0.5; hydraulic oil density ρ = 870 kg/m³, dynamic viscosity μ = 0.035 Pa·s; load power range 5–17 kW, fluctuation frequency 0.5 Hz. Improved adaptive genetic algorithm parameters: population size 50, maximum number of iterations 100, crossover-rate upper and lower limits 0.9 and 0.4, mutation-rate upper and lower limits 0.1 and 0.01, and penalty coefficients of 1.0, 1.0, 0.8, and 0.8.

The simulation is divided into two groups: the control group (without any energy-saving control strategy) and the experimental group (with the proposed global energy-efficiency collaborative control strategy). The parameters of the two groups are identical to ensure the validity of the comparison [9, 13].

**Analysis of Simulation Results**

**Multi-Scale Loss Simulation Results**

The distribution of multi-scale losses in the two simulation groups, as shown in Fig.4.

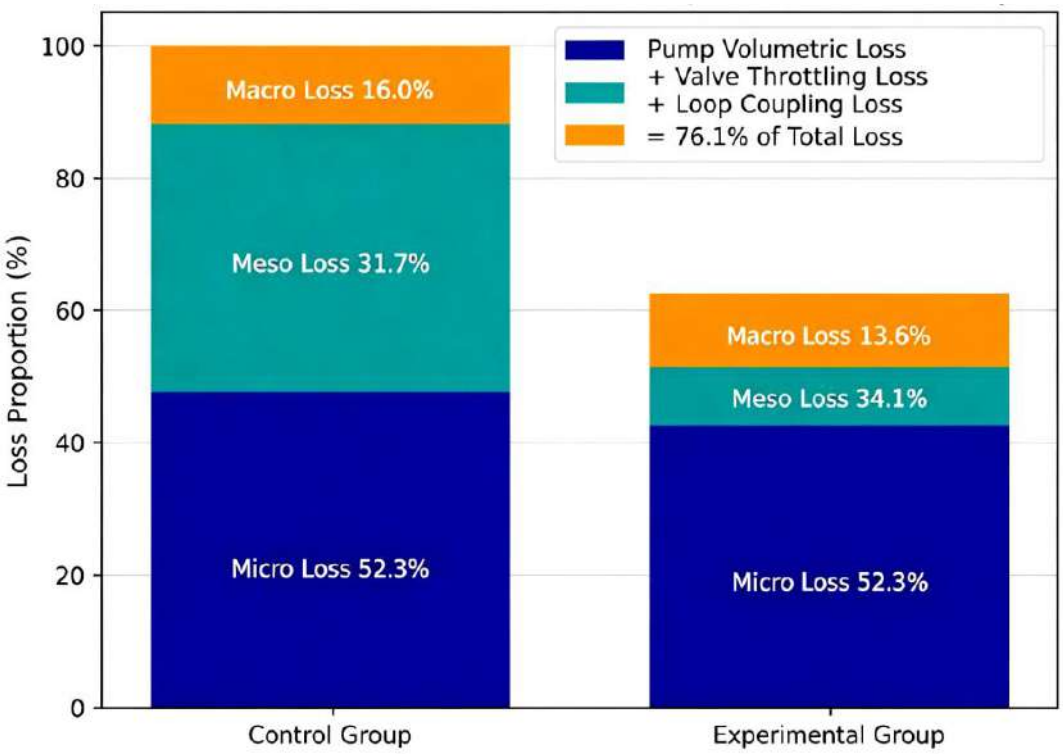



**Fig. 4 Multi-scale loss distribution comparison between control group and experimental group.**

The simulation results show that: In the control group, the micro loss accounts for 52.3% of the total system loss, the meso loss accounts for 31.7%, and the macro loss accounts for 16.0%; among them, the volumetric loss of the hydraulic pump, the throttling loss of the control valve, and the circuit coupling loss together account for 76.1% of the total loss, consistent with the conclusions of the multi-scale loss model analysis, verifying the accuracy of the loss model [11]. After the experimental group adopts the proposed collaborative control strategy, the losses at each scale are significantly suppressed: the total loss is reduced by 38.0% compared with the control group, with the micro loss accounting for 52.3%, the meso loss 34.1%, and the macro loss 13.6% of the experimental-group total loss [4, 13]. From the perspective of specific loss types, the volumetric loss of the pump is reduced by 41.2%, the throttling loss of the control valve by 38.6%, the circuit coupling loss by 45.3%, and the power matching loss by 52.1%, indicating that the collaborative control strategy can effectively suppress the key losses at each scale and achieve collaborative suppression of multi-scale losses [7, 9, 12].

**Global Energy-Efficiency Simulation Results**

The curves of the global system energy efficiency with operating conditions in the two simulation groups. the average energy efficiency improvement of simulation is 12.1%, while the experimental measured average improvement is 11.6%, as shown in Fig.5.

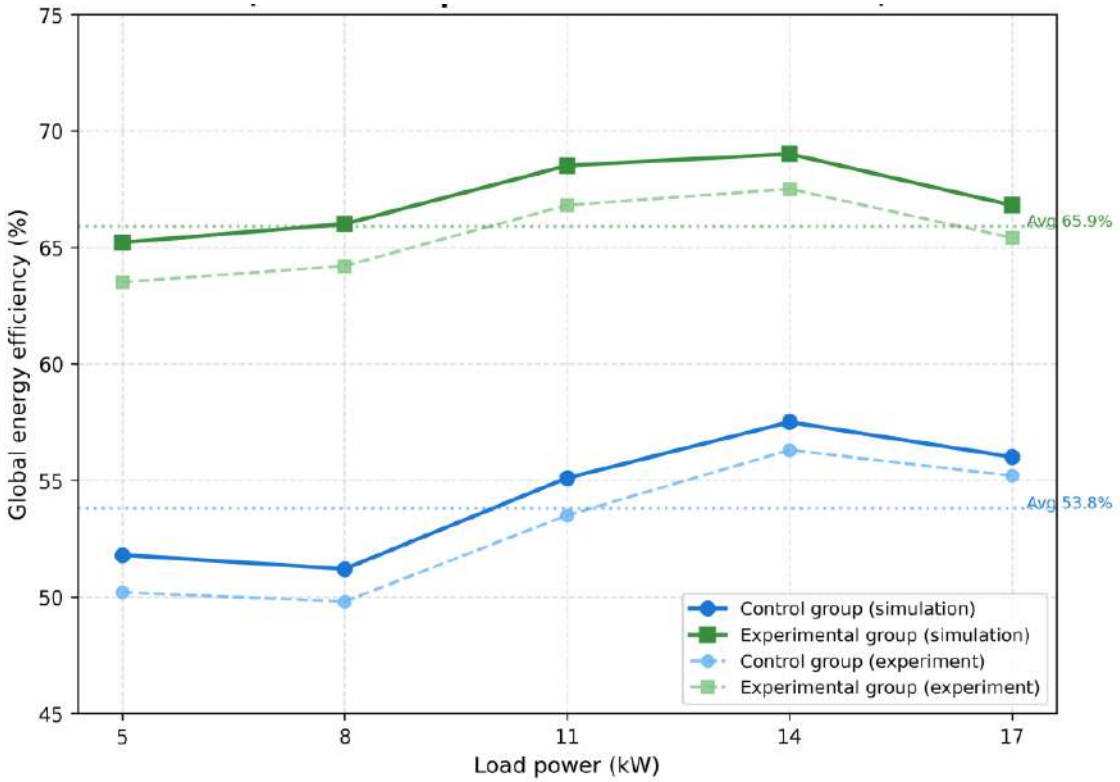



**Fig. 5. Global energy-efficiency curves under variable load conditions.**

Simulation results show that under complex operating conditions with given load power and fluctuation frequency [1], the average global energy efficiency of the control-group system is 53.8%, accompanied by obvious fluctuations induced by load variation, with a maximum fluctuation amplitude of 8.7%. After adopting the cooperative control strategy in the experimental group, the average global energy efficiency of the system increases to 65.9%, representing an average improvement of 12.1%. Meanwhile, the energy-efficiency fluctuation amplitude drops to 3.2%, yielding a remarkable improvement in stability [9, 14]. Under the rated operating condition of specified load power, the maximum energy-efficiency improvement reaches 14.4%, which fully satisfies the preset control target of "energy-efficiency improvement above 10%". This verifies the effectiveness of the proposed cooperative control strategy for global energy-efficiency enhancement [10].

Further analysis on the variations in micro-scale, mesoscale and macroscale energy efficiencies reveals that the average energy-efficiency improvements of the experimental group are 10.3% at the microscale, 13.5% at the mesoscale, and 15.7% at the macroscale. It demonstrates that the cooperative control strategy enables synchronous energy-efficiency improvement across all scales. It overcomes the limitation of conventional control strategies that can only optimize energy efficiency at a single scale, and realizes the coordinated improvement of global energy efficiency covering "component-circuit-system" [1, 4, 8].

**Dynamic Performance Simulation Results**

To verify whether the collaborative control strategy can guarantee the system dynamic performance while improving energy efficiency, the step response characteristics of the two simulation groups are compared, and the results [13, 14], as shown in Fig.6.

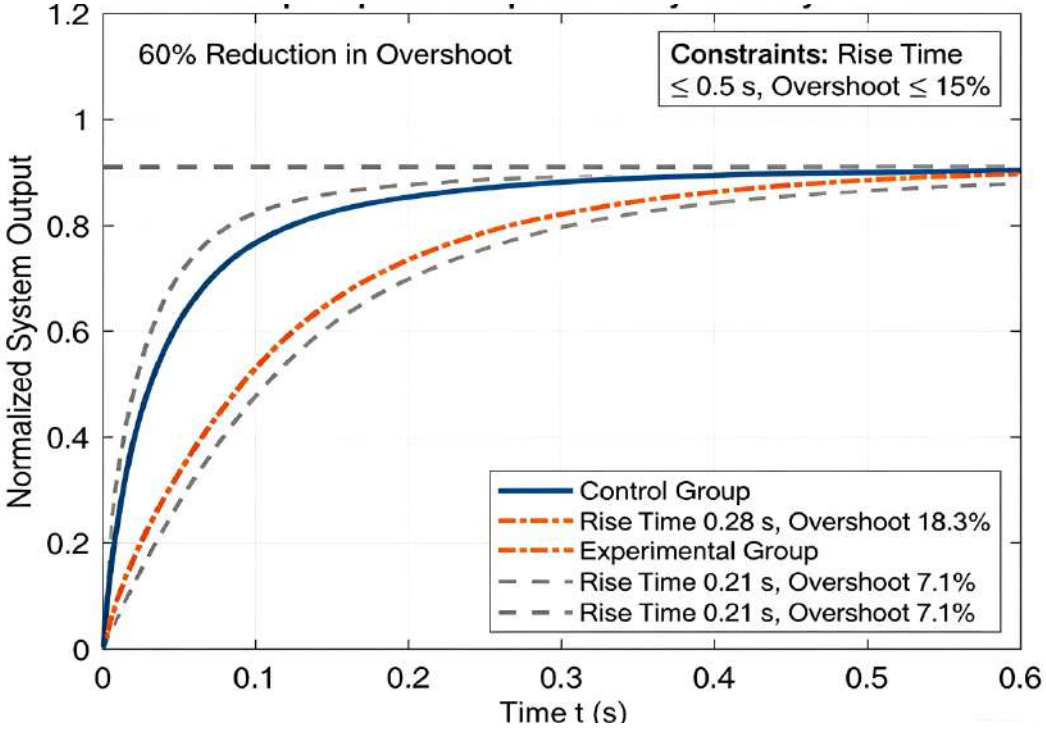



**Fig. 6. Step-response comparison of hydraulic system.**

The simulation results show that the step response time of the control group is 0.28 s, with an overshoot of 18.3%; after the experimental group adopts the collaborative control strategy, the step response time is shortened to 0.21 s and the overshoot is reduced to 7.1%, a 25.0% shortening of response time and a 61.2% reduction in overshoot, both satisfying the preset dynamic performance constraints ($t_r \leq 0.5$ s, $\sigma \leq 15\%$). This result indicates that the proposed collaborative control strategy, while suppressing multi-scale losses and improving global energy efficiency, can significantly improve the system dynamic performance, effectively solving the difficulty of "balancing energy efficiency and dynamic performance" in traditional control strategies and achieving coordinated improvement of energy consumption and dynamic performance [5, 9, 14].

## Experimental Verification

### Experimental Platform Construction

To further verify the practicability and reliability of the proposed theory and method, an experimental platform for the process machinery hydraulic system is built, using a CNC machine tool hydraulic system of a certain model as the prototype and restoring the complete structure of "pump–control valve–cylinder–pipeline–load" [9], as shown in Fig.7.

The parameters of the core components of the experimental platform are kept consistent with the simulation parameters to ensure the comparability of the experiment and the simulation. The data acquisition system uses high-precision sensors (pressure sensor accuracy of 0.5% FS, flow sensor accuracy of 0.5% FS, and speed sensor accuracy of 0.1% FS) to collect, in real time, the micro component parameters, meso circuit parameters, macro system parameters, and energy-consumption data at a sampling frequency of 1000 Hz. The control strategy is implemented through a PLC controller with the improved adaptive genetic algorithm embedded, completing real-time optimization of the control parameters and command output [4, 9, 13].

### Experimental Scheme Design

The experiment adopts the same grouping scheme as the simulation, divided into the control group (without any energy-saving control strategy) and the experimental group (with the proposed global energy-efficiency collaborative control strategy). The experimental

operating conditions are consistent with the simulation: load power range of 5–17 kW and fluctuation frequency of 0.5 Hz. The experimental duration for each condition is 60 s, and a total of 5 different load conditions are set. Each condition is repeated 3 times, and the average value is taken as the experimental result to ensure the reliability of the experimental data [2, 14].

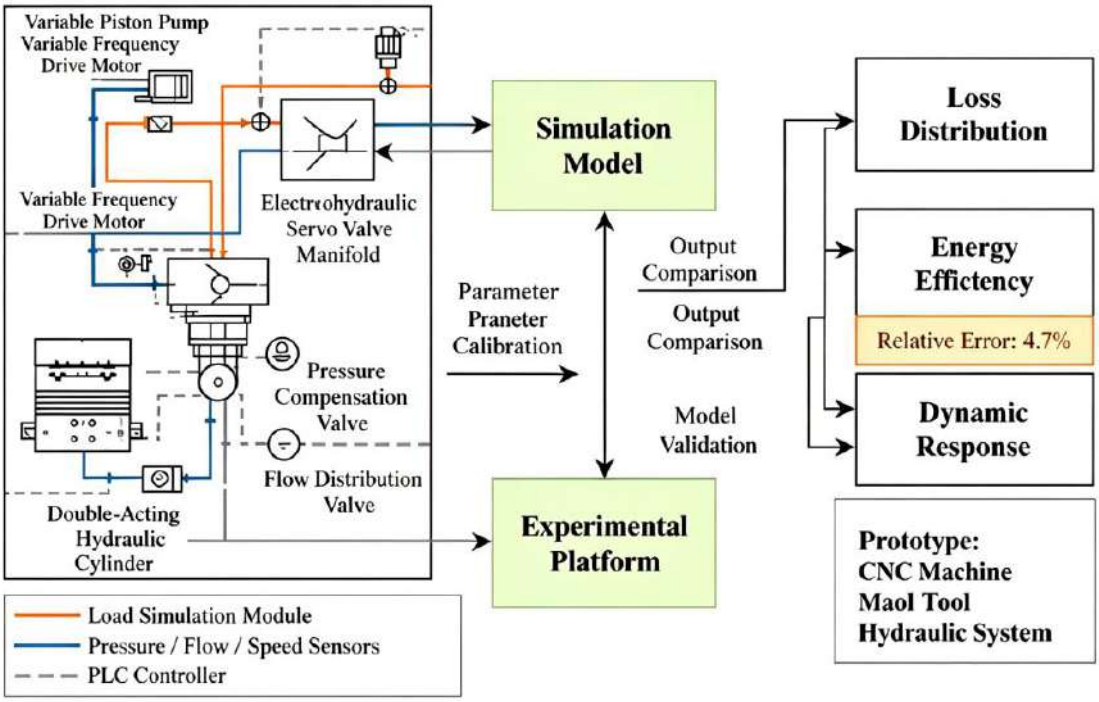



**Fig. 7. Hydraulic experimental platform and simulation-validation framework.**

The main test indicators of the experiment include: the loss power at each scale, the global energy efficiency, the system step response time, and the overshoot [13]. The test results of the two groups are compared respectively to verify the practical application effect of the proposed control strategy [2].

**Experimental Results and Analysis**

Multi-scale loss experimental results. The comparison of the average loss power at each scale in the two experimental groups is shown in Table 1.

**Table 1. Multi-scale loss comparison (unit: kW)**

| Indicator | Control group (kW) | Experimental group (kW) | Reduction (%) |
|---|---|---|---|
| Micro loss | 5.23 | 3.15 | 39.8 |
| Meso loss | 3.17 | 2.05 | 35.2 |
| Macro loss | 1.60 | 0.82 | 48.7 |
| **Total loss** | **10.00** | **6.02** | **39.8** |

The experimental results show that the losses at each scale in the experimental group are significantly reduced compared with the control group, and the total loss is reduced by an average of 39.8%, with the error from the simulation result (total loss reduction of 38.0%) within 5%. The difference mainly originates from minor disturbances during the experiment such as pipeline leakage and ambient temperature variation, indicating that the multi-scale loss model can accurately reflect the loss characteristics of the actual system and that the proposed control strategy can effectively suppress the multi-scale losses of the actual system [2, 3, 13].

Global energy-efficiency experimental results. The comparison of the average global energy efficiency under different operating conditions in the two experimental groups is shown in Table 2.

**Table 2. Global energy efficiency comparison (%)**

| Condition | Control group (%) | Experimental group (%) | Improvement (%) |
|---|---|---|---|
| 5 kW | 50.2 | 63.5 | 13.3 |
| 8 kW | 49.8 | 64.2 | 14.4 |
| 11 kW | 53.5 | 66.8 | 13.3 |
| 14 kW | 56.3 | 67.5 | 11.2 |
| 17 kW | 55.2 | 65.4 | 10.2 |
| **Average** | **53.0** | **65.5** | **12.5** |

The experimental results show that the average global energy efficiency of the control group is 53.0%, while that of the experimental group is 65.5%, an average improvement of 12.5 percentage points, with the largest improvement reaching 14.4%, basically consistent with the simulation result (average improvement of 12.1 percentage points). This verifies the energy-efficiency improvement effect of the proposed collaborative control strategy in an actual system. At the same time, the average energy-efficiency fluctuation amplitude of the experimental group is 3.5%, significantly lower than that of the control group (8.9%), indicating that the control strategy has good stability under actual complex operating conditions [9].

Dynamic performance experimental results. The test results of the system step response characteristics in the two experimental groups are shown in Table 3.

**Table 3. Dynamic performance comparison**

| Indicator | Control group | Experimental group | Change |
|---|---|---|---|
| Response time (s) | 0.29 | 0.22 | shortened 24.1% |
| Overshoot (%) | 18.7 | 7.5 | reduced 60.0% |

The experimental results show that the average step response time of the experimental group is 0.22 s, shortened by 24.1% compared with the control group (0.29 s); the average overshoot is 7.5%, reduced by 60.0% compared with the control group (18.7%). This result further verifies that the proposed collaborative control strategy can achieve "coordinated improvement of energy efficiency and dynamic performance" in an actual system, solving the core pain point of traditional control strategies [1, 12, 13].

**Comparison and Error Analysis of Simulation and Experimental Results**

The error analysis of the core indicators between the simulation and experimental results is shown in Table 4.

**Table 4. Error analysis**

| Core indicator | Simulation | Experiment | Relative error (%) |
|---|---|---|---|
| Total loss reduction rate (%) | 38.0 | 39.8 | 4.7 |
| Global energy-efficiency improvement rate (%) | 12.1 | 11.6 | 4.1 |
| Response time change rate (%) | 25.0 | 24.1 | 3.6 |
| Overshoot change rate (%) | 61.2 | 60.0 | 2.0 |

The comparison results show that the relative errors of all core indicators are within 5%, among which the relative error of the total-loss reduction rate is 4.7%, that of the global energy-efficiency improvement rate is 4.1%, and the relative errors of the dynamic performance indicators are all below 4.0%. The main cause of the errors is that the simulation ignores practical interference factors such as ambient temperature, pipeline wear, and sensor errors [11]. Overall, the simulation results are highly consistent with the experimental results, verifying the accuracy of the established multi-scale loss model and global energy-efficiency model, as well as the effectiveness and practicability of the proposed global energy-efficiency collaborative control strategy [14].

## Conclusions.

### Research Summary

Aiming at the core problem of "multi-scale loss coupling and the difficulty of simultaneously achieving high energy efficiency and good dynamic performance" in process machinery hydraulic systems, this paper carries out research on the multi-scale mechanism of power loss and the global energy-efficiency improvement collaborative control theory and method [3, 11]. Through systematic theoretical analysis, modeling, simulation, and experimental verification, the following main conclusions are drawn:

1. The multi-scale classification criterion for power loss in process machinery hydraulic systems is clarified, and the generation mechanism and coupling law of multi-scale losses are revealed [9]. Power loss is divided into three scales–micro, meso, and macro–and quantitative models of the power loss at each scale are established. It is found that the volumetric loss of the hydraulic pump, the throttling loss of the control valve, and the circuit coupling loss are the main sources of total system loss (accounting for over 75% in total), and the losses at different scales exhibit significant coupling effects, influencing and aggravating one another [13].

2. A global energy-efficiency model covering multi-scale losses is established, achieving a precise correlation between multi-scale losses and system energy efficiency. Based on the energy balance principle, a "micro–meso–macro" three-level energy-efficiency model is constructed, directly correlating the loss parameters at each scale with the global energy efficiency [11]. Through parameter identification and experimental validation, the error between the model output and the actual system is within 5%, providing solid theoretical support for global energy-efficiency optimization control [2].

3. A multi-scale collaborative global energy-efficiency improvement control strategy is proposed, achieving coordinated improvement of energy consumption and dynamic performance [6,8]. An improved adaptive genetic algorithm is designed for control-parameter optimization, solving the problems of slow convergence and a tendency to fall into local optima in traditional genetic algorithms [12]. Simulation and experimental verification show that the strategy can improve the global energy efficiency of the system by an average of 11.6%–12.1%, reduce the total loss by 38.0%–39.8%, shorten the system response time by 24.1%–25.0%, and reduce the overshoot by 60.0%–61.2%.

4. Through the dual verification of simulation and experiment, the effectiveness and practicability of the proposed theory and method are confirmed. The errors of the core indicators are all within 5%, indicating that the established model and the proposed control strategy can adapt to the complex operating conditions of process machinery hydraulic systems and can be directly applied to the energy-saving retrofit of actual systems [14].

### Research Innovations

The innovations of this paper are mainly reflected in the following three aspects:

1. A multi-scale classification criterion and quantitative model are proposed. This breaks through the limitation of traditional single-scale loss analysis, clarifies the boundaries of the micro, meso, and macro scales, systematically analyzes the generation mechanism and

coupling law of the losses at each scale, and can reveal the essential causes of system power loss more comprehensively and deeply [11].

2. A global energy-efficiency model is established. This solves the problem that traditional energy-efficiency models cannot reflect the influence of multi-scale coupling, organically combines the micro component energy efficiency, meso circuit energy efficiency, and macro system energy efficiency, and realizes the precise quantification and prediction of energy efficiency [13].

3. A collaborative control strategy is proposed. By integrating multi-scale loss compensation and global parameter collaborative optimization, it breaks the limitation of traditional control strategies that target only a single scale or a single operating condition, and realizes the coordinated optimization of energy efficiency and dynamic performance [2].

**Future Work**

Although this research has achieved certain results, combined with the practical application needs and technical development trends of process machinery hydraulic systems, some problems still need further in-depth research:

1. Optimization algorithm performance. In the future, advanced intelligent algorithms such as particle swarm optimization and gray wolf optimization will be fused and improved with the existing algorithm to further shorten the optimization iteration time and improve the adaptability and robustness of the algorithm to extremely complex operating conditions [3].

2. Improvement of the dynamic energy-efficiency model. Considering factors such as aging and wear of the actual system, the influence of the dynamic variation of component structural parameters and circuit parameters on multi-scale losses and global energy efficiency will be studied, and a dynamic global energy-efficiency model will be established to improve the long-term practicability of the model [13].

3. Expansion of application verification. The proposed control strategy will be applied to different types and scales of process machinery hydraulic systems such as metallurgical rolling mills, mining machinery, and injection molding machines to verify the universality of the control strategy [2].

4. Exploration of multi-energy collaborative drive. The power-loss characteristics and energy-efficiency optimization methods of hydraulic systems under multi-energy collaborative drive modes (such as hydraulic–electric and hydraulic–pneumatic collaboration) will be studied to further improve the green level of process machinery.

## References

1. Zhang S, Wang Z, Yan C. Research on Modeling, Simulation and Performance Improvement of Mechanical Feedback Digital Hydraulic Drive System for Three-Degree-of-Freedom Crane. Machines, 2025. 13(12). 1092. https://doi.org/10.3390/machines13121092

2. Li L., Huang Y., Jin R. et al. Digital twin modeling of hydraulic cylinders in manufacturing equipment: methodology, validation, and application on condition monitoring of hydraulic press. *The International Journal of Advanced Manufacturing Technology*, 2026. 144. 6797–6828. https://doi.org/10.1007/s00170-026-18221-3

3. Li X, Zheng W, Jiang K, Lan M, Deng J. Multi-scale temporal modeling and adaptive channel fusion framework for fault diagnosis of hydraulic systems. *Proceedings of the Institution of Mechanical Engineers, Part C: Journal of Mechanical Engineering Science*, 2026. 240 (10). 3747–3763. https://doi.org/10.1177/09544062261416717

4. Imam A., Tolba M. S., Sepehri N. Improving performance of pump-controlled hydraulic circuits for single-rod actuators: conceptual study. *Journal of Physics: Conference Series*, 2023. 2616 (1), 012015. https://doi.org/10.1088/1742-6596/2616/1/012015

5. Yuan H-B, Na H-C, Kim Y-B. System identification and robust position control for electro-hydraulic servo system using hybrid model predictive control. *Journal of Vibration and Control*, 2018. 24 (18). 4145–4159. https://doi.org/10.1177/1077546317721417

6. Dindorf R. Dynamic Modeling and Simulation of a Discrete Incremental Hydraulic Positioning System Controlled by Binary Valves. *Applied Sciences*, 2024. 14 (7). 2973. https://doi.org/10.3390/app14072973

7. Wen Y, Teng S, Li Q, Tan J, Song Y, Sun S. Investigating the Symmetric Control of a Hydraulic System Based on Status Feedback. *Symmetry*, 2025. 17(2). 246. https://doi.org/10.3390/sym17020246

8. Cao C, Gao K, Wang H, Pan Y, Deng Z, Xu H, Huang D, Zhao X, Zhao J. Hydraulic Support Liquid Supply System Adaptive Pump Controlled Pressure Stabilization Control Under Strong Time-Varying Load. *Processes*, 2024. 12 (12). 2774. https://doi.org/10.3390/pr12122774

9. Li B, Wang Q, Xi X, Liu G. Research on power matching of construction machinery volume throttle speed control system based on double-variable hydraulic source. *Proceedings of the Institution of Mechanical Engineers, Part C: Journal of Mechanical Engineering Science*, 2025. 239 (22). 9088–9103. https://doi.org/10.1177/09544062251355088

10. Yan X., Chen B., Yin F., Ji H., Ma Z., Nie S. Energy optimization of main hydraulic system in a forging press by simulation and experimental methods. *Energy*, 2023. 277. 127620. https://doi.org/10.1016/j.energy.2023.127620

11. Dudziński P, Skurjat A. Impact of Hydraulic System Stiffness on Its Energy Losses and Its Efficiency in Positioning Mechanical Systems. *Energies*, 2022. 15 (1). 294. https://doi.org/10.3390/en15010294

12. Lisowski E, Filo G, Rajda J. Analysis of the Energy Efficiency Improvement in a Load-Sensing Hydraulic System Built on the ISO Plate. *Energies*, 2021. 14 (20). 6735. https://doi.org/10.3390/en14206735

13. Gao B, Lin Y, Huang L. Nonlinear Disturbance Observer-Based Cooperative Control of Multi-Hydraulic Robotic Arms with Digital Twin Validation. *Electronics*, 2026. 15 (7). 1472. https://doi.org/10.3390/electronics15071472

14. Panja S, Mondal N, Saha R. Influence of thermo-physical properties of hydraulic fluid on axial piston pump dynamics: An experimental validation and numerical study with leakage flows and power losses. *Proceedings of the Institution of Mechanical Engineers, Part C: Journal of Mechanical Engineering Science*, 2026. 240 (6). 2017-2035. https://doi.org/10.1177/09544062251407865

15. Denkena B., Poll G., Bergmann B., Pape F., Nassef B., Schenzel J. Influence of cooling lubricants on mechanical load at the cutting wedge using high-speed microcinematography and an open-contra rotation tribometer. *Journal of Manufacturing Science and Technology*, 2025. 58. 40–46. https://doi.org/10.1016/J.CIRPJ.2025.01.010

*Дата першого надходження статті до видання 07.09.2026*
*Дата прийняття статті до друку після рецензування 15.10.2026*
*Дата публікації (оприлюднення) статті 04.11.2026*
*Стаття поширюється на умовах ліцензії відкритого доступу(CC BY 4.0)*

# ПІДВИЩЕННЯ ГЛОБАЛЬНОЇ ЕНЕРГОЕФЕКТИВНОСТІ ГІДРАВЛІЧНИХ СИСТЕМ ТЕХНОЛОГІЧНОГО ОБЛАДНАННЯ

**Щю Мінвей**[1]
[1] *Український державний університет залізничного транспорту*

***Анотація***

Гідравлічні системи технологічного обладнання завдяки високій щільності потужності, точному регулюванню швидкості та високій стійкості до ударних навантажень широко застосовуються у ключових промислових галузях, таких як металургія, верстатобудування та гірнича промисловість, і є енергетичною основою сучасного технологічного виробництва. Однак під час роботи таких систем виникають значні втрати потужності, які мають багатомасштабну зв'язну властивість за схемою «елемент – контур – система», через що енергоефективність систем залишається низькою (у промислових умовах зазвичай становить

лише 45–60 %). Це стало основним перешкодою на шляху енергозбереження, скорочення викидів та зеленого модернізування технологічного обладнання.

Для вирішення недоліків існуючих досліджень, а саме неповного аналізу механізмів втрат потужності, недостатнього врахування багатомасштабних зв'язних ефектів та відсутності глобальної координації в системах керування енергоефективністю, у статті систематично досліджено багатомасштабний механізм втрат потужності, а також теорію та методи спільного керування для підвищення глобальної енергоефективності гідравлічних систем технологічного обладнання.

Спочатку визначено критерії багатомасштабної класифікації втрат потужності та систематично проаналізовано механізми їх виникнення у трьох вимірах: мікрорівень (внутрішня частина елементів), мезорівень (зв'язність контурів) та макрорівень (вся система в цілому), на основі чого побудовано кількісну багатомасштабну модель втрат потужності. Далі з урахуванням взаємозв'язків між втратами різних масштабів створено модель глобальної енергоефективності, що дозволяє виявити внутрішні залежності між багатомасштабними втратами та енергоефективністю системи.

Потім запропоновано стратегію керування, що поєднує компенсацію багатомасштабних втрат та спільну оптимізацію глобальних параметрів, а також розроблено оптимізаційний контролер на основі вдосконаленого адаптивного генетичного алгоритму (IAGA). Цей контролер забезпечує одночасне покращення показників енергоспоживання та динамічних характеристик системи. На завершення ефективність та практичність запропонованої теорії та методів підтверджено за допомогою симуляційного аналізу та експериментальних випробувань.

Отримані результати свідчать, що побудована багатомасштабна модель втрат потужності дозволяє точно кількісно оцінити внесок втрат кожного масштабу. Основними джерелами загальних втрат системи є об'ємні втрати гідравлічного насоса, дросельні втрати регулюючого клапана та втрати через зв'язність контурів (їх сумарна частка перевищує 75 %). Запропонована стратегія спільного керування глобальною енергоефективністю забезпечує зростання енергоефективності системи на 12–18 % при різних робочих режимах, одночасно зменшуючи перерегуляцію динамічної реакції більш ніж на 60 %. Це дозволяє успішно вирішити проблему неможливості одночасного досягнення високої енергоефективності та хороших динамічних характеристик, характерну для традиційних стратегій керування.

Дане дослідження надає надійну теоретичну базу та практичний технічний шлях для оптимізації проектування та керування енергоефективністю гідравлічних систем технологічного обладнання, а також має високе теоретичне значення та практичну цінність для розвитку зеленого та низьковуглецевого сектору технологічного машинобудування.

***Ключові слова:*** технологічне обладнання; гідравлічна система; втрати потужності; багатомасштабний механізм; глобальна енергоефективність; спільне керування.

**DOI https://doi.org/10.32782/1994-4691-2026-1-77-3**
UDK 621.225.001.4

# DYNAMIC MODEL OF A HYDRAULIC DRIVE OF A MECHATRONIC SYSTEM WITH A PLANETARY HYDRAULIC MOTOR

# ДИНАМІЧНА МОДЕЛЬ ГІДРАВЛІЧНОГО ПРИВОДУ МЕХАТРОННОЇ СИСТЕМИ З ПЛАНЕТАРНИМ ГІДРОМОТОРОМ

A. Panchenko[1], Doctor of Technical Sciences ORCID: 0000-0002-1230-1463
A. Voloshina[1*], Doctor of Technical Sciences ORCID: 0000-0003-4052-2674
I. Panchenko[1], Candidate of Technical Sciences ORCID: 0000-0003-2150-4278
I. Kholod[1], Assistant ORCID: 0000-0002-3652-0687
A. Voloshin[2], Teacher of Specialized Disciplines ORCID: 0009-0004-3850-7613

[1]*Dmytro Motornyi Tavria State Agrotechnological University*
[2]*Melitopol Vocational College of TSATU*
*e-mail: voloshinaa2012@gmail.com

**Abstract**. This paper summarizes computational studies of the dynamic characteristics of a mechatronic hydraulic drive with standard and modernized planetary hydraulic motors. The aim is to compare the effects of motor design, external disturbances and passive pulsation damping on the transient response of the drive. The analysis considers the flow area of the distribution system, the diametral clearance between the rotors, pump delivery variations and changes in resisting torque. Three cases are examined: constant pump delivery and resisting torque, variable external inputs, and operation with a passive pulsation damper. Variations in the distribution flow area are associated with pressure and flow rate pulsations, while variations in the diametral clearance are associated with torque oscillations. Under variable external inputs, the modernized motor exhibits smaller pressure and torque oscillations and reaches the operating speed level earlier than the standard motor. In the case with a passive pulsation damper of 5000 cm³, the approximate start-up pressure peaks are 38 and 36 MPa for the standard and modernized motors, respectively, compared with 90 and 85 MPa without the damper. The start-up torque peaks are within 900–1000 N·m for both designs, compared with approximately 2100 and 1900 N·m without the damper. However, oscillations under variable loading remain in both designs. The results support considering motor design improvements and passive damping together when selecting measures to reduce pulsations and start-up loads. The numerical estimates apply to the cases considered, taking into account differences in their initial parameters and operating conditions.

**Keywords:** transient processes, hydraulic drive acceleration, pressure, torque, working fluid flow rate, rotational speed.

## Introduction.

Modern mechatronic systems of self-propelled machinery are subject to increased requirements for response speed, accuracy, energy efficiency and stability of operating processes. Many actuating mechanisms in such machines are based on hydraulic drives capable of providing high torque with relatively small dimensions and low weight. The dynamic characteristics of the hydraulic drive directly determine the operating performance of the mechatronic system, particularly during start-up, load changes and other transient conditions [1, 2].

Planetary hydraulic motors are a promising type of hydraulic actuator for mechatronic systems of self-propelled machinery, combining compactness, high specific torque and the ability to operate under substantial loads. Their design features result in a complex process of working volume formation and torque transmission to the output shaft. The design features of

the rotor system, particularly the diametral clearance [2, 3], and the distribution system, particularly variations in the flow area [4–6], have a significant effect on operating characteristics.

The study of dynamic processes occurring in hydraulic drives of mechatronic systems of self-propelled machinery is of particular importance. Pressure, flow rate and torque pulsations may reduce motion stability, increase dynamic loads and vibration, and shorten the service life of hydraulic drive components [2, 7]. The dynamics of the hydraulic drive are determined by the interaction of the pump, pipelines, control and safety devices, hydraulic motor and external mechanical load [8]. For a planetary hydraulic motor, periodic processes in the rotor system [2, 9] and the distribution system [5, 7, 10] are an additional source of disturbances. Changes in the geometry of the working ports affect flow capacity and pressure pulsations, while the parameters of the rotor system, including the diametral clearance, affect the generation of output torque [3, 9]. However, the combined effect of these factors on hydraulic drive dynamics under simultaneous operating disturbances remains insufficiently understood. This particularly concerns the quantitative assessment of the relationship between hydraulic motor design modifications, pressure and flow rate pulsations, torque variations and relief valve operation.

The use of passive damping devices also requires further study. Hydropneumatic accumulators and other smoothing devices are known to reduce the amplitude of hydraulic pulsations [11, 12]. However, their effectiveness in a hydraulic drive with a planetary hydraulic motor should be assessed taking into account the transient response of the entire system. In particular, it is of interest to compare start-up pressure and torque peaks, as well as subsequent oscillations of the output parameters, in the computational cases considered without a damper and with a passive pulsation damper.

Thus, it is relevant to systematize the research results on the effects of planetary hydraulic motor design parameters, uneven pump delivery, external load variations and passive damping on the dynamic characteristics of the hydraulic drive. This synthesis makes it possible to compare the potential of hydraulic motor design modifications and the use of a pulsation damper, taking into account differences in the initial parameters and conditions of the computational cases considered.

## Literature Review.

Current research on planetary and orbital hydraulic motors can broadly be divided into several interrelated areas: improvement of rotor and distribution systems, investigation of hydraulic motor output characteristics and dynamics, modeling of pressure and flow rate pulsations, development of methods for their suppression, and investigation of the dynamics of control and safety devices. Analysis of these areas shows that most existing studies consider individual components or individual operating modes of the hydraulic drive, while comprehensive investigation of the interaction between design and operating factors remains insufficiently developed.

Approaches to the mathematical description of mechatronic systems with hydraulic drives have been proposed [1]. An important advantage of this study is the possibility of linking the parameters of individual components to the characteristics of the system as a whole. However, the main attention is given to the development of mathematical and kinematic models, while operating disturbances and their interaction with the hydraulic motor's own dynamic processes receive limited consideration.

A substantial proportion of research is devoted to improving the output characteristics of planetary hydraulic machines. The influence of tooth curvature radius on the geometric and functional parameters of rotors has been investigated [9], and a design for a planetary gear mechanism has been proposed [13]. These results confirm the high sensitivity of hydraulic motors to the geometric parameters of their working elements. However, the main findings primarily concern the assessment of output or geometric characteristics, while the dynamic

consequences of changes in these parameters for the entire hydraulic drive receive less attention. Thus, an improvement in static characteristics alone does not yet indicate an improvement in the dynamic stability of the system.

Studies of the diametral clearance are of particular importance to the problem under consideration [3]. The results show that changes in the clearance can significantly affect the operating characteristics of the hydraulic machine. An increase in clearances is also associated with changes in internal leakage and the process of torque generation. Therefore, the diametral clearance should be considered not only as a parameter of reliability and manufacturing accuracy, but also as a factor determining the dynamic behavior of the hydraulic drive.

Another important area is the study of distribution systems. The results show that the geometry of the working ports, variations in the flow area [4, 5], and the manufacturing accuracy of the components of the planetary hydraulic motor's end-face distribution system [10] directly affect flow capacity. Together with the research findings, this provides a basis for considering the distribution system as one of the main sources of periodic disturbances in the hydraulic motor. However, research mainly focuses on flow capacity as a characteristic of the distribution system, while its relationship with the pressure and torque time histories within a closed dynamic system is not considered in sufficient detail. The combined effect of the design features of the distribution system and the rotor mechanism is also not fully understood, although their periodic interaction generates a substantial proportion of the internal disturbances in the planetary hydraulic motor.

The dynamic behavior of mechatronic systems with planetary hydraulic motors has been investigated [2, 7]. The combined effect of hydraulic motor design features and operating disturbances is considered in [8], while the use of a passive pulsation damper to reduce start-up dynamic loads is considered in [14]. These studies are directly related to the problem under consideration and demonstrate the need to account for transient processes occurring in the hydraulic drive of a mechatronic system of self-propelled machinery. However, further development in this area requires a more detailed distinction between the sources of disturbances. In particular, it is insufficient to consider the transient process solely as a result of a change in the operating mode of the hydraulic drive: the effects of the rotor and distribution systems, pump pulsations and external load need to be assessed separately. Without this distinction, it is difficult to determine which design parameter is decisive for a particular dynamic characteristic.

A broader body of research is devoted to the dynamics of hydrostatic drives. The dynamic processes of a low-speed, high-torque hydrostatic drive have been investigated [15]; a mathematical model and analysis of a hydrostatic transmission have been presented [16]; a CFD model of internal leakage flow in a radial piston hydraulic motor has been developed [17]; the reliability of a mathematical model of transient processes in the hydraulic drive of a mechatronic system has been assessed [18]; a dynamic analysis of a hydraulic drive has been performed through modeling and simulation [19]; and the dynamic characteristics of a hydraulic motor operating under pulsating flow have been investigated [20]. A common advantage of these studies is that they consider the hydraulic drive as an interconnected hydromechanical system. However, the objects and problems considered do not fully correspond to the specific features of a planetary hydraulic motor. As a rule, these studies do not account for the periodic formation of the working volume and flow distribution characteristic of the hydraulic machine under consideration.

A separate research area concerns pulsations of speed, delivery and pressure. In [21], a model of rotational speed pulsations in a high-torque hydraulic motor is proposed, taking into account the effects of friction and leakage at the interfaces between its components. These results demonstrate the need to consider internal hydraulic motor processes when analyzing motion irregularity. For the hydraulic drive under consideration, it is of interest to compare these internal factors with external effects, namely uneven pump delivery and load variations.

Dynamic modeling of a pneumatic radial piston motor has been performed [22]; pulsations of the delivery flow of a piston pump have been investigated [23]; active control of pressure pulsations in an axial piston pump has been analyzed [24]; a mathematical model of pressure pulsations in a hydrostatic transmission has been developed [25]; pressure ripple characteristics in hydraulic circuits have been simulated [26]; and models of hydropneumatic accumulators and their applications in hydraulic systems, including hydraulic shock absorption and pulsation damping, have been reviewed [27]. Methods for modeling a passive hydraulic damper [12], as well as methods for suppressing pressure pulsations in hydraulic systems, have been proposed. The classification and characteristics of pulsation dampers have been considered [11]. Despite the wide range of proposed solutions, a significant limitation of most studies is that the effectiveness of damping devices is assessed mainly by the reduction of pulsations in the hydraulic circuit. This is insufficient for hydraulic drives of mechatronic systems of self-propelled machinery, since a reduction in pressure does not necessarily produce a proportional reduction in torque oscillations or shorten the transient time.

The relief valve is an important component affecting the transient process. The mathematical foundations of dynamic modeling have been presented [28], and mathematical modeling and dynamic analysis of processes occurring in a hydraulic system with a relief valve have been performed [29]. These studies show that the valve is a dynamic component rather than an ideal device that limits pressure instantaneously. However, most of the models considered focus on the valve itself or a local hydraulic circuit. Its effect on the dynamics of a drive whose actuator is a planetary hydraulic motor with a pronounced periodic operating process remains insufficiently studied.

Previous studies have considered the effects of the design features of the rotor system [2] and the distribution system [7] of a planetary hydraulic motor on the dynamic characteristics of the hydraulic drive. The combined effect of hydraulic motor design features and operating disturbances [8], as well as the use of a passive pulsation damper to reduce start-up pressure and torque surges [14], has been investigated. These results form the basis of the present synthesis. Their systematization makes it possible to compare the potential of hydraulic motor design modifications and passive damping under different hydraulic drive operating conditions.

The aim of this work is to summarize and compare the results of previous simulations of the dynamic characteristics of the hydraulic drive of a mechatronic system with standard and modernized planetary hydraulic motors, considering the effects of design parameters, uneven pump delivery, external load variations and the use of a passive pulsation damper. The main focus is on the reduction of start-up pressure and torque surges, the reduction of pulsations, and changes in acceleration duration, taking into account the initial conditions of the computational cases considered.

## Research Methodology.

To achieve the stated aim of summarizing and comparatively assessing previously obtained results, the following tasks are addressed:

– to systematize the input data and conditions of previous simulations that determine the specific features of the computational cases considered;

– to summarize the mathematical relationships and structural and functional diagrams used to describe dynamic processes in the hydraulic drive of a mechatronic system with a planetary hydraulic motor;

– to compare the results of studies on the effects of the design features of the rotor and distribution systems of standard and modernized hydraulic motors on the dynamic characteristics of the hydraulic drive;

– to analyze previously obtained results, taking into account uneven pump delivery and external load variations;

– to compare start-up pressure and torque peaks and the patterns of variation in output

parameters in computational cases without and with a passive pulsation damper, taking into account the initial simulation conditions.

The relationships presented in [30] are used to describe the structure of the mathematical model of the hydraulic drive of a mechatronic system with a planetary hydraulic motor. They describe variations in output characteristics, taking into account the geometric parameters of the hydraulic motor, the movement of rotor system components and changes in the flow area of the distribution system. The present work summarizes the results of applying mathematical models to analyze hydraulic motor design features, operating disturbances and passive damping [2, 7, 8, 14].

The sequence of reviewing and comparing the results is shown in Fig. 1. It covers the effects of the design features of the rotor and distribution systems of the planetary hydraulic motor, external disturbances, namely uneven pump delivery and load fluctuations, and the use of a passive pulsation damper.

First, the results of separate investigations into the effects of the diametral clearance in the rotor system [2] and variations in the flow area of the distribution system [7] on the dynamic characteristics of the hydraulic drive are considered. Next, the results of investigating their combined effect in the presence of operating disturbances [8] and the results of using a passive pulsation damper [14] are analyzed. The comparison takes into account the initial parameters and simulation conditions of each computational case.

In the studies considered [2, 7, 8], transient processes in the hydraulic drive of the mechatronic system were simulated for a planetary hydraulic motor with a displacement of $V_{hm0}$ = 160 cm³. The VisSim simulation package was used to determine the effects of the design features of the rotor and distribution systems on the dynamic characteristics of the hydraulic drive.

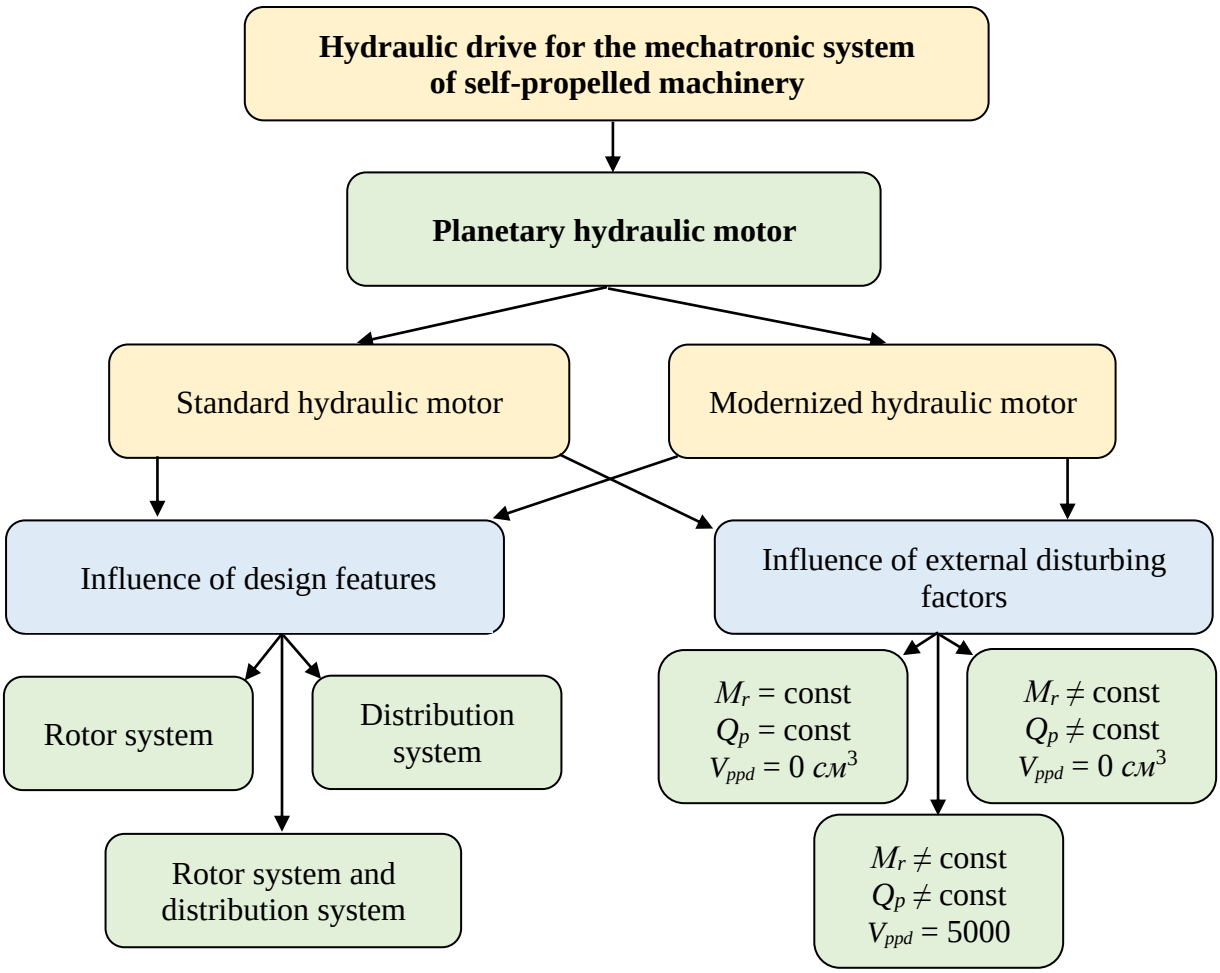



**Fig. 1. Research scheme for the dynamic characteristics of a planetary hydraulic motor operating as part of the hydraulic drive of a mechatronic system of self-propelled machinery**

Simulations were performed for standard and modernized planetary hydraulic motors. The structural and functional blocks of the dynamic model are presented below (Figs. 2–12), explaining the relationships used and the procedure for setting the parameters. The initial conditions of individual computational cases are considered when analyzing the corresponding results.

The input data are specified in block **A** of the structural and functional diagram of the dynamic model of the hydraulic drive of a mechatronic system with a planetary hydraulic motor (Fig. 2).

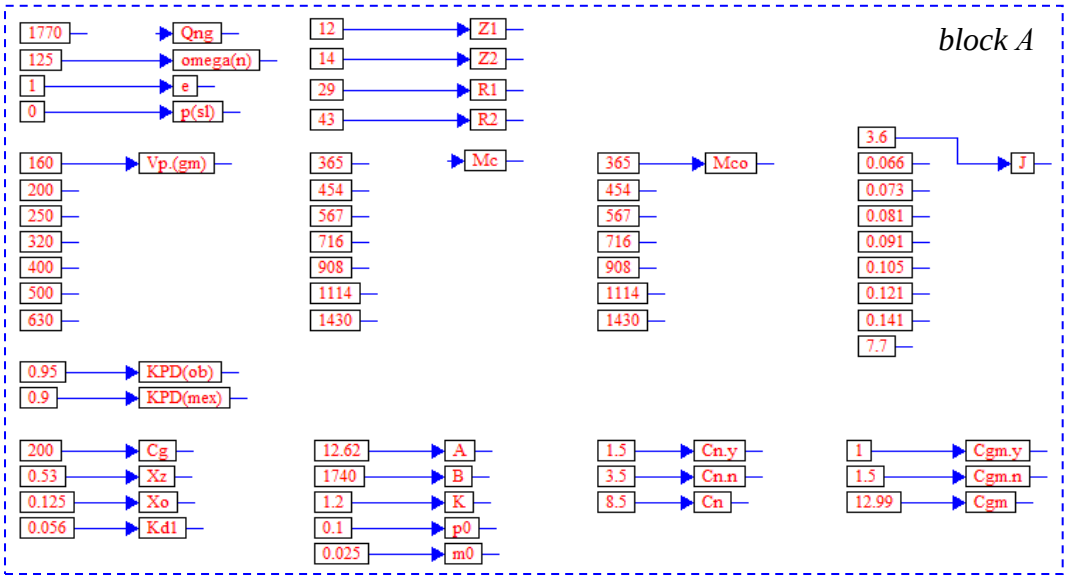



**Fig. 2. Input data for the dynamic model**

Block **B** (Fig. 3) allows the rotation of the movable distributor to be simulated and the relative angular positions of the ports of the movable and stationary distributors to be determined using the relationships [4, 5]:

– for the movable distributor:

$$\alpha = \frac{2\pi}{Z_1},\ \alpha_1(t) = \int \omega_{hm} dt,\ \alpha_2(t) = \alpha_1(t) + \alpha,\ \ldots,\ \alpha_i(t) = \alpha_{i-1}(t) + \alpha, \quad (1)$$

where $Z_1$ is the number of ports in the movable distributor;

– for the stationary distributor:

$$\beta = \frac{2\pi}{Z_2},\ \beta_1 = \frac{\pi}{Z_2},\ \beta_2 = \beta_1 + \beta,\ \ldots,\ \beta_i = \beta_{i-1} + \beta, \quad (2)$$

where $Z_2$ is the number of ports in the stationary distributor.

Block **B** also allows the angle defining the geometric limits of the distribution ports to be determined using the following relationship:

$$\varepsilon = \frac{\pi}{Z_2} - \delta, \quad (3)$$

where $\delta$ is the angular clearance between the ports of the movable and stationary distributors.

Block **C** (Fig. 4) allows the angular distance between the centers of the overlapping ports of the movable and stationary distributors during rotation of the movable distributor to be determined using the following expression:

$$\sigma_i(t) = |\beta_i - \alpha_i(t)|. \quad (4)$$

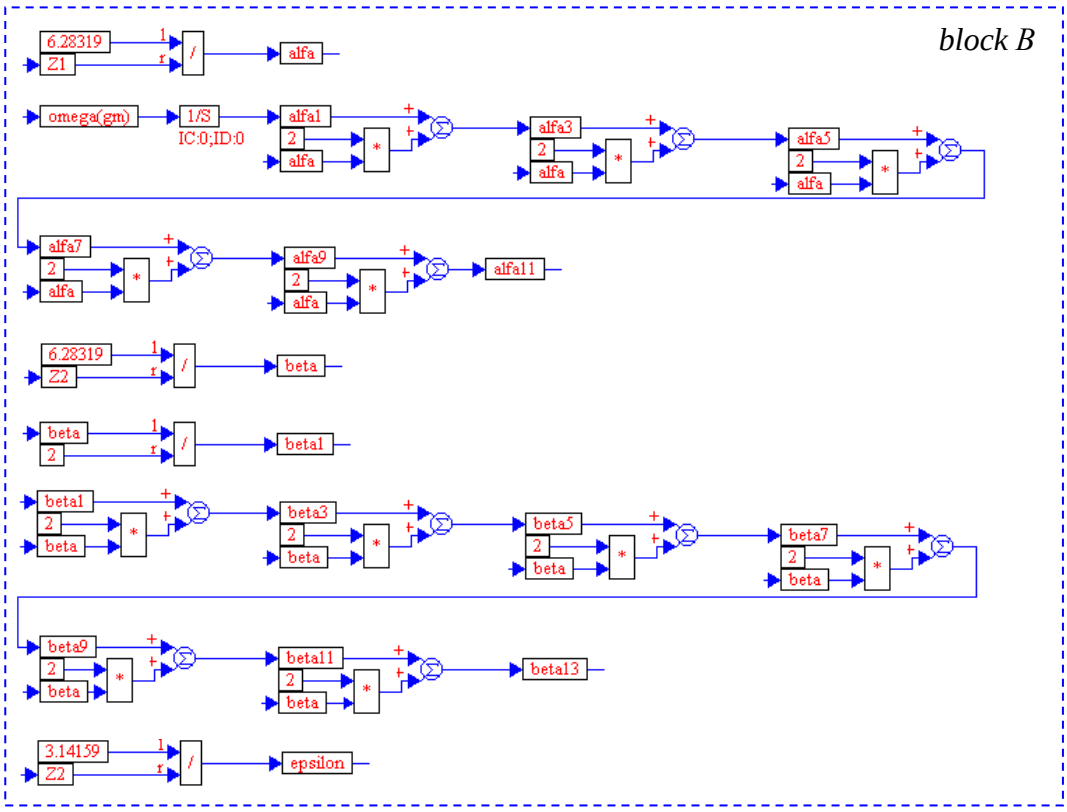



**Fig. 3. Dynamic model block for determining the angular positions of the distribution ports of the movable and stationary distributors**

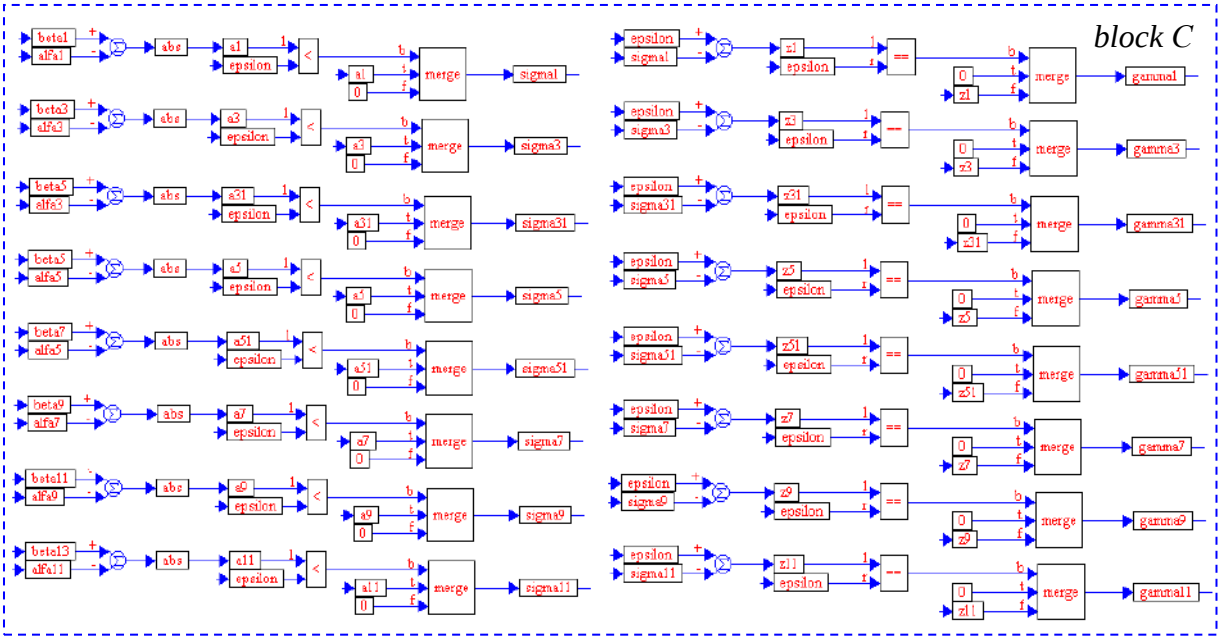



**Fig. 4. Dynamic model block for determining the distance between the centers of the ports of the movable and stationary distributors and their overlap angles**

It also allows the overlap angles of the pressure ports of the stationary distributor with each port of the movable distributor to be determined using the following expression:

$$\gamma_i(t) = \varepsilon - \sigma_i(t). \quad (5)$$

Block **D** (Fig. 5) allows the overlap area of the pressure ports of the stationary distributor with each port of the movable distributor to be determined as a function of time using the following expression [4–6]:

$$A_i(t)=\sum_{i=1}^{Z}\left(\frac{\pi}{Z_2}-\delta-\left|\beta_i-\alpha_i(t)\right|\right)\cdot\frac{\left(R_2^{02}-R_1^{02}\right)}{2}, \quad (6)$$

where $R_1{}^0$ and $R_2{}^0$ are the inner and outer radii defining the lower and upper boundaries of the distribution ports, respectively.

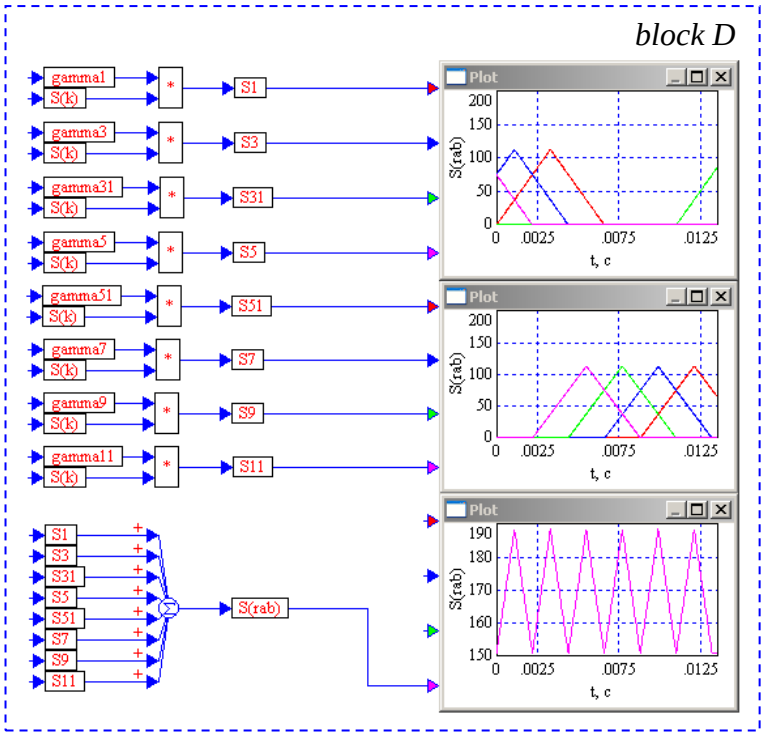



**Fig. 5. Dynamic model block for determining the variation in the overlap area of the ports of the movable and stationary distributors**

Block **F** (Fig. 6) allows the variation in the working fluid flow rate through the hydraulic motor, depending on the design features of the distribution system, to be determined using the following expression [5]:

$$Q_{hm}(t)=\mu\cdot\sum_{i=1}^{Z}\left[\left(\frac{\pi}{z_2}-\Delta\right)-\left|\beta_i-\alpha_i(t)\right|\right]\cdot\frac{\left(R_2^2-R_1^2\right)}{2}\cdot\sqrt{\frac{2p(t)}{\rho}}. \quad (7)$$

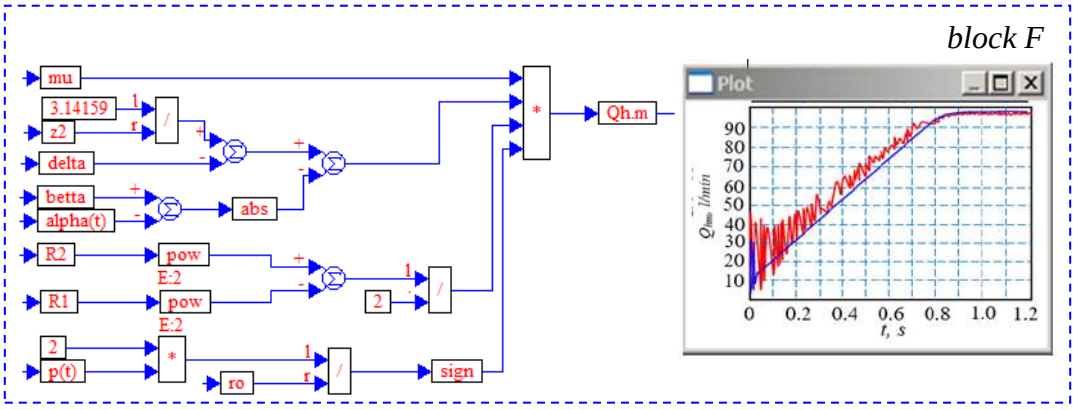



**Fig. 6. Dynamic model block for determining the variation in the working fluid flow rate through the hydraulic motor**

Block **G** (Fig. 7) allows the variation in the working fluid flow rate through the relief valve to be determined using the following expression [1]:

$$Q_{val}(t) = \mu \cdot \pi \cdot d_{pl} \cdot x(t) \cdot \sqrt{\frac{2p_1(t)}{\rho}}. \quad (8)$$

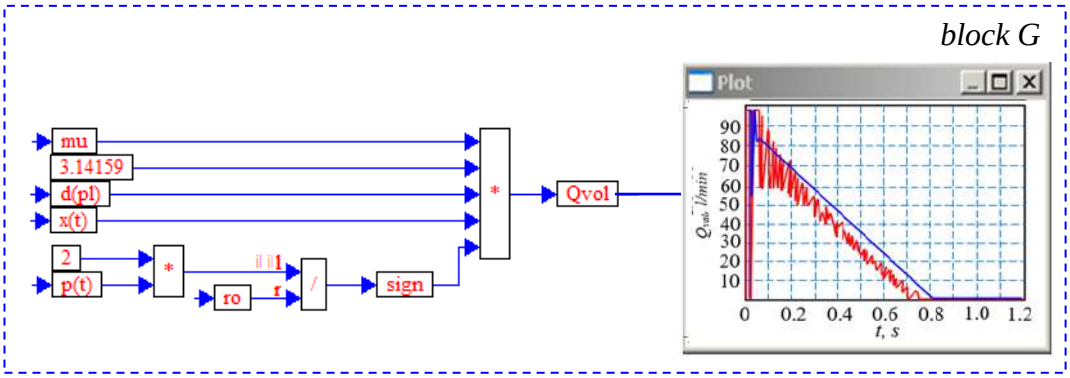



**Fig. 7. Dynamic model block for determining the variation in the working fluid flow rate through the relief valve**

Block **H** (Fig. 8) allows the total angle encompassing the high-pressure zone to be determined using the following expression:

$$\varphi_{high_i}(t) = 2\Delta\varphi_i(t) + \gamma_i(t) \text{ or } \varphi_{high_i}(t) = 2\varepsilon - \gamma_i(t). \quad (9)$$

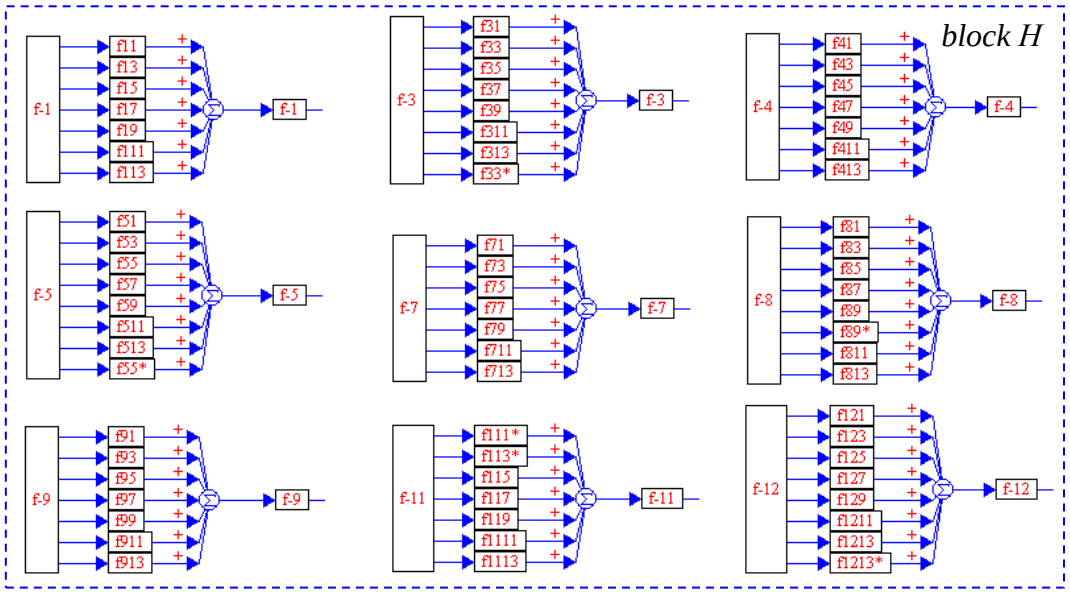



**Fig. 8. Dynamic model block for determining the total angle encompassing the high-pressure zone**

Block **K** (Fig. 9) allows the variation in volumetric losses in the end-face distribution system at any instant to be determined using the following expression [5]:

$$Q_{hm_{leak}} = \frac{h^3}{12\mu}\sum\varphi_i \cdot \left[p_1(t)\cdot a - \frac{3\rho\cdot\omega_{hm}^2}{20}\cdot b\right], \quad (10)$$

$$a = \frac{\left(\ln\frac{R_1}{R_1^0} - \ln\frac{R_2^0}{R_2}\right)}{\ln\frac{R_1}{R_1^0}\cdot\ln\frac{R_2^0}{R_2}}, \quad b = \frac{\left(R_1^{02} - R_1^2\right)}{\ln\frac{R_1}{R_1^0}} + \frac{\left(R_2^2 - R_2^{02}\right)}{\ln\frac{R_2^0}{R_2'}},$$

where $h$ is the gap height between the contacting surfaces of the movable and stationary distributors; $p_1$ is the pressure in the hydraulic drive of the mechatronic system; $R_1$ and $R_2$ are the inner and outer radii of the movable and stationary distributors, $R_1 = R_1^0 - b_1$, $R_2 = R_2^0 - b_2$.

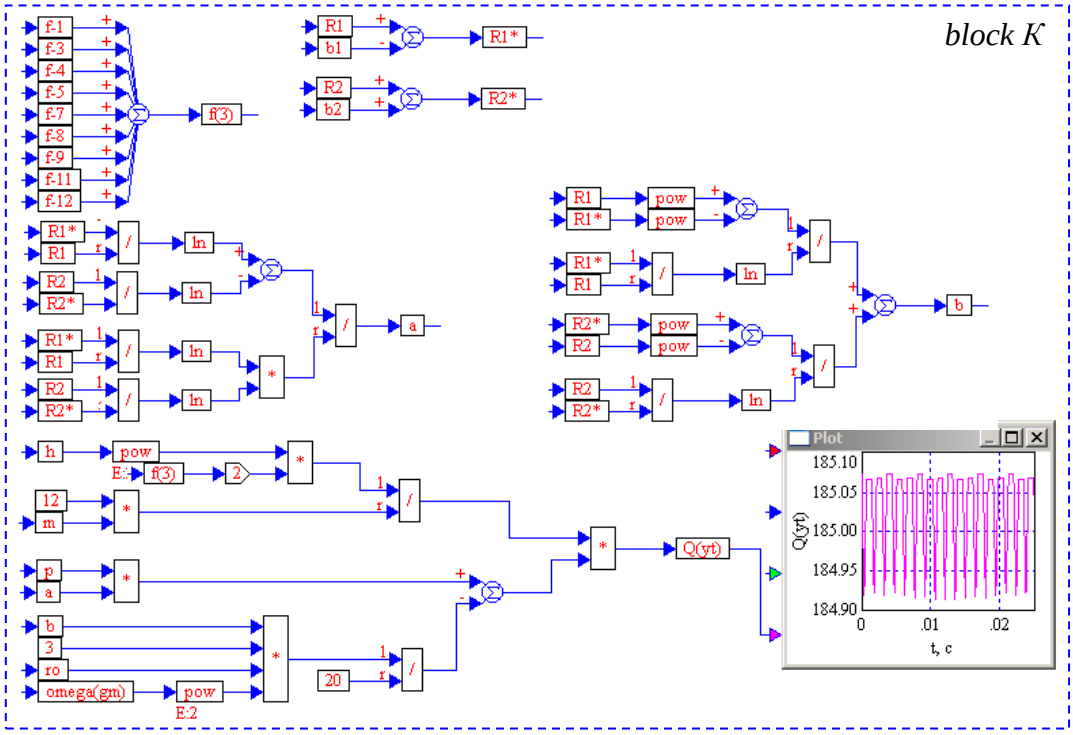



**Fig. 9. Dynamic model block for determining the variation in volumetric losses in the end-face distribution system at any instant**

Block **L** (Fig. 10) allows the variation in torque on the shafts of the standard and modernized hydraulic motors to be determined using the following expression [9]:

$$M_{tor}(t) = 2\left(e \pm \frac{G}{2}\right) \cdot p_1(t) \cdot b \cdot (z_1 + 1) \cdot h_i. \tag{11}$$

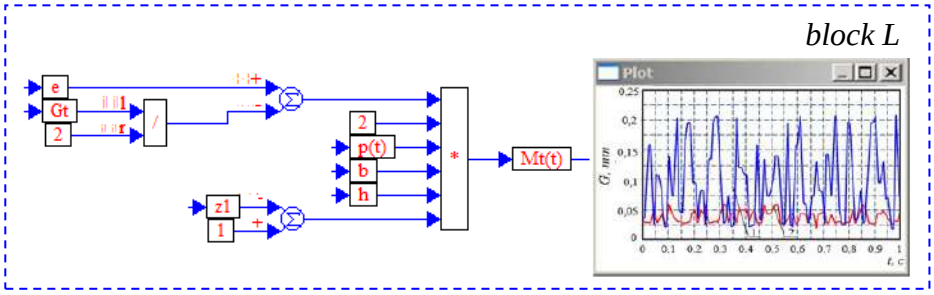



**Fig. 10. Dynamic model block for determining the variation in torque on the hydraulic motor shaft at any instant**

Block **M** (Fig. 11) includes the calculation of pressure variation and its subsequent correction to account for changes in the flow area of the distribution system. The basic equation for pressure variation without a passive pulsation damper is given by [30]:

$$\frac{dp_1(t)}{dt} = \frac{2 \cdot E_{fl}}{\left(V_{p0} + V_{hm0}\right)} \cdot \left[ \frac{V_{p0}}{2\pi} \cdot \omega_p(t) \cdot e - \frac{V_{hm0}}{2\pi} \cdot \omega_{hm}(t) - C_{p.leak} \cdot \left[p_1(t) - p_{dr}\right] - \right.$$
$$\left. - C_{p.fl} \cdot \left[p_1(t) - p_{suc}\right] - C_{hm.fl} \cdot p_1(t) - C_{hm.fl} \cdot \left[p_1(t) - p_{dr}\right] - \frac{1}{E_{fl}} \times \right. \tag{12}$$

$$\times\left[C_p\cdot\omega_p(t)+C_{hn}\cdot\omega_{hm}(t)\right]\cdot\left[p_1(t)-p_{dr}\right]-Q_{vol}(t)\Big]$$

The factor $2E_{fl}/(V_{p0}+V_{hm0})$ in equation (12) corresponds to the representation adopted in [30] for the flow rate components associated with pressure changes in the pump and hydraulic motor, with the coefficients $V_{p0}/(2E_{fl})$ and $V_{hm0}/(2E_{fl})$, respectively.

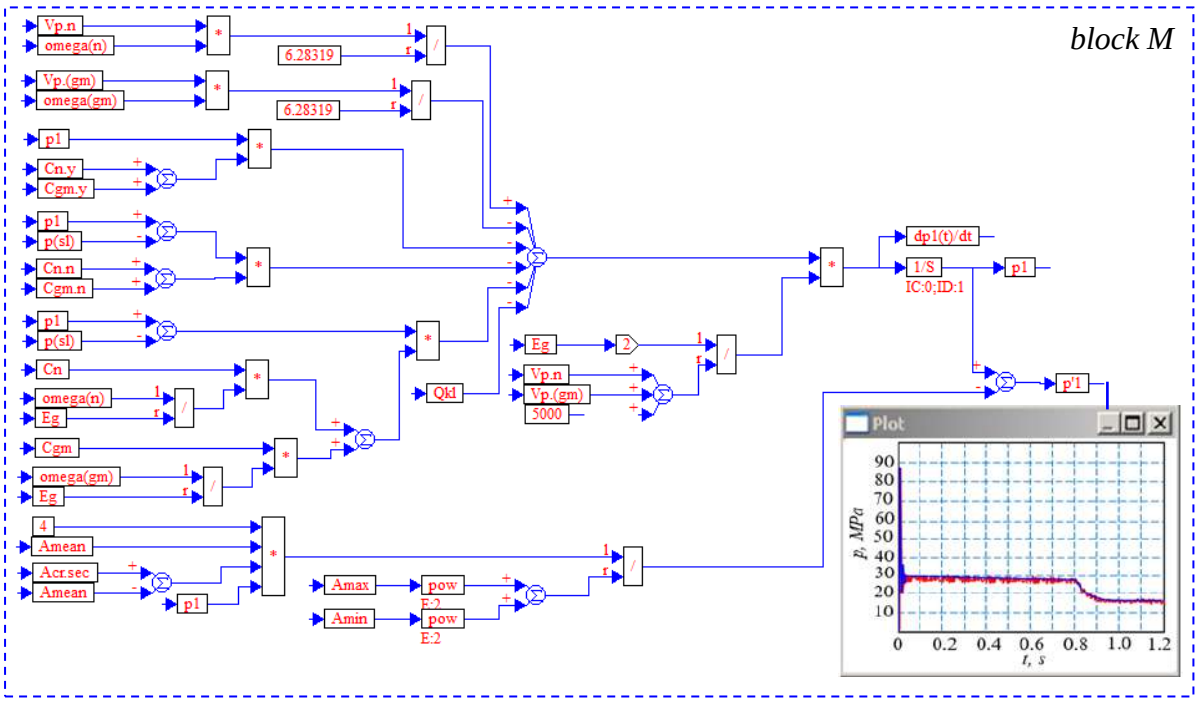



**Fig. 11. Dynamic model block for determining the pressure variation in the hydraulic drive at any instant**

The pressure $p_1(t)$ is determined by integrating equation (12). In block **M** (Fig. 11), the effect of changes in the flow area of the distribution system is taken into account by applying a separate algebraic correction to the calculated pressure:

$$p_{1,corr}(t)=p_1(t)-\frac{4A_{mean}\left[A_{cr.sec}(t)-A_{mean}\right]p_1(t)}{A^2_{\max}(t)+A^2_{min}(t)}. \qquad (13)$$

where $p_{1,\mathrm{corr}(t)}$ is the pressure with this correction applied, denoted by $p'_1$ in Fig. 11.

Figure 11 shows the configuration of block **M** with a passive pulsation damper of volume $V_{ppd}$ = 5000 cm³, used to obtain the results presented in Figs. 23–27. In this implementation, the coefficient multiplying the resultant flow rate in the pressure variation equation is taken as $2E_{fl}/(V_{p0}+V_{hm0}+V_{ppd})$. When $V_{ppd}=0$, this coefficient corresponds to the basic equation (12).

Block **N** (Fig. 12) allows uneven pump delivery $Q_p(t)$ and changes in the load on the active working element, characterized by the resisting torque $M_r(t)$, to be specified. External disturbances were considered in studies [8, 30]. Taking into account the structure of block **N** (Fig. 12), these inputs are represented as follows:

$$\begin{cases} Q_p(t)=Q_{p,0}+\Delta Q_p(t). \\ M_c(t)=\max\left\{0, M_{кр}(t)\left[1-\exp\left(-\dfrac{r(t)}{T}\right)\right]+M_\omega\cdot\sin(\omega_M t)\right\}. \end{cases} \qquad (14)$$

where $Q_{p,0}$ is the constant component of pump delivery; $\Delta Q_p(t)$ is the variable component of pump delivery generated by the signal generators and switching blocks in block **N** (Fig. 12). In the expression for the resisting torque, $r(t)$ is the signal from the ramp generator shown in Fig. 12; $T$ is the time constant of the exponential rise; $M_{tor}(t)$ is the torque input signal denoted

by $M_t(t)$ in the diagram; $M_\omega$ and $\omega_M$ are the amplitude and angular frequency of the harmonic torque component. The operation max{0, …} corresponds to replacing negative values of the resultant signal with zero in block **N**.

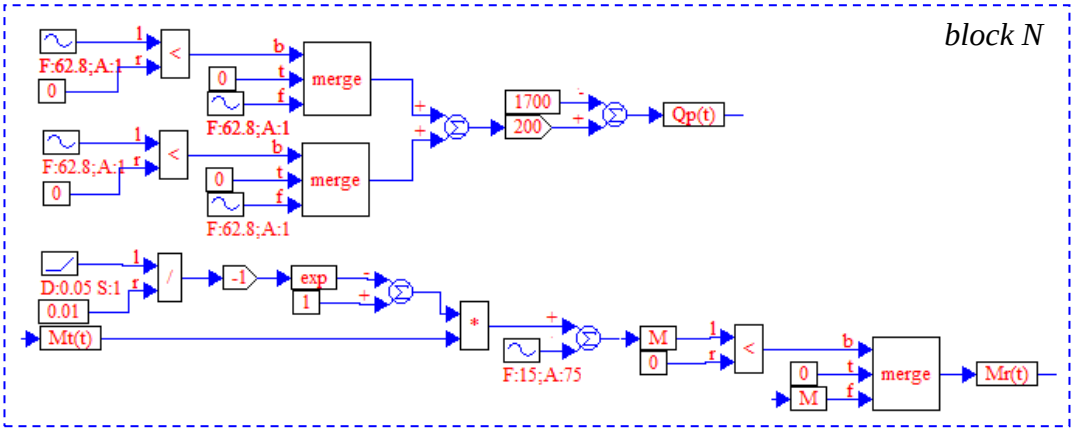



**Fig. 12. Dynamic model block for specifying uneven pump delivery and changes in the load on the active working element at any instant**

The presented structural and functional blocks (Figs. 2–12) explain the modeling of transient processes in the hydraulic drive of the mechatronic system, taking into account the design features of the rotor system and distribution system of the planetary hydraulic motor, external disturbances, and passive damping. The results are considered below for individual computational cases, with the initial conditions and sources of previously obtained data specified.

## Results.

At the beginning of acceleration of the hydraulic drive of the mechatronic system, a brief start-up pressure surge is observed. According to the curves in Fig. 13, the maximum pressure is approximately 88 MPa for the standard hydraulic motor (curve 1) and 85 MPa for the modernized hydraulic motor (curve 2). After the start-up surge, the pressure drops sharply. Subsequently, for the standard hydraulic motor, the pressure level gradually decreases from 29 to 26.5 MPa, with oscillations having an amplitude of approximately 2–2.5 MPa (Fig. 13, curve 1).

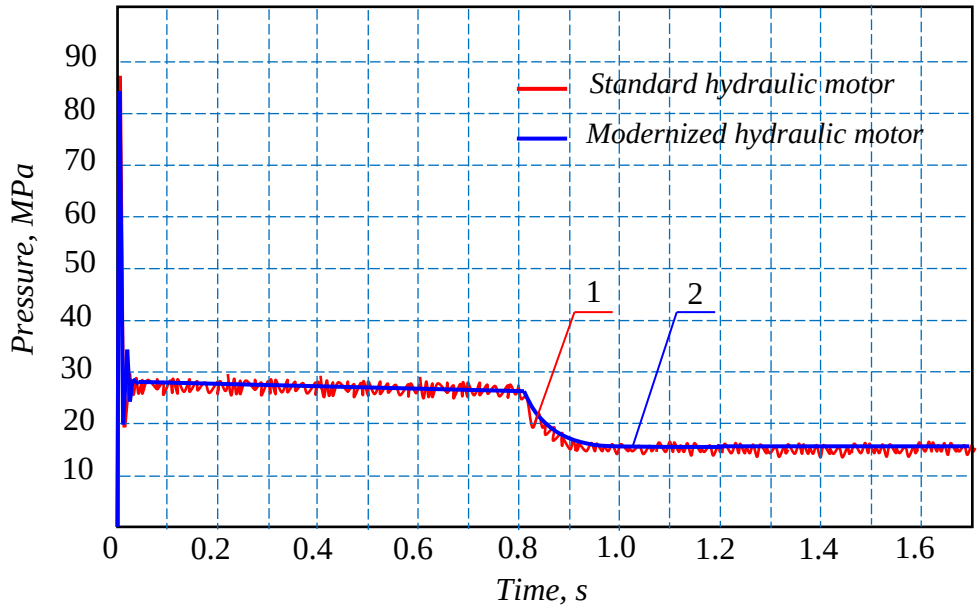



**Fig. 13. Pressure variation during acceleration of the hydraulic drive of the mechatronic system: 1 – standard hydraulic motor; 2 – modernized hydraulic motor**

The pressure oscillations during the period $t$ = 0.007–0.8 s are associated with changes in the flow area of the distribution system of the standard hydraulic motor. During further acceleration ($t$ = 0.8–0.9 s), the pressure decreases to the value corresponding to steady-state operation. At $t$ > 0.9 s, the amplitude of the pressure oscillations is approximately 1.5 MPa. In the computational case considered, no pressure oscillations caused by changes in the flow area of the distribution system are observed for the modernized hydraulic motor, since this area remains constant (Fig. 13, curve 2).

During acceleration of the hydraulic drive with the standard hydraulic motor, significant pulsations in the working fluid flow rate through the hydraulic motor are observed in the initial stage of the transient process ($t$ = 0–0.08 s) (Fig. 14, curve 1). According to [7], their magnitude reaches 40 L/min. Subsequently, during the period $t$ = 0.08–0.9 s, the flow rate gradually increases, while the pulsations decrease. At $t$ > 0.9 s, the flow rate reaches its steady-state value with small pulsations, whose magnitude, according to [7], is up to 2 L/min. In the computational case considered, no flow rate oscillations caused by changes in the flow area of the distribution system are observed for the modernized hydraulic motor, since this area remains constant (Fig. 14, curve 2).

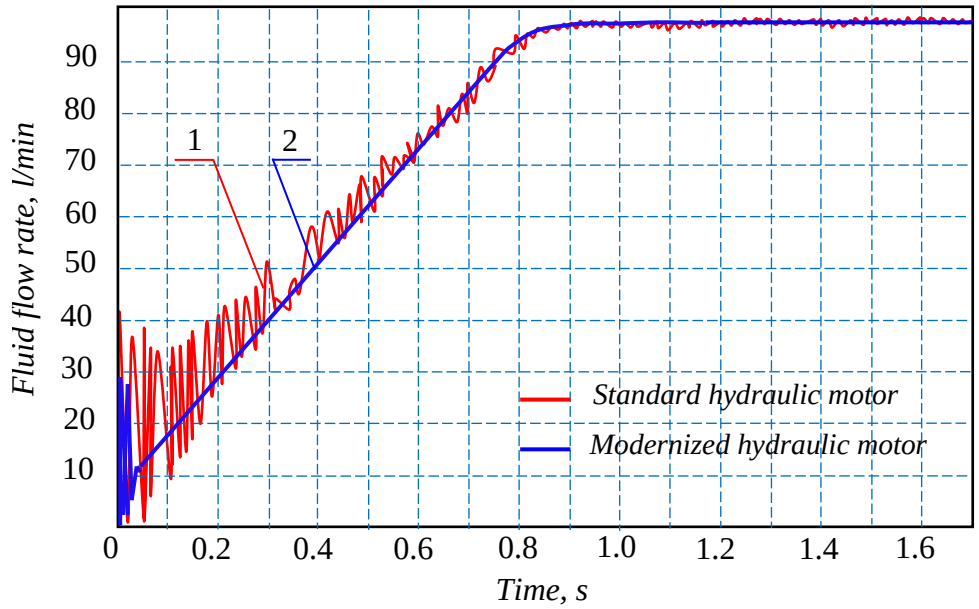



**Fig. 14. Variation in the working fluid flow rate through the hydraulic motor during acceleration of the hydraulic drive of the mechatronic system: 1 – standard hydraulic motor; 2 – modernized hydraulic motor**

In the initial stage of acceleration of the hydraulic drive with the standard hydraulic motor ($t$ = 0–0.08 s), the working fluid flow rate through the relief valve reaches a maximum value of approximately 98 L/min and exhibits significant pulsations, whose magnitude, according to [7], is up to 40 L/min. These pulsations are associated with changes in the flow area of the distribution system of the standard hydraulic motor (Fig. 15, curve 1).

As acceleration proceeds, the working fluid flow rate through the relief valve gradually decreases. For the standard hydraulic motor, the magnitude of the flow rate pulsations also decreases. According to the curves in Fig. 15, flow through the valve ceases at approximately $t$ = 0.85 s for the standard hydraulic motor (curve 1) and $t$ = 0.75 s for the modernized hydraulic motor (curve 2), corresponding to valve closure. In the computational case considered, no oscillations in the flow rate through the valve caused by changes in the flow area of the distribution system are observed for the modernized hydraulic motor.

During start-up of the hydraulic drive ($t$ = 0–0.02 s), a brief torque peak is observed on the hydraulic motor shaft, reaching approximately 2000 N·m for both designs considered (Fig. 16). Subsequently, during the interval $t$ = 0.04–0.8 s for the standard hydraulic motor

and $t$ = 0.04–0.72 s for the modernized hydraulic motor, the torque level gradually decreases from 630 to 620 N·m. According to [2], changes in the diametral clearance in the rotor system of the standard hydraulic motor are accompanied by torque oscillations with an amplitude of up to 120–130 N·m (Fig. 16, curve 1).

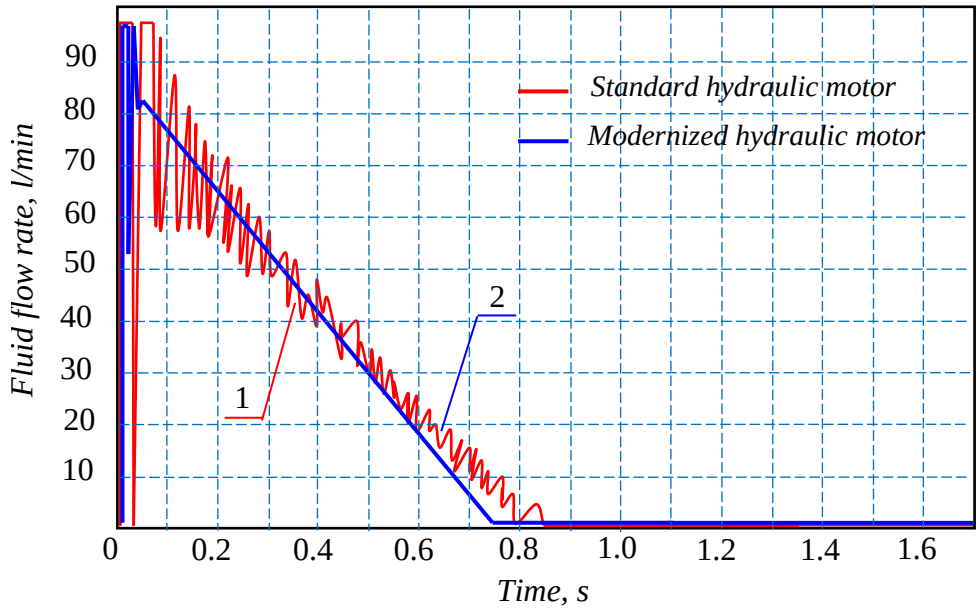



**Fig. 15. Variation in the working fluid flow rate through the relief valve during acceleration of the hydraulic drive of the mechatronic system: 1 – standard hydraulic motor; 2 – modernized hydraulic motor**

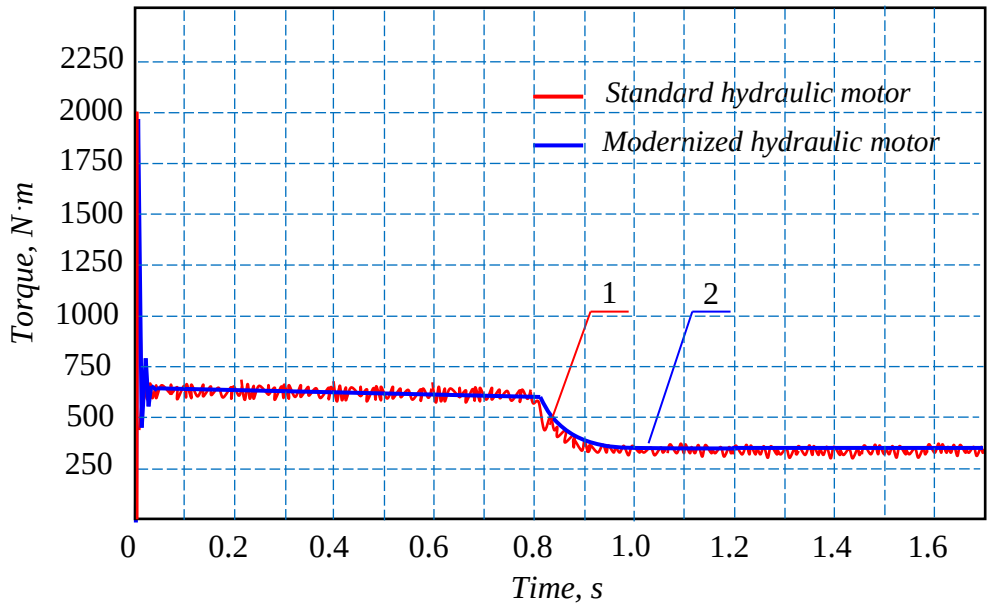



**Fig. 16. Torque variation during acceleration of the hydraulic drive of the mechatronic system: 1 – standard hydraulic motor; 2 – modernized hydraulic motor**

During further acceleration, the torque decreases to its steady-state level during the interval $t$ = 0.8–0.9 s for the standard hydraulic motor and $t$ = 0.72–0.8 s for the modernized hydraulic motor [2]. At $t$ > 0.9 s, the transient process is practically complete for both designs. However, torque oscillations persist in the standard hydraulic motor, with an amplitude of up to 63 N·m according to [2] (Fig. 16, curve 1). For the modernized hydraulic motor, no pronounced torque pulsations are observed in the curve for the computational case considered (Fig. 16, curve 2).

During acceleration of the hydraulic drive, the shaft rotational speed of the standard and modernized hydraulic motors gradually increases to a steady-state value of approximately 600 $min^{-1}$ (Fig. 17). According to [2], this operating condition is reached at approximately $t$ = 0.9 s for the standard hydraulic motor and $t$ = 0.8 s for the modernized hydraulic motor. Thus, under the conditions considered, both designs provide practically the same steady-state rotational speed, but their acceleration durations differ.

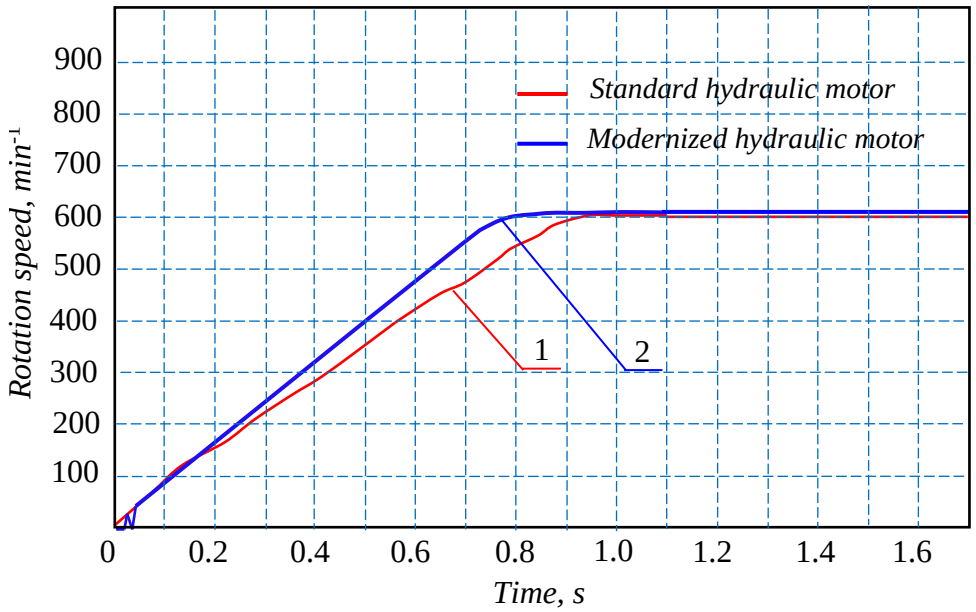



**Fig. 17. Variation in the hydraulic motor shaft rotational speed during acceleration of the hydraulic drive of the mechatronic system: 1 – standard hydraulic motor; 2 – modernized hydraulic motor**

The results considered [7] show that changes in the flow area of the distribution system of the standard hydraulic motor within the range $A_{th}$ = 222–226 mm² are accompanied by pulsations in pressure and working fluid flow rate. When the flow area of the modernized distribution system remains constant at $A_{th}$ = 226 mm², pulsations caused by changes in this area are not observed.

The results of the rotor system study [2] show that changes in the diametral clearance within the range $G$ = 0.055–0.21 mm are accompanied by torque pulsations in the standard hydraulic motor. For the modernized design, with clearance varying within the range $G$ = 0.05–0.06 mm, no pronounced torque pulsations are observed in the computational case considered. These results characterize the operation of the hydraulic drive at constant pump delivery and resisting torque, without a passive pulsation damper.

The results of the study of the dynamic characteristics of the hydraulic drive under variable external inputs, presented in [8], are considered below. Operating conditions were simulated by uneven pump delivery and changes in the resisting torque on the active working element. In study [8], the clearance between the rotors of the standard hydraulic motor varied within the range $G$ = 0.02–0.21 mm, and the flow area of the distribution system varied within the range $A_{th}$ = 200–226 mm². For the modernized hydraulic motor, the corresponding parameters were $G$ = 0.02–0.065 mm and $A_{th}$ = 226 mm². Thus, the geometric parameters of this computational case differ from those of studies [2, 7] considered above.

In the initial period of acceleration of the hydraulic drive ($t$ = 0–0.02 s), a brief pressure surge is observed, reaching approximately 90 MPa for the standard hydraulic motor and 85 MPa for the modernized hydraulic motor [8] (Fig. 18). After the start-up surge, the pressure drops sharply, and its level then gradually decreases from approximately 29 to 27 MPa. During this stage, pressure pulsations associated with changes in the flow area of the distribution system and uneven pump delivery are observed for the standard hydraulic motor.

For the modernized hydraulic motor, the pulsations during this stage are much less pronounced.

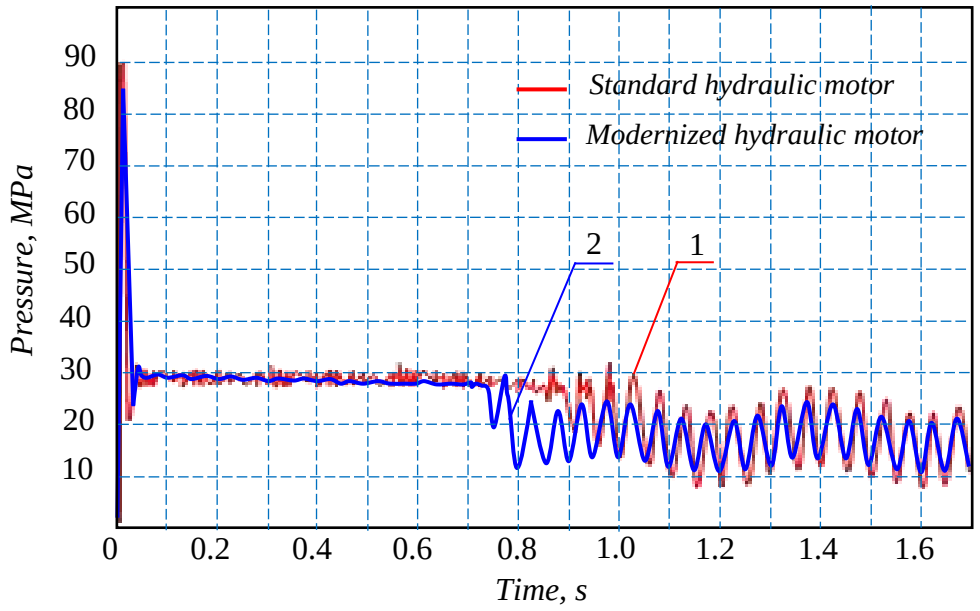



**Fig. 18. Pressure variation during acceleration of the hydraulic drive of the mechatronic system during operation of self-propelled machinery: 1 – standard hydraulic motor; 2 – modernized hydraulic motor**

During the subsequent stage of the transient process, the mean pressure level decreases, but pronounced oscillations caused by variable external inputs persist. According to the curves in Fig. 18, the peak-to-peak magnitude of these oscillations is smaller for the modernized hydraulic motor than for the standard hydraulic motor. Thus, modernization reduces pressure oscillations in the operating mode considered but does not eliminate them completely.

During acceleration of the hydraulic drive, the overall level of the working fluid flow rate through the hydraulic motor gradually increases (Fig. 19). For the standard hydraulic motor, this process is accompanied by pronounced pulsations associated with changes in the flow area of the distribution system and uneven pump delivery (curve 1). For the modernized hydraulic motor, the flow rate varies more smoothly, but the oscillations do not disappear completely (curve 2).

After the main acceleration stage, the flow rate oscillates around a steady mean level. According to [8], the magnitude of the pulsations during this stage is up to 3 L/min for the standard hydraulic motor and up to 2 L/min for the modernized hydraulic motor. The remaining pulsations are associated with uneven pump delivery.

During the initial start-up period of the hydraulic drive, the working fluid flow rate through the relief valve reaches approximately 98 L/min for both hydraulic motor designs considered [8]. As acceleration proceeds, the overall flow rate level decreases, while pronounced pulsations persist (Fig. 20). The flow rate oscillations are larger for the standard hydraulic motor than for the modernized hydraulic motor.

During the final stage of valve operation, the flow rate periodically drops to zero, after which individual flow pulses occur again. According to the curves in Fig. 20, flow finally ceases at approximately $t$ = 0.95 s for the standard hydraulic motor (curve 1) and $t$ = 0.75 s for the modernized hydraulic motor (curve 2). These values characterize the cessation of flow through the relief valve in the computational case considered.

During the initial start-up period of the hydraulic drive ($t$ = 0–0.02 s), a brief torque surge is observed, reaching approximately 2100 N·m for the standard hydraulic motor and 1900 N·m for the modernized hydraulic motor [8] (Fig. 21). After the start-up surge, the torque

level decreases to 640–620 N·m. During this stage, pronounced pulsations associated with the design features of the rotor system are observed for the standard hydraulic motor (curve 1). For the modernized hydraulic motor, the torque varies more smoothly (curve 2).

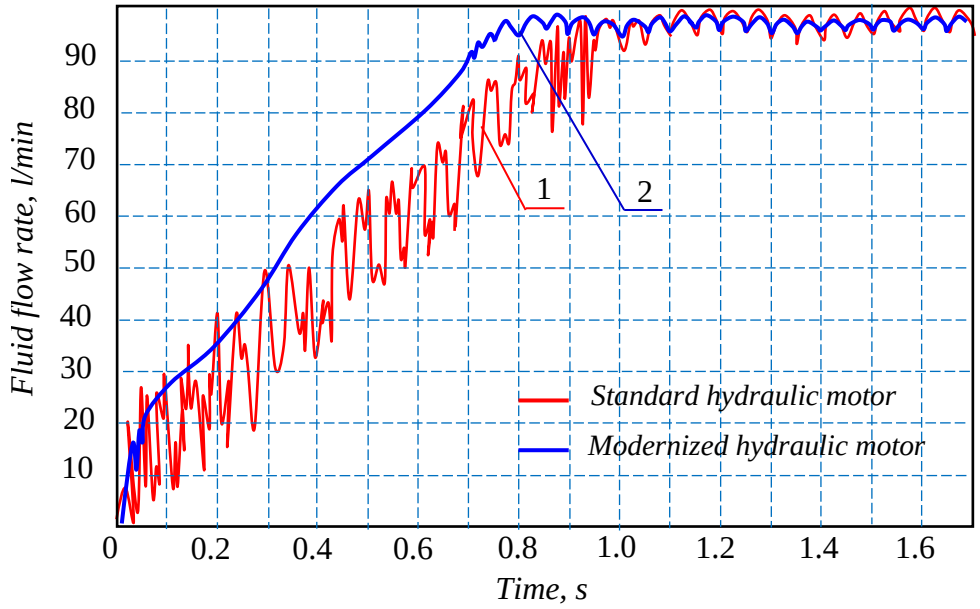



**Fig. 19. Variation in the working fluid flow rate through the hydraulic motor during acceleration of the hydraulic drive of the mechatronic system during operation of self-propelled machinery: 1 – standard hydraulic motor; 2 – modernized hydraulic motor**

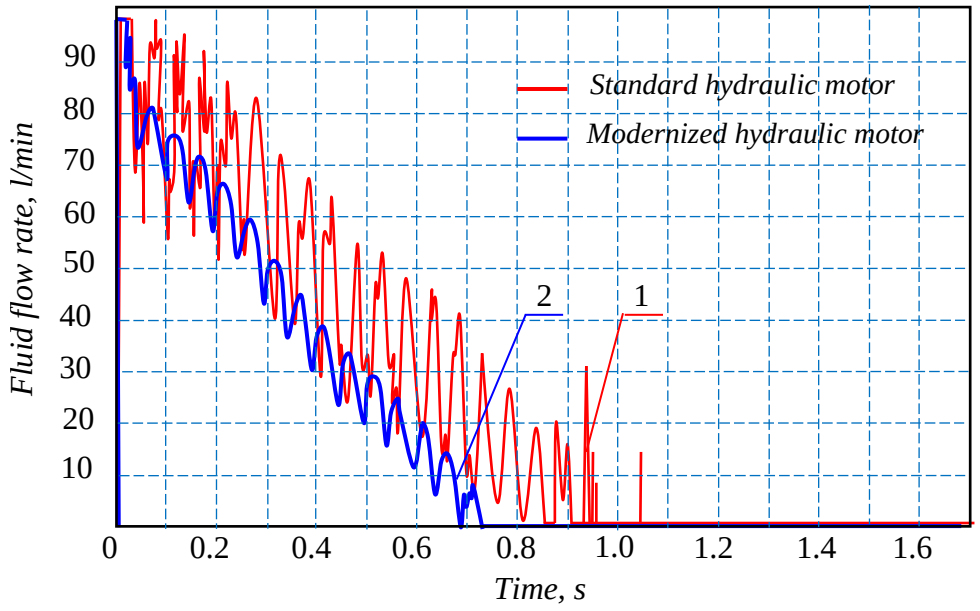



**Fig. 20. Variation in the working fluid flow rate through the relief valve during acceleration of the hydraulic drive of the mechatronic system during operation of self-propelled machinery: 1 – standard hydraulic motor; 2 – modernized hydraulic motor**

During the subsequent stage of the transient process, the mean torque level decreases. However, oscillations associated with changes in the resisting torque persist for both designs. According to the curves in Fig. 21, the peak-to-peak magnitude of these oscillations is smaller for the modernized hydraulic motor than for the standard hydraulic motor. Thus, in the operating mode considered, modernization reduces torque oscillations but does not eliminate them completely.

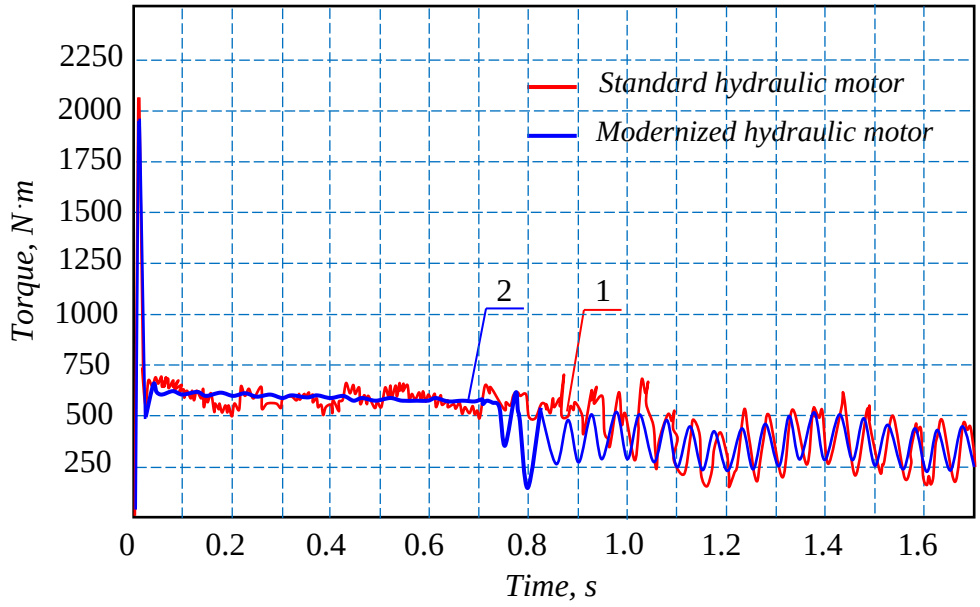



**Fig. 21. Torque variation during acceleration of the hydraulic drive of the mechatronic system during operation of self-propelled machinery: 1 – standard hydraulic motor; 2 – modernized hydraulic motor**

During acceleration of the hydraulic drive, the shaft rotational speed of the standard and modernized hydraulic motors increases, approaching a mean level of approximately 600 min$^{-1}$ (Fig. 22). The modernized hydraulic motor reaches this level earlier than the standard hydraulic motor. After the main acceleration stage, the rotational speed of both designs continues to oscillate around the mean value due to uneven pump delivery and changes in the resisting torque [8].

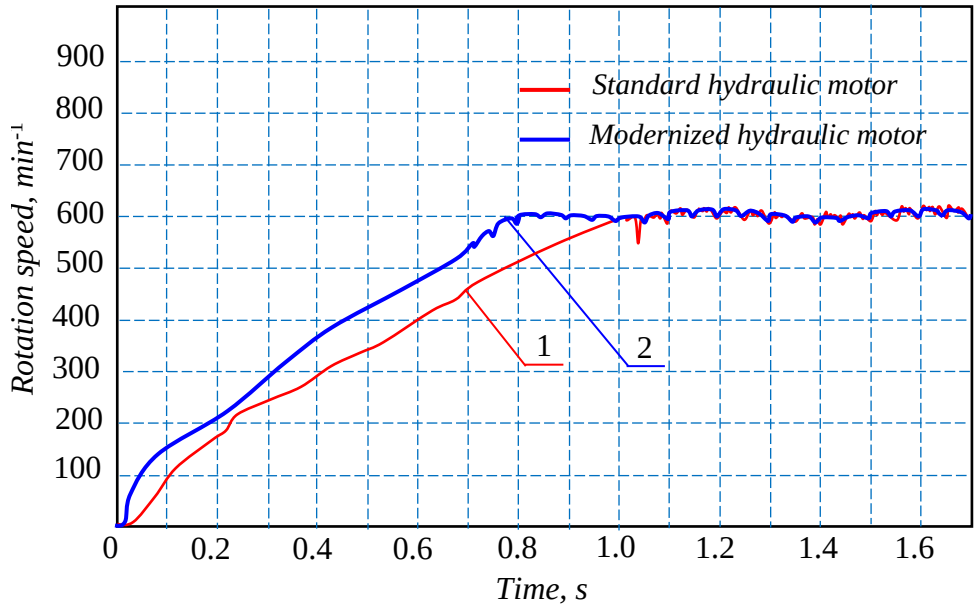



**Fig. 22. Variation in the hydraulic motor shaft rotational speed during acceleration of the hydraulic drive of the mechatronic system during operation of self-propelled machinery: 1 – standard hydraulic motor; 2 – modernized hydraulic motor**

The results considered [8] show that, under variable external inputs, the modernized hydraulic motor reaches the operating rotational speed level more quickly and exhibits smaller pressure and torque oscillations than the standard hydraulic motor. These differences are associated with a reduction in the clearance between the rotor teeth and the elimination of

changes in the flow area of the distribution system. However, modernization does not eliminate oscillations in the output characteristics caused by uneven pump delivery and changes in the load.

The third computational case considers the operation of the hydraulic drive with a passive pulsation damper of 5000 cm³ under variable external inputs. The use of such a damper to reduce dynamic loads is considered in [14]. Figures 23–27 present the simulation results for the corresponding processes in the standard and modernized hydraulic motors, obtained by the authors using the VisSim package.

During start-up of the hydraulic drive with a passive pulsation damper, a brief increase in pressure is observed. According to the curves in Fig. 23, the peak pressure is approximately 38 MPa for the standard hydraulic motor (curve 1) and 36 MPa for the modernized hydraulic motor (curve 2). These values are lower than the start-up maxima shown in Fig. 18 for the hydraulic drive without a damper. After the start-up surge, the pressure drops to approximately 29 MPa and then gradually decreases. During acceleration, the pressure oscillations are more pronounced for the standard hydraulic motor than for the modernized hydraulic motor.

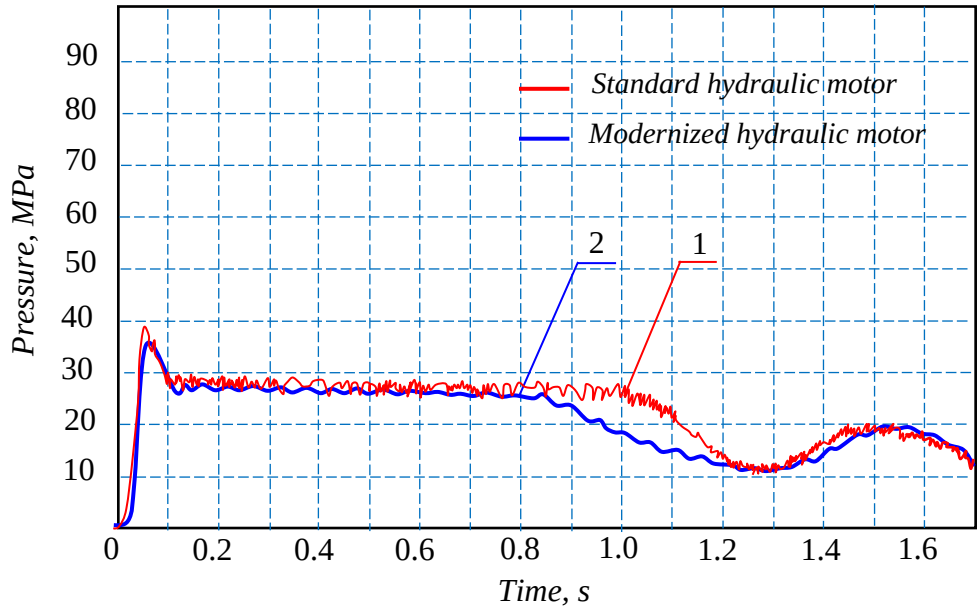



**Fig. 23. Pressure variation during acceleration of the hydraulic drive of the mechatronic system during operation of self-propelled machinery with a passive pulsation damper: 1 – standard hydraulic motor; 2 – modernized hydraulic motor**

As the mean pressure level decreases further, smooth oscillations associated with changes in the resisting torque persist for both designs. Thus, in the computational case presented, the use of a passive damper is accompanied by a reduction in start-up pressure peaks but does not completely eliminate oscillations under variable load.

The curves in Fig. 24 show the variation in the working fluid flow rate through the hydraulic motor when a passive pulsation damper is used. During acceleration, the mean flow rate increases, approaching 100 L/min. For the standard hydraulic motor (curve 1), this increase is accompanied by pronounced pulsations. For the modernized hydraulic motor (curve 2), the flow rate increases more smoothly and reaches the level corresponding to the end of the main acceleration stage earlier.

After acceleration, flow rate oscillations persist for both designs, with more pronounced oscillations in the standard hydraulic motor. Thus, in the hydraulic drive with a passive pulsation damper considered here, the modernized hydraulic motor exhibits smoother flow rate variation both during acceleration and during subsequent operation under variable external inputs.

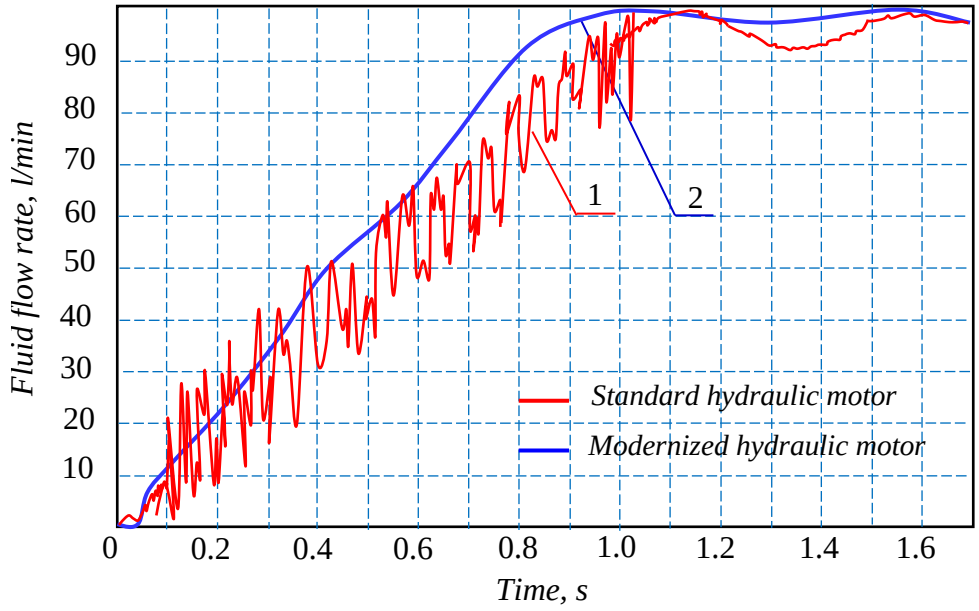



**Fig. 24. Variation in the working fluid flow rate through the hydraulic motor during acceleration of the hydraulic drive of the mechatronic system during operation of self-propelled machinery with a passive pulsation damper: 1 – standard hydraulic motor; 2 – modernized hydraulic motor**

Figure 25 presents the curves of the working fluid flow rate through the relief valve when a passive pulsation damper is used. At the beginning of start-up, there is no flow through the valve. The flow rate then briefly rises to a maximum value of approximately 98 L/min. Subsequently, as the hydraulic motor accelerates, the mean flow rate through the valve decreases. This process is accompanied by pulsations that are more pronounced for the standard hydraulic motor (curve 1) than for the modernized hydraulic motor (curve 2).

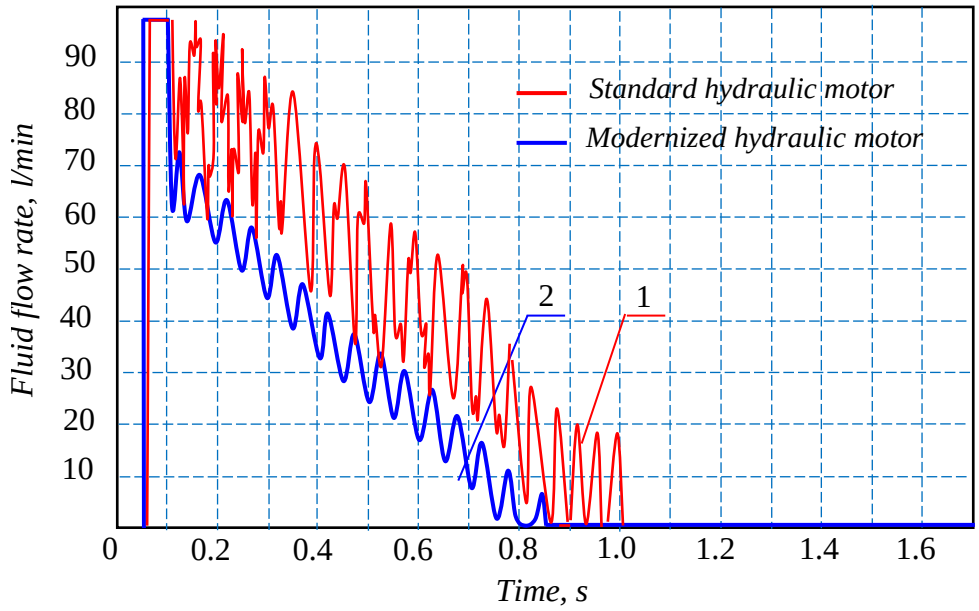



**Fig. 25. Variation in the working fluid flow rate through the relief valve during acceleration of the hydraulic drive of the mechatronic system during operation of self-propelled machinery with a passive pulsation damper: 1 – standard hydraulic motor; 2 – modernized hydraulic motor**

According to the curves, flow through the relief valve ceases after the final pulsations at approximately $t$ = 1.0 s for the standard hydraulic motor and $t$ = 0.85 s for the modernized

hydraulic motor. During the subsequent period shown in the curves, the flow rate through the valve remains zero.

During start-up of the hydraulic drive with a passive pulsation damper, a brief torque surge is observed (Fig. 26). According to the curves presented, the peak values for both designs are approximately within the range of 900–1000 N·m. After the start-up surge, the torque decreases to approximately 600–650 N·m, and its mean value then gradually decreases. During this stage, torque oscillations are more pronounced for the standard hydraulic motor (curve 1) than for the modernizsed hydraulic motor (curve 2).

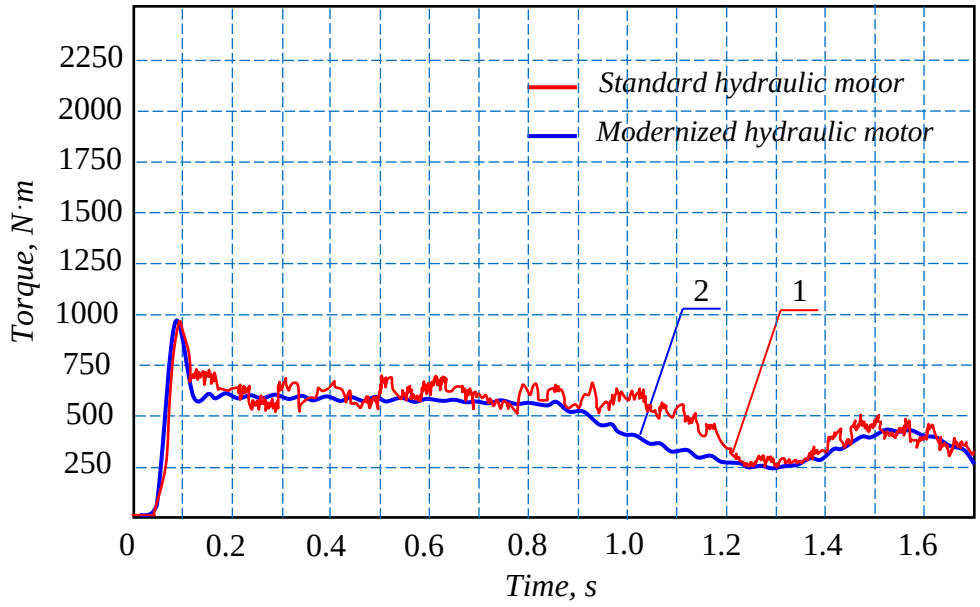



**Fig. 26. Torque variation during acceleration of the hydraulic drive of the mechatronic system during operation of self-propelled machinery with a passive pulsation damper: 1 – standard hydraulic motor; 2 – modernized hydraulic motor**

The subsequent decrease in the mean torque level begins earlier for the modernized hydraulic motor than for the standard hydraulic motor. During further operation, smooth torque oscillations persist for both designs under variable external load. A comparison of Figs. 21 and 26 shows that, in the computational case presented with a passive pulsation damper, the start-up torque maxima are substantially lower than in the case without a damper. However, torque oscillations are not completely eliminated.

Figure 27 presents the variation in the hydraulic motor shaft rotational speed when a passive pulsation damper is used. During acceleration, the rotational speed of both designs increases, approaching approximately 600 $min^{-1}$. The modernized hydraulic motor (curve 2) reaches this level earlier than the standard hydraulic motor (curve 1).

After the main acceleration stage, the rotational speed oscillates around the mean level reached. Under the variable external inputs considered, these oscillations are more pronounced for the standard hydraulic motor than for the modernized hydraulic motor. Thus, the use of a passive pulsation damper does not eliminate rotational speed oscillations during subsequent operation of the hydraulic drive.

A comparison of the computational cases considered without a damper and with a passive pulsation damper of 5000 $cm^3$ shows a reduction in start-up pressure and torque maxima when the damper is used. In Fig. 18, the peak pressure values are approximately 90 and 85 MPa for the standard and modernized hydraulic motors, respectively, whereas in Fig. 23 they are approximately 38 and 36 MPa. The start-up torque maxima decrease from approximately 2100 and 1900 N·m (Fig. 21) to values within the range of 900–1000 N·m (Fig. 26).

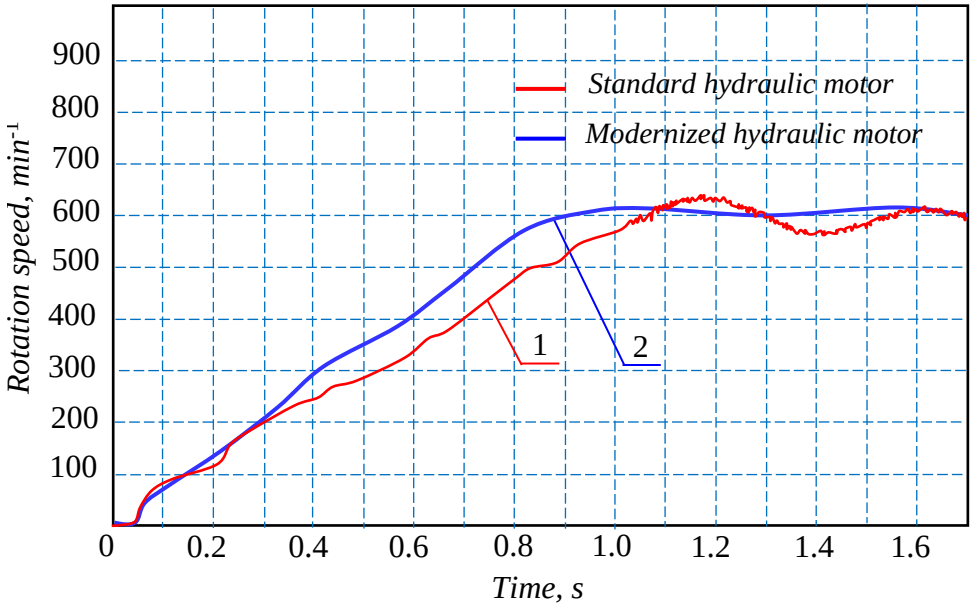



**Fig. 27. Variation in the hydraulic motor shaft rotational speed during acceleration of the hydraulic drive of the mechatronic system during operation of self-propelled machinery with a passive pulsation damper: 1 – standard hydraulic motor; 2 – modernized hydraulic motor**

Differences between the characteristics of the standard and modernized hydraulic motors persist in the hydraulic drive with a passive pulsation damper. The modernized hydraulic motor exhibits smoother variations in flow rate and torque during acceleration and reaches the operating rotational speed level earlier. However, under variable external inputs, oscillations in the output parameters persist for both designs.

## Discussion.

A comparison of the results considered allows discussion of the effects of the design features of the planetary hydraulic motor, variable external inputs, and a passive pulsation damper on the dynamic characteristics of the hydraulic drive. The computational cases presented bring together the results of studies of the rotor and distribution systems [2, 7], hydraulic drive operation under operating disturbances [8], and the use of a passive pulsation damper [14]. When comparing these cases, differences in the initial geometric parameters and calculation conditions must be taken into account. Therefore, differences between individual cases cannot always be explained by a change in only one factor.

At constant pump delivery and resisting torque, changes in the flow area of the distribution system are accompanied by pressure and flow rate pulsations [7], while changes in the diametral clearance between the rotors are accompanied by torque oscillations [2]. For the modernized design with a constant flow area and a smaller range of clearance variation, the corresponding pulsations are less pronounced. These results help identify directions for improving the hydraulic motor design. However, pressure, flow rate, and torque are interrelated, so the effects of the rotor and distribution systems should not be considered completely independent.

Under variable pump delivery and resisting torque, the modernized hydraulic motor also exhibits smoother variations in the output parameters and reaches the operating rotational speed level earlier [8]. However, design modernization does not eliminate oscillations caused by external inputs. Therefore, the reduction of internal sources of pulsations must be considered together with the operating conditions of the hydraulic drive.

In the computational case with a passive pulsation damper of 5000 cm³, the start-up pressure and torque maxima are lower than in the case considered without a damper. However, both the differences between the standard and modernized hydraulic motors and the

oscillations during subsequent operation under variable load persist. This allows the passive damper to be considered an additional means of reducing start-up dynamic loads. The results presented do not justify extending the degree of reduction in start-up maxima to all subsequent oscillations in pressure, flow rate, and torque.

The operation of the relief valve must also be taken into account when interpreting transient processes. The flow rate curves for the valve show individual flow pulses followed by cessation of flow. The time at which flow ceases characterizes valve operation but does not, by itself, determine the completion of hydraulic motor acceleration. The acceleration duration should be assessed from the rotational speed curve using a common criterion for reaching the operating mode.

The synthesis presented is limited to the designs, parameters, and computational operating conditions considered. Numerical estimates obtained directly from the curves are approximate. A quantitative comparison of oscillations requires identical time intervals and a consistent definition of the measure used, either amplitude or full peak-to-peak magnitude. The reduction in oscillations under the operating conditions considered indicates improved dynamic performance but does not replace a separate study of hydraulic drive stability.

The practical significance of the results considered lies in providing a basis for jointly considering the hydraulic motor design, operating disturbances, and passive damping measures when designing the hydraulic drive. Maintaining a constant flow area of the distribution system and reducing the range of clearance variation between the rotors help reduce the associated pulsations, while the use of a passive damper further limits start-up loads. The selection of specific parameters requires consideration of the operating conditions and permissible oscillations in the output characteristics.

## Conclusions.

1. The results of computational studies of the dynamic characteristics of the hydraulic drive of a mechatronic system with standard and modernized planetary hydraulic motors have been summarized. Cases with constant pump delivery and resisting torque, variable external inputs, and the use of a passive pulsation damper have been considered. A comparison of these results makes it possible to assess how design and operating factors are reflected in variations in pressure, flow rate, torque, and rotational speed.

2. Under the computational operating conditions considered, changes in the flow area of the distribution system are accompanied by pulsations in pressure and working fluid flow rate, while changes in the diametral clearance between the rotors are accompanied by torque oscillations. A constant flow area and a smaller range of clearance variation in the modernized hydraulic motor contribute to reducing the corresponding pulsations.

3. Under variable pump delivery and resisting torque, the modernized hydraulic motor exhibits smaller pressure and torque oscillations and reaches the operating rotational speed level earlier than the standard hydraulic motor. However, oscillations in the output parameters caused by external inputs persist for both designs.

4. In the computational case considered with a passive pulsation damper of 5000 $cm^3$, the start-up pressure maxima are approximately 38 and 36 MPa for the standard and modernized hydraulic motors, respectively, compared with approximately 90 and 85 MPa in the case without a damper. The start-up torque maxima are within the range of 900–1000 N·m for both designs, compared with approximately 2100 and 1900 N·m without a damper. These estimates characterize the reduction in start-up loads under the conditions considered; subsequent oscillations under variable load are not completely eliminated.

5. The results considered support the joint consideration of hydraulic motor design parameters, operating disturbances, and passive damping measures when designing the hydraulic drive. Modernization of the rotor and distribution systems reduces pulsations associated with their geometry, while a passive damper further limits start-up loads. The

quantitative results relate to the computational cases presented and should be applied with due consideration of differences in the initial parameters and operating conditions.

## References


1. Panchenko A., Voloshina A., Kiurchev S., Titova O., Onopreychuk D., Stefanov V., Safoniuk I., Pashchenko V., Radionov H., Golubok M. Development of the universal model of mechatronic system with a hydraulic drive. *Eastern-European Journal of Enterprise Technologies*. 2018. 4 (7(94)). 51–60. https://doi.org/10.15587/1729-4061.2018.139577
2. Panchenko A., Voloshina A., Titova O., Panchenko I., Zasiadko A. The Study of Dynamic Processes of Mechatronic Systems with Planetary Hydraulic Motors. *InterPartner 2020: Advanced Manufacturing Processes II*. LNME. Springer, Cham, 2021. 704–713. https://doi.org/10.1007/978-3-030-68014-5_68
3. Kyurchev V., Kiurchev S., Rezvaya K., Pastushenko A., Głowacki S. Experimental Evaluation of the Impact of the Diametral Clearance on Output Characteristics of a Planetary Hydraulic Motor. *DSMIE 2023: Advances in Design, Simulation and Manufacturing VI*. LNME. Springer, Cham, 2023. 84–94. https://doi.org/10.1007/978-3-031-32774-2_9
4. Kiurchev S., Luzan P., Zasiadko A., Radionov H., Boltianska N. Influence of the flow area of distribution systems on changing the operating parameters of planetary hydraulic motors. *IOP Conference Series: Materials Science and Engineering*, 2021. 1021. 012037. https://doi.org/10.1088/1757-899X/1021/1/012037
5. Hutsol T. European Green Deal: Improving the Efficiency of Using Planetary Hydraulic Machines. *Energies*, 2023. 16 (18). 6481. https://doi.org/10.3390/en16186481.
6. Yeremenko, O., Abdullo, M. A., Boltianska, N., Mikhalchenko, S., Verkholantseva, V. Reducing the Pulsation of the Working Fluid in Planetary Hydraulic Machines by Rational Design of Their Distribution Systems. *DSMIE 2022: Advances in Design, Simulation and Manufacturing V*. LNME. Springer, Cham, 2, 133-143 (2022). https://doi.org/10.1007/978-3-031-06044-1_13
7. Voloshina A, Panchenko A, Titova O, Panchenko I. Changes in the dynamics of the output characteristics of mechatronic systems with planetary hydraulic motors. Journal of Physics: Conference Series, 2021. Vol. 1741. 012045. https://doi.org/10.1088/1742-6596/1741/1/012045
8. Panchenko, A., Voloshina, A., Sadullozoda, S. S., Boltyansky, O., Panina, V.: Influence of the Design Features of Orbital Hydraulic Motors on the Change in the Dynamic Characteristics of Hydraulic Drives. *DSMIE 2022: Advances in Design, Simulation and Manufacturing V*. LNME. Springer, Cham, 2022. 2. 101–111. https://doi.org/10.1007/978-3-031-06044-1_10
9. Kiurchev S., Kyurchev V., Fatyeyev A., Tynyanova I., Mudryk K. Influence of the Radius of Curvature of the Teeth on the Geometric and Functional Parameters of the Rotors of the Planetary Hydraulic Motor. *Interpartner 2023: Advanced Manufacturing Processes V*. LNME. Springer, Cham, 2023. 450–461. https://doi.org/10.1007/978-3-031-42778-7_42.
10. Kiurchev S., Kyurchev V., Radkevych O., Fatyeyev O., Hrechka I. Monitoring the Accuracy of Manufacturing Elements of the End Distribution System of a Hydraulic Motor Planetary Type. *Interpartner 2024: Advanced Manufacturing Processes VI*. LNME. Springer, Cham, 2025. 712–723. https://doi.org/10.1007/978-3-031-82746-4_63
11. Wang Y., Shen T., Tan C., Fu J., Guo S. et al. Research Status, Critical Technologies, and Development Trends of Hydraulic Pressure Pulsation Attenuator. *Chinese Journal of Mechanical Engineering*. 2021. 34. 14. https://doi.org/10.1186/s10033-021-00532-z.
12. Eyres R. D., Champneys A. R., Lieven N. A. J. Modelling and Dynamic Response of a Damper with Relief Valve. *Nonlinear Dynamics*. 2005. 40 (2). 119–147. https://doi.org/10.1007/s11071-005-4144-6
13. Li D., Liu Y., Gong J., Wang T. Design of a Noncircular Planetary Gear Mechanism for Hydraulic Motor. *Mathematical Problems in Engineering*. 2021. 5510521. 1–9. https://doi.org/10.1155/2021/5510521
14. Panchenko, A., Voloshina, A., Fatyeyev A., Tynyanova I. and Mudryk K. Stabilization of the Transient Dynamic Characteristics for a Hydraulic Drive with a Planetary Hydraulic Motor. *DSMIE 2023: Advances in Design, Simulation and Manufacturing VI*. LNME. Springer, Cham, 2023. 2. 95–105. https://doi.org/10.1007/978-3-031-32774-2_10

15. Dasgupta K., Mandal S. K., Pan S. Dynamic analysis of a low speed high torque hydrostatic drive using steady-state characteristics. *Mechanism and Machine Theory*. 2012. 52. 1–17. https://doi.org/10.1016/j.mechmachtheory.2011.12.004

16. Zeman P., Kemmetmüller W., Kugi A. Mathematical Modeling and Analysis of a Hydrostatic Drive Train. *IFAC-PapersOnLine*. 2015. 48 (1). 508–513. https://doi.org/10.1016/j.ifacol.2015.05.064

17. Li C., Jiang T., Liu C., Xu H., Shi G. Investigation of the leakage in the flow distribution pair of radial piston hydraulic motors through CFD analysis and experiments. *Flow Measurement and Instrumentation*. 2024. 96. 102555. https://doi.org/10.1016/j.flowmeasinst.2024.102555

18. Kyurchev, V., Kiurchev, S., Rezvaya, K., Fatyeyev, A., Głowacki, S. Assessing the Reliability of a Mathematical Model of Working Processes Occurring in a Hydraulic Drive. *DSMIE 2024: Advances in Design, Simulation and Manufacturing VII*. LNME. Springer, Cham, 2024. https://doi.org/10.1007/978-3-031-63720-9_24

19. Ghoshal S. K., Pandey A. K , Dasgupta K., Bhola M. A segmental pump-motor control scheme to attain targeted speed under varying load demand of a hydraulic drive used in heavy earth movers. *Mechatronics*. 2021. 80. 102681. https://doi.org/10.1016/j.mechatronics.2021.102681

20. Gaheen O. A., Aziz M.A., Benini E. Experimental and modeled response of hydraulic motors under pulsating flow. *Engineering Science and Technology, an International Journal*. 2025. 72. 102234. https://doi.org/10.1016/j.jestch.2025.102234.

21. Fang Y., Yang H., Zhang G. et al.Multi-interface fusion speed pulsation model and behavior analysis for high-torque hydraulic motors. *Flow Measurement and Instrumentation*. 2026. 108. 103148. https://doi.org/10.1016/j.flowmeasinst.2025.103148

22. Grimaldi K., Najjaran A., Ma Z., Bao H., Roskilly T. Dynamic Modelling and Experimental Validation of a Pneumatic Radial Piston Motor. *Energies*, 2023. 16 (4). 1954. https://doi.org/10.3390/en16041954

23. Kojima E., Yamada T., Narikawa H., Moriyama K. A Simulation Model of the Delivery Flow Ripple produced by a Hydraulic Axial Piston Pump. *Transactions of the Japan Hydraulics & Pneumatics Society*. 1998. Vol. 29, No. 4. P. 100–106. https://doi.org/10.14888/jfps1998.29.100

24. Casoli P., Gherardini F., Campanini F. Active Pressure Ripple Control in Axial Piston Pumps through High-Frequency Swash Plate Oscillations – A Theoretical Analysis. *Energies*. 2019. 12 (7). 1377. https://doi.org/10.3390/en12071377.

25. Kojima E., Shinada M. Characteristics of Fluidborne Noise Generated by a Fluid Power Pump: 4th Report, Pressure Ripple in Hydrostatic Power Transmission. *Journal of the Japan Society of Mechanical Engineers*. 1986. 29 (258). 4147–4155. https://doi.org/10.1299/jsme1958.29.4147

26. Johnston D. N., Edge K. A. Simulation of the Pressure Ripple Characteristics of Hydraulic Circuits. *Proceedings of the Institution of Mechanical Engineers, Part I*. 1989. 203 (4). https://doi.org/10.1243/PIME_PROC_1989_203_114_02

27. Dindorf R., Takosoglu J., Wos P. Review of Hydro-Pneumatic Accumulator Models for the Study of the Energy Efficiency of Hydraulic Systems. *Energies*. 2023. 16 (18). 6472. https://doi.org/10.3390/en16186472.

28. Ray A. Dynamic modeling and simulation of a relief valve. *Simulation*. 1978. 31 (5). https://doi.org/10.1177/003754977803100504

29. Song W., Yang C. Mathematical Modelling and Dynamic Analysis of a Direct-Acting Relief Valve Based on Fluid-Structure Coupling Analysis. *Shock and Vibration*. 2021. 5581684. https://doi.org/10.1155/2021/5581684

30. Panchenko A. I., Voloshyna A. A., Rozhniatovskyi V. V., Zasiadko A. I. Model hidravlichnoho pryvodu mekhatronnoi systemy z planetarnym hidromotorom. *Promyslova hidravlika i pnevmatyka*, 2024. № 2(74). S. 12–32. https://doi.org/10.32782/1994-4691-2024-2-74-2

*Дата першого надходження статті до видання 25.09.2026*
*Дата прийняття статті до друку після рецензування 21.10.2026*
*Дата публікації (оприлюднення) статті 04.11.2026*
*Стаття поширюється на умовах ліцензії відкритого доступу(CC BY 4.0)*

# ДИНАМІЧНА МОДЕЛЬ ГІДРАВЛІЧНОГО ПРИВОДУ МЕХАТРОННОЇ СИСТЕМИ З ПЛАНЕТАРНИМ ГІДРОМОТОРОМ

**А. І. Панченко[1], А. А. Волошина[1], І. А. Панченко[1], І. М. Холод[1], А. А. Волошин[2]**
[1] *Таврійський державний агротехнологічний університет імені Дмитра Моторного,*
[2] *ВСП «Мелітопольський фаховий коледж ТДАТУ»*

***Анотація***

У статті узагальнено результати розрахункових досліджень динамічних характеристик гідроприводу мехатронної системи із серійним і модернізованим планетарними гідромоторами. Мета роботи – зіставити вплив конструкції гідромотора, зовнішніх збурень і пасивного гасіння пульсацій на перехідні процеси гідроприводу. В аналізі враховано площу прохідного перерізу розподільної системи, діаметральний зазор між роторами, нерівномірність подачі насоса та зміну моменту опору. Розглянуто три випадки: постійні подача насоса й момент опору, змінні зовнішні впливи та робота з пасивним гасником пульсацій. Зміна площі прохідного перерізу розподільної системи супроводжується пульсаціями тиску й витрати робочої рідини, а зміна діаметрального зазору — коливаннями крутного моменту. За змінних зовнішніх впливів модернізований гідромотор характеризується меншими коливаннями тиску й крутного моменту та раніше досягає робочого рівня частоти обертання порівняно із серійним. У випадку застосування пасивного гасника пульсацій об’ємом 5000 см³ пускові максимуми тиску становлять приблизно 38 і 36 МПа для серійного та модернізованого гідромоторів відповідно, порівняно з 90 і 85 МПа без гасника. Пускові максимуми крутного моменту перебувають у межах 900–1000 Н·м для обох конструкцій, порівняно з приблизно 2100 і 1900 Н·м без гасника. Водночас коливання за змінного навантаження зберігаються в обох конструкцій. Результати обґрунтовують доцільність спільного розгляду конструктивного вдосконалення гідромотора та пасивного демпфування під час вибору заходів зі зменшення пульсацій і пускових навантажень. Числові оцінки стосуються розглянутих випадків з урахуванням відмінностей їхніх вихідних параметрів та умов роботи.

***Ключові слова:*** перехідні процеси, розгін гідроприводу, тиск, крутний момент, витрата робочої рідини, частота обертання.

Conflict of Interest: The author is the journal’s editor-in-chief. To ensure the independence of the editorial process, the manuscript was handled by a designated editor who was not subordinate to the author and had no conflict of interest. The author did not participate in the selection of reviewers, the peer-review process, or the decision to publish the article. The manuscript underwent the standard double-blind peer review process.

**DOI https://doi.org/10.32782/1994-4691-2026-1-77-4**
UDK 621.565.9

# FEASIBILITY ASSESSMENT OF A VORTEX TUBE FOR EXHAUST AIR ENERGY RECOVERY IN A PNEUMATIC CYLINDER

# ОБҐРУНТУВАННЯ МОЖЛИВОСТІ ЗАСТОСУВАННЯ ВИХОРОВОЇ ТРУБИ ДЛЯ РЕКУПЕРАЦІЇ ЕНЕРГІЇ ВІДПРАЦЬОВАНОГО ПОВІТРЯ ПНЕВМОЦИЛІНДРА

A. Rogovyi[1], Dr. Sc., Professor ORCID: 0000-0002-6057-4845
M. Stryzhak[1*], Ph.D., Associate Professor ORCID: 0000-0003-3335-4086
D. Savenkov[1] ORCID: 0009-0008-8654-627X
D. Dyomin[1] ORCID: 0009-0003-0314-1191
R. Hasanov[1] ORCID: 0009-0002-4436-3359

[1]*National Technical University "Kharkiv Polytechnic Institute", Kharkiv, Ukraine*
*e-mail: Mariana.Stryzhak@khpi.edu.ua

**Abstract**. This article discusses an approach to improving the energy efficiency of pneumatic actuators by recovering energy from exhaust air using a vortex tube based on the Rank-Hirsch effect. Based on a review of the literature, the selection of the pipe's geometric parameters is justified, and a three-dimensional CAD model of the pipe is constructed, adapted to the conditions of supply from the exhaust line of a pneumatic cylinder. The methodology includes numerical simulation of the airflow in ANSYS CFX under steady-state boundary conditions corresponding to the characteristic parameters of the exhaust flow. The results confirm the formation of a cold axial core and a hot peripheral flow zone, with maxima of static entropy and turbulent kinetic energy localized immediately behind the nozzle rim. The obtained data indicate the fundamental possibility of using the cold flow for localized cooling of components in technological systems without the use of additional energy.

**Keywords**: pneumatic actuator, vortex tube, energy recovery, energy efficiency.

## Introduction.

Pneumatic actuators form the basis of modern automation systems and flexible manufacturing complexes. Their widespread integration into a wide variety of industrial processes is due to their high specific power, fast response time, reliability, and fire safety. However, a significant drawback of pneumatic systems remains their low overall efficiency, which typically does not exceed 15% [1, 2]. Given the high cost of producing and preparing compressed air, the task of energy conservation and fully utilizing the performance of compressed air is critically important for industry.

## Literature Review.

Various scientific approaches to improving the energy efficiency of pneumatic systems are currently being actively developed [3]: preventing compressed air leaks, maintaining an optimal pressure level in the system, correctly selecting the sizes of actuators, and so on. One such approach is the use of computational fluid dynamics methods for a detailed analysis and optimization of pneumatic actuator operating processes, which allows for the identification of hidden sources of losses that are inaccessible to classical calculation methods [4].

At the same time, there is another source of irreversible energy and exergetic losses in the operating cycle of a pneumatic actuator that is less frequently studied: the free expansion of compressed air into the atmosphere during the exhaust phase [5, 6]. A quantitative exergetic assessment of the efficiency of a pneumatic actuator with controlled piston braking and

compressed air recovery, which confirms the significant potential for reducing losses specifically during the exhaust phase, is presented in [7].

At the moment the exhaust line of the air distributor opens, the cylinder's working chamber is still under residual pressure. When this pressure is directly vented, up to 40-60% of the potential energy expended by the compressor during the intake stroke is lost [8, 9]. Such direct dissipation of energy into the environment is inefficient, since the exhaust flow possesses sufficient energy potential to perform useful work.

In this regard, a promising approach to energy conservation is the reuse of energy from the exhaust air [10]. Specifically, this is achieved by recovering air from the exhaust chamber and returning it to the intake system [11] using a check valve configuration.

Reference [12] describes a system that involves storing the air exiting the cylinder in a special receiver and subsequently reusing it in subsequent cycles, which has enabled savings of up to 23%. In [13], a scheme is proposed that cuts off the air supply once the required pressure level is reached, allowing air to be retained in the chambers without additional supply – this approach yielded savings of up to 71%.

The paper [14] describes an approach in which, instead of the traditional venting of air, it is redirected between the cylinder chambers or even returned to the network. As a result, savings of up to 87% are achieved, making such switching solutions among the most promising for energy-saving applications.

Overall, active research into energy recovery from exhaust flows indicates the promise of this approach to improving the energy efficiency of pneumatic actuators. The use of a vortex tube, device based on the Rank-Hilsch effect [15, 16], deserves special attention.

The phenomenon of energy separation of a swirling gas flow into a cold axial component and a hot peripheral component was first described in 1933 [15] and subsequently investigated in [16], where a characteristic design of a counter-flow cylindrical tube with a tangential nozzle inlet was proposed. Compressed air is accelerated through a ring of tangential nozzles to a high (transonic) velocity, resulting in the formation of vortex motion within the pipe, with energy transfer from the axial to the peripheral layers occurring primarily due to viscous shear. This causes an increase in the total temperature at the periphery of the flow and a decrease in the near-axis zone; accordingly, hot (through a conical valve) and cold (through a restricting diaphragm) flows are extracted at opposite ends of the tube.

The practical value of using a vortex tube lies in the ability to "passively" utilize the exhaust flow (Fig. 1). The tube is installed in the exhaust line of a pneumatic cylinder and requires no additional power consumption or complex mechanisms; it is fire-safe (since it uses only the exhaust air flow without electrical voltage) and is highly reliable.

The cold component, which forms in the axial zone of the tube, can be directed to dissipate heat from the electronic components of the pneumatic actuator, which are typically located in close proximity to the actuator and are sensitive to overheating, or to cool the tool (Fig. 1). The hot component, in turn, is discharged into the atmosphere according to the basic design, just like exhaust air without the use of a vortex tube; that is, it does not degrade the performance characteristics of the pneumatic system. However, the elevated temperature of this flow opens up additional potential for auxiliary applications. This could involve heating components of distribution equipment to prevent the freezing of moist compressed air at low temperatures, which is a common problem in industrial pneumatic systems during the winter.

A schematic diagram illustrating the proposed approach is shown using the example of a drilling machine feed drive (Fig. 1). Pneumatic cylinder 1, together with control box 2, drives the machine's spindle; when the valve switches to reverse operation, the exhaust air from the cylinder's working chamber is not vented to the atmosphere, as in a traditional circuit, but is directed to the nozzle inlet of the vortex tube 4. The swirled flow in the tube is divided into a cold axial component and a hot peripheral component: the cold flow is drawn off through the "cold" outlet 5 and, via a flexible hose 3, is directed directly into the cutting zone for

localized cooling of the drill bit; the hot flow is diverted through the “hot” outlet 6. This integration method requires no additional power sources or changes to the cylinder control circuit, since the vortex tube merely intercepts a flow that would otherwise be discharged into the atmosphere anyway.

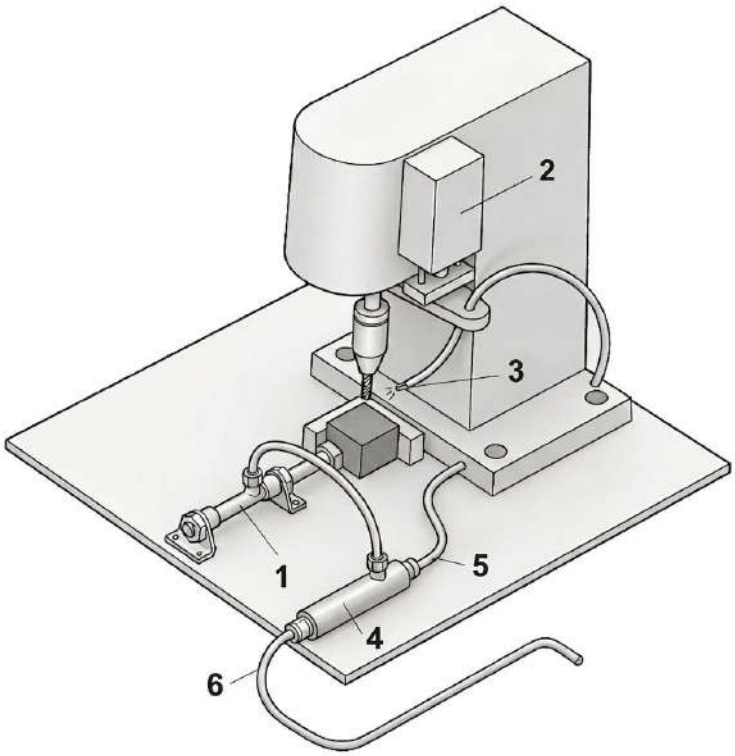



**Fig. 1. Schematic diagram of a drilling machine’s pneumatic drive with an integrated vortex tube for drill bit cooling: 1 – pneumatic cylinder; 2 – control box; 3 – hose with cooled air; 4 – vortex tube; 5 – “cold” outlet of the tube; 6 – “hot” outlet**

The efficiency of the energy separation of the flow into hot and cold components depends significantly on the pipe’s geometric parameters. The ratio of length to inner diameter $L/D_1$, according to data from various sources, is optimal in the range of 20-55 [17–19], although the flow separation process occurs primarily near the pipe inlet [17]. The ratio of the cold orifice diameter to the pipe diameter $d_c/D_1 = 0,5$ is recognized as optimal in a number of independent experimental studies [20–22], while some studies recommend a slightly higher value – up to 0.7 [23]. The number and shape of the tangential nozzles (typically, $N = 4\text{K}\,6$) [24, 25] and the opening angle of the conical valve at the hot outlet, whose optimum varies within the range of $45\text{K}\,80°$ depending on the total pressure ratio [26–28], also have a significant influence on the characteristics.

Despite nearly ninety years of research into this effect, there is still a lack of high-precision experimental data with a quantitative assessment of measurement uncertainty. One of the most comprehensive modern studies of this kind [29] presents the characteristics of a counter-flow vortex tube ($L/D_1 = 20$, $d_c/D_1 = 0,5$, $N = 6$, $\varphi = 80°$) for a feed pressure of 3.0–7.0 atm, demonstrating maximum separation efficiency under these conditions.

At the same time, the vast majority of existing studies focus on supplying the vortex tube from a continuous source of compressed air at mainline pressure. The issue of its application under conditions of cyclic, pulsating supply directly from the exhaust line of a pneumatic cylinder (performing a technological operation), without additional supply from the main line and at a high cycle frequency (approximately 20 cycles/min), remains virtually unexplored. At the same time, this particular configuration offers significant energy-saving potential: it

allows for the recovery of exergy from a flow that would otherwise be irretrievably dissipated into the atmosphere, without requiring additional consumption of compressed air or electricity.

The practical significance of the proposed approach lies in the fact that the cold flow obtained at the outlet of the vortex tube can be used for heat dissipation from the electronic components of a hybrid pneumatic actuator. For technological systems, the ability to obtain "free" coolant from the exhaust flow without using additional energy is of practical value and serves as the motivation for the chosen research direction.

## Research Methodology.

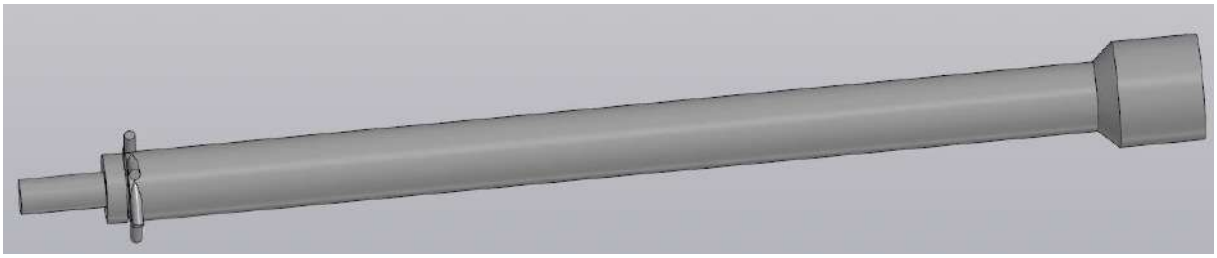
The objective of this work is to assess the fundamental feasibility of using a Rank-Gilsh vortex tube to recover energy from the exhaust air of pneumatic systems through a numerical study of the energy separation process under steady-state boundary conditions characteristic of the operating parameters of pneumatic actuator exhaust air.

To achieve this objective, an analysis of literature data on the geometric parameters of vortex tubes was conducted. Based on the recommendations obtained, a three-dimensional CAD model of a counter-flow vortex tube was constructed. Numerical simulation of the flow was performed in ANSYS CFX using the SST $k$-$\omega$ turbulence model. Based on the calculation results, the temperature, entropy, and turbulent kinetic energy fields were analyzed to assess the nature of the flow's energy separation.

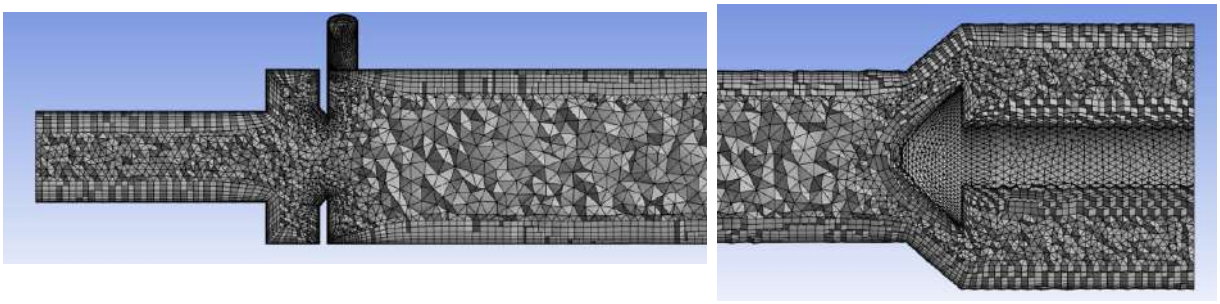
Since the objective of this work is to assess the fundamental feasibility of using a vortex tube, a design was adopted whose characteristics have been thoroughly investigated and experimentally verified in [29]. Using a geometry close to the optimal one according to the criteria of flow energy separation allows minimizing the influence of design factors on the simulation results and focusing on investigating the possibility of obtaining a cold flow under



*a*



*b*



*c*

**Fig. 2. Three-dimensional model of the internal geometry of the flow section of the vortex tube: a – longitudinal cross-section; b – external view; c – mesh partition**

supply parameters characteristic of pneumatic systems. Pipe geometric parameters: inner pipe ?diameter $D_1$ = 23 *mm*; length-to-diameter ratio $L/D_1$ = 20; ratio of the "cold" orifice diameter to the pipe diameter $d_c/D_1$ = 0.5; number of tangential nozzles N = 6 with the ratio of the total throat area of the nozzle ring to the cross-sectional area of the pipe $A_1/A$ = 0.22; the opening angle of the conical valve at the "hot" outlet $\varphi$ = 80°; the ratio of the valve's outer diameter to the pipe diameter $d_c/D_1$ = 1.51. Based on these parameters, a three-dimensional geometric model of the flow section of the vortex tube was constructed (Fig. 2).

The computational domain was meshed in ANSYS Meshing using an unstructured tetrahedral mesh with local refinement in the nozzle rim region, the axial region, and near the walls. To verify the correctness of the numerical solution, a mesh independence check was performed; based on its results, subsequent calculations were carried out on a mesh for which changes in the governing flow parameters were negligible.

The model was simulated using the ANSYS CFX software package under steady-state conditions for a compressible turbulent air flow. The Reynolds equations were closed using the SST $k$-$\omega$ turbulence model, which is traditionally used to simulate swirling high-velocity flows in vortex tubes due to its ability to accurately reproduce turbulence anisotropy in the near-axis region. The energy equation was solved jointly with the equations of motion to accurately reproduce the effect of energy separation in the flow [11].

At the inlet to the nozzle ring, parameters corresponding to the actual cylinder exhaust conditions were specified: total pressure $p_1$, temperature $T_{01}$ = 293 *K*. At the hot and cold outlets, the static pressure was set equal to atmospheric pressure $p_c = p_h$ = 1 *atm*, and the fraction of the cold flow $\varepsilon$ was controlled by the cross-sectional area of the nominal throttling element at the hot outlet. The process is assumed to be adiabatic; heat transfer through the cylinder walls is neglected, and there is no sliding.

The solution was performed using second-order discretization schemes; convergence was verified by the level of inconsistency (no worse than $10^{-5}$) and the stabilization of the integral temperature values at the outlets. The calculation results yielded fields of static (Figs. 3, 4) and total (Fig. 5) temperature, static entropy (Fig. 6), and turbulent kinetic energy along the pipe's longitudinal cross-section (Fig. 7), which were used to analyze the mechanism of energy separation in the flow and to assess the degree of irreversibility of the processes in the considered geometry.

## Results.

The calculations yielded the spatial distribution of key flow parameters along the longitudinal cross-section of the vortex tube (Figs. 3–7).

Fig. 3 shows the pattern of energy separation characteristic of the Rank–Hilsch effect: in the nozzle inlet region, the flow has a relatively low temperature (about 260 *K*). However, immediately after passing the nozzle rim, a pronounced field inhomogeneity forms: the axial region at a short distance from the inlet remains relatively cold (green zone on the contour), while the peripheral region heats up rapidly.

Further along the length of the pipe, the field evens out toward a high-temperature state (approximately 330 *K*), which corresponds to the conversion of the kinetic energy of the swirling flow into thermal energy due to viscous shear; this mechanism is described in [15, 16, 29]. Compared to Fig. 4, which shows a smoother, nearly monotonic heating along the length of the pipe from the inlet to the hot outlet, the total temperature field emphasizes the localized, rather than distributed, nature of the initial separation, where the main "jump" occurs within the first few pipe diameters from the nozzle rim, which is consistent with the conclusion in [17] regarding the concentration of the energy separation process near the inlet ($3 < L/D_1 < 5$).

The temperature contours in Fig. 4 and Fig. 5 reveal a characteristic periodic, "nested" structure of isolines in the form of elongated ovals that alternate sequentially along the pipe axis. This reflects not merely a monotonous decay of vorticity, but a wave-like, quasi-periodic

nature of temperature redistribution, which is a typical feature of the interaction between the vortex core and the wall-adjacent shear flow in counter-flow vortex tubes.

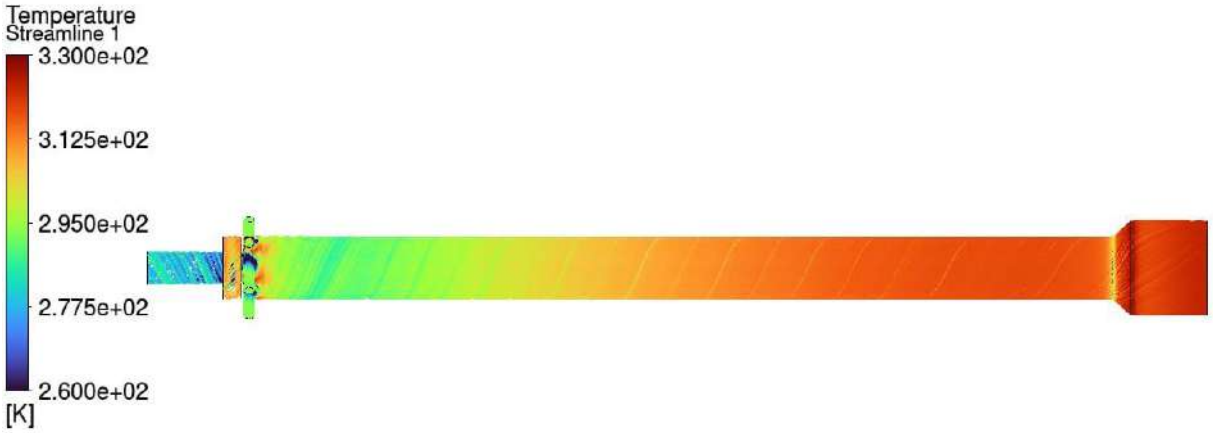



**Fig. 3. Distribution of static temperature along the flow line in the longitudinal cross-section of a vortex tube**

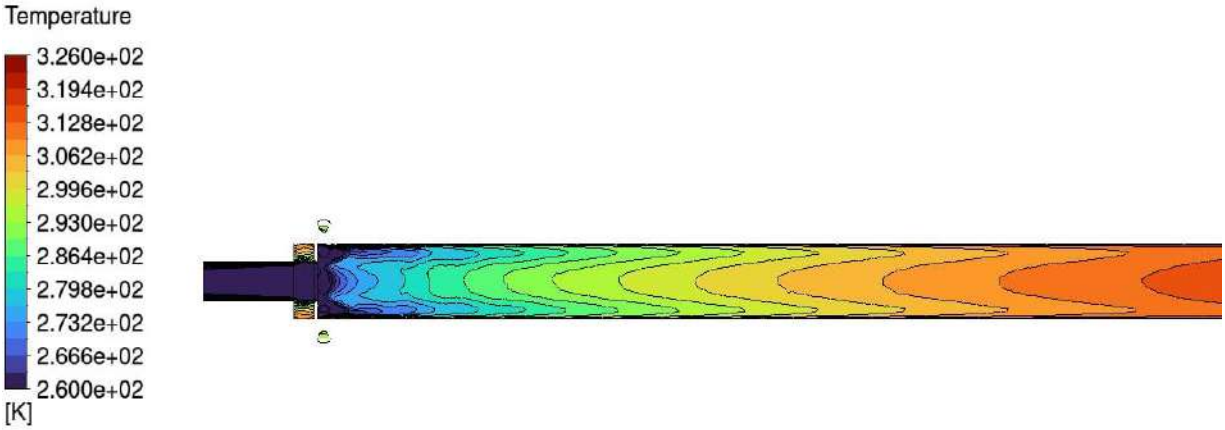



**Fig. 4. Static temperature field in the longitudinal cross-section of a vortex tube**

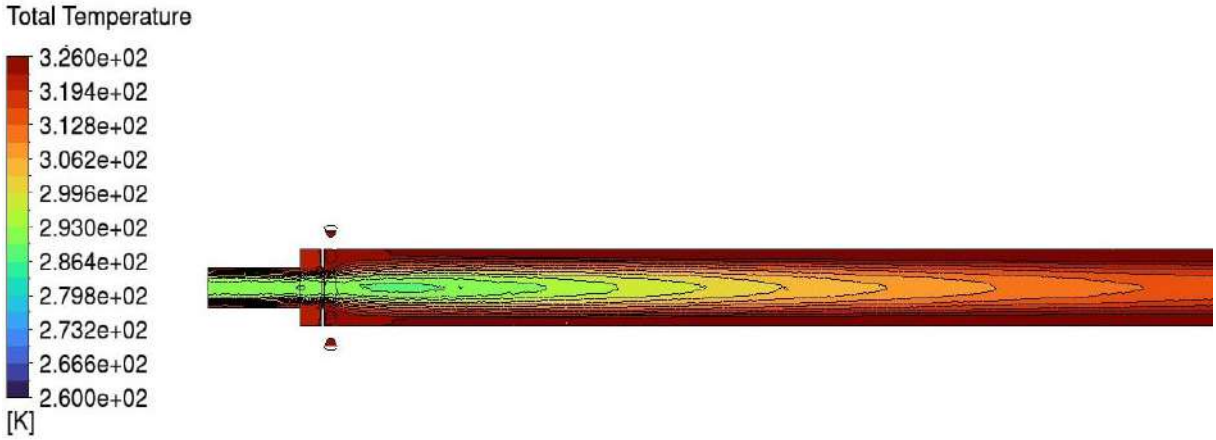



**Fig. 5. Total temperature field in the longitudinal cross-section of the vortex tube**

The number and scale of these structures gradually decrease along the length, indicating a gradual dissipation of flow vorticity and a transition from intense vortex motion immediately downstream of the nozzles to a practically axisymmetric, weakly vortical flow closer to the "hot" outlet.

The static entropy field (Fig. 6) clearly delineates the zone of maximum irreversibility of the process: peak values (up to 120.8 $J/(kg \cdot K)$ relative to the adopted reference) are observed

directly in the nozzle inlet zone and immediately beyond it, where a sharp acceleration of the flow occurs through the tangential nozzles and a vortex core forms. Further downstream, the entropy drops rapidly and stabilizes at a relatively uniform level (approximately 350…450 *J*/(*kg*·*K*) over most of the pipe's length, indicating a transition from intense generation of irreversibilities in the inlet zone to a quasi-equilibrium, low-dissipative flow regime further along the length. This result demonstrates a pronounced spatial localization of the source of irreversibility along the pipe coordinate.

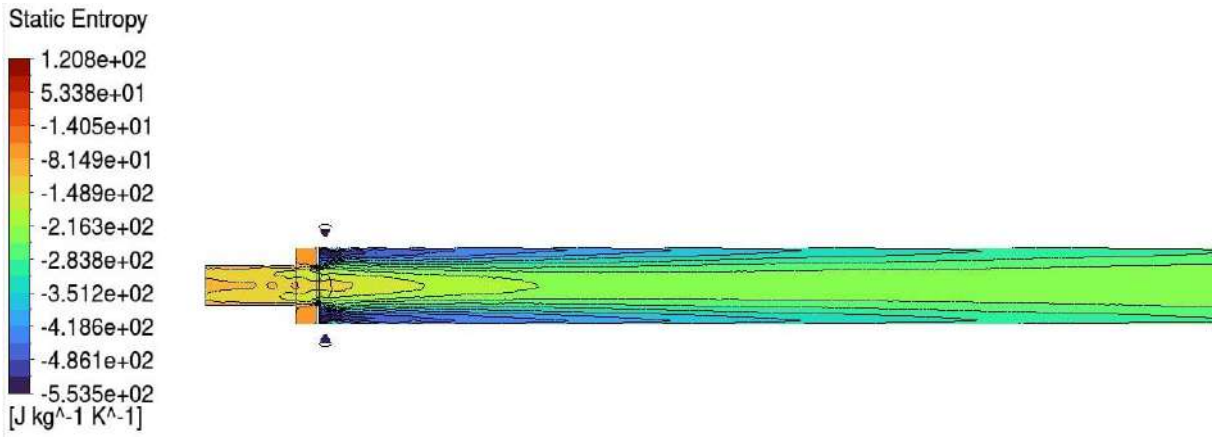



**Fig. 6. Static entropy field in the longitudinal cross-section of a vortex tube**

Fig. 7 confirms the conclusions made above: the maximum turbulent kinetic energy (up to 1,890 $m^2/s^2$) is concentrated in a narrow zone immediately behind the nozzle rim, where an intense shear layer forms between the high-velocity peripheral flow and the slower axial core. Further along the length of the tube, the level of turbulent kinetic energy decreases in a wave-like manner, with a gradual attenuation of the oscillation amplitude, which correlates with the structure of the temperature contours in Figs. 4-5 and confirms the "top-down" energy transfer mechanism through a cascade of turbulent vortices, which gradually decays with increasing distance from the vortex generation zone.

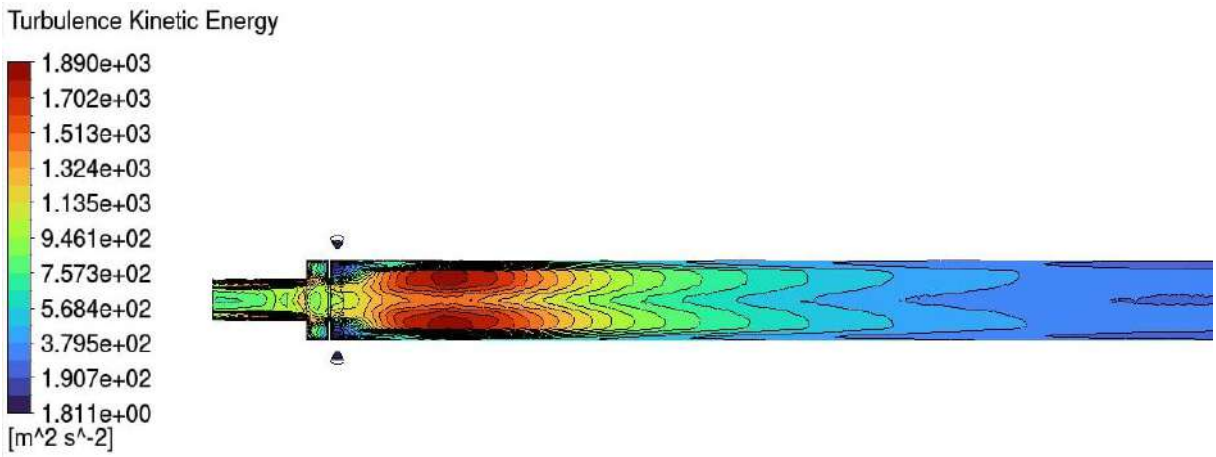



**Fig. 7. Turbulent kinetic energy field in the longitudinal cross-section of a vortex tube**

The results of the numerical simulations confirm that a stable zone of reduced temperature forms in the pipe in the near-axis region of the flow (the minimum values in the calculated fields correspond to a range of approximately 260–270 *K*, Figs. 3–5). This result opens up the practical possibility of using a cold flow, drawn from the corresponding outlet of the vortex tube, for heat removal from the electronic components of a hybrid pneumatic actuator located directly adjacent to the actuator mechanism. Unlike traditional cooling systems (fans, Peltier elements, liquid circuits), which require an additional power source, the

proposed approach utilizes a pneumatic flow, contains no electrical voltage, and is fire-safe, which is particularly relevant for electronics cabinets, mobile systems, and robotic systems.

## Conclusions.

Based on an analysis of existing approaches to improving the energy efficiency of pneumatic actuators, it has been established that a vortex tube based on the Rank–Hilsch effect is a promising but under-researched means of recovering energy from the exhaust flow of pneumatic cylinders, capable of providing effective cooling without the use of additional energy.

Based on a review of the literature, the choice of the vortex tube's basic geometry was justified, and this geometry was adapted for conditions of supply from the exhaust cavity of a pneumatic cylinder. Numerical flow simulation confirmed the qualitative correspondence of the obtained physical picture to the classical mechanism of energy separation in a swirled flow: the formation of a cold axial core and a hot peripheral zone, with maxima of static entropy (up to 120.8 $J/(kg \cdot K)$ and turbulent kinetic energy (up to 1890 $m^2/s^2$) localized in a narrow zone immediately behind the nozzle rim.

The spatial coincidence of the zones of maximum entropy and turbulent kinetic energy generation immediately behind the nozzle rim indicates that the majority of the irreversible losses of the flow's mechanical energy are concentrated in the initial section of the pipe (within a few diameters from the inlet), while the remainder of the length primarily serves a transport function, followed by a significantly slower decay of the residual vortex.

The obtained results are based on constant (in magnitude) boundary conditions at the inlet, corresponding to a single characteristic operating mode, without pulsating pressure and flow rate values throughout the entire operating cycle. Therefore, they should be regarded as confirmation of the fundamental applicability of the chosen geometry and the qualitative correctness of the physical picture of the energy separation process. Investigating this issue in a transient setting with time-dependent boundary conditions that reproduce the actual exhaust profile is a direction for future work.

The results obtained confirm the fundamental feasibility of using a cold flow from a vortex tube, powered by the exhaust energy of a pneumatic cylinder, to cool the electronic components of a hybrid drive, which determines the practical focus of future research.

## References

1. Radgen, P., Blaustein, E. Compressed Air Systems in the European Union: Energy, Emissions, Savings Potential, and Policy Actions. Stuttgart: Fraunhofer Institute for Systems Technology and Innovation, 2001. Available at: https://publica.fraunhofer.de/entities/publication/60fbadfb-caf9-4e21-bd6e-5095fbff1964 (accessed July 18, 2026).

2. Beater, P. Pneumatic Drives: System Design, Modeling, and Control. Berlin: Springer-Verlag, 2007, 330 p. Available at: https://link.springer.com/book/10.1007/978-3-540-69471-7 (accessed July 18, 2026).

3. Saidur, R., Rahim, N. A., Hasanuzzaman M. A review on compressed-air energy use and energy savings. *Renewable and Sustainable Energy Reviews*, 2010. 14(4). 1135–1153. https://doi.org/10.1016/j.rser.2009.11.013

4. Rogovyi, A., Strizhak, M., Korohodskyi, V., et al. Optimization of pneumatic actuator processes by means of computational fluid dynamics. *AIP Conference Proceedings*, 2026. 3496(1). 060001. https://doi.org/10.1063/12.0044441

5. Cai, M., Kawashima, K., Kagawa, T. Power assessment of flowing compressed air. IEEE/ASME *Journal of Fluids Engineering*, 2005, 128(2), 402–405. https://doi.org/10.1115/1.2170129

6. Gryboś, D., Leszczyński, J. S. Exergy analysis of pressure reduction, back pressure and intermittent air supply configuration of utilization/expansion stage in compressed air systems. *Energy*, 2023. 285. 129419. https://doi.org/10.1016/j.energy.2023.129419

7. Rogovyi, A., Strizhak, M. Exergy-Based Energy Efficiency Analysis of the Pneumatic Drive with Controlled Braking and Compressed Air Recuperation. *Problemele Energeticii Regionale*, 2026. 70(2). 65–77. https://doi.org/10.52254/1857-0070.2026.2-70.06

8. Dindorf, R. Estimating Potential Energy Savings in Compressed Air Systems. *Procedia Engineering*, 2012. 39. 204–211. https://doi.org/10.1016/j.proeng.2012.07.026

9. Gryboś, D., Leszczyński, J. S. A Review of Energy Overconsumption Reduction Methods in the Utilization Stage in Compressed Air Systems. *Energies*, 2024. 17(6). 1495. https://doi.org/10.3390/en17061495

10. Harris, P., Nolan, S., O'Donnell, G. E. Energy optimisation of pneumatic actuator systems in manufacturing. *Journal of Cleaner Production*, 2014. 72. 35–45. https://doi.org/10.1016/j.jclepro.2014.03.011

11. Rogovyi A., Romasevych Y., Stryzhak M. et al. Transient Energy Conversion and Compressed Air Recovery in Pneumatic Systems: Optimization and CFD-Based Analysis. *Actuators*, 2026. 15(3). 135. https://doi.org/10.3390/act15030135

12. Hepke, J., Weber J. Energy saving measures on pneumatic drive systems. SICFP2013, 2013, 475–483. https://doi.org/10.3384/ecp1392a47

13. Yang, A., Pu, J., Wong, C.B., Moore, P. By-pass valve control to improve energy efficiency of pneumatic drive system. Control Engineering Practice, 2009. 17(6). 623–628. https://doi.org/10.1016/j.conengprac.2008.10.013

14. Rihong, Z., Qungui, D. Dynamic Simulation and Optimization of Cushioning Performance in High Speed Pneumatic Cylinders. International Journal of Simulation: Systems, *Science & Technology*, 2016, 17(17). 17.1–17.6. https://doi.org/10.5013/IJSSST.a.17.17.17

15. Ranque, G. Experiments on expansion in a vortex with simultaneous exhaust of hot air and cold air. Le Journal de Physique et le Radium, 1933, 4, 112–114. Available at: https://www.scirp.org/reference/referencespapers?referenceid=624309 (accessed July 18, 2026).

16. Hilsch, R. The Use of the Expansion of Gases in a Centrifugal Field as Cooling Process. *Review of Scientific Instruments*, 1947. 18. 108–113. https://doi.org/10.1063/1.1740893

17. Raiskii, Yu. D., Tunkel, L. E. Influence of vortex-tube configuration and length on the process of energetic gas separation. *Journal of Engineering Physics*, 1974. 27. 1578–1581. https://doi.org/10.1007/BF00863014

18. Martynovskii, V. S., Alekseev, V. P. Investigation of the vortex thermal separation effect for gases and vapors. Soviet Physics. *Technical Physics*, 1956. 1(10). 2233–2243.

19. Gao, C. M., Bosschaart, K. J., Zeegers, J.C.H., de Waele, A.T.A.M. Experimental study on a simple Ranque-Hilsch vortex tube. *Cryogenics*, 2005. 45(3). 173–183. https://doi.org/10.1016/j.cryogenics.2004.09.004

20. Saidi, M. H., Valipour, M. S. Experimental modeling of a vortex tube refrigerator. *Applied Thermal Engineering*, 2003. 23(15). 1971–1980. https://doi.org/10.1016/S1359-4311(03)00146-7

21. Nouri-Borujerdi, A., Bovand, M., Rashidi, S., et al. Geometric parameters and response surface methodology on cooling performance of vortex tubes. *International Journal of Sustainable Energy*, 2016. 36(9). 872–886. https://doi.org/10.1080/14786451.2015.1127233

22. Promvonge, P., Eiamsa-ard S. Investigation of vortex thermal separation in a vortex tube refrigerator. *Science Asia*, 2005. 31. 215–223. https://doi.org/10.2306/scienceasia1513-1874.2005.31.215

23. Liu, X., Liu, Z. Investigation of the energy separation effect and flow mechanism inside a vortex tube. *Applied Thermal Engineering*, 2014. 67(1-2). 494–506. https://doi.org/10.1016/j.applthermaleng.2014.03.071

24. Behera, U., Paul, P. J., Kasthurirengan, S., et al. CFD analysis and experimental investigations toward optimizing the parameters of the Ranque-Hilsch vortex tube. *International Journal of Heat and Mass Transfer*, 2005. 48(10). 1961–1973. https://doi.org/10.1016/j.ijheatmasstransfer.2004.12.046

25. Eiamsa-ard, S., Promvonge, P. Review of Ranque–Hilsch effects in vortex tubes. *Renewable and Sustainable Energy Reviews*, 2008. 12(7). 1822–1842. https://doi.org/10.1016/j.rser.2007.03.006

26. Pise, A. T., Devade, K. D. Investigation of the refrigeration effect using a short divergent vortex tube. *International Journal of Earth Sciences and Engineering*, 2012. 5(1). 378–384.

27. Aydin, O., Baki, M. An experimental study on the design parameters of a counterflow vortex tube. *Energy*, 2006. 31(14). 2763–2772. https://doi.org/10.1016/j.energy.2005.11.017

28. Markal, B., Aydin, O., Avci, M. An experimental study on the effect of the valve angle of counter-flow Ranque-Hilsch vortex tubes on thermal energy separation. *Experimental Thermal and Fluid Science*, 2010. 34(7). 966–971. https://doi.org/10.1016/j.expthermflusci.2010.02.013

29. Chowdhury, N. H. K., Povey, T. High-accuracy experimental study of the performance characteristics of an optimized Ranque-Hilsch vortex tube. *Applied Thermal Engineering*, 2024. 251. 123385. https://doi.org/10.1016/j.applthermaleng.2024.123385

*Дата першого надходження статті до видання 25.08.2026*
*Дата прийняття статті до друку після рецензування 23.09.2026*
*Дата публікації (оприлюднення) статті 04.11.2026*
*Стаття поширюється на умовах ліцензії відкритого доступу(CC BY 4.0)*

# ОБҐРУНТУВАННЯ МОЖЛИВОСТІ ЗАСТОСУВАННЯ ВИХОРОВОЇ ТРУБИ ДЛЯ РЕКУПЕРАЦІЇ ЕНЕРГІЇ ВІДПРАЦЬОВАНОГО ПОВІТРЯ ПНЕВМОЦИЛІНДРА

**А.С. Роговий[1], М.Г. Стрижак[1], Д.А. Савенков[1], Д.Р. Дьомін[1], Р.С. Гасанов[1]**
[1] *Національний технічний університет "Харківський політехнічний інститут"*

***Анотація***

У статті розглянуто проблему підвищення енергоефективності пневматичних приводів шляхом рекуперації енергії відпрацьованого повітря за допомогою вихорової труби Ранка-Хілша. Пневматичні виконавчі механізми залишаються широко затребуваними в промислових системах автоматизації завдяки високій питомій потужності, швидкодії та пожежобезпечності; проте їхній загальний ККД рідко перевищує 15 %, переважно через те, що стиснене повітря, яке залишається в камері циліндра в момент вихлопу, стравлюється в атмосферу. Хоча кілька стратегій рекуперації енергії, зокрема накопичення в ресивері, відсікання подачі та перепускання між камерами циліндра, продемонстрували економію енергії до 87 %, потенціал термічної рекуперації самого вихлопного потоку досі залишається відносно малодослідженим. Вихорова труба є пасивним засобом реалізації цього потенціалу, розділяючи вихлопний потік на холодну та гарячу складові без додаткових витрат енергії; практичну схему інтеграції проілюстровано на прикладі пневмоприводу свердлильного верстата, де холодний потік спрямовується в зону різання для локального охолодження свердла.

Як зразок було прийнято базову геометрію вихорової труби, раніше експериментально валідовану в літературі, щоб відокремити вплив параметрів живлення від впливу геометричної оптимізації. Тривимірну CAD-модель розрахункової області було побудовано та дискретизовано в ANSYS Meshing із локальним згущенням сітки біля соплового кільця, в пристінній області та в осьовому ядрі. Стисливу турбулентну течію моделювали в ANSYS CFX у стаціонарній постановці з використанням моделі турбулентності SST $k$-$\omega$; на вході задавали повний тиск і температуру, репрезентативні для вихлопу циліндра, а на обох виходах – статичний атмосферний тиск.

Розраховані поля підтверджують класичний механізм енергетичного розділення на основі ефекту Ранка-Хілша: формується холодне осьове ядро та гаряча периферійна зона, при цьому пікові значення статичної ентропії (до 120,8 Дж/(кг·К)) і кінетичної енергії турбулентності (до 1890 м²/с²) зосереджені у вузькій області одразу за сопловим кільцем, після чого спостерігається поступове хвилеподібне згасання закрутки вздовж труби. Цей просторовий збіг свідчить, що основна частина незворотних втрат припадає на перші кілька діаметрів труби від входу, тоді як решта її довжини виконує переважно транспортну функцію.

Результати, отримані за стаціонарних репрезентативних граничних умов, слід розглядати як підтвердження якісної можливості реалізації запропонованого підходу. На практиці продемонстроване зниження температури холодного потоку (приблизно до 260-270 К) підтверджує доцільність використання вихорової труби як пасивного джерела охолодження без витрат енергії, що особливо актуально для компактних і мобільних робототехнічних систем.

***Keywords:*** пневмопривод, вихорова труба, рекуперація енергії, енергоефективність.

**DOI https://doi.org/10.32782/1994-4691-2026-1-77-5**
UDK 621.22

# QUANTITATIVE AND QUALITATIVE ANALYSIS OF THE GLOBAL HYDRAULIC MARKET DEVELOPMENT

# КІЛЬКІСНИЙ ТА ЯКІСНИЙ АНАЛІЗ РОЗВИТКУ ГЛОБАЛЬНОГО РИНКУ ГІДРАВЛІЧНОГО ОБЛАДНАННЯ

A. Skvorchevsky, Cand. Sc., Professor ORCID: 0000-0002-4572-7305

*Research Centre of Robotics, Mechatronics and Production Informatization, Kharkiv, Ukraine*
e-mail: skvorchevsky.alexander@gmail.com

**Abstract**. The article provides an integrative quantitative and qualitative assessment of the global hydraulic equipment market, combining data from recent commercial reports, consulting studies and scientific publications. The analysis confirms that, despite methodological differences, all major sources predict sustained market expansion with an average compound annual growth rate of about 4% over the next decade, indicating favourable conditions for entering industrial and mobile hydraulics. Particular attention is paid to regional distribution, sectoral structure and component-level dynamics, showing the leading roles of Asia-Pacific, construction and mobile hydraulics, as well as the rising importance of energy-efficient pumps, smart systems and advanced actuators. The study identifies three key transformation drivers: electrification, digitalisation and smart hydraulics, and the green transition, which jointly shape future R&D priorities.

**Keywords**: global hydraulics market; SMART hydraulics; electro-hydraulic systems; energy efficiency.

## Introduction.

The global hydraulic equipment market is undergoing simultaneous quantitative growth and qualitative transformation under the influence of electrification, digitalisation and the green transition in industry. Multiple analytical reports and scientific publications describe individual technological directions or forecast figures, but they usually focus on specific segments, regions or applications and therefore do not provide an integrated picture of how these trends interact at the system level. This fragmentation makes it difficult for researchers, OEMs and component suppliers to assess the real prospects of industrial, mobile and power hydraulics, to prioritise R&D, and to choose between electro-hydraulic and electromechanical solutions when planning future product portfolios. There is a lack of consolidated analysis that combines numerical market indicators with a structured overview of key technological shifts and sectoral demand changes. Consequently, a generalised quantitative and qualitative assessment of the global hydraulic market, based on an integrative review of the most authoritative market studies and technological reports, is required to support evidence-based decisions on launching new projects in the fluid power domain.

## Literature Review.

Numerous industry reports and scientific publications analyse different dimensions of the current hydraulic market and its prospective development trends. The report [1] explains how vehicle electrification is driving a renaissance in mobile hydraulics by forcing OEMs to radically improve hydraulic energy efficiency to protect battery life in off-highway machines. Traditional hydraulic systems remain attractive for their low cost and high-power density, but their poor efficiency makes them problematic in battery-electric architectures, so OEMs are

experimenting with multiple technical pathways rather than a single universal solution. Electric mini excavators are highlighted as an early testbed, representing a multibillion-dollar hydraulics market segment where new architectures can be trialled at a manageable scale. Three main technology directions are discussed: electromechanical actuators, which trade power density for precision, low noise and lower total cost of ownership in low-power applications; digital hydraulics, including digital displacement pumps that can raise fuel efficiency by around 30% while preserving familiar architectures; and electro-hydraulic actuation, where each actuator has its own pump and motor, enabling energy recuperation back to the battery but at significantly higher upfront cost. Overall, electrification is fragmenting the mobile hydraulics landscape, creating challenges but also strong innovation opportunities as suppliers and OEMs balance efficiency, cost, and application-specific requirements.

The report [2] argues that smart hydraulics are set to trigger a major transformation in the fluid power systems by combining significant energy savings with higher uptime and productivity. Industrial pumps already represent a huge market of about 70 billion dollars and are projected to reach 85–90 billion dollars in 2025, while accounting for nearly 15 % of total EU electricity consumption, making them an important target for efficiency gains. Smart pumps support three main value-creation cases: energy-efficiency optimization, predictive maintenance, and system-level optimization of entire fluid circuits, with particularly strong potential in energy-intensive process industries such as steel, oil and gas, and pulp and paper, where $CO_2$ reduction and lifecycle costs are critical. The study highlights that OEMs, component suppliers, and automation companies must shift from single-component offerings to integrated system solutions, expand digital capabilities, and build new business models around data and services, while end users should prioritize Return on Investment (ROI), total cost of ownership, and regulatory compliance in their investment strategies. Overall, the report positions smart fluid hydraulics as both a competitive necessity and a major growth opportunity, driven by rising energy prices, tightening environmental regulations, and the maturation of digital technologies and cloud-based analytics across pump applications.

The report [3] forecasts that the global hydraulics market will grow from 44.51 billion dollars in 2023 to 64.71 billion dollars by 2034, at a CAGR of 3.5 percent, driven by the rising use of hydraulic systems across construction, agriculture, manufacturing, mining, and other industrial sectors. Asia Pacific currently leads with 39 percent of global revenue and is expected to retain dominance due to strong manufacturing bases, rapid industrialisation, and cost-effective production, while North America is projected to post the fastest growth on the back of infrastructure investment and expanding industrial activity. Cylinders form the largest component segment today, reflecting their central role as the “heart” of hydraulic systems, whereas hydraulic pumps are set for notable growth as energy-efficient designs enable lower consumption and emissions. By application, mobile hydraulics dominate owing to their durability and suitability for harsh environments, but industrial hydraulics are also expected to expand steadily. Construction remains the leading end-use segment, with agriculture emerging as a key growth area as hydraulics support precision, productivity, and safety in modern farm machinery.

The report [4] projects the global hydraulic equipment market to grow from about 42.1 billion dollars in 2025 to 54.3 billion dollars by 2030, reflecting a CAGR of roughly 5.2 percent, driven mainly by infrastructure megaprojects, warehouse automation, and the electrification of off-highway machinery. Pumps remain the largest equipment segment with over 28 percent revenue share, while filters and accumulators post the fastest growth as stricter cleanliness and energy-recovery requirements raise demand for high-performance contamination control and storage components. Construction is the leading end-user industry with more than 30 percent of revenues, but aerospace and defence show the sharpest growth on the back of rising aircraft production and modernization programs. Mobile hydraulics account for nearly 59 percent of market revenue and are expected to see the highest growth as

electro-hydraulic hybrids and high-pressure systems gain adoption in compact, energy-efficient equipment. Geographically, North America currently contributes the largest share, supported by major water and infrastructure funding, while Asia-Pacific offers the strongest growth outlook, with an expected CAGR above 8 percent due to large-scale infrastructure and urbanization programs in China and India.

The article [5] shows that the main ways to save energy in hydraulic drives are to eliminate throttling losses in control valves and to provide energy recovery in hybrid mobile equipment. The focus on hydraulic excavators and wheel loaders has the greatest impact due to their dominant share in the off-road equipment fleet. Accordingly, a structured overview and critical analysis of their energy-efficient system architectures, including the internal combustion engine, is provided. The discussion [5] covers concepts about proportional valves for energy recovery, digital valve technology, motion control systems, electro-hydraulic control, and electro-hydraulic converters. This provides readers with a current synthesis of available solutions and their impact on performance, while indicating that future developments will combine hybridization and closer integration of hydraulics with internal combustion engines to achieve higher efficiency and lower emissions.

The research aims to generalise the key qualitative and quantitative trends in the development of the global hydraulic market, considering both industrial and mobile applications as well as regional differences between major economies. It focuses on identifying dominant product groups, technological shifts such as electrification and digitalisation, and structural changes in demand across sectors, including construction, agriculture, mining, and manufacturing. To achieve this aim, an integrative review approach was applied, combining data from market reports, scientific publications, and industry analyses to synthesise a coherent picture of the current state and prospective evolution of the hydraulic market worldwide.

## Research Methodology.

The study applies an integrative review approach, which allows the combination of heterogeneous sources (market reports, scientific papers, industry analyses) into a single analytical framework to identify both numerical trends and structural technological shifts in the hydraulic market. This design was chosen because primary statistical data are dispersed across commercial and open analytical studies that differ in time horizon, regional focus, and segmentation logic, which makes meta-analysis in the strict statistical sense impractical. Partially, for the information sources' generalisation the methods of generative AI were used, particularly Perplexity.ai.

The empirical base includes specialised market research reports on hydraulic equipment, open analytical reviews by consulting companies, and peer-reviewed scientific publications on energy-efficient hydraulics, smart fluid systems and electromechanical alternatives. Sources were selected according to the following criteria: explicit quantitative estimates of market size and compound annual growth rate (CAGR), clear segmentation by region, application or component, and direct relevance to industrial, mobile or power hydraulics. Priority was given to the most recent publications (mainly 2022–2025).

For the quantitative part, the reported market sizes, forecast horizons and CAGR values were extracted from each selected study and tabulated to enable cross-comparison. Where necessary, data were brought to a unified form (billion USD, explicit final forecast year) to calculate the average CAGR and to visually compare the growth trajectories of the hydraulic market across different reports. Qualitative descriptors of regional structure, sectoral demand (construction, agriculture, mining, manufacturing, aerospace, etc.) and component composition (cylinders, pumps, valves, filters, accumulators) were coded and grouped to identify recurring patterns.

A narrative synthesis was then performed to generalise the main technological trends affecting the hydraulic market, with a focus on electrification, digitalisation (smart and

connected hydraulics) and the green transition. Descriptions of electro-hydraulic architectures, digital hydraulics, hybrid systems, and electromechanical actuators from scientific and technical publications were compared with the strategic theses of consulting reports to reveal convergences or contradictions in expert expectations. Special attention was paid to the role of Industry 4.0/IoT integration, energy-efficiency requirements, and $CO_2$ reduction targets as drivers of new product development in industrial and mobile hydraulics.

The methodology is subject to several limitations arising from the secondary nature of the data and the commercial orientation of many market reports. Differences in scenario assumptions, baselines and segmentation may introduce dispersion into numerical indicators; therefore, the calculated average CAGR and generalised structural conclusions should be interpreted as indicative rather than exact. Nonetheless, the applied integrative review provides a sufficiently robust basis for assessing the prospects of entering the global hydraulic market and for identifying promising R&D directions in fluid power technologies. r achieving the aim integrative review method was used.

## Results.

Several research studies on the global hydraulic equipment market are available on the Internet. Although the quantitative forecasts differ, they all agree that the hydraulic equipment market will grow in the next 10 years. Table 1 presents a generalization of the numerical characteristics of the world hydraulic equipment market, according to different research.

**Table 1. Generalization of the numerical characteristics of the world hydraulic equipment market**

| № | Research name | Website`s link | Market size 2024, USD Billion | Market size/Final year of forecast, USD Billion | CAGR, % |
|---|---|---|---|---|---|
| 1 | 2 | 3 | 4 | 5 | 6 |
| 1 | Hydraulics Market Size, Share, and Trends 2024 to 2034 | https://www.precedenceresearch.com/hydraulics-market#:~:text=The%20global%20hydraulics%20market%20size,3.5%25%20from%202024%20to%202034. [3] | 44.51 | 64.71/2034 | 3.4 |
| 2. | Hydraulics Market Global Forecast to 2028 | https://www.marketsandmarkets.com/Market-Reports/hydraulics-market-209607944.html [6] | 42.5 | 50.5/2028 | 3.5 |
| 3. | Global Hydraulic Equipment Market Overview | https://www.marketresearchfuture.com/reports/hydraulic-equipment-market-8066 [7] | 49 | 97.09/2032 | 9.11 |
| 4. | Hydraulic Equipment Market Size & Share Analysis - Growth Trends & Forecasts (2024 - 2029) | https://www.mordorintelligence.com/industry-reports/hydraulic-equipment-market [4] | 46.94 | 56.07/2029 | 3.62 |
| 5. | Hydraulics Market Size and Forecast | https://www.verifiedmarketresearch.com/product/hydraulics-market/ [8] | 36,67 | 40.98/2031 | 1.4 |
| 6. | Global Hydraulics Market Size, Share & Trends Analysis Report, 2023-2030 | https://www.kbvresearch.com/hydraulics-market/ [9] | 43 | 54.9/2030 | 3.7 |

| 1 | 2 | 3 | 4 | 5 | 6 |
|---|---|---|---|---|---|
| 7. | Hydraulic Equipment Market Size, Share & Trends Analysis Report 2024-2032 | https://straitsresearch.com/report/hydraulic-equipment-market [10] | 47.23 | 65.82/2032 | 4.23 |
| 8. | Hydraulics Market Size to Surpass USD 60.36 Billion in 2032 | https://finance.yahoo.com/news/hydraulics-market-size-surpass-usd-150000627.html?guccounter=1&guce_referrer=aHR0cHM6Ly93d3cuZ29vZ2xlLmNvbS8&guce_referrer_sig=AQAAAHLpU6iuULvwCa-x3ZXJ9SiFta8_cgR3QZAJeltlVkCHNA5CmJN82W_kVIoapTJnUZw6cz5CaRkFYjSrEpVDk_3zeSjTnQLMnS4L7v7juqyA8riex47XiTBFEwl48dhK9YUfonHgPLrB42dUzuD1J7XTo7KOeZgw1nx29EKOQT4p [11] | 45.26 | 60.36/2032 | 3.5 |

To assess whether it is worth entering the industrial, mobile and power hydraulics business in 2024/2025, the most important parameter is the compound annual growth rate (CAGR). CAGR represents the mean annualized growth rate for compounding values over a given time. CAGR smoothest the effect of the volatility of periodic values that can render arithmetic means less meaningful. For the eight studies listed in Table 1, the CAGR average value is 4.07 %. This shows the prospects of the hydraulic equipment market in the foreseeable future.

The growth trajectory of the hydraulic equipment market is illustrated in Fig. 1 [3].

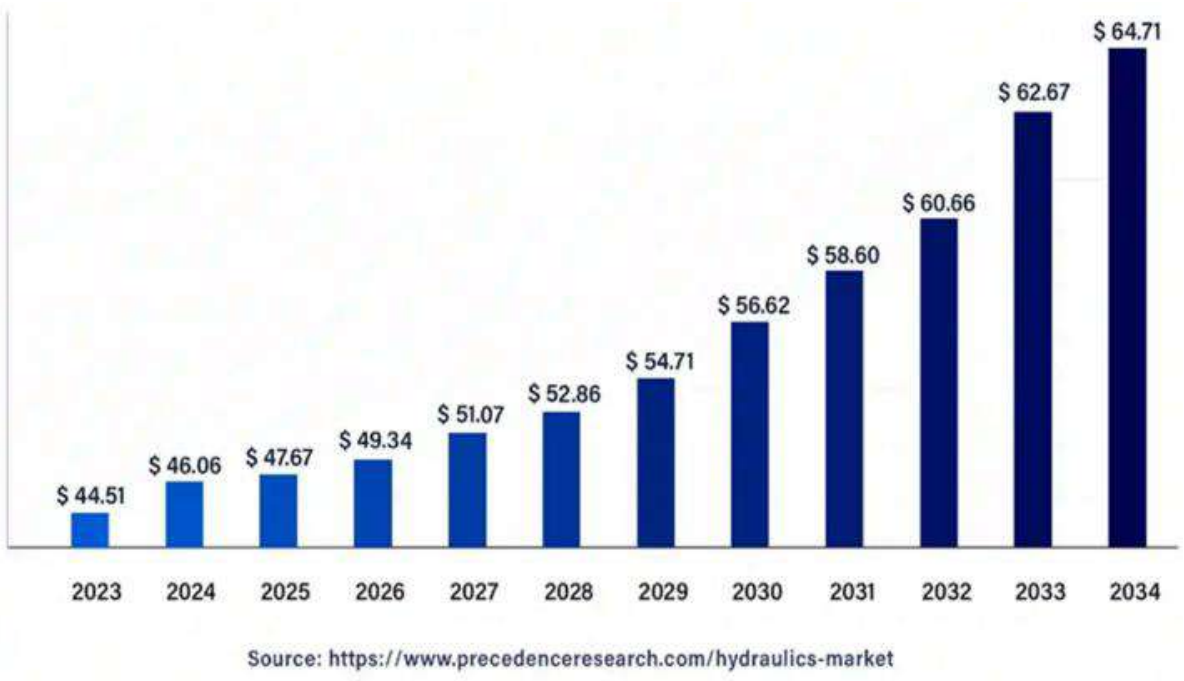



**Fig 1. Global Hydraulic Market Size 2023 to 2034 (USD Billion)** [3]

All the above analytical reports agree that Europe will occupy the middle position in hydraulic systems and their component consumption. Recent analytics [4] show that the Asia-

Pacific region is expected to remain the leading consumer of hydraulic equipment (Fig. 2) [4]. According to current fluid power market studies, the key driver of market transformation and expansion is the integration of heavy-duty industrial and mobile machinery with Industry 4.0 technologies, particularly the Internet of Things (IoT). This development underpins a second major trend: accelerating demand for smart, automated hydraulic equipment. In Fig. 3 [6], we see that the largest sector of consumption of hydraulic systems is construction. In my opinion, it would also be appropriate to separately add such sectors as agricultural equipment and the aerospace industry to the diagram in Fig. 3 [6].

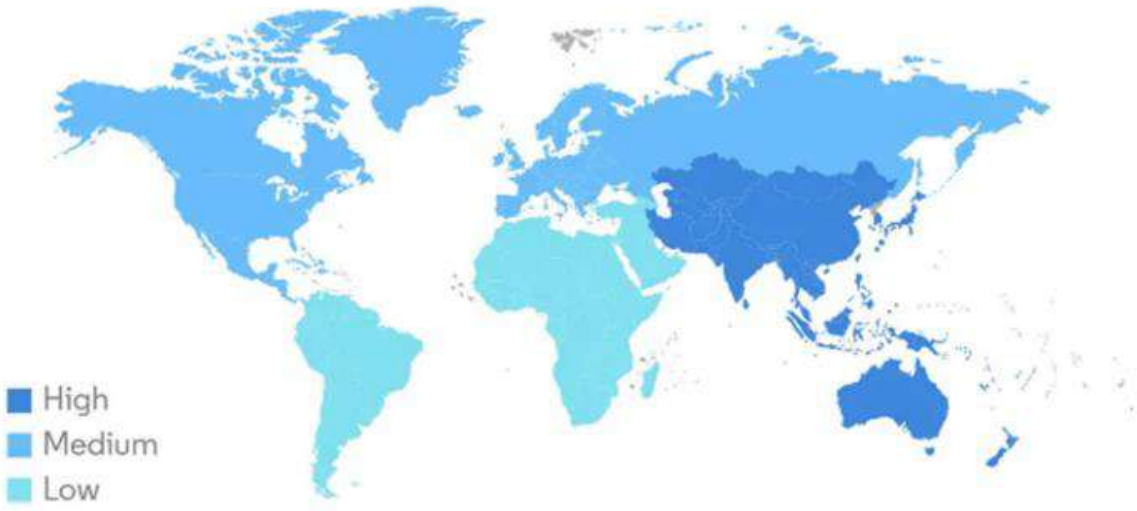



**Fig 2. Hydraulic Equipment Market CAGR (%), Growth Rate by Region, 2025-2030** [4]

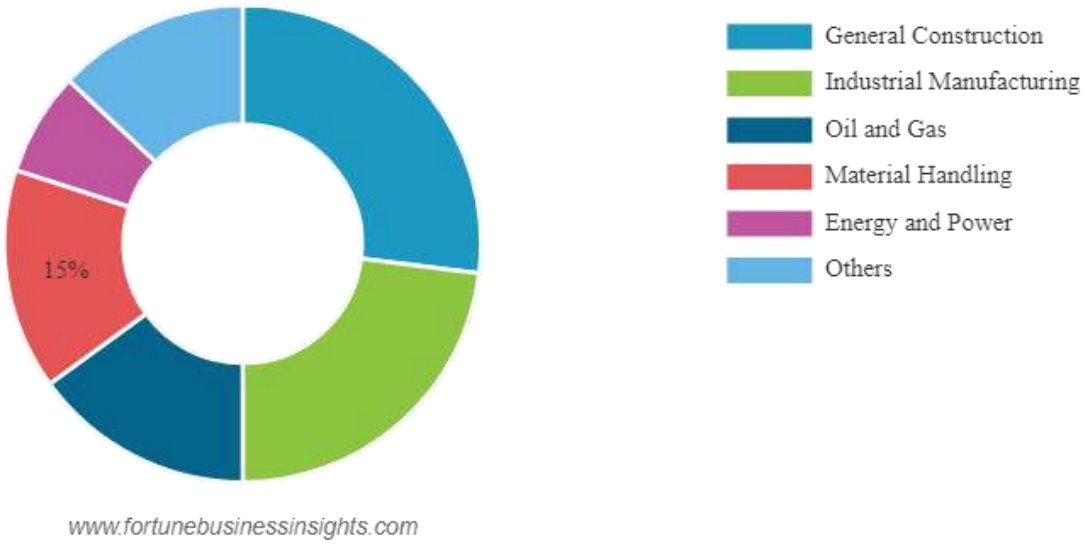



**Fig. 3. Global Industrial Hydraulic Equipment Market Share, By Application, 2022** [12]

In Fig. 3 [12] we see that the largest sector of consumption of hydraulic systems is construction. In my opinion, it would also be appropriate to separately add such sectors as agricultural equipment and the aerospace industry to the diagram in Fig. 3 [12]. List [13] of key players in the Hydraulic Equipment Market is the next: Daikin Industries Ltd, Danfoss. Eaton, Emerson Electric Co., Kawasaki Heavy Industries Ltd., Komatsu Ltd., Parker-Hannifin Corp.. Robert Bosch GmbH. Siemens AG. Wipro Limited.

According to [2, 5, 14, 15], companies can make progress in embracing the full potential of smart hydraulics if they quickly adopt these technologies [16].

The third trend involves the green transition of fluid power systems within the industrial equipment and machinery sectors. According to the data presented by the European academic Fluid Power Association, fluid power equipment produces 2.4 times more CO2 than global aviation, making energy-saving solutions for hydraulic systems an important contribution to climate change mitigation.

Some electromechanical technologies, e.g. planetary roller screws, linear actuators and ball screw linear actuators [17-20], can become a serious competitor to electrohydraulic drives in the process of ongoing industrial and mobile equipment electrification.

## Conclusions.

The conducted integrative review confirms that the global hydraulic equipment market is set to grow steadily over the next decade, with an average compound annual growth rate of about 4%, which indicates favourable conditions for launching new projects in this field. At the same time, the structure of demand is changing: Asia-Pacific and the construction sector retain leadership, while agriculture, mining, manufacturing and aerospace increase their contribution, and component priorities gradually shift towards energy-efficient pumps, smart systems and advanced actuators. Three interrelated transformation drivers have been identified: electrification of mobile and industrial machinery, digitalisation and emergence of smart hydraulics, and the green transition with strict $CO_2$ reduction and energy-efficiency requirements, which jointly shape the agenda for further R&D, standardisation and product portfolio renewal in industrial, mobile and power hydraulics.

## References

1. Electrification sparks mobile hydraulics growth. (2022) Plant Engineering. Access mode: https://www.plantengineering.com/electrification-sparks-mobile-hydraulics-growth/

2. Smart fluid hydraulics. Preparing for the imminent revolution in the fluid systems industry. (2022) Access mode: https://www.mckinsey.com/~/media/mckinsey/industries/advanced%20electronics/our%20insights/smart%20fluid%20hydraulics%20preparing%20for%20the%20imminent%20revolution%20in%20the%20fluid%20systems%20industry/smart-fluid-hydraulics-preparing-for-the-imminent-revolution-in-the-fluid-systems-industry.pdf

3. Hydraulics Market Size, Share and Trends 2025 to 2034. Precedence Research Access mode: https://www.precedenceresearch.com/hydraulics-market

4. Hydraulic Equipment Market Size & Share Analysis - Growth Trends And Forecast (2025-2030). Mordor Intelligence. Access mode: https://www.mordorintelligence.com/ industry-reports/hydraulic-equipment-market

5. Padovani, D., Dimitriou, P., & Minav, T. Challenges and solutions for designing energy-efficient and low-pollutant machines in off-road hydraulics. *Energy Conversion and Management*, 2024. 21, 100526. https://doi.org/10.1016/j.ecmx.2024.100526

6. Hydraulics Market Size, Share. Trends and Growth. Access mode: https://www.marketsandmarkets.com/Market-Reports/hydraulics-market-209607944.html

7. Hydraulic Equipment Market Access mode: https://www.marketresearchfuture.com/reports/hydraulic-equipment-market-8066

8. Global Hydraulics Market Size By Component (Motors, Pumps, Cylinders, Valves, Filters), By Product Type (Mobile Hydraulics, Industrial Hydraulics), By End User (Aerospace, Agriculture, Automotive, Construction), By Geographic Scope And Forecast Access mode: https://www.verifiedmarketresearch.com/product/hydraulics-market/

9. Global Hydraulics Market Size, Share & Trends Analysis Report By End User, By Type (Mobile, and Industrial), By Component (Cylinder, Motor & Pumps, Transmission, Valves, Filters, Accumulators, and Others), By Regional Outlook and Forecast, 2023 - 2030 Access mode: https://www.kbvresearch.com/hydraulics-market/

10. Hydraulic Equipment Market Size & Outlook, 2024-2032. Access mode: https://straitsresearch.com/report/hydraulic-equipment-market

11. Hydraulics Market Size to Surpass USD 60.36 Billion in 2032. Access mode: https://finance.yahoo.com/news/hydraulics-market-size-surpass-usd-

150000627.html?guccounter=1&guce_referrer=aHR0cHM6Ly93d3cuZ29vZ2xlLmNvbS8&guce_referrer_sig=AQAAAHLpU6iuULvwCa-x3ZXJ9SiFta8_cgR3QZAJeltlVkCHNA5CmJN82W_kVIoapTJnUZw6cz5CaRkFYjSrEpVDk_3zeSjTnQLMnS4L7v7juqyA8riex47XiTBFEwl48dhK9YUfonHgPLrB42dUzuD1J7XTo7KOeZgw1nx29EKOQT4p

12. Industrial Hydraulic Equipment Market Size, Share & COVID-19 Impact Analysis, By Component (Pumps, Motors, Cylinders, Transmission, and Others), By Application (General Construction, Industrial Manufacturing, Oil and Gas, Material Handling, Energy and Power, and Others), and Regional Forecast, 2023-2030. Access mode: https://www.fortunebusinessinsights.com/industrial-hydraulic-equipment-market-109029

13. Hydraulic Equipment Market Size & Outlook, 2024-2032. Access mode: https://straitsresearch.com/report/hydraulic-equipment-market

14. Skvorchevsky, A. Electronic load sensing for integrating electro-hydraulic mechatronic actuators with Industry 4.0 and 5.0 components. *International Conference on Reliable Systems Engineering*. Cham: Springer Nature, 2023. 440–455. https://doi.org/10.1007/978-3-031-40628-7_37

15. Скворчевський, О.Є. Математичне моделювання статичних робочих процесів електрогідравлічних перетворювачів нормально-закритого типу. Вісник НТУ «ХПІ»: Нові рішення у сучасних технологіях, 2011. 48-54. Режим доступу: https://repository.kpi.kharkov.ua/handle/KhPI-Press/15748

16. Volontsevich, D., Skvorchevsky, A. Restoration and transformation of high-tech machine building industry by implementing the principles of the CALS-concept in the context of Industry 4.0 development. // Eastern-European journal of enterprise technologies. – 2022. – 117(1). Access mode: https://doi.org/10.15587/1729-4061.2022.260045

17. Skvorchevsky A. The possibilities evaluation of replacing electro-hydraulic actuators with planetary roller screws linear actuators. Комп'ютерні технології і мехатроніка: Матеріали 5-ї міжнар. наук.-практ. конф., Харків: ХНАДУ, 2023. С. 89-93. Access mode: https://repository.kpi.kharkov.ua/handle/KhPI-Press/76872

18. Electric cylinders CEMC. EWELLIX. Access mode: https://medialibrary.ewellix.com/asset/16213

19. Electric Actuators, Planetary Roller Screw – Series XFC. Parker Hannifin Access mood: https://ph.parker.com/us/en/product-list/extreme-force-electromechanical-cylinder-series-xfc

20. Roller screw technology for electric actuators. Tolomatic. Access mood: https://www.tolomatic.com/blog/roller-screw-technology-for-electric-actuators/

*Дата першого надходження статті до видання 04.08.2026*
*Дата прийняття статті до друку після рецензування 03.09.2026*
*Дата публікації (оприлюднення) статті 04.11.2026*
*Стаття поширюється на умовах ліцензії відкритого доступу(CC BY 4.0)*

# КІЛЬКІСНИЙ ТА ЯКІСНИЙ АНАЛІЗ РОЗВИТКУ ГЛОБАЛЬНОГО РИНКУ ГІДРАВЛІЧНОГО ОБЛАДНАННЯ

**О. Скворчевський**
*Центр досліджень робототехніки, мехатроніки та інформатизації виробництва*

***Анотація***

У статті виконано кількісний та якісний аналіз розвитку глобального ринку гідравлічного обладнання на основі узагальнення даних провідних комерційних досліджень, консалтингових звітів і наукових публікацій за 2022-2025 роки. Показано, що попри відмінності у методиках розрахунку, усі розглянуті джерела демонструють стабільне зростання світового ринку з середньорічним темпом приросту (CAGR) близько 4%, що підтверджує доцільність запуску нових проєктів у сфері промислової та мобільної гідравліки. Проведено узагальнення регіональної структури попиту, галузевих сегментів та компонентної бази ринку, що дозволило виділити провідну роль Азійсько-Тихоокеанського регіону, домінування будівельної техніки та мобільної гідравліки, а також зростаюче значення енергоефективних насосів, «розумних»

гідросистем і високотехнологічних гідроциліндрів та виконавчих органів. Окрему увагу приділено тенденціям цифровізації та впровадженню SMART-гідравліки, інтегрованої з технологіями Індустрії 4.0 та IoT, що забезпечує перехід від постачання окремих компонентів до сервісно-орієнтованих рішень на рівні систем.

Обґрунтовано три ключові драйвери трансформації гідравлічного ринку: електрифікацію мобільних і промислових машин, цифровізацію та формування SMART-гідравліки, а також зелений перехід із посиленням вимог до енергоефективності й скорочення викидів $CO_2$. Показано, що ці фактори одночасно створюють нові ніші для гідравлічних систем і посилюють конкуренцію з електромеханічними приводами, зокрема на базі гвинтових передач кулькового й роликового типу.

Запропонований інтегральний огляд дозволяє сформувати цілісне уявлення про перспективи розвитку світового ринку гідравлічного обладнання, а також окреслити пріоритетні напрями R&D у галузі енергоефективних гідроприводів, SMART-гідравліки та гібридних електрогідравлічних і електромеханічних систем. Отримані результати можуть бути використані виробниками обладнання, постачальниками компонентів і дослідниками для прийняття обґрунтованих рішень щодо формування продуктового портфелю, вибору технологічних платформ та виходу на перспективні сегменти глобального ринку гідравліки.

***Ключові слова:*** глобальний ринок гідравліки; SMART гідравліка; електрогідравлічні системи; енергоефективність.

**DOI https://doi.org/10.32782/1994-4691-2026-1-77-6**
UDK 621.89:621.22

# EFFECT OF FATTY ACID CONCENTRATION IN THE WORKING FLUID OF MACHINE HYDRAULIC DRIVES ON BOUNDARY LUBRICATING FILM FORMATION

# ВПЛИВ КОНЦЕНТРАЦІЇ ЖИРНИХ КИСЛОТ У РОБОЧІЙ РІДИНІ ГІДРОПРИВОДІВ МАШИН НА ФОРМУВАННЯ ГРАНИЧНОЇ МАСТИЛЬНОЇ ПЛІВКИ

V. Stefanov[1*], PhD, Associate Professor ORCID: 0000-0002-7947-2718
M. Voronin[1], PhD Student ORCID: 0009-0001-8841-0615

[1] *Ukrainian State University of Railway Transport, Kharkiv, Ukraine*
*e-mail: stefanov.v@kart.edu.ua

**Abstract**. An analysis of research regarding the effect of fatty acid additives on enhancing the anti-wear properties of working fluids was conducted. The characteristics and molecular state of the additive within the oil were identified as factors influencing the formation of a boundary lubricating film on friction surfaces. A method for intensifying additive adsorption by subjecting the working fluid to an electric field was proposed. A methodology was developed to experimentally investigate how the concentration of surfactant molecules – specifically the fatty acids under study – affects the formation of a lubricating layer on the friction surfaces of machinery hydraulic drives. Experimental studies were carried out to examine the effect of stearic and oleic acid concentrations on changes in boundary lubricating film thickness when the working fluid undergoes electrostatic treatment. A non-linear relationship between lubricating film thickness and additive concentration was established, and the optimal concentrations of stearic and oleic acids – yielding the maximum boundary lubricating film thickness – were determined.

**Keywords**: hydraulic drive, working fluid, friction surface, surfactant, lubricating film, electric field, film thickness.

## Introduction.

Hydraulic drives and hydraulic transmissions have recently become widespread and are used to drive the working equipment of construction, track, and materials-handling machines. Owing to the high cost of these units and the considerable labor intensity of repair work, there is a need to develop and implement resource-saving technologies aimed at improving the design of these units and the characteristics of working fluids.

One of the most common ways to improve the anti-wear properties of working fluids is to add various additives, most of which are surfactants. Such molecules promote the formation of a more wear-resistant lubricating film, the thickness of which directly depends on their properties, state, and amount in the working fluid. However, because these substances possess an electric dipole moment, at a certain concentration they interact with one another and form supramolecular structures that are unable to form the required lubricating layer effectively. Surfactant molecules are also adsorbed not only on friction surfaces but also on components present in the working fluid (wear products and inorganic particles), which reduces their effective concentration and hinders efficient lubricating-film formation.

An effective method of activating the additive (breaking down aggregates of surfactant molecules) is treatment of the working fluid with an external electric field. Under such a field, the protective function of the working fluid is enhanced by reducing friction and wear losses

in hydraulic drives; wear of friction units in hydraulic machines is reduced, thereby increasing their service life.

However, the effect of fatty-acid concentration (stearic and oleic acids) in the working fluid on lubricating-film formation on the friction surfaces of hydraulic drives of construction and track machines under electrostatic treatment remains insufficiently established. Therefore, elucidating this process is a relevant scientific task.

## Literature Review.

Boundary lubricating films of liquid media play an important role during friction between solid surfaces. The mechanism of their formation has been considered in numerous research studies [1–12] because it is of considerable practical interest. Liquid lubricating media that form a lubricating film are inherently multicomponent systems in which surfactants play a decisive role [2–4, 7]. The structure of these molecules is such that all of them possess an electric dipole moment, which enables interaction with metal surfaces. At the same time, the properties of the boundary lubricating film are also influenced by the structure of the metal surface because it forms its force field [3–8]. Thus, formation of the anti-wear layer on hydraulic-drive surfaces in contact with the lubricant depends on two main factors: the force field of the metal surface and the molecular structure of the surfactants.

In [11], a mathematical model (1) was proposed for determining lubricating-film thickness, taking into account the structure of the friction-surface material and the internal state of additive molecules in the working fluid.

$$H = b\sqrt{\frac{\left(1-2ee_0\frac{W_M}{p\sigma}\right)^2}{1-\left(1-2ee_0\frac{W_M}{p\sigma}\right)^2}}, \quad (1)$$

where $H$ is the thickness of the lubricating film on the friction surfaces of machine hydraulic drives, m; $W_M$ is the interaction energy between surfactant molecules depending on their state in the working fluid (monomers, dimers, micelles), J; $p$ is the dipole moment of a surfactant molecule, C·m; $\sigma$ is the surface charge density, C/m²; $\varepsilon$ is the dielectric permittivity of the working fluid; $\varepsilon_0$ is the vacuum permittivity; $b$ is the radius of the friction-surface contact area, m.

However, this mathematical model does not make it possible to construct an actual dependence of the effect of surfactant-molecule concentration on lubricating-layer formation, because the parameter $W_M$ [11], calculated using equation (2), depends only on the critical micelle concentration of fatty-acid molecules (which is a constant for different surfactants) and on temperature.

$$W_M = \frac{RT\ln(CMC)}{N_a}, \quad (2)$$

where $R$ is the Boltzmann constant, J·K⁻¹; $N_a$ is the Avogadro constant, mol⁻¹; $T$ is the fluid temperature, K; $CMC$ is the critical micelle concentration of surfactant molecules, mol/L.

Analysis of studies [10–15] shows that the use of electric fields to control lubricant properties and increase the service life of technical systems is a promising research direction. The theoretical basis of this approach is provided by electrodynamics concepts concerning the interaction of an electric field with matter, polarization processes, and the behavior of matter in an electric field [10]. Application of these principles to technical systems is considered in [13], where electric and magnetic fields are regarded as means of purposefully influencing the processes that determine the service life of machine hydraulic drives.

The results of [11] indicate the difficulty of establishing a universal relationship between additive concentration and the effectiveness of electrical treatment. The optimum concentration is determined by the specific composition of the working fluid, the type of additive, the electrical-treatment mode, and the operating conditions of the hydraulic unit. Therefore, the obtained relationships require additional verification for other lubricants and hydraulic-drive designs.

The effect of liquid-crystal additive concentration and an electric field on the physicochemical properties of a lubricant was investigated in greater detail in [15]. The authors analyzed changes in the kinematic viscosity, viscosity index, and pour point of an industrial oil depending on the concentration of a liquid-crystal additive and exposure to an electric field [15]. The results demonstrate that additive introduction and electrical treatment can change oil characteristics; however, the effect is not unequivocally positive for all properties. Increasing the additive concentration may cause undesirable changes in certain operating characteristics.

A practical assessment of the applicability of electrostatic treatment to engine oil was carried out in [14]. Unlike laboratory studies, the authors conducted operational tests of an electrostatic engine-oil treatment device directly on an engine. This approach is of considerable practical importance because it enables the effectiveness of the technology to be evaluated under actual operating conditions of a technical system [14].

However, the results of operational tests should be considered with due regard to the limitations of the experimental basis. Device effectiveness depends on engine type, oil grade and condition, load mode, temperature, operating duration, and the design parameters of the electrostatic device. Therefore, results obtained for a specific technical system cannot be directly extended to other engine types or lubricants without additional studies [14].

An important complement to these studies is [12], which addresses the mechanisms of tribochemical-film formation on friction surfaces. Unlike [11], [14], and [15], which focus mainly on the effects of the electric field and additives on lubricant characteristics or on the technical system, [12] gives considerable attention to processes occurring directly at the friction surface. Investigation of polymethacrylate components demonstrated the possibility of forming thin tribochemical films on metal surfaces, the characteristics of which are associated with the anti-wear action of the lubricant [12].

This result broadens the understanding of the mechanism of additive action. Improvement in tribological characteristics may be associated not only with changes in viscosity or other bulk properties of the oil, but also with the formation of a protective layer on friction surfaces. At the same time, [12] does not directly investigate the effect of an electric field on lubricating-film formation. Therefore, the possible influence of an electric field on the formation rate, structure, and chemical composition of such films remains insufficiently studied.

Generalization of the results of [11], [12], [14], and [15] suggests a complex interaction among three main factors: lubricant composition, the electric field, and the friction surface. Changes in oil properties under the action of an electric field may affect surface-contact conditions, while the additive may alter the interaction between the lubricant and the metal. In turn, processes at the friction surface determine the actual wear level and service life of the technical unit.

At the same time, the reviewed literature does not provide a complete explanation of the mechanism of interaction among these factors. Studies [11] and [15] mainly establish experimental relationships between additive concentration, electrical exposure, and working-fluid characteristics. Study [14] demonstrates the feasibility of practical electrostatic treatment in a real technical system. Study [12] helps explain the role of protective tribochemical films. However, a comprehensive study simultaneously linking electric-field parameters, additive concentration, physicochemical oil characteristics, surface-layer formation processes, and wear intensity requires further development.

Thus, analysis of sources [10–15] indicates that electrical treatment of lubricants can be regarded as a promising means of controlling their physicochemical and tribological properties. At the same time, the effectiveness of such treatment depends substantially on oil composition, additive type and concentration, electric-field parameters, and operating modes of the friction unit [11, 14, 15]. Establishing the mechanism of this interaction requires a combination of physicochemical, tribological, and operational research methods. Particular attention should be paid to the formation of protective surface films and their relationship with electrical-treatment parameters.

The analysis shows that numerous methods for improving the lubricity of working fluids already exist; however, there is a need to refine existing mathematical models or verify them experimentally.

## Research Methodology.

The aim of the study is to determine the thickness of the lubricating film formed by surfactant molecules on metal friction surfaces as a function of additive concentration (stearic and oleic acids) in the working fluid when its action is intensified by electrostatic treatment.

To achieve this aim, an experimental methodology was developed for determining lubricating-film thickness on a laboratory test bench. Before the experiments, the ranges of additive concentration were selected: 0–0.35% for stearic acid and 0–2.8% for oleic acid. The working-fluid temperature in both cases was maintained at 80 °C with an error of 0.5 °C. The electrostatic-field strength was $2\times10^6$ V/m.

## Results.

According to earlier studies [2, 12–15], the introduction of additives (fatty-acid molecules) into the working fluid of hydraulic machines results in their adsorption on friction surfaces, accompanied by an increase in the service life of hydraulic-system units. However, these studies did not consider what concentration of molecules in the base oil is rational or how it changes under the influence of an electrostatic field.

In previous studies, thin metal plates wetted with the lubricant under investigation were used to determine lubricating-film thickness. During the experiment, several plates with lubricant applied between them were compressed, after which their total thickness was measured. The resulting value was then compared with the thickness of the dry plates to determine the actual thickness of the lubricating layer.

A drawback of this method was that contaminant particles entered between the plates together with the lubricant. Their size was several orders of magnitude greater than the thickness of the lubricating layer, which increased the error of the experimental results. Therefore, a device developed at the Department of Mechanical Engineering and Technical Service of Machines was used to determine lubricating-film thickness. In this device, balls arranged consecutively one after another are used instead of plates (Fig. 1). With this arrangement, the probability of contaminant particles entering the ball contact point is very low.

The test bench (Fig. 1) consists of frame 1, on which a tube is installed using mounting 6. Thirty metal balls 4 are rolled into this tube. The tube is then closed on one side with mounting bracket 7, while a dial indicator 2 (ИЧЦ-10) is installed on the other side; its stem contacts the first ball through loading mechanism 3. The indicator pointer is thereby displaced by a certain amount.

At the first stage of the study, dry balls were used. They were rolled into tube 5 (Fig. 1) and pressed by the indicator spring. The readings obtained on its scale were taken as the initial values for subsequent measurements.

At the second stage, the mounting bracket was removed, the dry balls were rolled out of the tube, and each ball was successively wetted with I-20 working fluid as supplied and with I-20 containing different concentrations of stearic and oleic acids. Oleic acid is liquid at room

temperature, which allowed it to be introduced into the base oil without difficulty. Stearic acid is solid under normal conditions and has a melting point of 68 °C; therefore, it was preheated to the liquid state. The acids were introduced at the same temperatures, followed by mixing. After wetting in the resulting I-20 oil–acid solution, the balls were rolled into the tube again. Mounting bracket 7 (Fig. 1) was then installed, and the indicator head was pressed with the same force. The indicator reading shifted relative to the first value obtained for the dry balls. The difference between these two values, divided by the number of gaps between the balls, was taken as the thickness of the boundary lubricating layer.

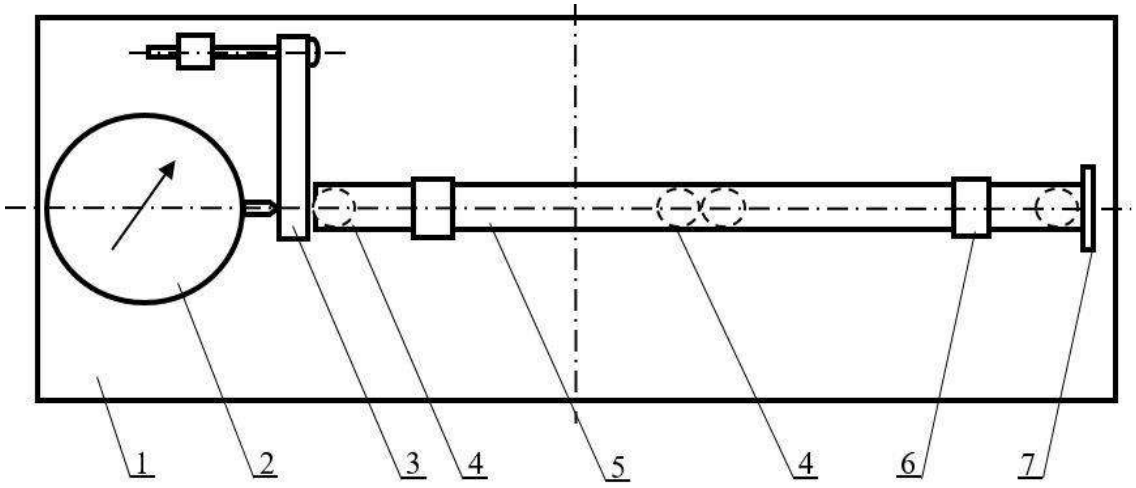



**Fig. 1. Test-bench arrangement for determining lubricating-film thickness: 1 – frame; 2 – dial indicator; 3 – loading mechanism; 4 – metal balls; 5 – metal tube; 6 – tube mounting; 7 – mounting bracket**

At the third stage, similar tests were conducted; however, in this case the investigated working fluid containing the additive was treated with an electrostatic field. Each lubricating-film thickness value was determined in eight repeated measurements.

The results of the planned experimental studies of the effect of additive concentration under electrostatic treatment of the working fluid are presented in Tables 1 and 2.

**Table 1. Experimental results for determining lubricating-film thickness as a function of stearic- and oleic-acid concentration**

| Additive | Additive concentration in oil, % | Mean lubricating-film thickness (without fluid treatment), µm | Mean lubricating-film thickness (with fluid treatment), µm |
|---|---|---|---|
| Stearic acid | 0 | 0,21 | 0,42 |
| | 0,05 | 0,33 | 0,45 |
| | 0,1 | 0,35 | 0,52 |
| | 0,15 | 0,43 | 0,62 |
| | 0,2 | 0,42 | 0,62 |
| | 0,25 | 0,36 | 0,58 |
| | 0,3 | 0,28 | 0,56 |
| | 0,35 | 0,27 | 0,54 |
| Oleic acid | 0 | 0,21 | 0,42 |
| | 0,4 | 0,25 | 0,43 |
| | 0,8 | 0,27 | 0,48 |
| | 1,2 | 0,32 | 0,48 |
| | 1,6 | 0,31 | 0,51 |
| | 2 | 0,28 | 0,49 |
| | 2,4 | 0,27 | 0,49 |
| | 2,8 | 0,23 | 0,48 |

**Table 2. Regression equations obtained from the experimental studies**

| Additive | Working-fluid treatment | Regression equation |
|---|---|---|
| Stearic acid | With treatment | $H_1(C) = -4{,}5476C^2 + 1{,}9988C + 0{,}3894$ |
| | Without treatment | $H_2(C) = -5{,}7381C^2 + 2{,}1012C + 0{,}2071$ |
| Oleic acid | With treatment | $H_3(C) = -0.029C^2 + 0.1086C + 0.3992$ |
| | Without treatment | $H_4(C) = -0.0472C^2 + 0.1421C + 0{,}1996$ |

The graphical representation of the research results shown in Fig. 2 demonstrates that the thickness of the boundary lubricating film between balls lubricated with I-20 oil was 0.2 μm, while electrostatic treatment increased it to 0.4 μm. This indicates the presence of surfactant molecules in the base oil as supplied. With a gradual increase in stearic-acid concentration, the layer thickness first increases and then decreases. This is explained by the transition of fatty-acid surfactant molecules from the monomeric state to an aggregated state. The maximum *H* value corresponds to the rational concentration of stearic acid in the working fluid. Without treatment, the rational concentration is 0.17%, whereas with an electrostatic field it is 0.22%.

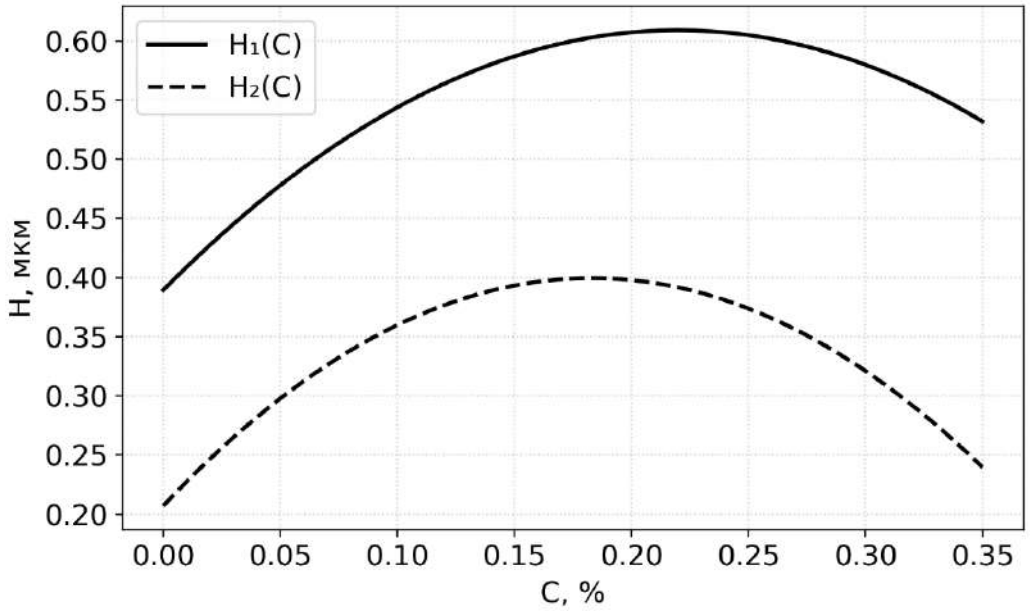



**Fig. 2. Dependence of lubricating-film thickness on stearic-acid concentration in I-20 oil at 80 °C**

A similar relationship is observed when oleic acid is used in the working fluid (Fig. 3). Without treatment, the rational concentration is 1.5%, whereas with an electrostatic field it is 1.9%.

According to the experimental results, all graphs exhibit a concentration of surfactant molecules at which the maximum lubricating-film thickness is formed. For stearic acid, the thickness increased from 0.2 μm to 0.4 μm without treatment and from 0.4 μm to 0.62 μm with treatment. For oleic acid, it increased from 0.2 μm to 0.32 μm without treatment and from 0.4 μm to 0.51 μm with treatment. This confirms the positive effect of additives in the working fluid and the use of external fields to intensify their action.

The obtained results can be used to verify models for determining lubricating-film thickness and friction-surface wear intensity and for predicting hydraulic-drive service life as a function of fatty-acid concentration in the working fluid.

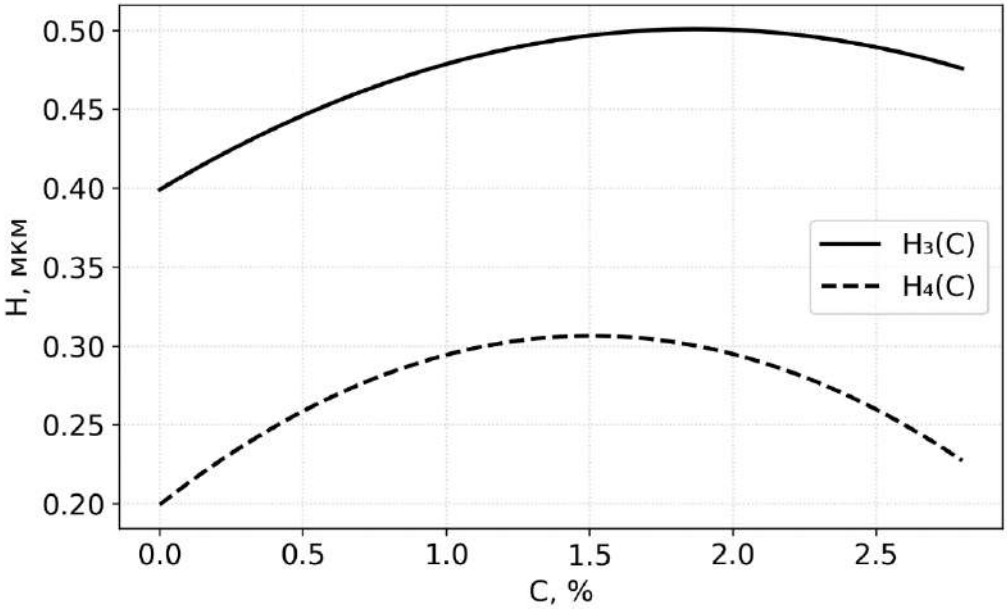



**Fig. 3. Dependence of lubricating-film thickness on oleic-acid concentration in I-20 oil at 80 °C**

However, future work should separately determine the contributions of the additive itself and the electric field. For this purpose, comparative experiments should be conducted in at least four modes: base oil without additive and without an electric field; oil with additive but without electrical exposure; base oil after electrical treatment; and oil with additive after electrical treatment. This methodology will make it possible to determine the contribution of each factor and establish whether an additional effect arises from their simultaneous application.

## Conclusions.

Based on the analysis of scientific studies, it was established that the effectiveness of boundary lubricating-film formation is determined not only by the presence of surfactants in the working fluid, but also by their concentration and molecular state. As additive concentration increases, aggregated structures may form, as a result of which some surfactant molecules lose the ability to adsorb effectively on friction surfaces. One way to intensify additive action is to apply an external electric field.

A non-monotonic dependence of boundary lubricating-film thickness on fatty-acid concentration in I-20 oil was established experimentally. For both additives studied, increasing the concentration initially increased the lubricating-film thickness; after the maximum value was reached, the thickness decreased. This indicates the existence of a rational additive concentration that provides the greatest thickness of the formed lubricating film. For stearic acid, the rational concentration is approximately 0.17% without electrostatic treatment and 0.22% with electrostatic treatment of the working fluid. For oleic acid, the corresponding values are approximately 1.5% and 1.9%. The results indicate that the electrostatic-treatment mode must be taken into account when determining the rational additive concentration.

Electrostatic treatment was found to increase boundary lubricating-film thickness under the investigated conditions. The maximum film thickness was 0.62 μm for stearic acid and 0.51 μm for oleic acid, whereas without electrostatic treatment the corresponding maximum values were 0.43 μm and 0.32 μm. The experimental results support further investigation of electrostatic treatment of working fluids as a means of intensifying the action of surfactants. At the same time, the established dependence of lubricating-film thickness does not directly determine hydraulic-drive service life; therefore, additional tribological and operational

studies are required to establish a quantitative relationship among additive concentration, film thickness, wear intensity, and technical-system service life.

The research results can be used to refine and experimentally verify mathematical models for determining lubricating-film thickness and as input data for subsequently establishing relationships among working-fluid parameters, electrostatic-treatment conditions, friction-surface wear, and hydraulic-drive service life.

**Future Research Directions**

Further research should focus on establishing a quantitative relationship between fatty-acid additive concentration, the parameters of electrostatic treatment, boundary lubricating film formation, friction-surface wear, and the service life of hydraulic drive components. The results obtained in the present study characterize the change in lubricating film thickness; however, this parameter alone does not provide a direct quantitative assessment of wear intensity or hydraulic-system durability.

A priority task is to separate the individual and combined effects of the additive and the electric field. For this purpose, comparative experiments should be carried out under four conditions: base oil without an additive and without electrostatic treatment; oil containing an additive without electrostatic treatment; base oil subjected to electrostatic treatment; and oil containing an additive subjected to electrostatic treatment. Such an experimental design will make it possible to determine the contribution of each factor and to identify a possible interaction effect between fatty-acid additives and electrostatic treatment.

Further experimental studies should also extend the ranges of operating conditions. In particular, the effects of working-fluid temperature, electric-field strength, treatment duration, contact pressure, sliding velocity, and contamination level should be investigated. Particular attention should be paid to verifying whether the rational concentrations determined for stearic and oleic acids remain stable when the operating conditions of hydraulic friction units change.

Another important direction is the tribological verification of the established relationships using friction pairs representative of hydraulic machines. Measurements of friction coefficient, wear rate, surface roughness, and changes in the morphology and chemical composition of the formed boundary films would allow the experimentally determined film-thickness relationships to be linked with the actual anti-wear performance of the working fluid.

The resulting experimental data can subsequently be used to refine and validate mathematical models describing boundary lubricating film formation and wear processes. A combined model incorporating additive concentration, molecular state, electrostatic-treatment parameters, lubricating film thickness, and wear intensity could provide a basis for predicting the durability of hydraulic drive friction units and for selecting rational working-fluid treatment conditions.

## References

1. Meng Y., Xu J., Ma L., Jin Z., Prakash B., Ma T., Wang W. A review of advances in tribology in 2020–2021. *Friction*, 2022. 10 (10). 1443–1595. https://doi.org/10.1007/s40544-022-0685-7

2. Charoo M. S., Akhter F., Hanief M., Shafi W. K., Nissar M. Effect of Saturated Fatty Acids on the Antiwear and Rheological Properties of Olive Oil. *Tribology in Industry*, 2023. 45 (1). 121–128. https://doi.org/10.24874/ti.1404.11.22.02

3. Li H., Yin Z., Jiang D., Jin L., Cui Y. A study of the tribological behavior of transfer films of PTFE composites formed under different loads, speeds and morphologies of the counterface. *Wear*, 2015. Vol. 328–329. P. 17–27. https://doi.org/10.1016/j.wear.2015.01.028

4. Ligier J.-L., Noel B. Friction Reduction and Reliability for Engines Bearings. *Lubricants*, 2015. 3 (3). 569–596. https://doi.org/10.3390/lubricants3030569

5. Zhao J., Huang Y., He Y., Shi Y. Nanolubricant additives: A review. *Friction.* 2021. 9. 891–917. https://doi.org/10.1007/s40544-020-0450-8

6. Minkin V. I., Osipov O. A., Zhdanov Y. A. Dipole Moments in Organic Chemistry. New York: Springer Science+Business Media, 1970. XII, 288 p. https://doi.org/10.1007/978-1-4684-1770-8

7. Dou P., Jia Y., Zheng P., Wu T., Yu M., Reddyhoff T., Peng Z. Review of ultrasonic-based technology for oil film thickness measurement in lubrication. *Tribology International*, 2022. 165. 107290. https://doi.org/10.1016/j.triboint.2021.107290

8. Gu H., Hirayama T. Effect of surfactant self-assembly on lubrication performance in oil-based systems: the role of reverse micelles and vesicles. *Frontiers in Mechanical Engineering*, 2025. 11. 1608716. https://doi.org/10.3389/fmech.2025.1608716

9. Zangwill A. Physics at Surfaces: monograph. – New York: Cambridge University Press, 1988. 454 p.

10. Purcell E.M., Morin D. J. Electricity and magnetism: textbook. New York: Cambridge University Press, 2013. 839 p.

11. Стефанов В. О. Вплив концентрації присадки на ресурс гідроагрегатів засобів транспорту в умовах електрообробки робочої рідини. *Енергозбереження. Енергетика. Енергоаудит*, 2014. № 7 (125). С. 2–11.

12. Erck R. A., Song M., Li D., Cosimbescu L. Investigations of polymethacrylate tribochemical films using X-Ray spectroscopy and optical profilometry. *Tribology Letters*, 2021. 69 (1), № 1. 26. https://doi.org/10.1007/s11249-020-01388-5

13. Александров Є. Є., Кравець І. А., Лисіков Є. М. Підвищення ресурсу технічних систем шляхом використання електричних та магнітних полів : монографія. Харків : НТУ «ХПІ», 2006. 544 с.

14. Воронін С. В., Стефанов В. О., Харківський О. С. Експлуатаційні випробування пристрою для електростатичної обробки моторної оливи. *Збірник наукових праць Українського державного університету залізничного транспорту*. Харків : УкрДУЗТ, 2022. Вип. 200. С. 11–24. https://doi.org/10.18664/1994-7852.200.2022.262678

15. Воронін С. В., Сафонюк І. Ю., Аношкіна Н. М., Харківський О. С. Дослідження впливу концентрації рідкокристалічної присадки та електричного поля на фізико-хімічні властивості індустріальної оливи. *Вісник Національного авіаційного університету*. 2020. № 2 (83). С. 70–76. https://doi.org/10.18372/2306-1472.83.14654

*Дата першого надходження статті до видання 07.09.2026*
*Дата прийняття статті до друку після рецензування 05.10.2026*
*Дата публікації (оприлюднення) статті 04.11.2026*
*Стаття поширюється на умовах ліцензії відкритого доступу(CC BY 4.0)*

# ВПЛИВ КОНЦЕНТРАЦІЇ ЖИРНИХ КИСЛОТ У РОБОЧІЙ РІДИНІ ГІДРОПРИВОДІВ МАШИН НА ФОРМУВАННЯ ГРАНИЧНОЇ МАСТИЛЬНОЇ ПЛІВКИ

**В.О. Стефанов[1], М.О. Воронін[1]**
[1]*Український державний університет залізничного транспорту*

***Анотація***

У цьому дослідженні вивчається вплив концентрації присадок на основі жирних кислот на формування граничної мастильної плівки на металевих поверхнях тертя під час електростатичної обробки робочих рідин гідравлічних машин. Особливу увагу приділено молекулярному стану присадки, оскільки підвищення її концентрації може сприяти утворенню надмолекулярних агрегатів і, як наслідок, зменшувати частку молекул, доступних для адсорбції на поверхнях тертя. Зовнішнє електричне поле розглядається як засіб інтенсифікації адсорбції присадок та модифікації молекулярного стану поверхнево-активних речовин у робочій рідині. Було розроблено експериментальну методику визначення товщини граничної мастильної плівки з використанням випробувального стенда, що містить 30 послідовно розміщених металевих кульок. Така конфігурація зменшує ймовірний вплив забруднювальних частинок на результати вимірювань. Експерименти проводили з використанням базової оливи І-20 за

температури 80 °С. Досліджували концентрації стеаринової кислоти в діапазоні 0–0,35 % та олеїнової кислоти — 0–2,8 % як за умов електростатичної обробки, так і без неї. Результати експериментів продемонстрували нелінійну залежність між концентрацією присадки та товщиною граничної плівки. Для обох жирних кислот товщина плівки спочатку зростала зі збільшенням концентрації присадки, а після досягнення максимального значення — зменшувалася. Для стеаринової кислоти раціональна концентрація становила приблизно 0,17 % без електростатичної обробки та 0,22 % — з обробкою. Для олеїнової кислоти відповідні значення становили приблизно 1,5 % та 1,9 %. Максимальна товщина плівки для стеаринової кислоти становила 0,43 мкм без обробки та 0,62 мкм з електростатичною обробкою, тоді як для олеїнової кислоти ці показники дорівнювали 0,32 мкм та 0,51 мкм відповідно. Отримані результати свідчать про те, що як концентрація присадки, так і електростатична обробка впливають на формування граничної мастильної плівки за досліджуваних умов. Отримані експериментальні залежності можуть бути використані для уточнення та верифікації математичних моделей, що описують формування мастильної плівки, а також для подальшого вивчення взаємозв’язку між складом робочої рідини, молекулярним станом присадки, зношуванням і ресурсом гідравлічних систем. Висновки дослідження створюють підґрунтя для вибору раціональних концентрацій присадок на основі жирних кислот з урахуванням застосування електростатичної обробки.

**Ключові слова:** гідравлічний привід, робоча рідина, поверхня тертя, поверхнево-активна речовина, мастильна плівка, електричне поле, товщина плівки.

**DOI https://doi.org/10.32782/1994-4691-2026-1-77-7**
УДК 510.621.9

# COMPONENTS OF HYDRAULIC CONTROL SYSTEMS FOR WHEELLESS GROUND ROBOTIC COMPLEXES

# ЕЛЕМЕНТНА БАЗА СИСТЕМ ГІДРОАВТОМАТИКИ БЕЗКОЛІСНИХ НАЗЕМНИХ РОБОТИЗОВАНИХ КОМПЛЕКСІВ

V. Strutynsky[1*], Dr. Tech. Sciences, Professor ORCID: 0000-0001-7167-0085

[1] *National Technical University of Ukraine "Igor Sikorsky Kyiv Polytechnic Institute", Kyiv, Ukraine*
* e-mail: vbstrutynskiy@gmail.com

**Abstract**. The article addresses the development of components for hydraulic control systems of wheelless ground robotic complexes with high terrain mobility. Typical wheelless ground robotic complexes are considered. They have a central section that slides along the surface using inertial propulsion devices and is equipped with long, flexible peripheral elements, 2–3 m in length, with knives, saws, or milling cutters mounted at their ends to break down obstacles. The complex has a large manipulator, approximately 4 m in length, which provides surface inspection and examination, orientation, and communication. Wheelless ground robotic complexes include special units, hydraulic drives, and hydraulic control systems using industrial water as the working fluid. It is proposed to implement them using innovative components based on high-pressure jet and vortex devices and units operating at approximately 25 MPa. The developed schematic solutions for innovative jet and vortex devices are presented. The hydrodynamic processes in the devices were investigated theoretically and experimentally. It was established that singular flow regions, where the rate-of-strain tensor becomes degenerate, determine the operating processes of jet and vortex devices. The results of studies of the static and dynamic characteristics of the jet devices forming the set of components are presented. A structural design and manufacturing methods are proposed for small channels, approximately 0.3 mm in size, with increased wear resistance. The manufacturing methods were tested using experimental prototypes that were designed and manufactured.

**Keywords**: jet units, vortex devices, singular regions, turbulent jets, static characteristics.

## Introduction.

Special-purpose ground robotic complexes are widely used in humanitarian demining [1]. Therefore, research aimed at developing advanced designs of ground robotic complexes is relevant. The proposed special-purpose ground robotic complexes have a central section that moves along the surface using inertial propulsion devices. This section is equipped with long, flexible peripheral elements, 2–3 m in length, with knives, saws, or milling cutters mounted at their ends to break down obstacles.

Ground robotic complexes operate under off-road conditions [2], with considerable variations in temperature and humidity and without the necessary repair facilities and equipment. Therefore, the general problem is to improve the reliability of these complexes under harsh operating conditions [3]. One aspect of this problem is to improve their terrain mobility [4]. This is consistent with practical applications of ground robotic complexes [5] and general trends in the development of mobile robots [6].

## Literature Review.

A reasonable approach to improving terrain mobility is to develop wheelless robots that move by sliding [7]. Several technical solutions for wheelless ground robotic complexes have been developed [8]. An analysis of the literature [9] indicates that snake-like robotic

complexes are a promising direction.

The use of mechatronic systems is recommended to improve robot performance [10]. The performance of mechatronic systems [11, 12] largely depends on their dynamic characteristics [13]. The use of hydraulic and pneumatic control systems and hydraulic drives is promising [14, 15]. These systems help address the challenges of operating wheelless robots under difficult temperature and humidity conditions [16].

The use of mineral oil as the working fluid in the hydraulic drives of ground robotic complexes is not considered appropriate [17]. Industrial water is a reasonable alternative. However, its use creates several problems in the development of hydraulic and pneumatic control systems for ground robotic complexes [18]. The main problem is the inability to achieve the required fineness of working fluid filtration [19].

An analysis of the literature discussed above and other information sources [1, 6] indicates that clear proposals for the development of wheelless ground robotic complexes are currently lacking. Recommendations for the use of control components are also unavailable. Therefore, the development of components for hydraulic and pneumatic control systems remains an unresolved aspect of the broader problem of developing advanced ground robotic complexes.

The aim of this study is to develop fundamentally new components for hydraulic and pneumatic control systems based on high-pressure jet and vortex devices that use industrial water containing a considerable amount of contaminants as the working fluid. The proposed high-pressure jet devices are adapted for use in wheelless ground robotic complexes.

## Research Methodology.

To achieve this aim, the following research objectives were formulated and addressed:

- to analyse the specific operating conditions of hydraulic control systems in wheelless ground robotic complexes;
- to develop schematic and design solutions for high-pressure jet and vortex devices;
- to investigate the operating processes in jet and vortex devices;
- to determine the specific features of the characteristics of the devices forming the set of control components;
- to identify promising design and manufacturing approaches for developing components of hydraulic and pneumatic control systems for wheelless ground robotic complexes.

The study used materials from a wide range of engineering developments, including innovative designs, results from tests of experimental prototypes of jet and vortex devices, and operating experience with jet and vortex devices, including series-produced devices, in various engineering applications [20, 21]. These materials were adapted to the development of components for hydraulic control systems in wheelless ground robotic complexes [2, 22].

Theoretical and experimental methods were used in the study. The hydrodynamic processes in jet and vortex devices were investigated by numerical integration of the governing equations of fluid mechanics. The finite element and finite difference methods were applied.

The theoretical calculations of jet and vortex flows were confirmed by experimental data obtained through flow visualisation in model jet devices. In these experiments, MS-20 oil containing a finely dispersed gas phase flowed at velocities of up to 50 m/s. High-pressure turbulent flows at 20–30 MPa were investigated using miniature Pitot tubes, 0.2–0.3 mm in size, on a specially designed test rig that provided positioning accuracy of 0.5–1 μm for the device components. The equipment and measuring instruments used provided a measurement accuracy of 1–2%.

Special methods were developed and used to investigate high-pressure fluid flows in jet devices. An effective method involves analysing singular regions in the moving fluid where the stress tensor and the rate-of-strain tensor become degenerate. Innovative methods for investigating the operating processes were proposed based on an analysis of wear in jet device

parts after 10 million operating cycles.

Both analytical and experimental methods were used to investigate the static characteristics of the devices forming the set of control components. The theoretical analysis of the characteristics of jet and vortex devices was based on solving the equations of fluid mechanics in integral form [20]. Experimental studies were conducted using specially designed test equipment. This equipment made it possible to measure the static characteristics of jet devices with assembled nozzles and receiver channels measuring 0.1–1 mm, at operating pressures of up to 30 MPa and flow rates of up to 15 l/min.

The theoretical study of the dynamic characteristics of jet devices was based on fuzzy and stochastic mathematical models [16, 23]. The computational models accounted for the inertia and compressibility of the working fluid. Experimental studies of the dynamic behaviour were conducted using high-precision pressure sensors. The measurement results were processed using statistical methods and specialised software to determine correlation functions, spectral densities, and other characteristics of dynamic processes in jet devices.

Advanced manufacturing and metalworking methods were used to produce the main control components [24, 25]. On this basis, innovative designs were developed for assemblies and parts of jet and vortex devices forming the components of hydraulic control systems in wheelless ground robotic complexes. Manufacturing issues related to the main parts of jet and vortex devices were addressed.

## Results.

### Developed Ground Robotic Complexes

Several schematic and design solutions for wheelless ground robotic complexes have been developed. The most effective are ground robotic complexes that incorporate flexible elements. The developed wheelless ground robotic complex has a central section 1 containing batteries as the power source, a hydraulic power unit, and a control system (Fig. 1).

The front section 2 of the ground robotic complex is connected to the central section. It carries a rotating milling cutter 3 with its drive. The rear section of the wheelless robot consists of two branches, 4 and 5, attached to the central section 1. The ends of the rear branches are equipped with positioning devices in the form of rotors 6 and 7, which have ribs for interaction with the ground. The rotors are powered by drives located in the end modules 8 and 9 of the rear branches. The front section 2 and the rear branches 4 and 5 consist of flexible modules connected in series. These modules allow limited spatial movement of the front and rear sections relative to the central section 1.

The front section 2 moves in the horizontal plane so that the milling cutter sweeps an arc $F_1F_0F_2$ whose width $B_n$ exceeds the overall width $B_a$ of the rear section of the robot. As a result, the milling cutter breaks down obstacles in the robot's path, allowing the robot to move freely along the x-axis.

The front section of the ground robotic complex can move vertically. During this movement, the milling cutter follows an arc $F_3F_0F_4$ (see Fig. 1b). Its vertical sweep $H_n$ exceeds the overall height $H_a$ of the robot with the manipulator mounted on it. Obstacles in the robot's path are therefore broken down to provide sufficient clearance for the robot and its manipulator to pass.

The large manipulator, with a total length of approximately 4 m, has a main link 10 of length $L_1$. Links 11 and 12 form the main linkage of the manipulator. The links are connected by single-axis joints $A_0$ and $B_0$. The manipulator has a static balancing system consisting of a balancing lever 13 connected to link 10 and a balancing mass 14. A hexapod mechanism 15 is mounted at the end of link 12 for fine spatial movements of the tactile device 16.

In the folded position, the manipulator is placed and secured on the rear section of the robot, while the balancing lever 13 is secured on the front section. Link 10 is mounted on the rotary base 17 through a two-axis joint $O$. Link 11 has an aerodynamic control system consisting of a propeller 18 and its drive.

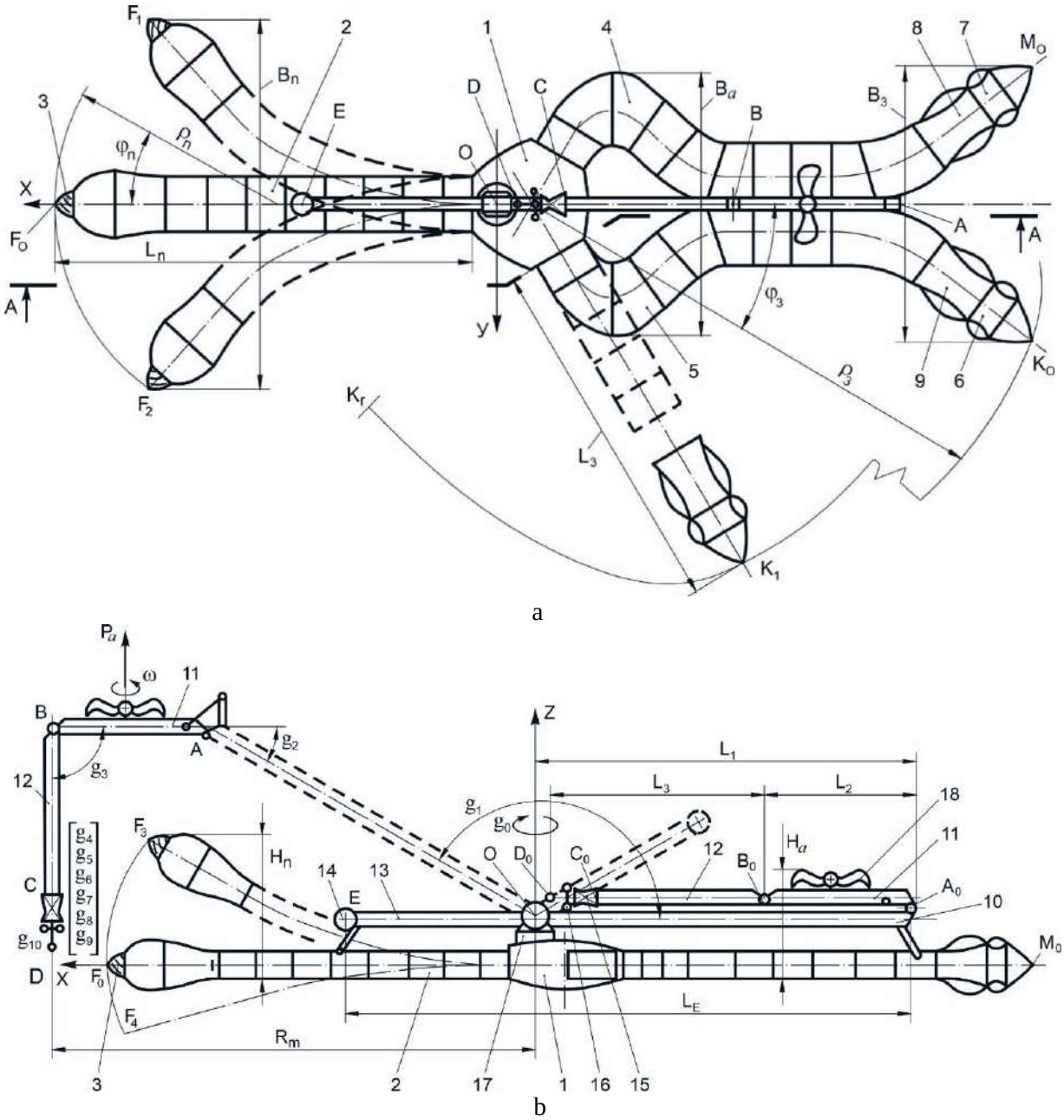



**Fig. 1. Typical wheelless ground robotic complex: (a) top view; (b) side view; 1 – central section; 2 – front section; 3 – rotating milling cutter; 4, 5 – rear branches; 6, 7 – working rotors; 8, 9 – end modules; 10 – main link; 11, 12 – links; 13 – balancing lever; 14 – balancing mass; 15 – hexapod mechanism; 16 – tactile device; 17 – rotary base; 18 – propeller.**

In the operating position, the manipulator assumes the configuration *OABCD*. Link 11 is positioned so that its axis (*AB*) is nearly horizontal. The propeller lift vector $P_a$ is directed approximately along the direction of the gravitational forces acting on the manipulator. Changing the direction of the propeller lift vector allows the position of the tactile device to be adjusted within the region *D*. The manipulator has the required number of controlled coordinates.

The drives for coarse (rapid, macro-scale) movements provide rotation of the manipulator (coordinate $q_0$), adjustment of the position of link 10 through an angle $q_1$, adjustment of the relative angular position of links 10 and 11 through an angle $q_2$, and variation of the angle $q_3$ between links 11 and 12. To improve positioning accuracy, the manipulator is equipped with a six-coordinate fine-positioning drive implemented as a hexapod mechanism 15 with six degrees of freedom: $q_4$, $q_5$, …, $q_9$ [26].

Three controlled coordinates of the hexapod provide translational movements of the tactile device 16, while the other three provide its angular movements in space. The tactile device has an additional controlled coordinate $q_{10}$, which determines the position of point $D$ relative to the hexapod platform.

Thus, in its operating position, the manipulator has 10 controlled coordinates. Its workspace is bounded by a spherical surface with a radius $R=max(R_m)=L_1+L_2+L_3$. To ensure reliable operation of the manipulator without loss of static equilibrium, the wheelless robot must have a sufficient support area. When the manipulator is positioned close to the plane *xoz*, the front section 2 and the rear branches 4 and 5, extending along the axis *x*, provide this support area. The outermost points $F_0$, $K_0$ and $M_0$ define the limits of the support areas.

The flexibility of the front and rear sections should be taken into account when determining the static stability of the manipulator. Positioning the manipulator away from the robot's plane of symmetry requires support areas located away from the plane *xoz*. The maximum distance of the front section (points $F_1$ and $F_2$) from the axis *x* is determined by the possible deformation of the elastic front section 2.

The width $B_n$ of the arc can be used to estimate the extent of the support area provided by the front section. The support areas at the rear of the robot are formed at points $K_0$ and $M_0$. If necessary, the rear branches 4 and 5 change their configuration to increase the distance between their outermost points. A straight configuration of the branches is a reasonable choice and corresponds to the movement of point $K_0$ along the curve $K_0K_1K_2$. The region in which branch 5 can be positioned is bounded by the curve whose radius $\rho_3$ depends on the angle $\varphi_3$.

Changing the position of the rear branches significantly affects the robot's terrain mobility. Moving branches 4 and 5 and their end modules 8 and 9 away from the axis *x* allows the robot to generate resistance forces to withstand the cutting forces of the milling cutter. Wave-like movements of the rear branches provide translational motion of the robot in different directions. The ability to turn in the plane *xoy* is particularly important. This compensates for a limitation of a robot with a linear configuration, for which turning is a difficult operation.

The presence of three long, flexible elements reduces the likelihood of unwanted twisting of the flexible branches, which is characteristic of robots with a linear configuration. The robot can also move backwards along the axis *x*. The proposed design improves the reliability of robot operation when travelling over rough terrain with steep slopes.

**Features of Hydraulic and Pneumatic Control Systems of Ground Robotic Complexes**

According to the basic design scheme [27], the front section 2 of the wheelless robot has a rotating milling cutter 1 mounted on a spherical fluid-film bearing with a sphere 3 (Fig. 2).

The milling cutter 1 is rotated by a high-torque hydraulic motor 17 controlled by a directional control valve 18. The hydraulic motor shaft is connected to the sphere 3 through an involute gear coupling 19. The geometric centre of the coupling 19 is located at the centre of the sphere 3. This allows limited spatial rotation of the sphere 3. The sphere can rotate through an angle $\varphi_0$ in the *xoy* plane and through an angle $\theta_0$ in the perpendicular *xoz* plane.

The sphere is rotated in these planes by hydraulic drives. They include hydraulic cylinders 20 and 21 controlled by a directional control valve 22. The piston rods interact with the outer part of a rolling-element bearing 23 mounted on a shank 24 attached to the sphere 3. Hydraulic cylinders 20 and 21 rotate the sphere 3 through an angle $\varphi_0$ in the *xoy* plane. Similar drives with a corresponding directional control valve are used to rotate the sphere in the perpendicular *xoz* plane (not shown in the figure).

The spherical fluid-film bearing has a series of hydrostatic bearings 25 supplied with fluid through throttles 26 from the robot's common high-pressure line 27. Fluid is drained from the spherical fluid-film bearing through a drain line 28 connected to its low-pressure cavity 29. The spherical fluid-film bearing also has a series of hydrodynamic bearings 30.

Various cutting forces act on the milling cutter 1.

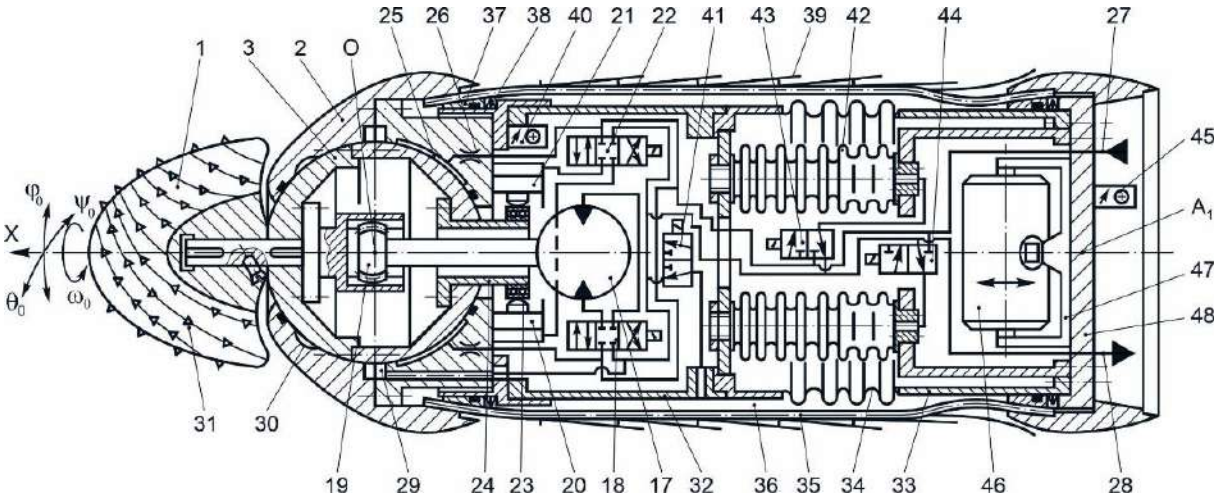



**Fig. 2. Design scheme of the front section of the wheelless robot: 1 – milling cutter; 2 – front section of the robot; 3 – sphere; 17 – high-torque hydraulic motor; 18 – directional control valve; 19 – involute gear coupling; 20, 21 – hydraulic cylinders; 22 – directional control valve; 23 – rolling-element bearing; 24 – shank; 25 – hydrostatic bearings; 26 – throttles; 27 – common high-pressure line of the robot; 28 – drain line; 29 – low-pressure cavity of the spherical bearing; 30 – hydrodynamic bearings; 31 – inserts made of superhard materials; 32, 33 – tubular elements; 34 – bellows; 35 – outer elastic shell; 36 – sealed annular cavity; 37 – movable conical sleeves; 38 – disc springs; 39 – protective plates; 40 – gyroscopic inertial navigation device for tubular element 32; 41 – directional control valve for regulating the pressure in the annular cavity; 42 – bellows-type actuators; 43, 44 – directional control valves for controlling the bellows-type actuators; 45 – gyroscopic inertial navigation device for tubular element 33; 46 – vibration device; 47 – fixed base of the vibration device; 48 – plate.**

The maximum forces act in the direction opposite to the x-axis. They are supported by the system of hydrostatic bearings 25. The milling cutter 1 is made of a high-hardness material. To improve the efficiency of the cutting process, inserts 31 made of superhard materials are placed on the cutter surface. The use of synthetic diamonds, boron nitride, or boron carbide for these inserts is promising. The systematically arranged inserts ensure effective destruction of obstacles such as metal structures, barbed wire, concrete, stone, and other materials.

The efficiency of the cutting process is ensured by the proposed technical solution, which provides spatial rotations of the sphere 3 about the *x*, *y*, and *z* axes. The rotating milling cutter 1, connected to the sphere 3, acts as a gyroscope rotating at a frequency $\omega_0$. Hydraulic cylinders 20 and 21, together with the hydraulic cylinders located in the plane perpendicular to the plane of the figure, do not rigidly fix the shank 24 mounted on the sphere 3. The cutting forces produce considerable spatial torques acting on the rotating milling cutter. These torques give rise to corresponding gyroscopic moments and cause precessional motion of the sphere and the milling cutter.

Spatial movement of the sphere allows useful force effects to be generated. For example, a sudden movement of the shank 24 in the xoy plane produces a considerable gyroscopic moment acting on the wheelless robot in the *xoz* plane. This can raise the front section of the robot above the ground surface or push it into the soil.

The front section of the robot contains tubular elements 32 and 33 connected by a bellows 34. These elements and the bellows are enclosed by an outer elastic shell 35, forming a sealed annular cavity 36. The edges of the elastic shell are sealed by movable conical sleeves 37. The sleeves are moved by disc springs 38. This ensures sealing and secures the elastic shell relative to tubular elements 32 and 33. Protective plates 39 are attached to the

shell surface. A special gyroscopic inertial navigation device 40 is used to measure the spatial position of tubular element 32.

The pressure in the annular cavity 36 is regulated by a directional control valve 41. The shell 35 is reinforced with cords made of ultra-high-strength fibre, oriented along the axes of tubular elements 32 and 33. As the pressure in cavity 36 increases, the elastic shell 35 expands in the diametrical direction. The reinforcing cords shorten the shell, compressing the bellows 34 and displacing tubular elements 32 and 33. Actuators for their relative spatial displacement are installed inside the tubular elements. A reasonable solution is to use bellows-type actuators 42 controlled by directional control valves 43 and 44. It is advisable to use three or more bellows-type actuators to provide relative spatial displacement of tubular elements 32 and 33.

A special gyroscopic inertial navigation device 45 is used to measure the spatial position of tubular element 33. A vibration device 46 is installed inside tubular element 33. It allows the direction of movement of its inertial mass to be adjusted. This device produces movement of the mass and, consequently, inertial loads in the *xoz* plane. The vibration device has a fixed base 47 attached to a plate 48 connected to tubular element 33.

The drive mechanisms of all parts of the ground robotic complex include an extensive hydraulic control system. Its main components, the first- and second-stage amplifiers, form the basis of the system's set of control components.

A specific feature of the hydraulic control system is the compact arrangement of devices within enclosed spaces. This requires minimising the mass and overall dimensions of hydraulic control devices, allowing them to be combined into blocks, and combining the functions of hydraulic units. The use of industrial water as the working fluid requires eliminating or reducing the number of precision friction pairs. The limited internal space of wheelless robots requires a special approach to cooling the units and hydraulic control systems.

The main problem in operating hydraulic control systems is contamination of the working fluid. The design features of these systems do not allow the necessary filtration equipment to be installed. Considering the above requirements for hydraulic and pneumatic control systems, high-pressure jet and vortex units are proposed as the basis for their control components. These units have no precision friction pairs and allow relatively large clearances between parts in the flow passage of the device.

**Developed High-Pressure Jet and Vortex Devices Forming the Basis of the Set of Control Components**

The schematic and design solutions for high-pressure jet and vortex devices allow them to operate with contaminated working fluids. The absence of small clearances between parts allows relatively large contaminant particles to pass through and prevents clogging (obliteration) (Fig. 3).

Several schematic and design solutions for jet and vortex devices have been developed. The universal high-pressure jet unit (Fig. 4) has a supply nozzle 1. To form a compact jet at the nozzle outlet, its peripheral parts are formed by control jets 3 flowing from nozzles 2. Varying the pressure $P_y$ at the control nozzle inlet adjusts the shape and direction of the main jet, which propagates in a low-pressure chamber at $P_c \approx 0.1–0.5$ MPa. A focusing deflector 4 is located in the chamber and compresses the jet in the vertical direction.

This deflector has a wedge-shaped slot, in the plane of which a rectangular jet is formed in region 5. Moving the deflector 4 provides the required shape and position of the jet in the chamber. A control deflector 6 is installed in the chamber downstream of the focusing deflector 4. It has a focusing wall 7 and an edge 8 for deflecting the jet. To improve the stability of jet deflection, a channel 9 is formed in the deflector to supply part of the jet to the rear side of the deflector 6. Shields 10 and 11 are installed downstream of the control deflector in the low-pressure chamber. They divert the reverse flows entering the low-pressure chamber from the receiver channels.

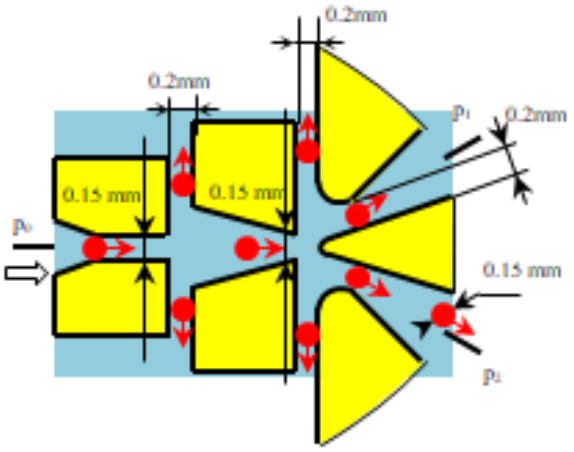



**Fig. 3. Passage of particles up to 150 μm in size through the hydraulic channels of a first-stage jet amplifier.**

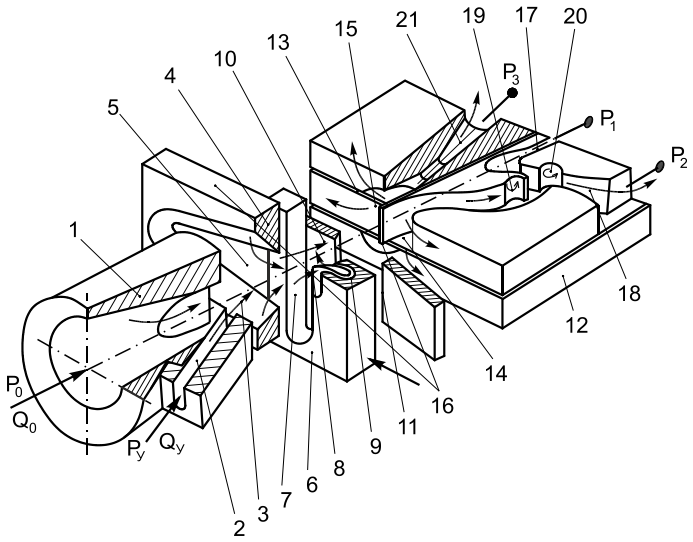



**Fig. 4. Developed universal high-pressure jet unit: 1 – supply nozzle; 2 – control nozzles; 3 – control jets; 4 – focusing deflector; 5 – region of rectangular jet formation; 6 – control deflector; 7 – focusing wall; 8 – edge for jet deflection; 9 – channel supplying part of the jet to the rear side of the control deflector; 10, 11 – shields for diverting reverse flows; 12 – receiver channel block; 13 – bridges between plates; 14, 15 – main receiver channels; 16 – separating wedge; 17 – receiver channel outlet; 18 – additional receiver channel outlet; 19, 20 – recesses for flow stabilisation; 21 – additional outlets for utilising the peripheral parts of the main jet.**

The kinetic energy of the jet is converted into the potential energy of the compressed fluid in the receiver channel block 12. The receiver channel block 12 contains a stack of plates separated by bridges 13. The main receiver channels 14 and 15 are formed in the central plate and separated by a wedge 16. Each receiver channel has an outlet 17 and an additional outlet 18. Recesses 19 and 20 are formed in the hydraulic line of the receiver channel to stabilise fluid flow in its branched hydraulic line. The plate stack of the receiver channel block has additional outlets 21 for utilising the peripheral parts of the main jet.

The proposed jet devices have chamber lengths ranging from 2 to 4 mm. The nozzle outlet diameters are 0.2–1.0 mm. The receiver channel dimensions are 0.3–0.8 mm. The device parts are subjected to high-pressure fluid flows with velocities reaching 200 m/s and above.

The set of control components comprises various jet devices. They have nozzles with openings of different shapes that form corresponding jets (Fig. 5a).

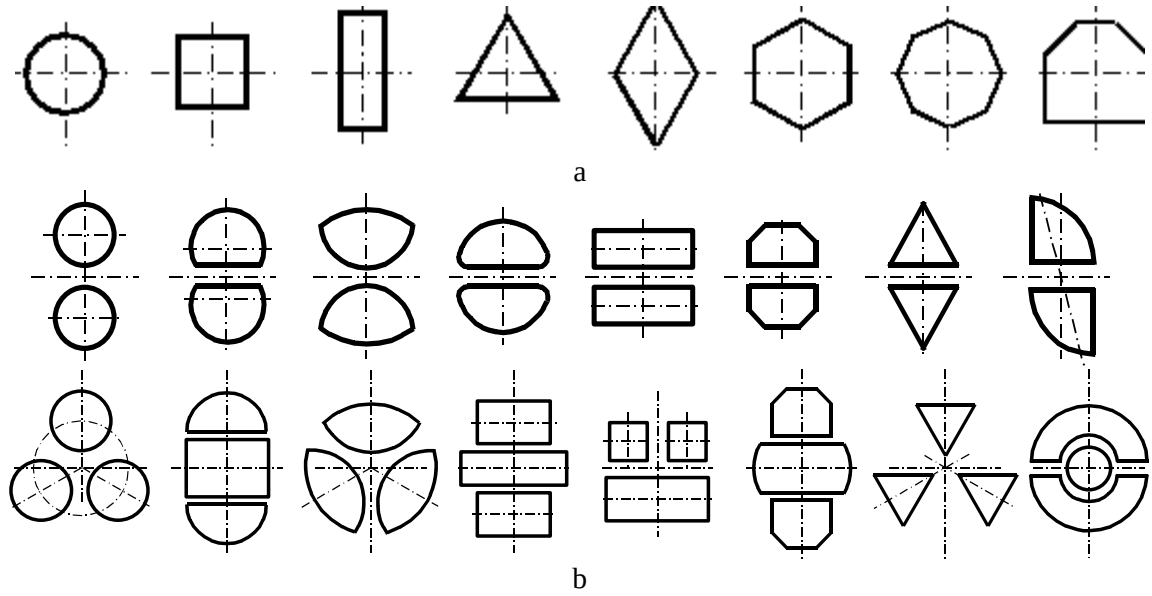


**Fig. 5. Typical shapes of outlet openings: (a) small nozzle devices (approximately 1 mm in size); (b) receiver channel systems.**

A symmetrical pair of receiver channels in a jet device is generally formed by two openings of identical size and shape (Fig. 5b). A system of three receiver channels can be symmetrical about two axes or have axial symmetry about three or more axes. A system of four or more receiver channels is generally arranged symmetrically about two mutually perpendicular planes. Devices with more than four receiver channels are also used.

**Formation of Finite-Volume Vortex Flows and High-Pressure Vortex Devices**

To improve the efficiency of high-pressure jet devices, innovative methods have been proposed for forming jets with isolated, periodic, high-pressure vortex flows of finite volume incorporated into them. These finite-volume flows take the form of a spatial dipole [28], a vortex ring, or a vortex filament.

A vortex ring is formed in an annular gap through which fluid flows. An additional pulsed fluid flow is introduced into and withdrawn from this flow (Fig. 6).

Fluid flows through the annular gap at a flow rate $Q_0$ (Fig. 6). Let us assume that the fluid particle velocities $V_0$ are parallel to the $x$-axis and that the velocity profile $V_0(y)$ in the annular gap is nearly uniform, with sharply varying regions at the walls corresponding to the boundary layers.

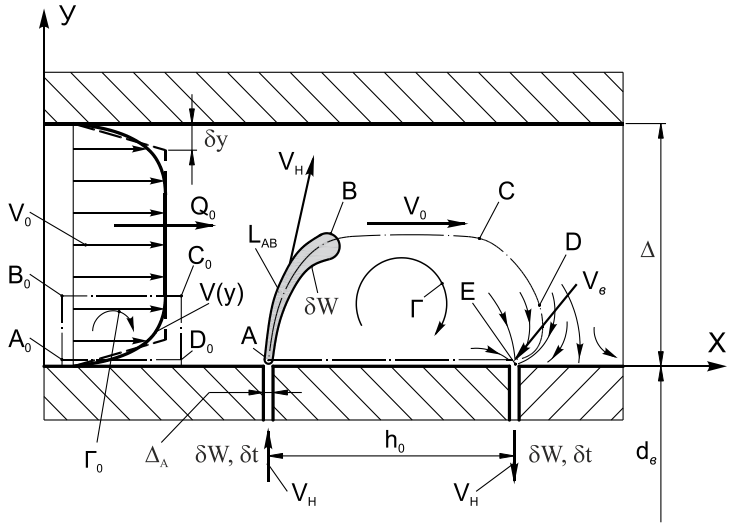



**Fig. 6. Schematic diagram of the formation of an isolated vortex in an annular gap.**

The presence of boundary layers gives rise to a region of vortex formation (a vortex sheet) at the walls of the annular gap. This occurs in both laminar and turbulent fluid flow. Vortex formation is most intense in the fluid layers adjacent to the solid walls. Therefore, for the selected closed contour $A_0B_0C_0D_0$ near the wall, the velocity circulation around the contour is determined by the velocity along segment $B_0C_0$ and is given by

$$\Gamma_0 = \oint VdL \approx V_0 \cdot B_0 \cdot C_0. \quad (1)$$

For a contour of unit length $B_0C_0 = 1$, we obtain $\Gamma_{01} = V_0 \cdot 1$.

The flux of the curl of velocity through the surface bounded by this contour is determined by the surface integral

$$\int_s rotVds = \Gamma_0 = \int_s 2\omega dS = (rotV)_0 S = 2\omega_0 \cdot S, \quad (2)$$

where $S$ is the area of the surface bounded by the contour, $S = A_0B_0 \cdot B_0C_0$; $\omega_0$ is the mean angular velocity of rotation of the fluid particles; and $(rotV)$ is the local value of the curl of velocity within the contour.

The circulation $\Gamma_0$ around the contour, described by equation (1), depends on the dimensions of the contour $A_0B_0C_0D_0$. In the region corresponding to the boundary layer, at small values of the contour height $A_0B_0 = C_0D_0$, the circulation increases as the velocity $V(y)$ increases. For simplicity, let us assume that the velocity profile is approximately trapezoidal within the boundary layer of thickness $\delta y$. Within the boundary layer, the velocity circulation then increases linearly, while outside it the circulation remains constant. Thus, for a contour of unit length $B_0C_0 = 1$

$$\Gamma_{01} = \begin{cases} V_0 \cdot y / \delta y & for\ y \le \delta y \\ V_0 & for\ y > \delta y \end{cases} \quad (3)$$

Thus, a steady vortex motion of the fluid exists in the annular gap. It is concentrated near the solid walls and has a stable vorticity corresponding to the velocity circulation per unit length $\Gamma_{01}$.

Let us select a toroidal control volume with a radial cross-section $ABCDE$ in the annular gap. Points $A$ and $E$ of this volume correspond to the positions of the outlet openings of small radial slots. Through these slots, a pulsed fluid flow of volume $\delta W$ is introduced into and withdrawn from the annular gap over a time interval $\delta t$, starting at time $t_0$. Before time $t_0$, the velocity circulation around contour $A...E$ is determined solely by the flow in the annular gap and is equal to $\Gamma_0 = h_0V_0$. The sign of the circulation corresponds to the clockwise rotation of fluid particles within the selected contour, as indicated by arrow $\Gamma$.

During a short time interval $\delta t$, a fluid volume $\delta W$ enters the annular gap through slot $A$. The mean fluid flow rate through the slot is

$$Q = \frac{\delta W}{\delta t}, \quad (4)$$

and the mean velocity of the fluid particles in the slot cross-section is

$$V_H = \frac{Q}{S_A},$$

where $S_A = \Delta_A \cdot \pi d_B$ is the cross-sectional area of the slot, $\Delta_A$ is the slot width, and $d_B$ is the insert diameter.

The slot is oriented perpendicular to the channel wall. The fluid particles moving through the slot acquire considerable kinetic energy. As the fluid leaves the slot and enters the annular gap, it forms a fan-shaped flow $AB$. This flow is acted upon by a perpendicular fluid flow in the annular channel with a velocity $V_0$. As a result, the fan-shaped flow is deflected, and its cross-section takes a parabolic shape corresponding to curve $AB$. Given the short time

required for the flow to form, it can be assumed that the fluid from the slot is concentrated in a narrow region whose width differs little from the slot width $\Delta_A$. Accordingly, the length of this region is

$$L_{AB} = \frac{\delta W}{\pi d_B \Delta_A} = \frac{\delta W}{S_A},$$

Let us assume that diffusion of the radial flow is negligible. Taking equation (4) into account, the velocity circulation along segment *AB* is then

$$\Gamma_{AB} = V_H \cdot L_{AB} = \frac{Q}{S_A} \cdot \frac{\delta W}{S_A} = \frac{\delta W^2}{S_A^2 \delta t}. \quad (5)$$

This estimate of the circulation establishes how individual parameters affect its magnitude. Equation (5) shows that increasing the circulation requires increasing the fluid volume $\delta W$, reducing the cross-sectional area of the slot, and increasing the response speed of the device supplying fluid to the slot.

This simplified approach was refined by taking into account the effect of the outflow at *E* in the annular gap. A flow model consisting of a source interacting with an incoming uniform fluid flow was used. According to this model, fluid entering slot *E* forms curved streamlines corresponding to contour *CDE*. A region of flow deceleration develops on the insert surface. Fluid entering slot *E* promotes rotational motion in the annular gap, increasing the overall vorticity of the flow.

Isolated vortices form periodically in the annular gap. As a result, a vortex system consisting of successive vortices is generated in the fluid flow. Several schematic and design solutions have been developed for devices that generate vortex systems. In particular, a design has been proposed for a jet device that forms a vortex system in the nozzle channel.

The device incorporated into the flow passage of the nozzle of a nozzle–flapper amplifier (Fig. 7) has a nozzle 1 with a conical bore and a cylindrical outlet section of diameter $d_c$. A sleeve 2 is located in the central part of the nozzle and is secured axially by a cover 3. The nozzle mounting bore of diameter $d_П$, together with the outer surface of the sleeve, forms an annular nozzle 4 and an annular receiver channel 5 of the jet device. Fluid is supplied to the annular nozzle through hydraulic line 6 at pressure $P_H$. A pressure $P_K$ develops at the outlet of channel 5 of the jet device. This pressure is determined, in particular, by the volume of the outlet cavity 7. Pressure $P_K$ reaches its maximum value $P_H$ when the distance between the outlet of annular channel 4 and the inlet of receiver channel 5 does not exceed four times the slot width of channel 4.

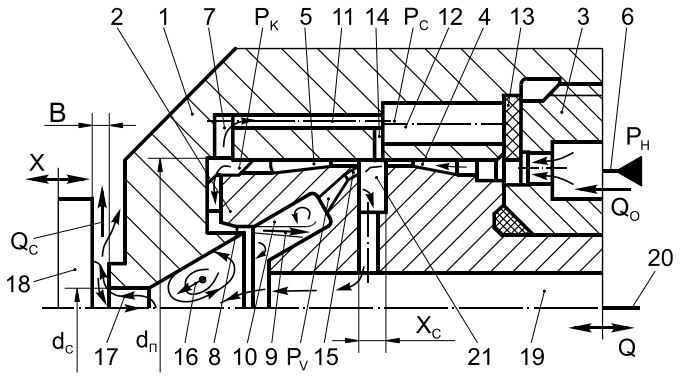



**Fig. 7. Design scheme of a vortex device incorporated into the flow passage of the nozzle of a nozzle–flapper amplifier: 1 – nozzle; 2 – sleeve; 3 – cover; 4 – annular nozzle; 5 – annular receiver channel; 6 – fluid supply line; 7 – outlet cavity; 8 – vortex-forming nozzle; 9 – fluid jet; 10 – conical vortex chamber; 11 – capillary channels; 12 – cavity; 13 – sealing gasket; 14 – control channel; 15 – annular outlet channel; 16 – direction of vortex movement; 17 – quasi-steady flow at the nozzle outlet and on the flapper surface; 18 – flapper; 19 – outlet opening; 20 – hydraulic line connecting to the second-stage amplifier; 21 – jet device chamber.**

Fluid from cavity 7 enters the vortex-forming nozzle 8 (Fig. 7). The fluid jet 9 leaving nozzle 8 creates a vortex flow with positive circulation in the conical vortex chamber 10. At the same time, fluid from cavity 7 passes through capillary channels 11 into cavity 12, which is sealed by a deformed gasket 13. The inertia of the fluid in capillary channels 11 and the compression of the fluid in cavity 12 cause a delay in the pressure rise $P_c$ in cavity 12. As pressure $P_c$ rises in control channel 14 of the jet device, the jet leaving annular nozzle 4 is deflected. The jet then enters annular outlet channel 15 instead of receiver channel 5.

An excess pressure $P_V$ develops at the outlet of channel 15 and exerts a force on the vortex formed in vortex chamber 10. Deflection of the jet leaving nozzle 4 causes pressure $P_K$ to drop at the outlet of receiver channel 5 in cavity 7. The presence of compressed fluid in cavity 7 somewhat slows this pressure drop. As pressure $P_K$ in cavity 7 decreases, the flow in nozzle 8 and jet 9 slows down. Under the action of pressure $P_V$, the vortex is expelled from chamber 10. It travels along the nozzle wall in the flow direction indicated by arrow 16.

Due to the inertia of the fluid in capillary channels 11 and the compression of the fluid in cavity 12, pressure $P_c$ in control channel 14 decreases with a certain delay. This ensures that the vortex formed in chamber 10 is completely expelled from the chamber. After the vortex is expelled, the control pressure $P_c$ drops to zero, and the fluid jet from annular channel 4 again enters receiver channel 5, creating an excess pressure $P_K$ at its outlet in cavity 7. The cycle of vortex formation in chamber 10 then repeats.

The nozzle design described above is used in a nozzle–flapper device. The resulting vortex ring moves along the wall of nozzle 1 in direction 16. As the vortex moves through the cylindrical section of the nozzle, it transforms into a high-pressure flow of ellipsoidal shape. This ellipsoidal flow merges with flow 17, which is in a quasi-steady state at the outlet opening and on the surface of flapper 18. The flows merge and undergo transformation.

Thus, flow 17 exists in a quasi-steady state in the gap between nozzle 1 and flapper 18. It reduces the effective flow area of the opening in nozzle 1 and, consequently, reduces the mean flow rate $Q_c$ through the nozzle–flapper device.

The reduction in the mean flow rate through the nozzle is equivalent to a reduction in its cross-sectional area. It was established that the flow rate decreases by a factor of 1.6–1.7. Accordingly, at equal flow rates, a nozzle in which vortex systems are generated has a diameter 2.5–2.8 times that of a nozzle in a device without vortices.

For example, a nozzle with a diameter $d_c$ = 0.5 mm in the presence of vortices is equivalent to a nozzle with a diameter $d_c$ = 0.3 mm used in existing nozzle–flapper devices. Increasing the diameter leads to a corresponding increase in the gap $B$ between the nozzle end face and the flapper. This substantially reduces the sensitivity of the device to contaminants in the working fluid.

The nozzle has an outlet opening 19 connected to the second-stage amplifier through hydraulic line 20. The pressure $P$ and flow rate $Q$ in this line are the nozzle output parameters, which depend on the displacement x of flapper 18. Given the high frequency of vortex formation and passage through the nozzle opening, the output parameters $P$ and $Q$ remain practically constant over time (quasi-static). The proposed device design essentially combines a throttle and a nozzle–flapper device. Annular nozzle 4 acts as the throttle. The pressure in chamber 21 of the jet device is practically the same as the output pressure $P$.

This provides a nozzle–flapper device in which the fluid flow contains periodic high-pressure vortex flows of finite volume.

A specific feature of this device is its considerably lower sensitivity to working fluid contamination. An additional advantage is its reliable operation at low temperatures. Increasing the minimum flow area of the nozzle improves the reliability of the device when the working fluid thickens at low temperatures. The jet components of hydraulic control systems require optimal geometry of the flow passages in the jet devices. The geometry was optimised on the basis of studies of the fluid flow processes.

**Study of the Features of Hydrodynamic Working Processes in Jet Devices of Hydraulic Control Systems**

The working processes were studied through numerical flow calculations supplemented by a wide range of experimental studies. The calculations were performed by integrating the Navier–Stokes equations using the finite element method [28]. The flow patterns in a deflector-type jet device were determined (Fig. 8).

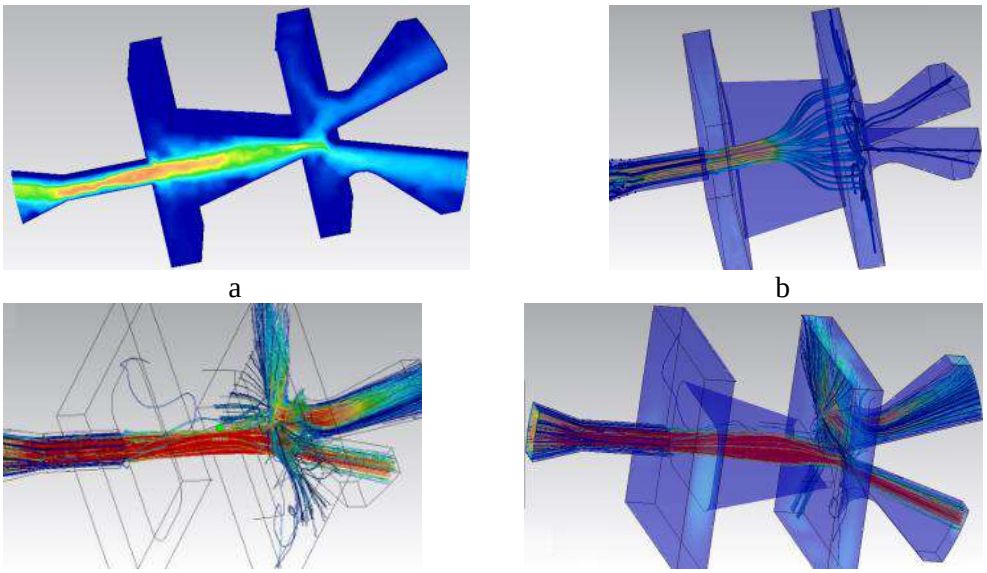



**Fig. 8. Results of numerical flow calculations for a deflector-type jet device: (a) distribution of the fluid particle velocity magnitude in the plane of symmetry of the device; (b) streamline pattern during jet deflection by the deflector; (c) trajectories of individual fluid particles in the region between the deflector and the receiver channels; (d) overall visualisation of the three-dimensional flow.**

The calculations showed that the compact jet at the nozzle outlet exhibits static instability (Fig. 8a). This is caused by the presence of a section of constant cross-sectional area at the nozzle outlet. The boundary layers developing along the walls of this section narrow the uniform-velocity core of the flow at the nozzle outlet. The numerical calculations revealed specific features of the working processes, particularly the deformation of the jet as it interacts with the deflector surface (Fig. 8b). When the jet interacts with the receiver channels, which allow through-flow in these calculations, reverse flows from the channels into the chamber are observed (Fig. 8c).

The calculations showed that the deformed jet has low-power peripheral regions that do not enter the receiver channels but spread over the end face. Analysis of the fluid particle trajectories in the three-dimensional flow within the jet device indicates the presence of fluid flows in different directions in the region between the deflector and the receiver channels (Fig. 8d).

The numerical calculations identified qualitative features of the working processes and characteristic flow regions that were subsequently studied in greater detail. These include the jet flow at the nozzle outlet, the interaction of the jet with the deflector, the flow in the receiver channels, and the reverse flows formed in the receiver channels. All these regions contain singular flow regions where the stress tensor and the rate-of-strain tensor become degenerate.

**Singular Flow Regions**

The analysis of singular regions is based on experimental flow studies using visualisation in a planar model device. In particular, a jet entering a chamber was studied. The jet entrains the surrounding fluid in the chamber and expands (Fig. 9a).

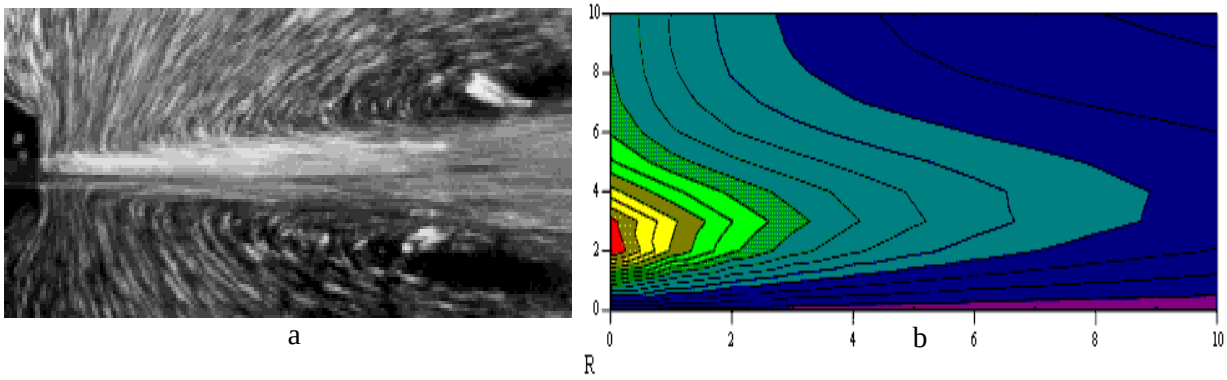



**Fig. 9. Experimental flow visualisation: (a) flow around a jet propagating in a chamber; (b) calculated distribution of the magnitude of the curl of velocity at the jet boundary, represented by vorticity contours.**

A specific feature of the flow is the singular region at the nozzle edge. In this region, the stress tensor and the rate-of-strain tensor become degenerate. In the experiments, this manifests itself in vortex and cavitation phenomena near the nozzle edge. The calculated value of vorticity (the curl of velocity) was used to quantitatively assess changes in the hydrodynamic parameters of the fluid in this region (Fig. 9b).

The flow in the singular region was studied analytically.

The following method was developed for analysing differential equations at singular points. At a singular point, the fluid particle velocity vector $\vec{v} \cong 0$, and, accordingly, the velocity components along the coordinate axes *x*, *y*, and *z* are:

$$v_x \cong v_y \cong v_z \cong 0.$$

The velocity components are functions of the coordinates:

$$\frac{dx}{dt} = v_x(x,y,z),\ \frac{dy}{dt} = v_y(x,y,z),\ \frac{dz}{dt} = v_z(x,y,z). \tag{6}$$

Let us expand functions (6) in a Taylor series, retaining the linear terms:

$$\begin{aligned} v_x &= \varepsilon\left(\frac{\partial v_x}{\partial x}\right)\Big|_0 x + \varepsilon\frac{\partial v_x}{\partial y}\Big|_0 y + \varepsilon\frac{\partial v_x}{\partial z}\Big|_0 z + 0(\varepsilon) \\ v_y &= \varepsilon\left(\frac{\partial v_y}{\partial x}\right)\Big|_0 x + \varepsilon\frac{\partial v_y}{\partial y}\Big|_0 y + \varepsilon\frac{\partial v_y}{\partial z}\Big|_0 z + 0(\varepsilon)\ \ (\varepsilon \to 0). \\ v_z &= \varepsilon\left(\frac{\partial v_z}{\partial x}\right)\Big|_0 x + \varepsilon\frac{\partial v_z}{\partial y}\Big|_0 y + \varepsilon\frac{\partial v_z}{\partial z}\Big|_0 z + 0(\varepsilon) \end{aligned} \tag{7}$$

The matrix of coefficients of series (7) has the form:

$$K = \begin{vmatrix} \frac{\partial v_x}{\partial x}\Big|_0 & \frac{\partial v_x}{\partial y}\Big|_0 & \frac{\partial v_x}{\partial z}\Big|_0 \\ \frac{\partial v_y}{\partial x}\Big|_0 & \frac{\partial v_y}{\partial y}\Big|_0 & \frac{\partial v_y}{\partial z}\Big|_0 \\ \frac{\partial v_z}{\partial x}\Big|_0 & \frac{\partial v_z}{\partial y}\Big|_0 & \frac{\partial v_z}{\partial z}\Big|_0 \end{vmatrix}. \tag{8}$$

The rate-of-strain tensor of the fluid $\dot{S}$ [28] is defined as:

$$\dot{S} = \begin{bmatrix} \frac{\partial V_x}{\partial x} & \frac{1}{2}\left(\frac{\partial V_y}{\partial x} + \frac{\partial V_x}{\partial y}\right) & \frac{1}{2}\left(\frac{\partial V_z}{\partial x} + \frac{\partial V_x}{\partial z}\right) \\ \frac{1}{2}\left(\frac{\partial V_x}{\partial y} + \frac{\partial V_y}{\partial x}\right) & \frac{\partial V_y}{\partial y} & \frac{1}{2}\left(\frac{\partial V_z}{\partial y} + \frac{\partial V_y}{\partial z}\right) \\ \frac{1}{2}\left(\frac{\partial V_x}{\partial z} + \frac{\partial V_z}{\partial x}\right) & \frac{1}{2}\left(\frac{\partial V_y}{\partial z} + \frac{\partial V_z}{\partial y}\right) & \frac{\partial V_z}{\partial z} \end{bmatrix}. \quad (9)$$

Let us assume that the fluid flow in the singular region is irrotational. Accordingly:

$$rot\vec{V} = 0. \quad (10)$$

From (10), we obtain the relations:

$$\frac{\partial V_z}{\partial y} = \frac{\partial V_y}{\partial z}, \quad \frac{\partial V_x}{\partial z} = \frac{\partial V_z}{\partial x}, \quad \frac{\partial V_y}{\partial x} = \frac{\partial V_x}{\partial y}. \quad (11)$$

Substituting (11) into (9), we obtain the matrix of the rate-of-strain tensor in the form:

$$\dot{S}_{\omega=0} = \begin{bmatrix} \frac{\partial V_x}{\partial x} & \frac{\partial V_x}{\partial y} & \frac{\partial V_x}{\partial z} \\ \frac{\partial V_y}{\partial x} & \frac{\partial V_y}{\partial y} & \frac{\partial V_z}{\partial z} \\ \frac{\partial V_z}{\partial x} & \frac{\partial V_z}{\partial y} & \frac{\partial V_z}{\partial z} \end{bmatrix}. \quad (12)$$

Comparison of matrices (8) and (12) shows that matrix K corresponds to the matrix of components of the rate-of-strain tensor $\dot{S}$.

For a Newtonian fluid, there is a linear relationship between the stress tensor P and the rate-of-strain tensor $\dot{S}$:

$$P = a\dot{S} + bE,$$

where $a$ and $b$ are scalars; $\mathbf{a} = 2\mu$, where $\mu$ is the dynamic viscosity of the fluid; and $E$ is the identity tensor.

Therefore, degeneracy of the rate-of-strain tensor corresponds to degeneracy of the stress tensor.

To determine the principal components of the rate-of-strain tensor $\dot{S}$, which correspond to the eigenvalues of the matrix, we obtain the characteristic equation:

$$\det\left|A - \lambda E\right| = 0, \quad (13)$$

where $E$ is the identity matrix.

The coefficients of equation (13) do not depend on the choice of coordinate system and are invariants of the rate-of-strain tensor $\dot{S}$.

Let us analyse the eigenvalues of matrix $K$, which coincide with the principal components of the rate-of-strain tensor (12) and, accordingly, of the stress tensor in the fluid. If all eigenvalues are positive, $\lambda_1 > 0$, $\lambda_2 > 0$, $\lambda_3 > 0$, an unstable node is obtained. If $\lambda_1 > 0$, $\lambda_2 < 0$, $\lambda_3 < 0$, a three-dimensional flow of the stable saddle type occurs. This type of flow occurs in the singular region at the nozzle edge. In this region, fluid from the jet and the surroundings moves in the $z$-direction (Fig. 10a).

An elementary fluid particle flowing near a stable saddle is deformed (Fig. 10b) and loses its continuity due to cavitation. More complex singular regions occur in the receiver channels

(Fig. 10c). Singular regions largely determine the overall flow parameters in jet devices. These regions were identified through experimental studies.

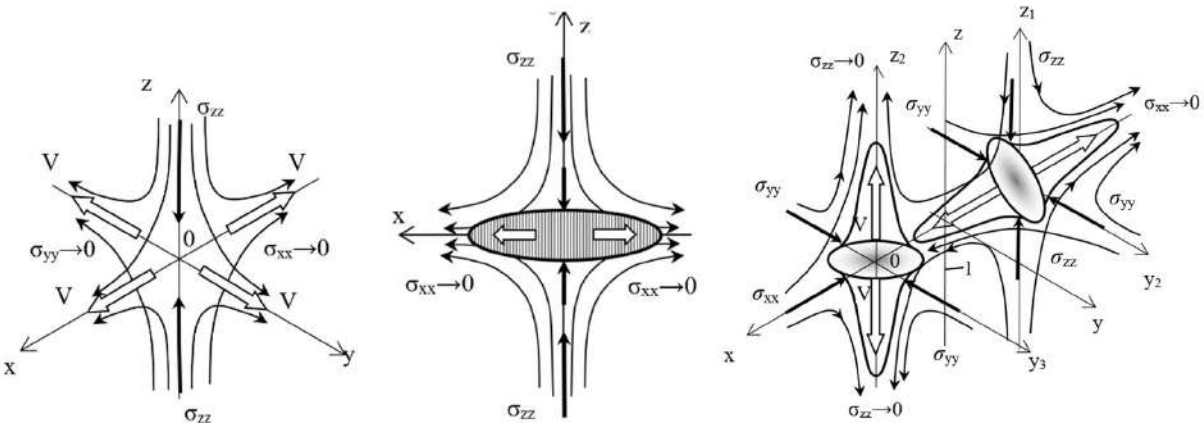



**Fig. 10. Schemes of flow and fluid particle deformation in singular regions: (a) three-dimensional representation of a stable saddle-type flow near the nozzle edge when the stresses σxx and σyy instantaneously drop to zero; (b) deformation of a fluid particle in this region; (c) scheme of deformation of elementary fluid particles in a singular region corresponding to two mutually perpendicular lines of expansion.**

### Experimental Flow Studies and Features of the Working Processes in Jet Devices

The interaction of the jet with the deflector produces a complex flow pattern with vortex zones 2 and critical points 3 and 4 on the deflector walls (Fig. 11a).

The jet is compressed, forming jet 5, and intense reverse flows develop, bounded by streamlines 6, 8 and 7, 9. Flows 10 initiate vortex zones 11. Jet compression causes deformation of the outlet velocity profile. In the two-dimensional problem considered, the fluid particles accelerate near the deflector walls. This is reflected in changes in velocity profile 12.

The calculation results were confirmed experimentally (Fig. 11b). The photograph shows singular regions of the stable saddle type that occur on the deflector walls.

The three-dimensional flow in the region of interaction between the jet and the deflector was studied experimentally. It was established that the interaction of a round or square jet with a flat deflector changes the jet shape to an elliptical (oval) form. The jet dimensions in the direction perpendicular to the deflector edge increase by a factor of 2–3.

Theoretical (Fig. 12a) and experimental studies of the interaction between the jet and the receiver channel were carried out.

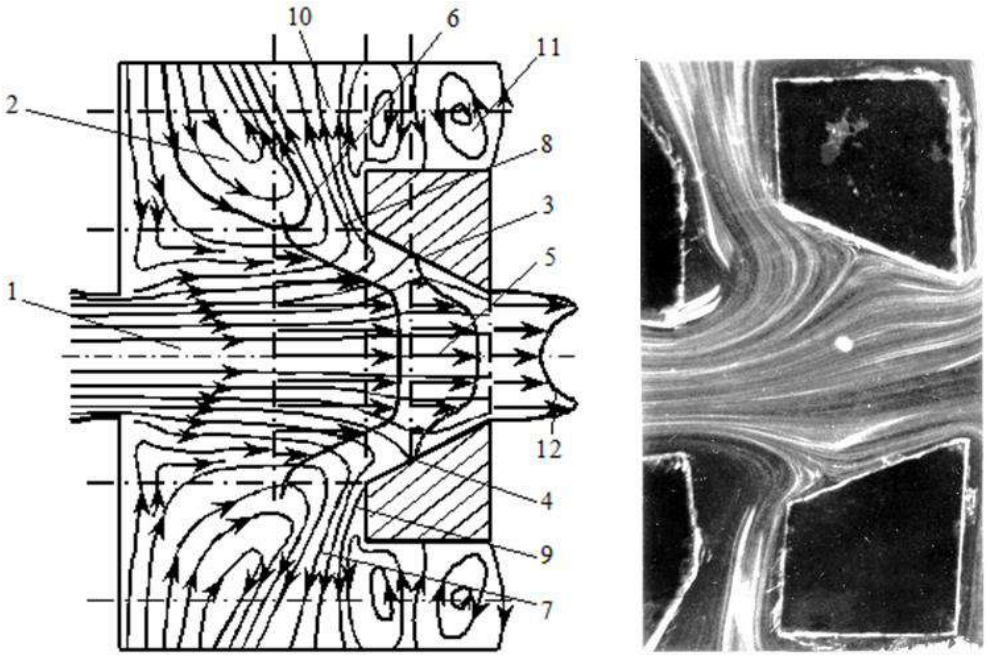
Jet 1 entering the channel initiates an opposing fluid flow 2. The jet turns in region 3, forming reverse flows 4 outside the channel. Vortex regions 5 form in the receiver channel. At the channel inlet, velocity profile 6 changes sign, and the net fluid flow rate through the inlet cross-section is zero. A singular flow region of the stable saddle type occurs at the interface between flows 1 and 2 in the centre of the channel (Fig. 10a).

The calculated flow pattern was confirmed experimentally (Fig. 12b). The singular region manifests itself in the almost complete stopping of fluid particles.

The interaction of a jet with two receiver channels was studied, including by experimental methods. Intense vortex formation occurs in the flow passages of the receiver channels, where singular flow regions are also present (Fig. 13a).

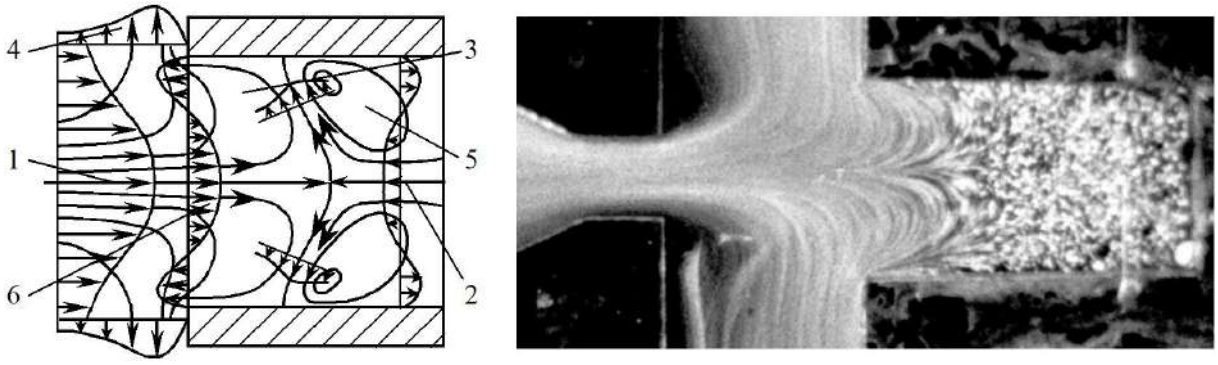
Singular flow regions corresponding to the intersection of two mutually perpendicular lines of expansion occur at the edges of the receiver channels (Fig. 10c).

Non-circular turbulent jets are mainly used in high-pressure jet devices. These jets were studied experimentally (Fig. 14).




a b

**Fig. 11. Interaction of a jet with a converging deflector: (a) calculated streamlines and velocity profiles; (b) photograph of the visualised flow in the model device; 1 – incoming jet; 2 – vortex zones; 3, 4 – critical points on the deflector walls; 5 – compressed jet; 6, 8 and 7, 9 – streamlines bounding the reverse flows; 10 – flows initiating vortex zones 11; 12 – velocity profile at the deflector outlet.**




a b

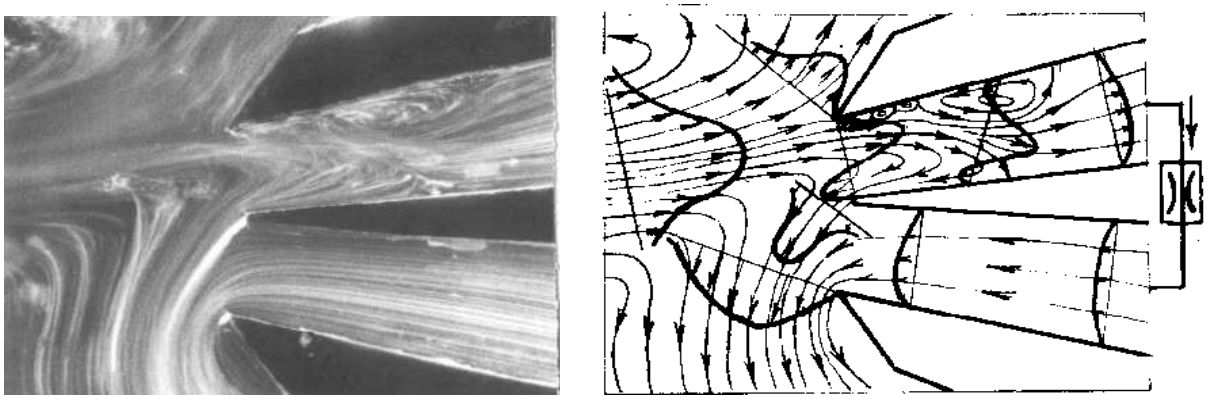
**Fig. 12. Interaction of a jet with a receiver channel without through-flow: (a) calculated streamline pattern and velocity profiles; (b) photograph of the visualised flow; 1 – incoming jet; 2 – opposing fluid flow; 3 – region where the jet turns; 4 – reverse flows outside the channel; 5 – vortex regions in the receiver channel; 6 – velocity profile with a change of sign at the channel inlet.**

The nature of the flow determines the device characteristics and the surface wear of its parts. The flow features were identified from the surface wear of the parts, and a three-dimensional diagram of the fluid flows in the region where the jet enters the receiver channels was constructed (Fig. 15).

The oval jet *Sc* formed at the deflector outlet splits into two forward flows $\Pi_N$ and $\Pi_V$, which are associated with two symmetrical parts of the vortex filaments $\Omega_1$ and $\Omega_2$ formed in the jet deflected by the deflector. The intensity of vortex filaments $\Omega_1$ and $\Omega_2$ is low, and the helical motion in flows $\Pi_N$ and $\Pi_V$ rapidly decays. The upper forward flow $\Pi_V$ and the lower forward flow $\Pi_N$ enter receiver channels 2 and 1, respectively, penetrate to a small depth, and then turn back, forming a system of three-dimensional reverse flows.

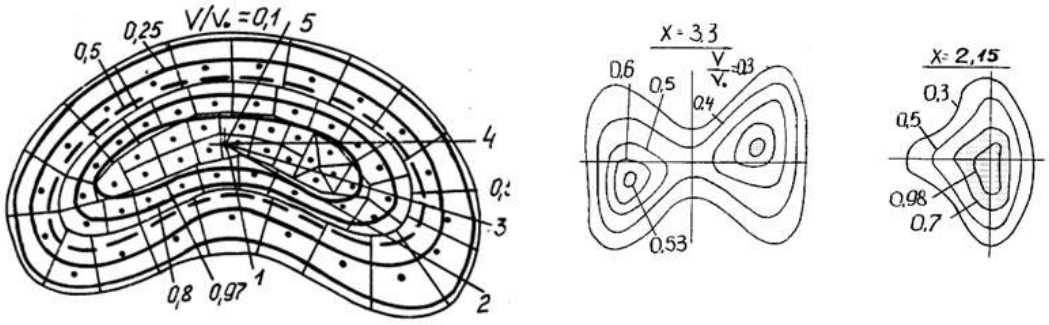
The lower forward flow $\Pi_N$ forms two localised forward flows $P_{N1}$ and $P_{N2}$ in receiver channel 1. These flows then spread over the surface of the lower sleeve $W_N$, causing abrasive

wear and forming wear recesses $V_{N1}$ and $V_{N3}$ on the surface. Reverse flows $Z_{N2}$ and $Z_{N4}$ are similarly formed in channel 1.



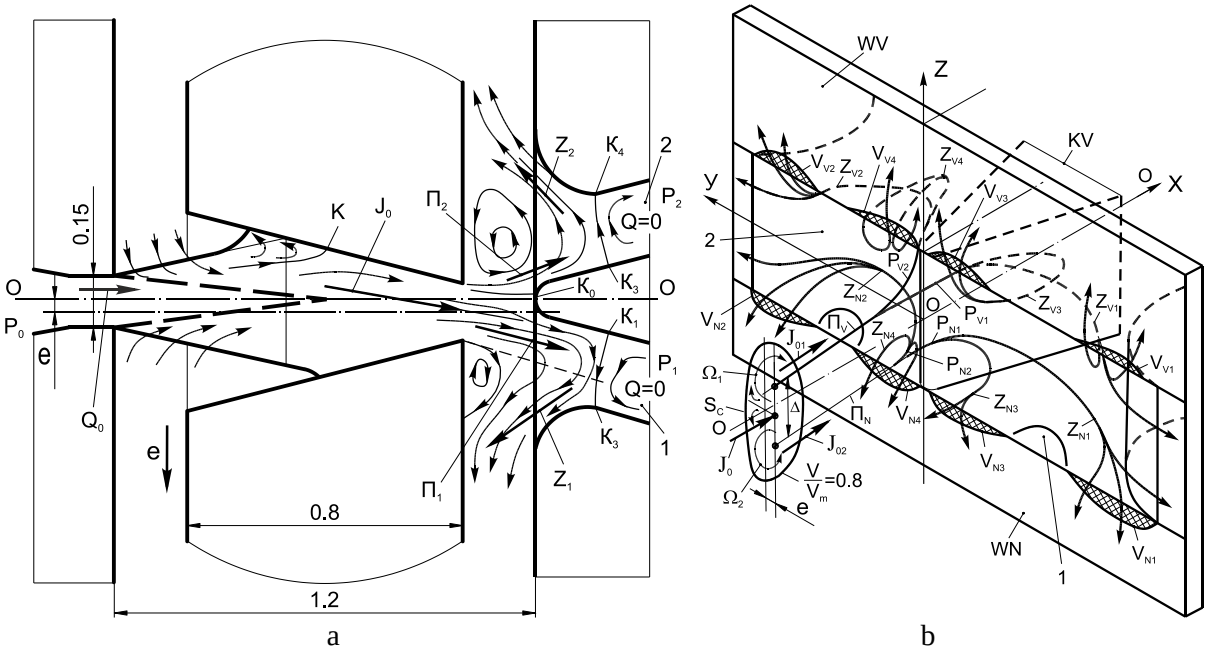
a b

**Fig. 13. Interaction of a jet with two receiver channels: (a) photograph of the visualised flow; (b) corresponding diagram of streamlines and velocity profiles.**




a b c

**Fig. 14. Results of experimental measurements of velocity distributions in the cross-sections of non-circular turbulent jets: (a) segment-shaped jet; (b) pair of jets; (c) T-shaped jet.**




a b

**Fig. 15. Flow diagram in the middle cross-section of the jet device (a) and locations of three-dimensional flows at the end face of the receiver channels, determined from surface wear (b); Sc – oval jet at the deflector outlet; ПN, ПV – lower and upper forward flows; Ω₁, Ω₂ – vortex filaments; PN1, PN2, PV1, PV2 – localised forward flows; ZN1–ZN4, ZV1–ZV4 – reverse flows; VN1–VN4, VV1–VV4 – surface wear regions; WN, WV – lower and upper sleeves; KV – wedge-shaped protrusion; O – region in the middle part of the protrusion.**

The upper forward flow $П_V$ of jet $S_c$ also splits into $P_{V1}$ and $P_{V2}$, which subsequently turn back as reverse flows $Z_{V1}$, $Z_{V3}$, $Z_{V4}$ and $Z_{V2}$. These reverse flows form wear regions $V_{V1}$, $V_{V3}$, $V_{V4}$ and $V_{V2}$. The reverse flows near the tip of the wedge-shaped protrusion $K_V$, namely $Z_{N3}$, $Z_{N4}$, $Z_{V3}$ and $Z_{V4}$, act not only on the surfaces of sleeves $W_V$ and $W_N$ but also on the edge of the wedge-shaped protrusion $K_V$. Therefore, the tip of the wedge-shaped protrusion is worn over its entire height. In the middle part of the protrusion (region $O$), in addition to the reverse flows, forward flows $П_N$ and $П_V$ act on the wedge tip. The tip divides these flows into $P_{N1}$ and $P_{N2}$, and $P_{V1}$ and $P_{V2}$.

The forward and reverse flows shown in the figure form cyclically in accordance with the cyclic movement of the deflector. The total number of cycles was 10 million. Therefore, the surface wear of the jet device parts results from the cumulative action of the entire system of high-pressure jets and flows occurring in the region of the receiver channels. Accordingly, the identified three-dimensional flow diagram represents an integrated average flow pattern corresponding to the fluid flow in the jet device averaged over the cycles.

The results of the working process studies provided the basis for determining the static characteristics of the jet devices.

**Static Characteristics of Jet Devices**

The characteristics were determined theoretically by solving the equations of fluid mechanics in integral form [28]. In its general form, the energy characteristic relates the pressures and flow rates at the device outlet and inlet:

$$\frac{p}{p_0} = \frac{p_m}{p_0} + \frac{p_m \cdot V}{k_3} \cdot V_0 \cdot p_m \cdot s_0 \cdot \frac{Q}{p_0 \cdot V_m \cdot Q_0} + k_4 \cdot \left( \frac{s_0 \cdot Q}{s \cdot Q_0} \right)^2, \quad (14)$$

where the constants depend on the device parameters.

In fully developed turbulent flows, energy losses depend mainly on the square of the velocity. Therefore, characteristic (14) takes the form:

$$\frac{p}{p_0} = \frac{p_m}{p_0} - k_2 \cdot \left( \frac{s_0 \cdot Q}{s \cdot Q_0} \right)^2. \quad (15)$$

Calculations using relationship (15) agree with the experimental data to within 5–8% for jet devices with different shapes of receiver channel openings (Fig. 16a, b).

The energy characteristics show saturation in the outlet fluid flow rate. This is caused by the limited energy of the jet formed in the nozzle and by cavitation processes in the receiver channels. If the ratio of the receiver channel area to the nozzle area is less than 2, the maximum pressure in the receiver channels reaches the pressure at the nozzle inlet.

It was established that jet devices remain operational when fluid flows out of the receiver channel at a rate exceeding the nozzle flow rate. This occurs during braking of the hydraulic drive actuators. The static characteristics of jet devices under these outflow conditions were determined for receiver channels of different sizes (Fig. 16c).

When the receiver channel area is limited, the device outlet pressure remains stable in the presence of outflow. Increasing the receiver channel area changes the shape of the characteristic. This leads to a change in the nature of the flow.

The shape of the characteristics depends on the dimensions and shape of the jet interaction chamber. Increasing the chamber length changes the shape of the characteristic (Fig. 16d). A chamber length of no more than eight times the nozzle size is recommended.

The control characteristics of the jet device were determined in terms of the outlet flow rate at zero outlet pressure and the outlet pressure at zero flow rate (Fig. 17a, b).

The flow-rate control characteristics of the device (Fig. 17b) depend only slightly on the deflector shape and are described by the expressions:

$$\frac{Q}{Q_m} = EXP\left[-\chi_Q \cdot \left(\frac{y_\partial}{d_0}\right)^2\right], \quad \frac{p}{p_m} = EXP\left[-\chi_p \cdot \left(\frac{y_\partial}{d_0}\right)^2\right]. \qquad (16)$$

where the constant values are $\chi_Q$ = 11.0–16.0 and $\chi_p$ = 10.0–15.0.

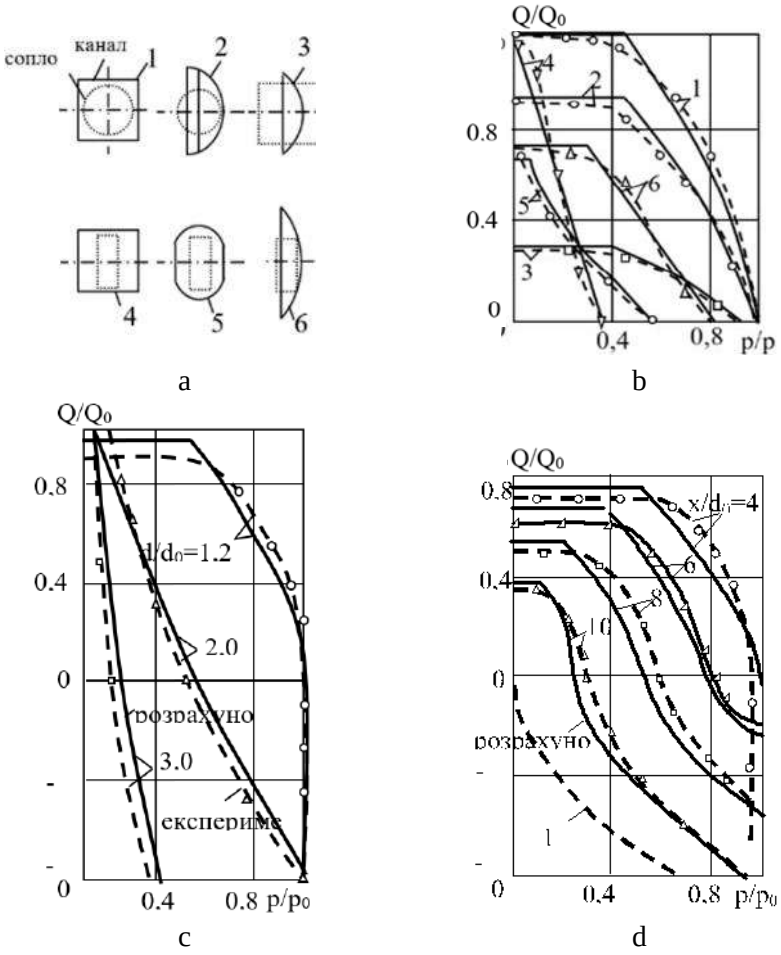



**Fig. 16. Schemes of jet devices with different nozzle and receiver channel shapes (a) and the corresponding energy characteristics: (b) device energy characteristics (curves 1–6), with the curve numbers corresponding to the receiver channel shapes numbered in diagram (a); (c) energy characteristics of a jet device with a flow rate that changes sign, for different ratios of receiver channel diameter to nozzle diameter; (d) effect of the jet interaction chamber length on the energy characteristics of the jet device.**

The energy characteristics of the devices (Fig. 18), measured at different fixed deflector positions, are affinely similar and correspond to the characteristic of the basic device.

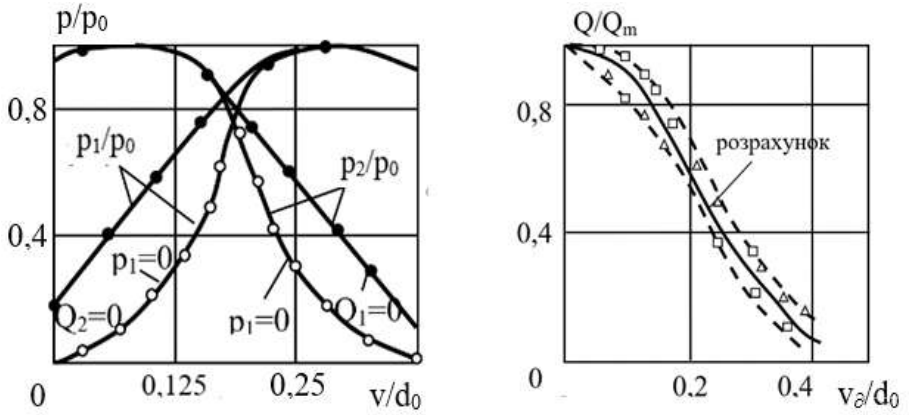
High-pressure jet devices were tested with different working media. It was established that their characteristics (14), (15), and (16) are practically independent of the chemical composition of the fluid. The tests were carried out using AMG-10 working fluid, which is typical of aircraft hydraulic drive systems.

Reliable operation of the jet devices was observed when industrial water and aqueous detergent solutions used for flushing hydraulic systems were employed as working fluids. Therefore, jet devices are recommended as components of hydraulic control systems for wheelless ground robotic complexes.

**Dynamic Characteristics of Jet Devices**

The dynamics of jet and vortex devices are determined by complex processes occurring in different frequency ranges. The jet device itself is a high-frequency device characterised by stochastic variations in its parameters. The dynamic properties of the jet device were studied

theoretically and experimentally. A special dynamic model accounting for the presence of undissolved air in the fluid was used (Fig. 19).




a b

**Fig. 17. Control characteristics of the jet device: (a) receiver channel pressures as functions of nozzle displacement; (b) outlet flow rate as a function of deflector displacement.**

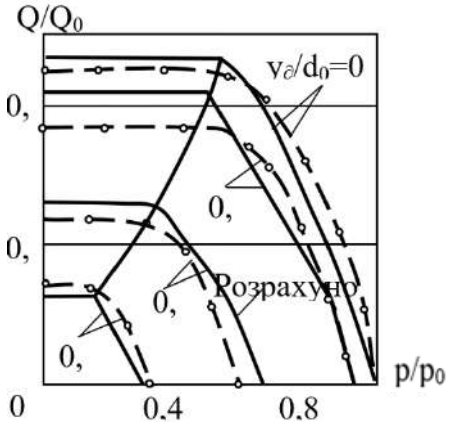



**Fig. 18. Energy characteristics of the jet device at different fixed deflector positions.**

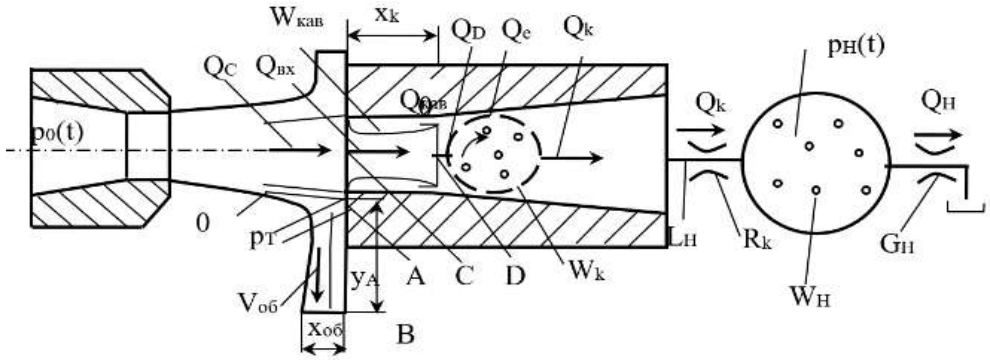


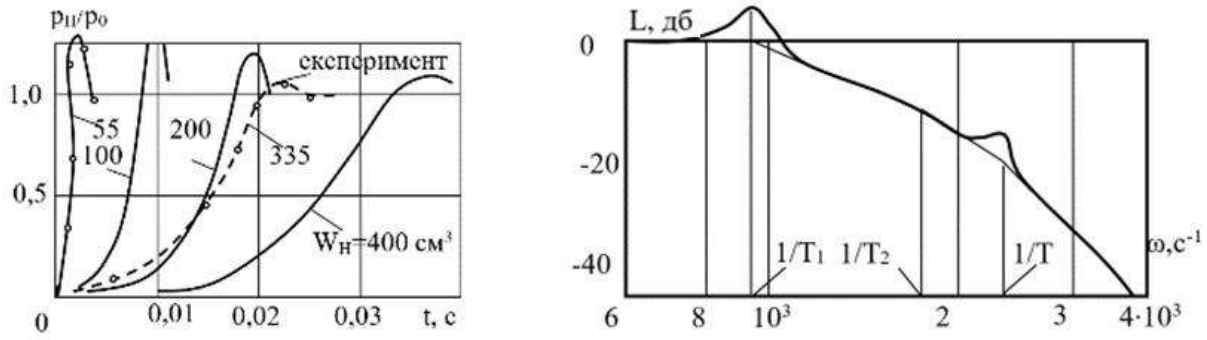

**Fig. 19. Dynamic model of a jet device with a hydraulic capacitance load.**

The overall transfer function of the system was determined using the dynamic model:

$$W_p(s)=\frac{p(s)}{p_0(s)}=\frac{k\cdot k_0\cdot(1-T_3\cdot s)\cdot(1-T_7\cdot s)}{(T_1\cdot s+1)\cdot(T_2^2\cdot s^2+2\xi\cdot T_2\cdot s+1)\cdot(T_3\cdot s+1)(T_8^2\cdot s^2+2\xi_k\cdot T_8\cdot s+1)}, \quad (17)$$

where $s$ is the Laplace operator.

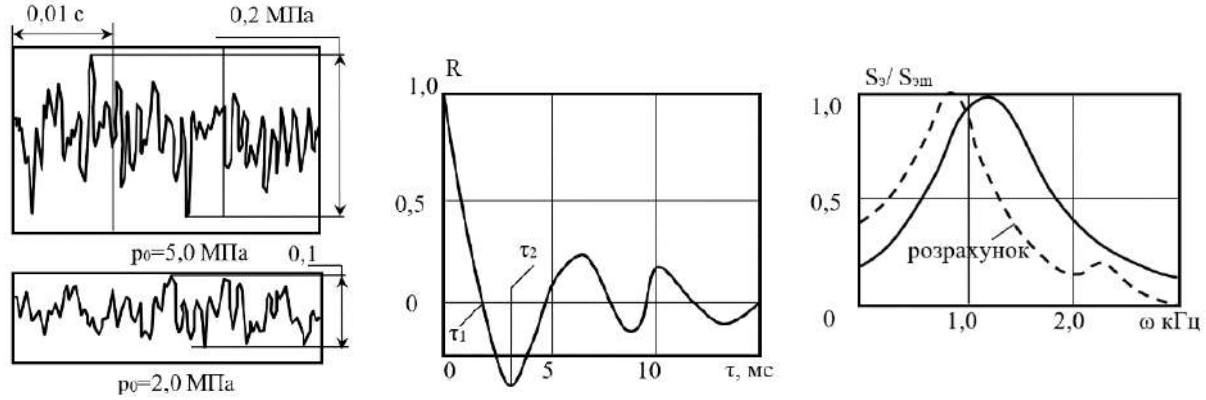
The frequency characteristics and transient responses were obtained from transfer function (17) (Fig. 20a), and the logarithmic amplitude–frequency characteristic of the jet device with a blocked receiver channel was plotted (Fig. 20b).




a b

**Fig. 20. Dynamic characteristics of the jet device: (a) transient responses for different volumes of the hydraulic capacitance load; (b) logarithmic amplitude–frequency characteristic of the device with a blocked receiver channel.**

Experimental studies of the dynamics were carried out using high-precision pressure sensors. Stochastic pressure fluctuations at the jet device outlet were determined (Fig. 21a).




a b c

**Fig. 21. Pressure fluctuations in a chamber connected to the jet device outlet and their statistical characteristics: (a) oscillographic records at supply pressures $p_0$ = 5.0 MPa (upper trace) and $p_0$ = 2.0 MPa (lower trace); (b) correlation function; (c) spectral density of pressure fluctuations.**

The experimental measurement results were processed using statistical methods and specialised software. Assuming that the random pressure fluctuations were stationary and ergodic, the correlation function (Fig. 21b) and the spectral density of the process (Fig. 21c) were determined by processing the oscillographic records.

The study results indicate that the high-pressure jet device has resonant frequencies of approximately 1 kHz. A chamber with a volume of 100 cm³ connected to the device outlet reduces the resonant frequency to 100 Hz.

**Technological Features of the Design and Manufacture of Jet and Vortex Devices for Hydraulic Control Systems**

High-pressure hydraulic jet devices are extremely small and are subjected to dynamic flows of fluid containing considerable contamination. Therefore, their flow passages are subject to wear. The effects of cavitation add to the dynamic action of the flow. Accordingly, these components require special techniques for machining the flow passages of jet devices. A number of design and manufacturing approaches have been proposed for producing nozzles with opening cross-sectional dimensions of 0.1–1 mm. Nozzles with non-circular openings are manufactured by plastic deformation or fitted with special cover plates (Fig. 22).

When necessary, small nozzles are assembled from separate parts (Fig. 23a). The flow passage of this nozzle is formed by wedge-shaped plates 3 pressed into body 1. At the nozzle ends, the plates are sealed with polymer 2. A cavity 4 is formed between the plates and the body, and pressurised fluid is supplied to it through openings 6. A flange 8 with a groove 7 is

provided at the nozzle edge. These serve to seal the inlet opening 9. Plates 3 form a conical channel with a polygonal opening. The equivalent diameter of the channel at its minimum cross-section is 0.3–0.5 mm.

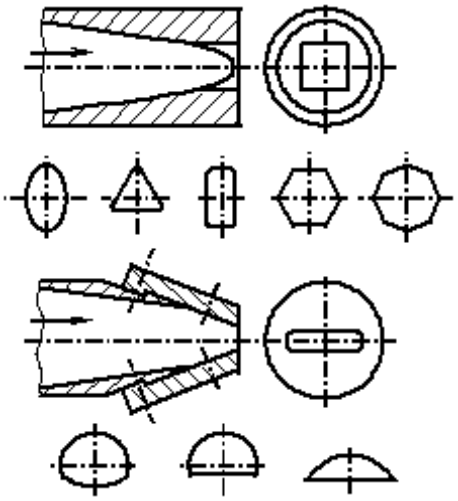


**Fig. 22. Schemes of nozzle devices with non-circular openings.**

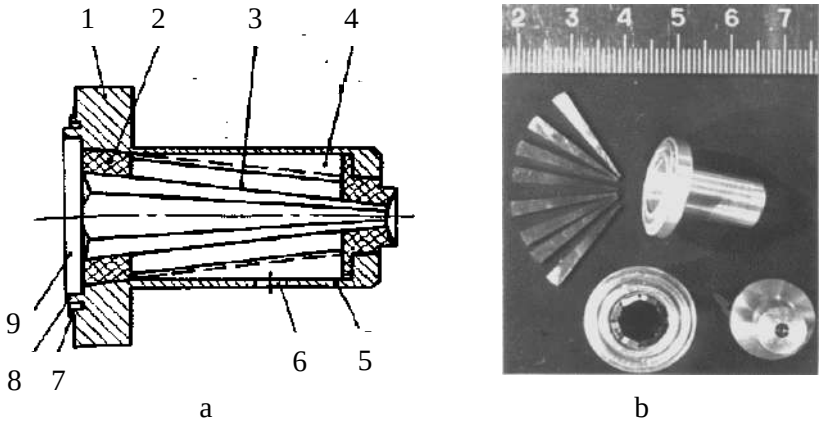



**Fig. 23. Assembled nozzle made of wedge-shaped plates: (a) design scheme; (b) nozzle parts and external appearance; 1 – body; 2 – polymer for sealing the plates; 3 – wedge-shaped plates; 4 – cavity between the plates and the body; 6 – fluid supply openings; 7 – sealing groove; 8 – flange; 9 – inlet opening.**

The plates (Fig. 23b) are made of 95Х18-Ш steel and heat-treated to a hardness of 62–64 HRC. The finishing operation involves grinding the working surface of the plate, with the grooves and ridges oriented along its length. Subsequently, the plates belonging to a particular nozzle or receiver channel are ground together in a stack to form a special microprofile on their side surfaces. The grooves of this side-surface microprofile are oriented perpendicular to the longitudinal axis of the plate. Micromilling methods were used in machining the plates [25, 29].

The microprofile of the working surfaces of the plates forming the nozzle flow passage has a system of longitudinal grooves. Therefore, as fluid flows at high velocity through the nozzle channel, boundary layers develop along the grooves and ridges of the microprofile. This flow is resistant to separation and transition to turbulence, which reduces energy losses in the nozzles. The anisotropy of this microprofile considerably increases nozzle wear resistance. Solid contaminant particles carried by the fluid at high velocity interact with the local ridges between the grooves. This causes local wear of the ridges and consequently improves the quality of the internal nozzle surface.

The slots between the plates are used to inject fluid into or withdraw it from the boundary layers on the nozzle surface. The fluid passes through the slots between the side surfaces of the plates. Fluid injection or suction substantially reduces flow separation in the nozzle channel.

An assembled nozzle with a rectangular opening cross-section was developed, consisting of two body parts with inserts (Fig. 24a).

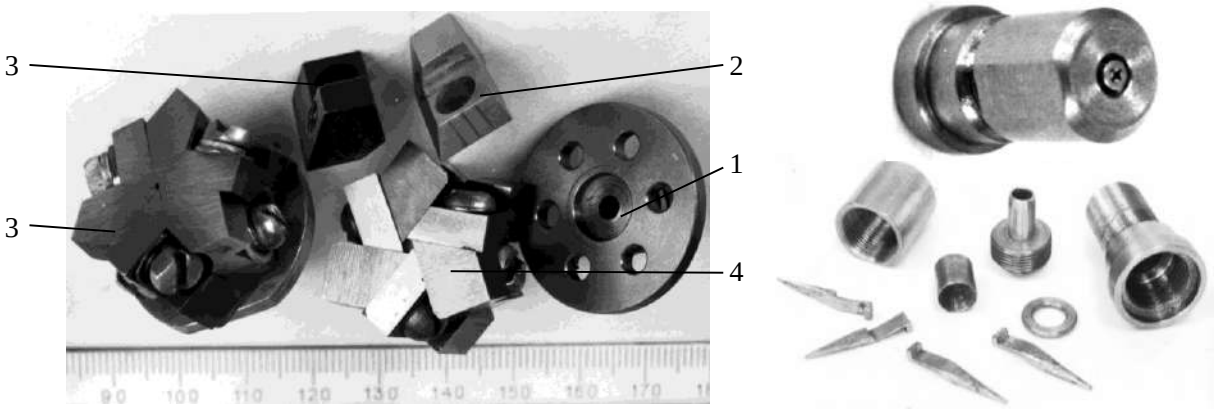


a b

**Fig. 24. External appearance and parts of assembled nozzle devices: (a) adjustable nozzle device with a rectangular outlet opening; (b) nozzle device with a curved channel.**

The nozzle size is adjusted by moving the inserts. A nozzle with a curved channel was manufactured in a similar way (Fig. 24b). The dimensions of the rectangular nozzle opening are (0.2–0.5) × 0.5 mm.

Nozzles with adjustable hexagonal opening dimensions are assembled on flange 1 from separate prismatic parts 2, 3, and 4 with high surface hardness (Fig. 25a).




a b

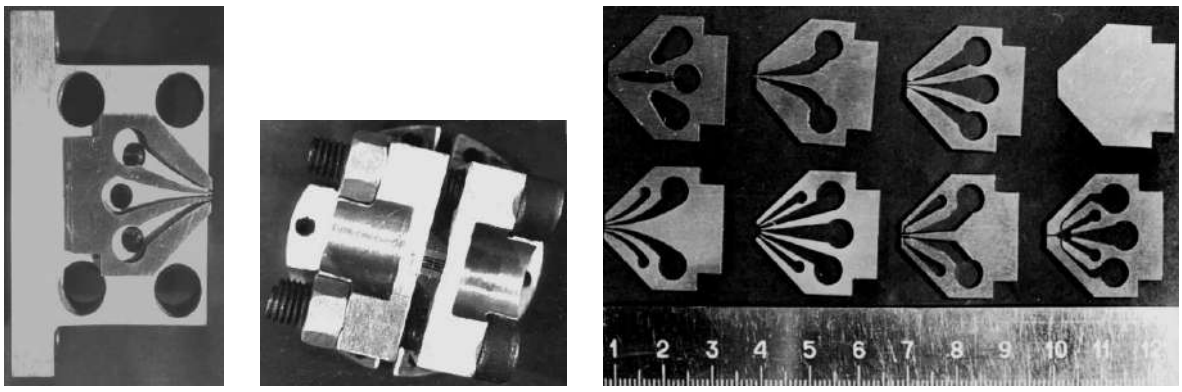
**Fig. 25. Assembled nozzle devices and their parts: (a) nozzle device with a hexagonal opening cross-section; (b) nozzle with a cross-shaped opening and a collet mechanism for adjusting its dimensions; 1 – flange; 2, 3, 4 – prismatic parts.**

A nozzle with a small cross-shaped opening has a collet mechanism for adjusting the opening dimensions (Fig. 25b). Manufacturing the receiver channels presents a complex technological problem.

Jet devices with rectangular receiver channel openings are constructed using a set of plates with shaped slots. The plates are placed between the flat surfaces of the body parts and sealed to form a stack (Fig. 26a, b).

The plate thickness is 0.08–0.2 mm, and the minimum slot width is 0.1–0.3 mm (Fig. 26c). Assembled receiver channels with non-circular openings were proposed and tested experimentally.

A nozzle device with two converging–diverging receiver channels separated by a spacer allows channels with segment-shaped openings to be formed (Fig. 27).



a b c

**Fig. 26. Design of a jet device with receiver channels formed by a stack of plates: (a) placement of a plate on a body part; (b) assembled device with eight channels with rectangular openings; (c) plates with shaped slots.**

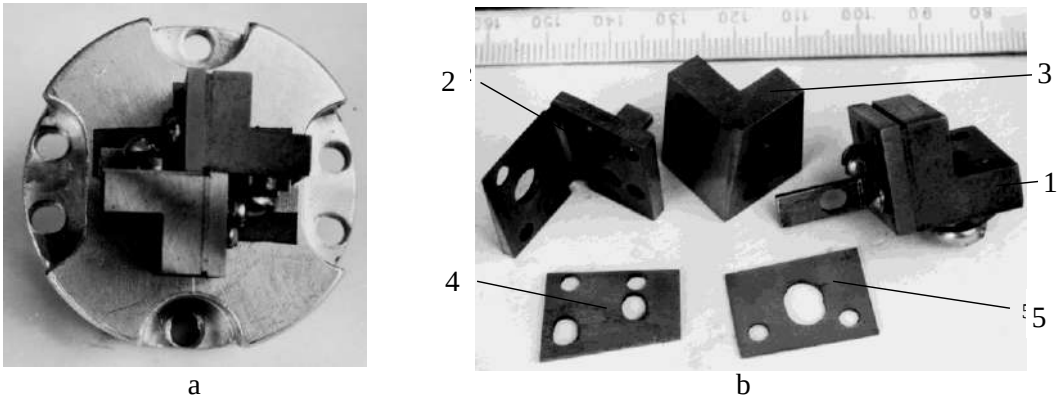


a b

**Fig. 27. External appearance and parts of receiver channel blocks with segment-shaped openings.**

The proposed designs allow adjustable receiver channels with opening dimensions of 0.1–0.5 mm to be manufactured from high-carbon chromium and chromium–molybdenum steels. Appropriate heat treatment provides a surface hardness of 62–65 HRC in the channel flow passages. This improves the operational reliability and service life of high-pressure jet devices.

The proposed assembled design of the receiver channels (Fig. 28) allows adjustment of the dimensions of their rectangular outlet openings.




a b

**Fig. 28. Receiver channel block with rectangular openings: (a) general view of the block; (b) block parts; 1, 3 – body parts; 2 – insert; 4, 5 – flat plates for adjusting the opening dimensions.**

The opening dimensions are adjusted by moving flat plates 4 and 5, with thicknesses of 0.2 and 0.5 mm, installed between body parts 1, 3 and insert 2. This device allows adjustment

of the rectangular opening dimensions within the ranges (0.2–0.5) × 0.5 mm and (0.1–1.0) × 0.2 mm.

## Discussion.

The use of industrial water as the working medium in hydraulic control systems for wheelless ground robotic complexes is a matter for discussion. The difficult operating conditions are undoubtedly an argument in favour of industrial water. On the other hand, the dimensions of wheelless robotic complexes and the specified loads require the use of high-pressure systems operating at 50–60 MPa. Such systems generally operate with mineral oil. The use of water is problematic. This problem is addressed by using high-pressure jet devices.

To improve efficiency, the cross-sectional areas of the channel and nozzle openings are minimised. The minimum cross-section is limited by the possibility of channel blockage. To prevent blockage, unsteady fluid flow incorporating periodic isolated three-dimensional vortices is proposed for the nozzle channels. These vortices are formed by pulsed fluid flows generated by resonant pulsation systems.

Another matter for discussion is the change in the energy balance of a jet device when vortex systems are introduced into its flow passage. Energy is expended on forming isolated vortices. Overall, the energy expenditure of the device increases. However, since the fraction of energy used to form vortices is small, only a slight reduction in the efficiency of the hydraulic control device should be expected. Most jet devices are flow-through devices. All the energy of the fluid flowing through the nozzle is lost. Therefore, introducing vortex systems does not change the overall energy balance of the device.

In most cases, vortex systems increase the mean equivalent hydraulic resistance of the device. This corresponds to a reduction in the fluid flow rate through the nozzle at constant pressure. The reduced flow rate decreases the power losses of the flow-through device. Therefore, the presence of vortex systems in the flow passage of a jet device will reduce the energy consumed by the hydraulic control jet device. This reduction depends on the design parameters and can be optimised.

Another matter for discussion is the usefulness of analysing singular flow regions in jet and vortex devices. The complexity of the hydrodynamic processes provides an argument in favour of such analysis.

Both laminarised and fully developed turbulent fluid flows occur in jet devices. However, the flow regimes are generally transitional. Laminar flow loses stability, and partial transition to turbulence occurs. Singular regions are present in all flow regimes. They are closely related to the flow boundary conditions and, accordingly, to the specific geometry of the jet devices. Singular regions characterise fundamental processes in fluid mechanics: blockage and cavitation. Therefore, analysing singular flow regions is useful and provides effective means of studying the features of the working processes and characteristics of jet devices.

## Conclusions.

1. Analysis of the specific operating conditions and the proposed design solutions for hydraulic control systems of wheelless ground robotic complexes showed that the use of conventional hydraulic control devices would significantly reduce the operational reliability and functionality of these systems. The main reason is the high contamination level and aggressiveness of the working medium, namely industrial water at pressures above 25 MPa.

2. To improve the operational reliability of wheelless robots, it is proposed to use specially developed high-pressure jet and vortex devices (20–30 MPa) as components of hydraulic control systems. These devices allow a working fluid filtration rating of 25–50 μm.

3. The components were developed on the basis of studies of the working processes in jet and vortex devices. Numerical studies of fluid flow parameters using the finite element and finite difference methods were confirmed and refined by experimental studies of laminar and turbulent high-pressure fluid jets. Fluid flow patterns were established in singular regions

where the stress and rate-of-strain tensors become degenerate. The effect of three-dimensional high-pressure fluid flows of finite width on the surface wear of jet device parts was determined.

4. It was demonstrated that the proposed innovative high-pressure vortex devices enable the development of highly reliable hydraulic control devices with low sensitivity to working fluid contamination. Vortex devices allow the minimum flow passage dimensions of first-stage hydraulic amplifiers to be increased from 0.3 mm to 0.5 mm without reducing their energy efficiency. This relaxes the working fluid filtration requirements from the 5–10 μm required by conventional hydraulic control devices to 25–50 μm, which is typical of industrial water used as the working medium in hydraulic systems.

5. The features of the static characteristics of high-pressure jet devices were established through studies of their working processes. In particular, stable operating ranges were substantiated for flow rates up to 40% and pressures up to 80% of their maximum values, with linear ranges of the control characteristics reaching 60%. It was demonstrated that these devices operate reliably for 10 million cycles.

6. The features of the dynamic characteristics of jet devices were determined, particularly the presence of continuous random high-frequency pressure fluctuations in the range of 500–1000 Hz. Analysis of the correlation and spectral properties of these fluctuations provided the basis for developing high-pass filters to ensure stable characteristics and eliminate resonant operating conditions in jet devices. The use of pulsating parameter variations was proposed to reduce device sensitivity to working fluid contamination. This enabled reliable device operation with a working fluid filtration rating of 25–50 μm.

7. Promising manufacturing approaches were substantiated for the components of hydraulic control systems for wheelless ground robotic complexes, including high-pressure jet and vortex devices. The development of assembled nozzles and receiver channels is recommended. This allows device parts to be manufactured from corrosion-resistant and wear-resistant chromium and chromium–molybdenum steels, with finish grinding of the internal surfaces of small nozzles and channels. Micromilling methods were proposed for forming an anisotropic microprofile on these internal surfaces. This provides the required anisotropy of the microprofile of the machined internal nozzle and channel surfaces at a hardness of 62–64 HRC and, accordingly, considerably increases device wear resistance.

## References

1. Isakova T.O. Problemy formuvannia stratehichnykh priorytetiv derzhavnoi polityky shchodo rozvytku robototekhniky: perspektyvy dlia Ukrainy. Ofitsiinyi sait Natsionalnoho Instytutu stratehichnykh doslidzhen vid 13.09.2019 r. [Elektronnyi resurs]. Rezhym dostupu: https://niss.gov.ua/doslidzhennya/informaciyni-strategii/problemi-formuvannya-strategichnikh-prioritetiv-derzhavnoi.

2. Strutynskyi, V. B., Hurzhii A. M. Nazemni robotyzovani kompleksy: monohrafiia. Zhytomyr: PP «Ruta», 2023. 497 s. https://ela.kpi.ua/handle/123456789/57111

3. Chepkov I. B., Dovhopolyi A. S., Husliakov O. M. Kontseptualni zasady stvorennia vitchyznianykh udarno-rozviduvalnykh nazemnykh robotyzovanykh kompleksiv vazhkoho klasu. Ozbroiennia ta viiskova tekhnika. Kyiv: TsNDI OVT, 2019. 3 (23). 16–25.

4. Strutynsky, V., Hurzhii, A., Kozlov L. Determination of static equilibrium conditions of a mobile terrestrial robotic complex. *Natsional'nyi Hirnychyi Universytet. Naukovyi Visnyk*, 2019. 5. 79-86. https://doi.org/10.29202/nvngu/2019-5/7

5. Strutynsky, V., Kotsiuruba, V., Dovhopoliy, A., Husliakov, O., Budianu, R., Kolos, O., Hrechka, I. Substantiating the requirements to functional indicators for the manipulators of mobile robotic demining complexes. *Eastern-European Journal of Enterprise Technologies*, 2019. 5(7 (101). 42–50. https://doi.org/10.15587/1729-4061.2019.178466

6. Shuhurov O. S. Rozvytok viiskovykh nazemnykh robotyzovanykh system v konteksti novykh kontseptsii upravlinnia: perspektyvy Ukrainy. http://sp.niss.gov.ua/content/ articles/files/27-1445867323.pdf.

7. Moosavi S. K. R., Zafar M. H., Sanfilippo F. Snake robots: A state-of-the-art review on design, locomotion, control, and real-world applications. *Mechatronics*, 2025. 112. 103418. https://doi.org/10.1016/j.mechatronics.2025.103418

8. Bianchi G., Lanzetti L., Mariana D., Cinquemani S. Bioinspired Design and Experimental Validation of an Aquatic Snake Robot. *Biomimetics*, 2024. 9. 87. https://doi.org/10.3390/biomimetics9020087

9. Bi Zh., Zhou Q., Fang H. A worm-snake-inspired metameric robot for multi-modal locomotion: Design, modeling, and unified gait control. *International Journal of Mechanical Sciences*, 2023. 254. 108436. https://doi.org/10.1016/j.ijmecsci.2023.108436

10.Panchenko A.I., Voloshyna A.A., Panchenko I.A., Voloshyn A.A. Proektuvannia mekhatronnykh system z zadanymy vykhidnymy kharakterystykamy. *Pratsi TDATU*. Melitopol: TDATU. 2020. 20 (4). 18–35. https://doi.org/10.31388/2078-0877-2020-20-4-18-35

11. Panchenko A.I., Voloshyna A.A., Panchenko I.A., Voloshyn A.A. Model hidravlichnoho pryvodu mekhatronnoi systemy. *Pratsi TDATU*, 2018. 18 (2). 59–83. https://doi.org/10.31388/2078-0877-18-2-58-82

12. Panchenko A., Voloshina A., Kiurchev S. et al. Development of the universal model of mechatronic system with a hydraulic drive. *Eastern-European Journal of Enterprise Technologies: Applied mechanics*, 2018. 4(7 (94)). 51–60. https://doi.org/10.15587/1729-4061.2018.139577

13. Panchenko A.I., Voloshyna A.A., Rozhniatovskyi V.V., Zasiadko A. I. Model hidravlichnoho pryvodu mekhatronnoi systemy z planetarnym hidromotorom. *Promyslova hidravlika i pnevmatyka*, 2024. 2 (74). 12–32. https://doi.org/10.32782/1994-4691-2024-2-74-2

14.Panchenko A.I., Voloshyna A.A., Panchenko I.A., Voloshyn A.A. Doslidzhennia dynamichnykh kharakterystyk mekhatronnykh system z hidravlichnym pryvodom. *Pratsi TDATU*, 2020. 20 (4). 58–72. https://doi.org/10.31388/2078-0877-2020-20-4-58-72

15. Panchenko A.I., Voloshyna A.A., Panchenko I.A., Voloshyn A.A. Zmina funktsionalnykh parametriv mekhatronnykh system z planetarnymy hidromotoramy pry riznykh umovakh ekspluatatsii. *Naukovyi visnyk TDATU*, 2025. 15 (2). 127–135. https://doi.org/10.32782/2220-8674-2025-15-2-15

16. Strutynskyi V.B., Kolot O.V. Matematychne modeliuvannia stokhastychnykh protsesiv u systemakh pryvodiv. Kramatorsk: ZAT "Tyrazh-51", 2005. 530 c.

17. Li R., Wei W., Liu H., Geng X., Cui J., et al. Design and experimental validation of a valve-distributed pump. *Proceedings of the Institution of Mechanical Engineers, Part C: Journal of Mechanical Engineering Science*, 2024. 238 (12). 5488–5497. https://doi.org/10.1177/09544062231220736

18. Xu, S., He, Y., Chen, Y., Nan, M., & Luo, M. Design, modelling and control of hyper-redundant robots in constrained environments: A review. *Robotics and Autonomous Systems*, 2026. 204. 105572. https://doi.org/10.1016/j.robot.2026.105572

19. Andersson, C. A. The unmanned ground vehicles to be used in future military operations. *Tiede Ja Ase*, 2022. 2021(79). https://journal.fi/ta/article/view/113769

20. Strutynskyi V.B. Matematychne modeliuvannia protsesiv ta system mekhaniky. Zhytomyr: ZhITI, 2001. 611 s.

21. Sun E., Camacho-Arreguin J., Zhou J., et al. Macro-mini collaborative manipulator system for welding in confined environments. *Robotics and Computer-Integrated Manufacturing*, 2025. 94. 102975. https://doi.org/10.1016/j.rcim.2025.102975

22. Anguek O., Belkacem B. Multi-objective design optimization of a Turret's U-bracket mounted on moving platform. *Proceedings of the Institution of Mechanical Engineers Part C Journal of Mechanical Engineering Science*, 2022. 236 (24). (2), 11371–11388. https://doi.org/10.1177/09544062221115106

23. Le Q. D., Yang E. Adaptive Fault-Tolerant Tracking Control for Multi-Joint Robot Manipulators via Neural Network-Based Synchronization. *Sensors*, 2024. 24 (21). 6837. https://doi.org/10.3390/s24216837

24. Jia, B. Vibration Propagation Characteristics of Micro-Milling Tools. *Machines*, 2022. 10. 946. https://doi.org/10.3390/machines10100946

25. Bai Q, Wang P, Cheng K, et al. Machining dynamics and chatters in micro-milling: A critical review on the state-of-the-art and future perspectives. *Chinese Journal of Aeronautics*, 2024. 37(7). 59–80. https://doi.org/10.1016/j.cja.2024.02.022

26. Mobilnyi robototekhnichnyi kompleks z dystantsiinym keruvanniam: pat. 127035 Ukraina : B25J 5/00, B25J 9/00, B25J 5/02 (2006.01), B25J 9/06 (2006.01), B25J 19/00, B25J 19/04 (2006.01) /

V.B. Strutynskyi; A.M. Hurzhii; S.Yu. Vakulenko; V.V. Novak. – № a201908587; zaiavl. 18.07.2019; opubl. 22.03.2023, Biul. № 12/2023. https://sis.nipo.gov.ua/uk/search/detail/1727728/

27. Bezkolisnyi robot zaiavka pa patent Ukrainy: B62D 57/04(2026.01) / V.B. Strutynskyi. – № a214407165; zaiavl. 18.08.2026.

28. Strutynskyi V.B. Tenzorni matematychni modeli protsesiv ta system: monohrafiia. Zhytomyr : ZhDTU, 2005. 635 s.

29. Strutynskyi V. B., Perfilov I. V. Vibratsiini protsesy mekhanichnoi obrobky: monohrafiia. Kyiv: Khimdzhest, 2015. 579 s.

*Дата першого надходження статті до видання 05.09.2026*
*Дата прийняття статті до друку після рецензування 09.10.2026*
*Дата публікації (оприлюднення) статті 04.11.2026*
*Стаття поширюється на умовах ліцензії відкритого доступу(CC BY 4.0)*

# ЕЛЕМЕНТНА БАЗА СИСТЕМ ГІДРОАВТОМАТИКИ БЕЗКОЛІСНИХ НАЗЕМНИХ РОБОТИЗОВАНИХ КОМПЛЕКСІВ

**В. Б. Струтинський[1]**
[1] *Національний технічний університет України «КПІ імені Ігоря Сікорського»,*

***Анотація***

Стаття присвячена розробленню елементної бази систем гідроавтоматики безколісних наземних роботизованих комплексів високої прохідності. Розглянуті типові безколісні наземні роботизовані комплекси які мають центральну частину яка ковзає по поверхні за допомогою інерційних рушіїв і оснащена гнучкими протяжними (довжиною 2..3 м) периферійними елементами на кінцях яких встановлені ножі, пили або фрези для руйнування перешкод. Комплекс має великогабаритний (порядку 4 м) маніпулятор, що забезпечує огляд і дослідження поверхні , орієнтацію та зв'язок. Безколісні наземні роботизовані комплекси включають спеціальні агрегати та системи гідроприводу та гідроавтоматики з робочим середовищем типу технічної води. Їх запропоновано реалізувати з використанням інноваційної елементної бази на основі струменевих та вихрових пристроїв і агрегатів високого тиску (порядку 25 МПа). Наведені розроблені схемні рішення інноваційних струменевих та вихрових пристроїв. Теоретично та експериментально досліджені гідродинамічні процеси в пристроях. Встановлено, що сингулярні області течії, де вироджується тензор швидкостей деформацій, визначають робочі процеси струменевих та вихрових пристроїв. Наведено результати досліджень статичних та динамічних характеристик струменевих пристроїв які складають елементну базу. Запропонована конструктивна реалізація та технологічні методи виконання малорозмірних (порядку 0.3 мм) каналів підвищеної зносостійкості. Технологічні методи апробовані розробленими і виготовленими експериментальними зразками.

***Ключові слова:*** струменеві агрегати, вихрові пристрої, сингулярні області, турбулентні струмені, статичні характеристики.

**DOI https://doi.org/10.32782/1994-4691-2026-1-77-8**
UDK 621.22

# CONTROL MODES OF A HYDRAULIC DRIVE WITH INDEPENDENT CONTROL OF FLOWS UNDER DIFFERENT LOAD CONDITIONS

# РЕЖИМИ КЕРУВАННЯ В ГІДРОПРИВОДІ З НЕЗАЛЕЖНИМ КЕРУВАННЯМ ПОТОКАМИ ПРИ РІЗНИХ УМОВАХ НАВАНТАЖЕННЯ

O. A. Syrotin[1], graduate student ORCID: 0009-0002-4992-3845
D. O. Lozinskyi[1*], Ph.D., Associate Professor ORCID: 0000-0002-1077-1621

[1] *Vinnytsia National Technical University, Vinnytsia, Ukraine*
* e-mail: lozinskiy_dmitriy@vntu.edu.ua

**Abstract**. A hydraulic drive of a mobile machine under a passive load is considered, based on proportional metering elements that independently control the inlet and outlet flows of the hydraulic cylinder and on controlled check valves. The influence of the load mass, the load force direction and the required rod velocity on the choice of the control mode is studied. Four modes are analysed: meter-in control, meter-out control with pump unloading, combined control and control by the pump flow rate. A quasi-static model with constraints on cavitation, pressure, flow rate and controllability is compiled; the comparison criterion is the total pressure drop across the metering elements. A mode map in the coordinates “load mass – required velocity” is built and the energy consumed from the pump over a loader cycle is analysed.

**Keywords**: proportional metering element, controlled check valve, quasi-static model, total pressure drop, cavitation, front loader, pump unloading, energy efficiency.

## Introduction.

Hydraulic drives of mobile machines used for loading and unloading operations work under a passive load for a considerable part of their operating time; the sign of this load with respect to the velocity of the working element changes during the cycle, while its magnitude is determined by the load mass and the position of the links. The hydraulic drives of such machines usually employ directional control valves in which the flows at the inlet and outlet of the hydraulic motor are controlled by a common spool, so the ratio of the flow areas of the inlet and outlet passages is fixed by the spool geometry and cannot be changed according to the load conditions. Metering elements with independent flow control (independent metering) [1, 2] do not have this limitation: the opening of each metering element can be set separately, while controlled check valves ensure the sealing of the working chambers of the hydraulic cylinder. However, such a structure is more complex and, in order to realise its advantages, requires the choice of a rational control mode for every combination of operating conditions.

The boom circuit of the PKU-0.8 front loader mounted on the MTZ-82 tractor (Fig. 1) is taken for the study. The boom OB rotates about the pivot O on the frame, the hydraulic cylinder CD rests on the frame at point C and acts on the boom at point D, and the load of mass *m* is applied at point B. The mass on the boom varies from the mass of the empty bucket to the rated one, i.e. approximately six times, and the sign of the load force with respect to the rod velocity changes twice per cycle. With coupled meter-in/meter-out control, the overrunning load during lowering is controlled by the outlet passage, whereas the inlet passage of the same spool throttles the pump flow without any functional need, the pump remains under pressure in all phases of motion, and the energy dissipated across the metering elements is converted into heat and causes heating of the working fluid.

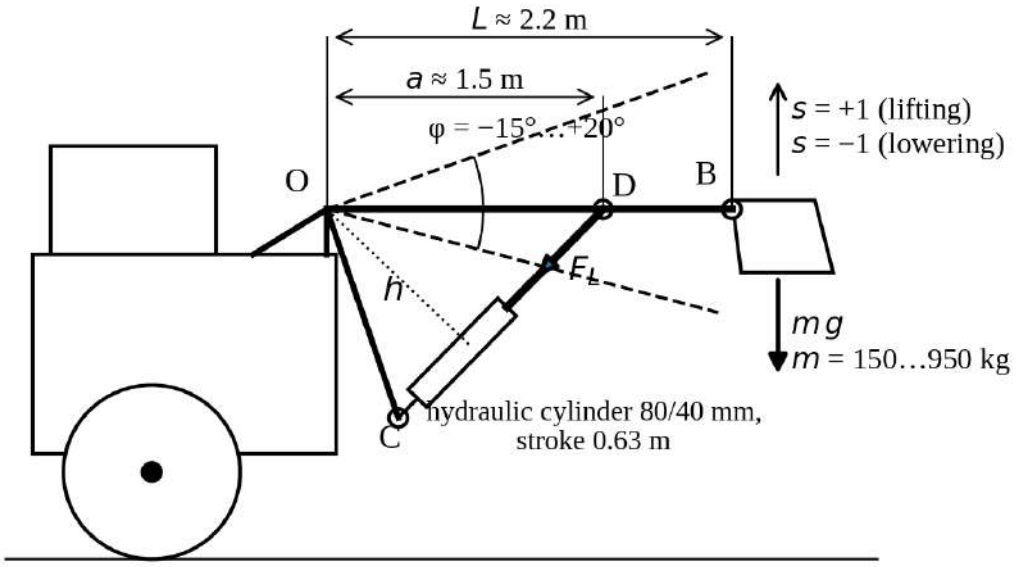



**Fig. 1. Kinematic diagram of the boom circuit of the PKU-0.8 loader: O – boom pivot on the frame; C, D – hydraulic cylinder pivots; B – point of load application; *L*, *a* – link lengths; *h* – lever arm of the cylinder force about O (in the middle position *h* ≈ 1.08 m); φ – boom rotation angle; $F_L$ – force on the rod; *s* – sign of the force direction with respect to the velocity. The dimensions are estimates and are to be refined according to the machine data sheet**

At a small mass, the pressure produced by the load in the piston-side chamber is insufficient to pass the required flow rate through the outlet passage, which limits the lowering velocity. Independent flow control removes the structural coupling of the passages but gives rise to the problem of choosing the control mode for every combination of mass, sign of the force and required velocity. In the absence of appropriate recommendations, or when irrational control modes are applied, the advantages of independent control are not realized or are realised only partially, and an erroneous choice of the mode under an overrunning load may lead to cavitation and uncontrolled motion.

## Literature Review.

Independent control of the inlet and outlet of a hydraulic cylinder as a means of reducing throttling losses and of solving the overrunning-load problem was proposed in [3]. The authors of [4, 5] identified five control modes for a four-valve hydraulic unit and formulated the mode-switching problem according to an energy criterion in a quasi-static formulation; in their work, meter-out control with subsequent regeneration is preferable under an overrunning load. In [6] a method of controlling four valves with cavitation prevention was proposed, and in the patent [7] the control mode is selected according to the sign and magnitude of the load pressure and the required velocity.

The authors of [8] systematised the structures of independent-metering systems and their problems, in particular the loss of controllability at small pressure drops and shocks during switching. In [9] the operating modes of “programmable valves” were selected according to an energy criterion.

In [10–13] the coordination of the pump and the valves [10], bumpless mode switching [11], the reduction of oscillations during switching [12] and switching between flow and pressure control [13] were investigated. The state of the field is summarised in the reviews [14, 15], and a separate review is devoted to the coordinated control of the inlet and outlet under a sustained overrunning load [16]. The architectures of independent-metering systems and their operating modes are summarised in [17–19], trends in the control of multi-actuator

hydraulic systems of mobile machines in [20, 21], and the effect of such systems on the energy consumption of excavators is investigated in [22–24].

The author of [25] substantiated the application of adaptive control systems for the hydraulic drives of manipulators of mobile machines. In [1, 2] a proportional directional control valve with independent flow control was developed and optimised, and in [26] a multi-mode hydraulic drive of a front loader was investigated. In previous works of the authors, approaches to improving the energy efficiency of electrohydraulic systems [27], a test bench for studies under a passive load [28], the influence of the control system parameters on the drive dynamics and the energy performance of throttling, load-sensing and displacement control over a duty cycle were considered [29].

At the same time, for a two-spool valve without regenerative connections, the regions of applicability of the control modes under a passive load in the coordinates “mass – force direction — velocity” have not been quantified. The available selection rules were obtained for four-valve units with regeneration or are formulated in general terms.

## Research Methodology.

The aim of the work is to investigate different control modes of a hydraulic drive with a passive load according to the criterion of minimising the total pressure drop across the metering elements and reducing the energy consumption. To achieve this aim, the following tasks have to be solved: 1) to substantiate the design scheme of the hydraulic drive and to identify the flow control modes; 2) to build a quasi-static mathematical model of the steady state with constraints on cavitation, pressure, flow rate and controllability; 3) to calculate the pressures, pressure drops, power and efficiency for a grid of conditions “mass — force direction — velocity” and to identify inadmissible combinations; 4) to build a mode map for resistive and overrunning loads; 5) to analyse the energy effect of mode switching on a conventional duty cycle of the loader.

The hydraulic circuit diagram of the drive is shown in Fig. 2.

The pump 1 feeds the pressure line; the metering section 2 contains the proportional two-position metering elements 5 of lines A and B, each of which in the rest position (under the spring action) connects its line to the return line through a throttling orifice and in the working position – to the pressure line. The intermediate position of the spool of the proportional element sets the flow area $A_1$ (line A) or $A_2$ (line B). The load-holding section 3 contains the controlled check valves 6, which in the rest position pass the flow only towards the working chamber (load holding and make-up of the chamber from the return line) and, when energised, open a free passage in both directions. The shuttle valve 7 transmits the higher of the pressures of lines A and B to the bypass compensator 8 – the pump flow control element, which discharges the surplus pump flow to the return line and maintains the pressure in the pressure line at a level exceeding the load pressure by a constant margin. During load holding and during motion under the action of the load, the compensator is fully open and the pump pressure falls to $P_{\text{unl}}$. The pressure relief valve 9 limits the pressure in the pressure line. The hydraulic cylinder 4 has a piston-side chamber of area $F_1$ (pressure $P_1$) and a rod-side chamber of area $F_2$ (pressure $P_2$); the load force $F_{\text{L}}$ acts on the rod, and the rod moves with velocity $v$. The design of the metering elements is considered in [1, 2].

Hereinafter the subscripts “in” and “out” denote the role of the working chamber and of the metering element: “in” – the chamber being filled and the element through which the flow enters it, “out” – the chamber being emptied and the element through which the flow goes to the return line. The sign $s = +1$ corresponds to a resistive load (the force is directed against the rod velocity, lifting of the load), $s = -1$ – to an overrunning load (lowering of the load). At $s = +1$, $P_{\text{in}} = P_1$, $F_{\text{in}} = F_1$, $A_{\text{in}} = A_1$, $P_{\text{out}} = P_2$, $F_{\text{out}} = F_2$, $A_{\text{out}} = A_2$; at $s = -1$ the roles are interchanged.

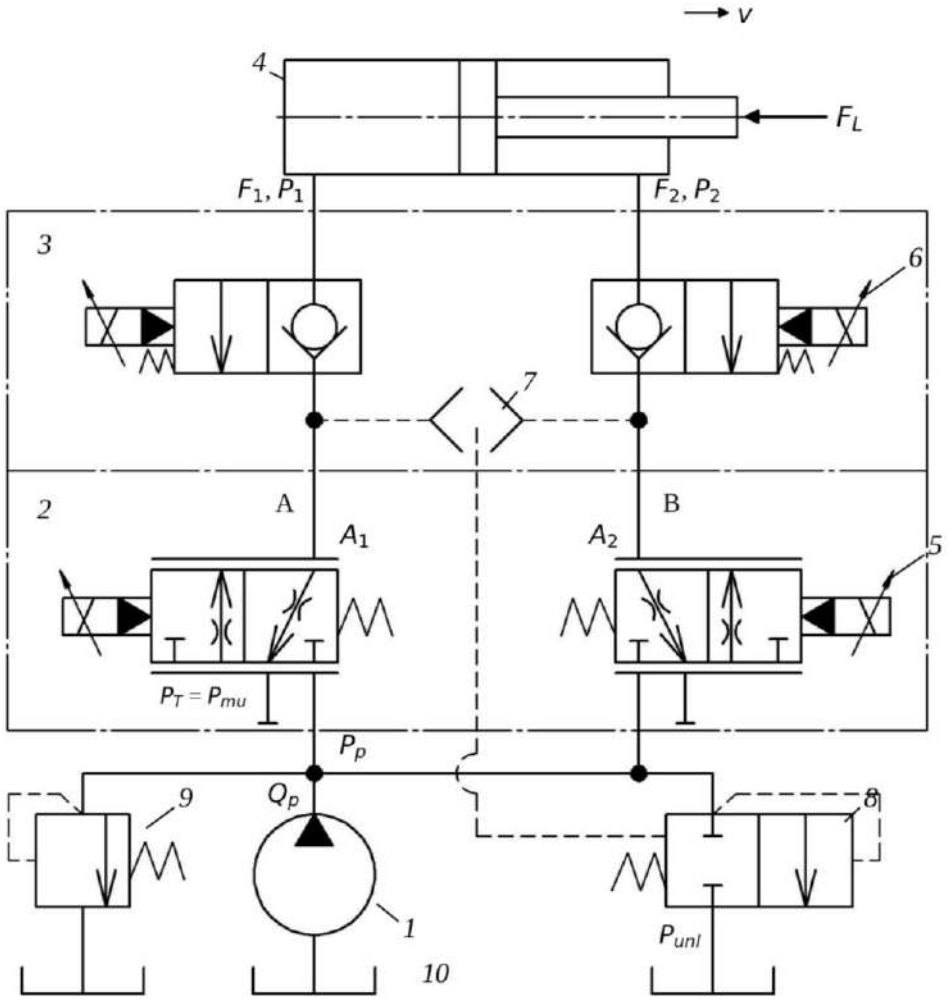



**Fig. 2. Hydraulic circuit diagram of the drive with independent flow control: 1 – pump; 2 – metering section; 3 – load-holding section; 4 – hydraulic cylinder; 5 – proportional two-position metering elements of lines A and B (flow areas $A_1$, $A_2$); 6 – controlled check valves; 7 – shuttle valve; 8 – bypass compensator (pump flow control element); 9 – pressure relief valve; 10 – tank. $P_p$, $Q_p$ – pump pressure and flow rate; $P_T$, $P_{mu}$ – return-line and make-up pressures; $P_{unl}$ – pressure of the unloaded pump; $P_1$, $P_2$, $F_1$, $F_2$ – pressures and areas of the working chambers; $F_L$ – load force; $v$ – rod velocity**

Four flow control modes are distinguished for this circuit (Table 1). In mode M1 the velocity is set by the meter-in element while the meter-out element is fully open, which is the conventional variant for a resistive load. In mode M2 the flow is controlled by the meter-out element while the meter-in element is fully open; under an overrunning load the inlet chamber is filled by the make-up flow from the return line and the pump is unloaded. Mode M3, in which both elements are partially closed, is intended for intermediate cases where M1 may cause cavitation and M2 does not provide controllability. In mode M4 both elements are open and the velocity is set by the supply flow rate (displacement or rotational speed of the pump); this mode is the limiting one and is equivalent to displacement control [30].

A quasi-static model of steady motion is used to compare the modes. The choice is due to three circumstances. First, the mode selection rule is formulated for conditions that change slowly in comparison with the transient processes: the phases of the loader duty cycle last for seconds, whereas the transients in the drive last for fractions of a second [29], and the energy balance of a phase is determined by the steady values of pressures and flow rates. Second, the constraints that determine the admissibility of a mode (cavitation, admissible pressure, flow rate, controllability) are formulated for the steady state. Third, the dynamics of switching between the modes is a separate problem which will be considered at the next stage.

**Table 1. State of the drive elements in the flow control modes**

| Mode | Meter-in element $A_{in}$ | Meter-out element $A_{out}$ | Power source (pump) |
|---|---|---|---|
| M1 | controls the flow | fully open | under pressure |
| M2 | fully open (at $s = -1$ – line on make-up) | controls the flow | under pressure (at $s = -1$ – unloaded) |
| M3 | controls the flow | controls the flow | under pressure |
| M4 | fully open | fully open | controlled flow rate |

The following assumptions are adopted: 1) the working fluid is incompressible, its density and temperature are constant, wave processes in the hydraulic lines are not considered; 2) the rod velocity is constant, inertia forces and viscous damping forces are neglected; 3) leakages in the metering elements and in the hydraulic cylinder as well as pressure losses in the hydraulic lines are neglected; 4) the friction force in the hydraulic cylinder is proportional to the load force; 5) the flow rate through a metering element is described by a quadratic dependence on the pressure drop with a constant discharge coefficient; 6) the power source is a fixed-displacement pump with a bypass compensator that maintains the pressure in the pressure line at the minimum necessary level and discharges the surplus flow to the return line at this pressure (a load-sensing scheme with a fixed-displacement pump according to [30]); losses in the pump itself are not considered; 7) the make-up of a working chamber from the return line through the throttling orifice of the metering element in the rest position and the check valve maintains a constant pressure in the chamber at a flow rate not exceeding the pump flow rate; 8) a metering element retains controllability if the pressure drop across it is not less than the minimum controllable one and its opening does not exceed the admissible fraction of the maximum; the metering element operates at the lowest admissible pressure drop.

For given mass $m$, force direction $s$ and velocity $v^*$, the steady state is described by the system of equations:

$$P_{in}\cdot F_{in} - P_{out}\cdot F_{out} = s\cdot F_L + k_{fr}\cdot F_L, \quad F_L = k_r\cdot m\cdot g \tag{1}$$

$$Q_{in} = F_{in}\cdot v^*, \quad Q_{out} = F_{out}\cdot v^* \tag{2}$$

$$\Delta p_{in} = (\rho/2)\cdot(Q_{in}/(\mu\cdot A_{in}))^2, \quad \Delta p_{out} = (\rho/2)\cdot(Q_{out}/(\mu\cdot A_{out}))^2 \tag{3}$$

$$P_{out} = P_T + \Delta p_{out}; \quad P_p = P_{in} + \Delta p_{in} \text{ (M1, M3, M4; M2 at } s = +1) \tag{4}$$

$$P_{in} = P_{mu}, \quad P_p = P_{unl} \text{ (M2 at } s = -1) \tag{5}$$

$$A = A_{max} \text{ (open element)}; \quad \Delta p = \max(\Delta p_c; \Delta p(A_{max})) \text{ (metering element, } s = +1) \tag{6}$$

$$P_{in}, P_{out} \ge P_{min}; \quad P_p \le P_{max}; \quad Q_{in} \le Q_p; \quad \Delta p_{met} \ge \Delta p_c; \quad A_{met} \le k_A\cdot A_{max} \tag{7}$$

$$\Sigma\Delta p = \Delta p_{in} + \Delta p_{out}; \quad N_d = \Delta p_{in}\cdot Q_{in} + \Delta p_{out}\cdot Q_{out} \tag{8}$$

$$N_p = P_p\cdot Q_p \text{ (M1–M3)}, \quad N_p = P_p\cdot Q_{in} \text{ (M4)}; \quad \eta = (s + k_{fr})\cdot F_L\cdot v^*/N_p, \tag{9}$$

where $P_{in}$, $P_{out}$ are the pressures in the chambers being filled and emptied; $F_{in}$, $F_{out}$ are their areas; $F_L$ is the load force on the rod; $k_{fr}$ is the friction coefficient; $k_r$ is the coefficient of reduction of the mass to the force on the rod according to the boom kinematics (Fig. 1); $g$ is the gravitational acceleration; $Q_{in}$, $Q_{out}$ are the flow rates through the meter-in and meter-out elements; $\Delta p_{in}$, $\Delta p_{out}$ are the pressure drops across them; $\rho$ is the working fluid density; $\mu$ is the discharge coefficient; $A_{in}$, $A_{out}$ are the flow areas; $A_{max}$ is the flow area of a fully open element; $P_p$ is the pump pressure; $P_T$, $P_{mu}$, $P_{unl}$ are the return-line pressure, the make-up pressure and the pressure of the unloaded pump; $P_{min}$ is the pressure below which cavitation occurs; $P_{max}$ is the admissible pressure; $Q_p$ is the pump flow rate (for M2 at $s = -1$ — the capacity of the make-up path); $\Delta p_{met}$, $A_{met}$ are the pressure drop across and the flow area of the

metering element; $\Delta p_c$ is the minimum controllable pressure drop; $k_A$ is the admissible opening fraction; $\Sigma\Delta p$ is the total pressure drop across the metering elements (the comparison criterion); $N_d$ is the power dissipated across them; $N_p$ is the power consumed from the pump; $\eta$ is the transmission efficiency from the pump to the rod (calculated at $s = +1$; during lowering there is no useful work and $N_p$ serves as the indicator). For mode M3 at $s = -1$ a pressure not lower than the guaranteed value $P_g$ is maintained in the inlet chamber.

The initial data of the model and the ranges of their variation are summarised in Table 2. The design example corresponds to the boom circuit of the PKU-0.8 loader: hydraulic cylinder 80/40 mm, NSh-32 gear pump. The area $A_{max}$ is chosen so that at full opening the pressure drop is 0.3 MPa at the pump flow rate. The highest attainable lifting velocity is $Q_p/F_1 = 0.182$ m/s and the lowering velocity is $Q_p/F_2 = 0.243$ m/s; therefore a velocity of 0.3 m/s is unattainable with the NSh-32 pump in any mode and is replaced by 0.15 m/s in the calculation grid.

**Table 2. Initial data of the mathematical model**

| Symbol | Parameter | Value / range | Unit |
|---|---|---|---|
| $F_1$ / $F_2$ | areas of the piston-side and rod-side chambers (cylinder 80/40 mm) | 50.3 / 37.7 | $cm^2$ |
| $S$ | rod stroke | 0.63 | m |
| $Q_p$ | flow rate of the NSh-32 pump at 1700 rpm | 55 | l/min |
| $m$ | load mass (5 levels; continuous for the map) | 150…950 | kg |
| $k_r$ | coefficient of reduction of the mass to the force on the rod (estimate) | 2.04 | — |
| $F_L$ | load force on the rod | 3…19 | kN |
| $k_{fr}$ | friction coefficient | 0.03 | — |
| $s$ | direction of the load force | +1; −1 | — |
| $v^*$ | required velocity (grid; 0.02…0.30 for the map) | 0.05; 0.10; 0.15 | m/s |
| $\mu$; $\rho$ | discharge coefficient; working fluid density | 0.65; 870 | —; $kg/m^3$ |
| $A_{max}$ | flow area of a fully open element | 54 | $mm^2$ |
| $P_{min} = P_{mu} = P_T$ | cavitation, make-up and return-line pressures | 0.15 | MPa |
| $P_{max}$; $P_{rv}$ | admissible pressure; relief valve setting | 16; 17 | MPa |
| $\Delta p_c$; $k_A$ | minimum controllable pressure drop; admissible opening fraction | 0.5; 0.8 | MPa; — |
| $P_g$; $P_{unl}$ | guaranteed pressure in the inlet chamber (M3); pressure of the unloaded pump | 0.5; 0.3 | MPa |
| $P_{sb}$ | standby pressure of the supply with coupled control (cycle, strategy A) | 0.5 | MPa |

The system of equations (1)–(9) is solved sequentially without iterations. The flow rates are determined from (2), the pressure drops across the open and metering elements from (3) and (6), $P_{out}$ from (4), $P_{in}$ from (1) and $P_p$ from (4). Then the constraints (7) are checked and the indicators (8), (9) are calculated. For M2 and M3 at $s = -1$ the order is different: $P_{in}$ is prescribed (the make-up pressure according to (5) or the guaranteed pressure), $P_{out}$ and the

pressure drop across the meter-out element are found from (1), and its flow area is found from (3) and checked against (7). For M3 the pressure $P_{in}$ is raised to the value at which the meter-out element satisfies (7). A mode is considered inadmissible if at least one of the constraints (7) is violated. For M1 at $s = -1$ the calculated pressure deficit in the inlet chamber and the velocity of uncontrolled motion with a fully open meter-out element are recorded. The calculation is implemented in Python (NumPy and Matplotlib libraries) for a grid of 5 × 3 × 2 × 4 = 120 combinations "mass × velocity × direction × mode" and for the mode map on a grid of 81 × 141 points in the coordinates ($m$, $v^*$). The conventional cycle is calculated with the same model phase by phase.

## Results.

Under a resistive load (Fig. 3) the total pressure drop across the metering elements does not depend on the mass (Fig. 3, a): the adaptive supply raises the pressure together with the load, and the pressure drops are determined only by the flow rate and the minimum controllable pressure drop. At $v^* = 0.15$ m/s, $\Sigma\Delta p$ is 0.61 MPa for M1, 0.70 MPa for M2, 1.00 MPa for M3 and 0.32 MPa for M4. The dependence on velocity (Fig. 3, b) explains the origin of this difference: in M1 and M2 one element operates at the constant pressure drop $\Delta p_c$, while the other, open, element adds a pressure drop that grows quadratically with velocity. In M4 both elements are open, so at 0.05 m/s $\Sigma\Delta p = 0.04$ MPa against 0.51 MPa in M1, i.e. 14 times less, and at 0.15 m/s — 0.32 against 0.61 MPa, 1.9 times less.

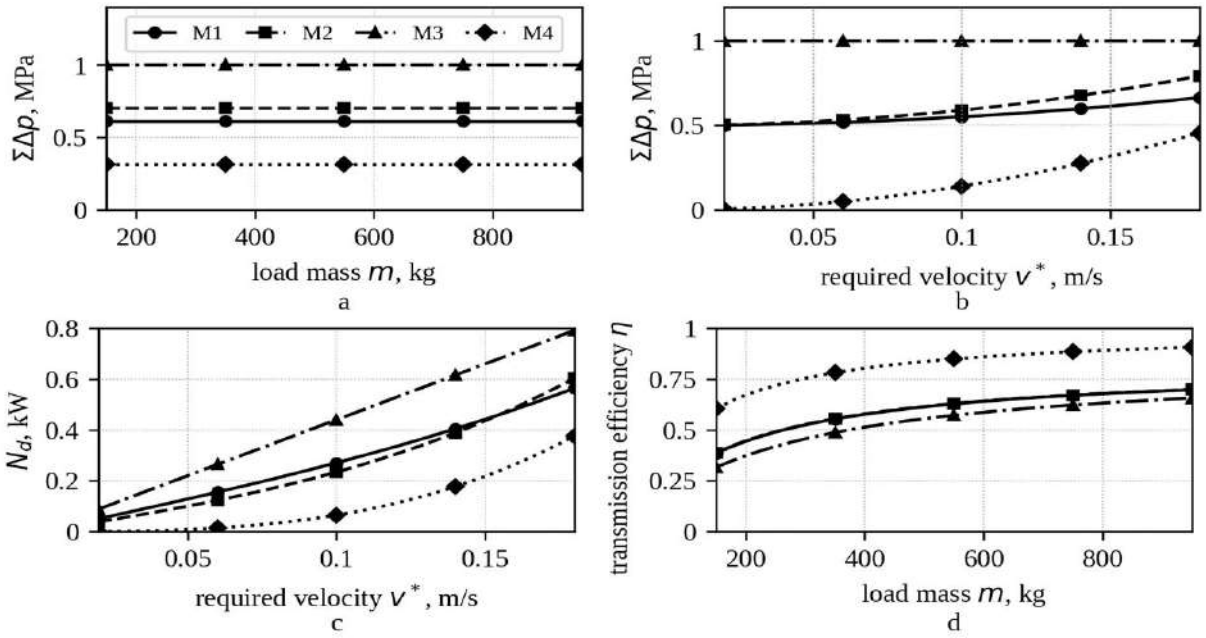



**Fig. 3. Mode indicators under a resistive load ($s$ = +1): a – total pressure drop versus mass; b – total pressure drop versus required velocity; c – power dissipated across the metering elements; d – transmission efficiency**

The advantage of M1 over M2 is due to the fact that the open element in M1 passes the smaller flow rate $Q_{out} = 0.75 \cdot Q_{in}$. In terms of the power dissipated across the elements (Fig. 3, c), M1 and M2 are equivalent, because the pressure drop across the meter-out element acts on the smaller flow rate, and at low velocities M2 has a slight advantage. Mode M3 is inferior to M1 by a factor of two in $\Sigma\Delta p$ and by 6…22 % in the power consumed from the pump (Table 3); therefore, under a resistive load it can be justified only by positioning accuracy requirements, which are not analysed in the quasi-static formulation. The transmission efficiency (Fig. 3, d) increases with the mass for all modes: for M1 from 0.39 at 150 kg to 0.70 at 950 kg, for M4 from 0.61 to 0.91. The pressure constraint is not reached in the example: at 950 kg $P_p$ does not exceed 4.9 MPa.

Under an overrunning load (Fig. 4) the relations between the indicators change. In mode M1 with a fully open meter-out element the pressure in the chamber being emptied is only 0.17…0.35 MPa, and the force balance (1) requires a negative pressure in the inlet chamber: from −0.30 MPa at 150 kg to −4.42 MPa at 950 kg (Fig. 4, b). This corresponds to a discontinuity of the flow in the inlet chamber, opening of the make-up path and uncontrolled motion with a velocity limited only by the resistance of the fully open meter-out element. According to (1), (3), at $P_{in} = P_{min}$ this velocity is 0.24 m/s at 150 kg and 0.63 m/s at 950 kg. M1 is unsuitable for an overrunning load over the whole range, which agrees with the known result for meter-in control [3, 8]. Mode M4 is also unsuitable: control by the supply flow rate does not limit the velocity under an overrunning load, since the motion is produced by the load force and not by the supply flow.

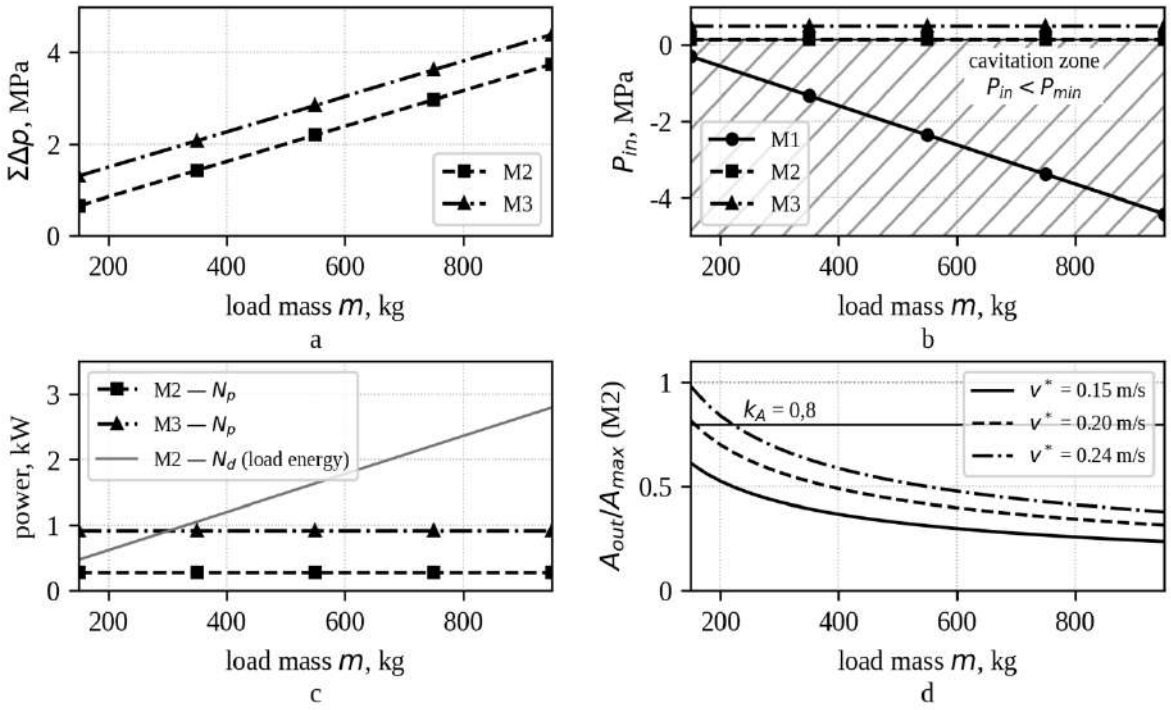



**Fig. 4. Mode indicators under an overrunning load ($s = -1$), $v^* = 0.15$ m/s: a – total pressure drop; b – pressure in the inlet chamber (hatching – cavitation zone); c – power consumed from the pump $N_p$ and power $N_d$ dissipated across the elements in M2; d – relative opening of the meter-out element in M2 at three velocities**

In mode M2 the pressure in the inlet chamber is maintained by the make-up flow, and the potential energy of the load is dissipated across the meter-out element: $P_{out}$ = 0.69 MPa at 150 kg and 3.78 MPa at 950 kg, $\Sigma\Delta p$ = 0.66…3.74 MPa (Fig. 4, a). This pressure drop corresponds to the dissipation of the potential energy of the load (curve $N_d$ in Fig. 4, c) and cannot be eliminated in a throttling scheme.

The energy difference between the modes consists only in whether the pump work is added to it. In M2 the pump is unloaded and consumes 0.28 kW. In mode M3 the pump produces $P_{in}$ = 0.5 MPa in the inlet chamber, which raises $P_{out}$ by 0.26 MPa and adds a pressure drop of 0.5 MPa across the meter-in element: $\Sigma\Delta p$ = 1.30…4.39 MPa, i.e. 2.0 times more than in M2 at 150 kg and 17 % more at 950 kg, while the power consumed from the pump increases to 0.92 kW (Fig. 4, c). M3 can be justified only by the controllability condition. Fig. 4, d shows the relative opening of the meter-out element in M2: at 0.15 m/s it does not exceed 0.6 for all masses, but at 0.20…0.24 m/s and masses up to 230 kg it exceeds the admissible value $k_A$ = 0.8, i.e. the element is almost fully open and loses its ability to control the flow. This corresponds to the case of fast lowering of the empty bucket: the pressure produced by the bucket in the piston-side chamber is insufficient to pass the required

flow rate through the meter-out element, and an additional force from the pump pressure in the inlet chamber is needed to reach the required velocity. The results for the characteristic points are summarised in Table 3.

**Table 3. Calculation results for the characteristic points, $v^* = 0.15$ m/s**

| Condition | Mode | $P_{in}$, MPa | $P_{out}$, MPa | $P_p$, MPa | $\Sigma\Delta p$, MPa | $N_p$, kW | η | Note |
|---|---|---|---|---|---|---|---|---|
| $m$ = 950 kg, $s$ = +1 | M1 | 4.09 | 0.26 | 4.59 | 0.61 | 4.21 | 0.70 | — |
| | M2 | 4.38 | 0.65 | 4.58 | 0.70 | 4.20 | 0.70 | — |
| | M3 | 4.38 | 0.65 | 4.88 | 1.00 | 4.47 | 0.66 | — |
| | M4 | 4.09 | 0.26 | 4.29 | 0.32 | 3.24 | 0.91 | controllable-flow supply |
| $m$ = 150 kg, $s$ = +1 | M1 | 0.81 | 0.26 | 1.31 | 0.61 | 1.20 | 0.39 | — |
| | M2 | 1.10 | 0.65 | 1.31 | 0.70 | 1.20 | 0.39 | — |
| | M3 | 1.10 | 0.65 | 1.60 | 1.00 | 1.47 | 0.32 | — |
| | M4 | 0.81 | 0.26 | 1.02 | 0.32 | 0.77 | 0.61 | controllable-flow supply |
| $m$ = 950 kg, $s$ = −1 | M1 | −4.42 | 0.35 | — | — | — | — | cavitation, uncontrolled motion 0.63 m/s |
| | M2 | 0.15 | 3.78 | 0.30 | 3.74 | 0.28 | — | pump unloaded |
| | M3 | 0.50 | 4.04 | 1.00 | 4.39 | 0.92 | — | — |
| $m$ = 150 kg, $s$ = −1 | M1 | −0.30 | 0.35 | — | — | — | — | cavitation, uncontrolled motion 0.24 m/s |
| | M2 | 0.15 | 0.69 | 0.30 | 0.66 | 0.28 | — | pump unloaded |
| | M3 | 0.50 | 0.95 | 1.00 | 1.30 | 0.92 | — | — |

* Note. M4 at $s$ = −1 is unsuitable: the supply flow does not restrain an overrunning load.

The effect of mode switching is analysed on a conventional cycle of a loader with a bucket: lifting of a 950 kg load over the full stroke at a velocity of 0.15 m/s (4.2 s), holding during transport (10 s), lowering of the empty 150 kg bucket at the same velocity (4.2 s) and holding of the empty bucket (6 s). Strategy A reproduces a conventional spool valve with coupled meter-in/meter-out control: the openings of the meter-in and meter-out elements are equal, the pump is under pressure in all phases of motion, and during holding the compensator standby pressure $P_{sb}$ is maintained. Strategy B is the mode selected by the load conditions: M1 during lifting, M2 with the unloaded pump during lowering, and unloading during holding (the load is held by the check valve). The results are shown in Fig. 5. During lifting the strategies are almost equivalent (18.2 and 17.7 kJ): the equality of the openings creates an additional back pressure of 0.28 MPa in strategy A. The difference arises during lowering (4.3 against 1.2 kJ), where in strategy A the pump supplies the working fluid under pressure into the rod-side chamber, the filling of which could be provided by the make-up flow, and during holding (7.3 against 4.4 kJ). Over the cycle, 29.8 kJ is consumed with strategy A and 23.2 kJ with strategy B: mode switching reduces the energy consumed by 22 %, and the cycle efficiency at a useful work of 12.0 kJ increases from 0.40 to 0.52. This result is conservative: at the standby pressure of 1.5 MPa typical of load-sensing systems [30], the saving reaches 48 %.

A generalisation of the calculations on a grid of 81 × 141 points in the coordinates ($m$, $v^*$) is shown in Fig. 6. Under a resistive load (Fig. 6, a) the region of admissible modes is bounded from above by the pump flow rate, $v^* \le 0.182$ m/s, and inside it M1 is optimal in terms of $\Sigma\Delta p$ at any mass, while the mass affects only the efficiency (isolines η = 0.3…0.7).

Under an overrunning load (Fig. 6, b) M1 is inadmissible everywhere because of cavitation, M4 is unsuitable, and the region is bounded from above by the capacity of the make-up path, $v^* \le 0.243$ m/s. M2 is optimal almost over the whole region, while M3 is needed in the wedge of small masses and high velocities bounded by the curve $A_{out} = 0.8 \cdot A_{max}$ (see Fig. 4, d). The $\Sigma\Delta p$ isolines for M2 show that during lowering the pressure drop is determined by the mass and is almost independent of the velocity.

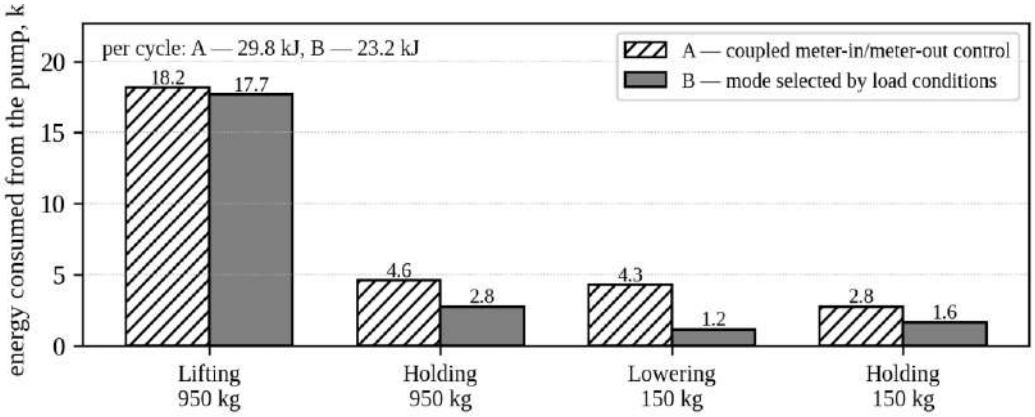



**Fig. 5. Energy consumed from the pump by phases of the conventional loader cycle for the two control strategies**

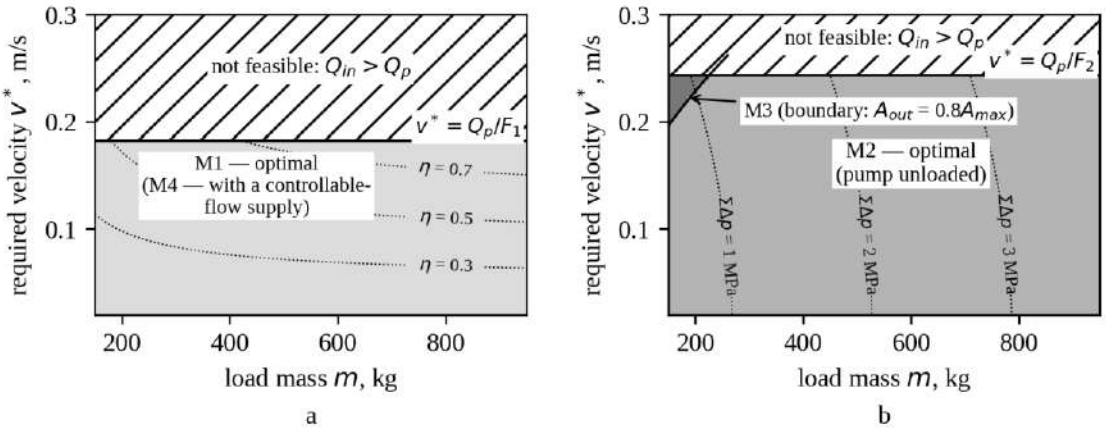



**Fig. 6. Map of control modes in the coordinates "load mass — required velocity" under resistive (a) and overrunning (b) loads; hatching – infeasible combinations; at $s = -1$, M1 is inadmissible because of cavitation and M4 is unsuitable**

Thus, the most influential parameters for the choice of the control mode are the sign of the load force, the ratio of the required flow rate to the supply flow rate, and the ratio of the required opening of the meter-out element to the admissible one.

## Conclusions.

A quasi-static model of a hydraulic drive with a two-spool valve has been built for four flow control modes with constraints on cavitation, admissible pressure, pump flow rate, minimum controllable pressure drop and opening margin of the metering element; the assumptions and the solution procedure have been substantiated. For the boom circuit of the PKU-0.8 loader (hydraulic cylinder 80/40 mm, NSh-32 pump), 120 combinations "mode × mass × force direction × velocity" have been calculated.

Under a resistive load the total pressure drop across the metering elements does not depend on the mass and at 0.15 m/s amounts to 0.61 MPa for M1, 0.70 MPa for M2, 1.00 MPa for M3 and 0.32 MPa for M4. M1 is optimal among the modes of control by metering elements at all masses, and M4 defines the lower limit, which is 1.9 times lower at 0.15 m/s

and 14 times lower at 0.05 m/s. The transmission efficiency with a fixed-displacement pump increases with the mass from 0.39 to 0.70. The flow-rate limits of the NSh-32 pump are 0.182 m/s for lifting and 0.243 m/s for lowering.

Under an overrunning load M1 is inadmissible over the whole range of 150…950 kg: the calculated pressure in the inlet chamber is from −0.30 to −4.42 MPa, the uncontrolled motion velocity is 0.24…0.63 m/s; M4 is unsuitable. M2 with the unloaded pump provides $\Sigma\Delta p$ = 0.66…3.74 MPa at a power consumed from the pump of 0.28 kW. M3 increases $\Sigma\Delta p$ by 1.2…2.0 times and the power to 0.92 kW; therefore it is justified only for masses up to 230 kg at velocities of 0.20…0.24 m/s, where the meter-out element in M2 loses its ability to control the flow.

For the conventional loader cycle, mode switching according to the load conditions (M1 — lifting, M2 with unloading — lowering and holding) reduces the energy consumed from the pump by 22 % (from 29.8 to 23.2 kJ) in comparison with coupled meter-in/meter-out control, and the cycle efficiency increases from 0.40 to 0.52.

The mode map in the coordinates “mass — velocity” shows that the choice of the mode of a two-spool valve is determined by the sign of the load force, the ratio of the required flow rate to the supply flow rate and the ratio of the required opening of the meter-out element to the admissible one. The information of this map is the basis for choosing an appropriate method of controlling the hydraulic drive. Further work will be devoted to the dynamics of switching between the modes and to the implementation of the mode map in the form of a neural-network approximator with verification on the test bench [28].

## References


1. Козлов Л. Г., Лозінський Д. О. Гідропривід з пропорційним електрогідравлічним управлінням : пат. 41887 Україна : МПК F15B 11/00. № u200900907 ; заявл. 06.02.2009 ; опубл. 10.06.2009, Бюл. № 11. 4 с.
2. Лозінський Д. О., Козлов Л. Г., Піонткевич О. В., Кавецький О. І. Оптимізація електрогідравлічного розподільника з незалежним керуванням потоків. *Вісник машинобудування та транспорту*, 2023. № 1 (17). С. 87–91. https://doi.org/10.31649/2413-4503-2023-17-1-87-91
3. Jansson A., Palmberg J.-O. Separate Controls of Meter-in and Meter-out Orifices in Mobile Hydraulic Systems. *SAE Transactions*. 1990. 99. 377–383. https://doi.org/10.4271/901583
4. Shenouda A. Quasi-Static Hydraulic Control Systems and Energy Savings Potential Using Independent Metering Four-Valve Assembly Configuration : PhD thesis. Atlanta : Georgia Institute of Technology, 2006
5. Shenouda A., Book W. Optimal Mode Switching for a Hydraulic Actuator Controlled with Four-Valve Independent Metering Configuration. *International Journal of Fluid Power*, 2008. 9 (1). 35–43. https://doi.org/10.1080/14399776.2008.10781295
6. Tabor K. A. Optimal Velocity Control and Cavitation Prevention of a Hydraulic Actuator Using Four Valve Independent Metering. *SAE Technical Paper*, 2005. 2005-01-3620
7. Pfaff J. L., Tabor K. A. Method of Selecting a Hydraulic Metering Mode for a Function of a Velocity Based Control System : US Patent 6,880,332 B2 ; assignee HUSCO International, Inc. 2005
8. Eriksson B., Palmberg J.-O. Individual metering fluid power systems: challenges and opportunities. *Proceedings of the Institution of Mechanical Engineers, Part I: Journal of Systems and Control Engineering*, 2011. 225 (2). 196–211. https://doi.org/10.1243/09596518JSCE1111
9. Liu S., Yao B. Coordinate Control of Energy Saving Programmable Valves. *IEEE Transactions on Control Systems Technology*, 2008. 16 (1). 34–45. https://doi.org/10.1109/TCST.2007.903073
10. Xu B., Ding R., Zhang J., Cheng M., Sun T. Pump/valves coordinate control of the independent metering system for mobile machinery. *Automation in Construction*, 2015. 57. 98–111. https://doi.org/10.1016/j.autcon.2015.04.012
11. Ding R., Xu B., Zhang J., Cheng M. Bumpless mode switch of independent metering fluid power system for mobile machinery. *Automation in Construction*, 2016. 68. 52–64. https://doi.org/10.1016/j.autcon.2016.04.006

12. Ding R., Xu B., Zhang J., Cheng M. Self-tuning pressure-feedback control by pole placement for vibration reduction of excavator with independent metering fluid power system. *Mechanical Systems and Signal Processing*, 2017. 92. 86–106. https://doi.org/10.1016/j.ymssp.2017.01.012

13. Cheng M., Zhang J., Xu B., Ding R. An electrohydraulic load sensing system based on flow/pressure switched control for mobile machinery. *ISA Transactions*, 2020. Vol. 96. P. 367–375. https://doi.org/10.1016/j.isatra.2019.06.018

14. Abuowda K., Okhotnikov I., Noroozi S., Godfrey P., Dupac M. A review of electrohydraulic independent metering technology. *ISA Transactions*, 2020. 98. 364–381. https://doi.org/10.1016/j.isatra.2019.08.057

15. Nguyen T. H., Do T. C., Ahn K. K. Independent Metering Valve: A Review of Advances in Hydraulic Machinery. *Journal of Drive and Control*, 2020. 17 (4). 54–71. https://doi.org/10.7839/ksfc.2020.17.4.054

16. Liu W., Li Y., Li D. Review on Inlet/Outlet Oil Coordinated Control for Electro-Hydraulic Power Mechanism under Sustained Negative Load. *Applied Sciences*, 2018. 8 (6). 886. https://doi.org/10.3390/app8060886

17. Weber J. Independent metering systems. *International Journal of Hydromechatronics*, 2018. (1). 91–106. https://doi.org/10.1504/IJHM.2018.090307

18. Lübbert J., Sitte A., Weber J. Pressure compensator control – a novel independent metering architecture. *Proceedings of the 10th International Fluid Power Conference*, 2016. 231–245

19. Kolks G., Weber J. Modiciency – Efficient industrial hydraulic drives through independent metering using optimal operating modes. *Proceedings of the 10th International Fluid Power Conference*, 2016. 1. 105–120

20. Xu B., Cheng M. Motion control of multi-actuator hydraulic systems for mobile machineries: Recent advancements and future trends. Frontiers of Mechanical Engineering? 2018. Vol. 13, No. 2. P. 151–166. https://doi.org/10.1007/s11465-018-0470-5

21. Ding R., Zhang J., Xu B., Cheng M. Programmable hydraulic control technique in construction machinery: Status, challenges and countermeasures. *Automation in Construction*, 2018. 95. 172–192. https://doi.org/10.1016/j.autcon.2018.08.001

22. Ding R., Zhang J., Xu B., Cheng M., Pan M. Energy efficiency improvement of heavy-load mobile hydraulic manipulator with electronically tunable operating modes. Energy Conversion and Management. 2019. Vol. 188. P. 447–461. https://doi.org/10.1016/j.enconman.2019.03.023

23. Lyu L., Chen Z., Yao B. Development of pump and valves combined hydraulic system for both high tracking precision and high energy efficiency. *IEEE Transactions on Industrial Electronics*, 2019. 66 (9). 7189–7198. https://doi.org/10.1109/TIE.2018.2875666

24. Vukovic M., Leifeld R., Murrenhoff H. Reducing fuel consumption in hydraulic excavators – A comprehensive analysis. *Energies*, 2017. 10 (5). 687. https://doi.org/10.3390/en10050687

25. Козлов Л. Г. Наукові основи розробки систем гідроприводів маніпуляторів з адаптивними регуляторами на основі нейромереж для мобільних робочих машин : дис. ... д-ра техн. наук : 05.02.02. Київ : НТУУ «КПІ», 2015. 421 с.

26. Піонткевич О. В. Підвищення ефективності багаторежимного гідроприводу фронтального навантажувача : дис. ... канд. техн. наук : 05.02.02. Київ, 2019. 249 с.

27. Лозінський Д. О., Піонткевич О. В., Сиротін О. А. Інноваційні підходи до підвищення енергоефективності електрогідравлічних систем. *Наукові праці Вінницького національного технічного університету*, 2025. № 2. https://doi.org/10.31649/2307-5376-2025-2-214-221

28. Лозінський Д. О., Сиротін О. А. Експериментальний стенд для дослідження характеристик електрогідравлічних систем для роботи з пасивним навантаженням. *Наукові праці Вінницького національного технічного університету*, 2025. № 4. https://doi.org/10.31649/2307-5376-2025-4-164-171

29. Lozinskyi D., Piontkevych O., Serdiuk O. Investigation of dynamic characteristics of a hydraulic drive for loading and unloading machines. International Journal of Mechatronics and Applied Mechanics. 2026. Issue 25, Vol. II. P. 39–49. https://doi.org/10.17683/ijomam/issue25/v2.4

*Дата першого надходження статті до видання 11.09.2026*
*Дата прийняття статті до друку після рецензування 15.10.2026*
*Дата публікації (оприлюднення) статті 04.11.2026*
*Стаття поширюється на умовах ліцензії відкритого доступу(CC BY 4.0)*

# РЕЖИМИ КЕРУВАННЯ В ГІДРОПРИВОДІ З НЕЗАЛЕЖНИМ КЕРУВАННЯМ ПОТОКАМИ ПРИ РІЗНИХ УМОВАХ НАВАНТАЖЕННЯ

**О. А. Сиротін[1], Д. О. Лозінський[1]**
[1] *Вінницький національний технічний університет*

***Анотація***

Розглянуто гідропривод мобільної машини з пасивним навантаженням, побудований на пропорційних розподільчих елементах, які незалежно керують потоками робочої рідини на вході та виході гідроциліндра, і керованих зворотних клапанах, що забезпечують герметичність його робочих камер. Показано, що при зміні маси вантажу, знака сили навантаження відносно швидкості та заданої швидкості штока така структура потребує вибору режиму керування — призначення регулювального і повністю відкритого розподільчих елементів та стану джерела живлення. Виділено чотири режими: керування на вході, керування на виході з розвантаженням насоса, комбіноване керування і керування подачею насоса. Обґрунтовано квазістатичну постановку задачі, сформульовано припущення і складено систему рівнянь сталого режиму, яка містить рівняння рівноваги сил на поршні, рівняння витрат через розподільчі елементи та обмеження за кавітацією, допустимим тиском, подачею насоса і керованістю регулювального елемента. Критерієм порівняння режимів прийнято сумарний перепад тиску на регулювальних елементах, додатковими показниками — потужність, спожиту від насоса, і ККД передачі. На прикладі стрілового контуру фронтального навантажувача виконано розрахунок для діапазону мас вантажу, обох знаків сили навантаження і кількох заданих швидкостей, виділено недопустимі поєднання умов та їх причини. Побудовано карту режимів у координатах «маса вантажу — задана швидкість» для зустрічного і попутного навантаження; встановлено, що межі областей оптимальності визначаються знаком сили навантаження, відношенням заданої витрати до подачі джерела і потрібним відкриттям вихідного розподільчого елемента. На умовному робочому циклі навантажувача проаналізовано зменшення енергії, спожитої від насоса, при перемиканні режимів за умовами навантаження порівняно зі спільним керуванням входом і виходом. Результати призначені для синтезу алгоритмів керування гідроприводами мобільних машин з незалежним керуванням потоками.

***Ключові слова:*** пропорційний розподільчий елемент, керований зворотний клапан, квазістатична модель, сумарний перепад тиску, кавітація, фронтальний навантажувач, розвантаження насоса, енергоефективність.

**DOI https://doi.org/10.32782/1994-4691-2026-1-77-9**
UDK 621

# EXPERIMENTAL TEST BENCH FOR INVESTIGATING THE CHARACTERISTICS OF A HYDRAULIC DRIVE WITH AN ANTI-SLIP DEVICE

# ЕКСПЕРИМЕНТАЛЬНИЙ ВИПРОБУВАЛЬНИЙ СТЕНД ДЛЯ ДОСЛІДЖЕННЯ ХАРАКТЕРИСТИК ГІДРОПРИВОДУ З АНТИБУКСУВАЛЬНИМ ПРИСТРОЄМ

V. O. Trehubov[1], graduate student ORCID: 0009-0004-1022-366X
O. V. Piontkevych[1*], Ph.D., Associate Professor ORCID: 0000-0002-3460-8060

[1] *Vinnytsia National Technical University, Vinnytsia, Ukraine*
*e-mail: piontkevych@vntu.edu.ua.

**Abstract**. The article presents the development and methodological substantiation of a specialized experimental test bench for investigating the characteristics of a hydrostatic drive with an anti-slip control system. The study used hardware-in-the-loop (HIL) modeling methods, stall test (maximum-load test) and transient response test protocols. The scientific novelty lies in the comprehensive assessment of the transition from passive flow dividers to systems of individual electronic control of hydraulic motor displacement. The proposed control algorithms are expected to provide more effective damping of critical pressure pulsations than classical proportional controllers. The practical value of the work lies in providing accurate efficiency mapping, which creates a basis for optimizing energy saving in hybrid technology and the modern mobile machines.

**Keywords**: hydraulic drive, anti-slip device, experimental test bench, control algorithms, hydraulic motor.

## Introduction.

Hydrostatic transmission of mobile machines is a system for transmitting mechanical energy from the prime mover to the drive wheels using hydrostatic pressure of a working fluid [1, 2]. Due to their ability to provide continuous and smooth speed control, extremely high specific power, low inertia of moving masses and the possibility of effective dynamic braking, hydrostatic transmissions have become the absolute standard for a wide range of mobile machinery [3]. This category includes agricultural tractors, combine harvesters, crop protection machines, construction machinery, skid steer loaders, excavators, road paving machines and modern unmanned ground vehicles [4, 5]. However, one of the most important and most complex problems that arise during the operation of such specialized machines in difficult conditions (off-road, snow, ice, viscous soil, rocky slopes) is the loss of traction of the wheels with the supporting surface, which inevitably leads to wheel slip [6, 7].

To fundamentally solve this problem, various anti-slip devices and traction control systems are being developed and implemented, which limit wheel slip and dynamically redistribute traction effort and torque between the wheels [4, 8]. The creation and implementation of anti-slip devices for hydrostatic transmissions remains a difficult scientific and technical task due to the nonlinearity of the characteristics of the interaction of the drive with the supporting surface. Anti-slip devices from the company "Poclain Hydraulics" demonstrate high efficiency [9, 10], but require adaptation to specific operating conditions and integration with existing domestic control systems. Therefore, the development of our own solutions and specialized stands for their testing is relevant.

## Literature Review.

Modern hydrostatic transmissions of high-mobility vehicles are built according to a closed hydraulic circuit [11]. In such a circuit, the output of the main pump is connected directly to the input of the hydraulic motor (or a system of parallel-connected motors), and the output from the motor is returned directly to the pump suction, bypassing a large hydraulic tank. An additional make-up pump and make-up circuit are used to compensate for internal leaks and cooling.

Vehicle traction control fundamentally boils down to optimizing the micro- and macroscopic forces of interaction between a pneumatic tire (or track) and a supporting surface. In order to develop an adequate control algorithm on an experimental test bench, it is necessary to rely on mathematical models of the longitudinal dynamics of the vehicle and differential equations of the characteristics of the hydraulic circuit [12, 13].

To overcome the differential effect of parallel-connected hydraulic motors, several fundamentally different engineering and algorithmic approaches have been proposed and investigated over the past decade. Each of these approaches has its own advantages, disadvantages, and requires a specific experimental test bench architecture for full validation.

Conceptually, the simplest solution was to install flow dividers or special synchronizing valves in the hydraulic circuit [14]. These devices, often built on the basis of spool or gear dividers, forcibly branch the total flow from the pump into equal parts, regardless of the pressure drop across each individual hydraulic motor. The reviewed studies on a self-propelled plant protection machine showed that the introduction of a synchronizing valve allowed to significantly reduce wheel slip in field conditions. At the same time, at speeds of 3 km/h and 6 km/h, the wheel slip coefficient was acceptable 3.79% and 6.17%, respectively. However, the main and critical disadvantage of this method is the large throttle energy losses.

Another approach is to use the automotive anti-slip regulation system [15]. The anti-slip regulation system constantly monitors the angular velocities of the wheels using encoders, and when excessive acceleration of one of them is detected, it applies braking to the slipping wheel.

A similar principle is used in hydrostatic transmissions [4], but a mechanical or hydraulic brake mechanism is applied to the wheel slip. The brake creates artificial external resistance on the hydraulic motor shaft, which leads to a forced increase in pressure in the general hydraulic line. This restores the pressure drop and allows the wheels with good traction to again receive torque for movement. As a result, for unmanned ground platforms weighing more than 300 kg, it has been theoretically and practically proven that the use of an external braking system instead of classic flow dividers minimizes the internal pressure drop in the hydraulic equipment and allows for much more efficient overcoming of difficult terrain, reducing the overall energy consumption of the platform.

The most technological solution in the concept of mobile hydraulic control is the use of hydraulic motors with independent adjustable working volume (for example, Poclain Twin Lock systems [9], Danfoss H1 series technology [16]). The essence of this solution is to completely abandon energy-consuming throttling or mechanical braking with friction pads. If a wheel starts to slip, the microcontroller instantly sends a PWM signal to the servo valve of the corresponding hydraulic motor to reduce its working volume. In this case, the traction force on the slipping wheel is proportionally reduced, which exactly corresponds to its current low tire–road adhesion coefficient. The torque is dynamically redistributed between the axles or wheels according to their ability to realize traction, and without overheating the mineral oil.

Leading scientific research centers and industrial corporations were analyzed regarding the experimental test bench and parameters they investigated for hydrostatic transmissions of mobile machines (Table 1).

Thus, the nonlinearity of the working fluid requires an inevitable transition from simple PID controllers to advanced control systems based on fuzzy logic, differential speed algorithms and active suppression systems of uncontrolled disturbances.

**Table 1. Analysis of the main achievements of research centers in the field of hydrostatic transmissions of mobile machines**

| Research Center | Research direction | Experimental base | Main achievements |
|---|---|---|---|
| Faculty of Mechanical Engineering and Marine Technology, University of Rostock [17] | Improvement of hydrostatic transmission control algorithms, compensation of nonlinearities, spatial trajectory tracking | A sophisticated cyber-physical test bench for testing electro-hydraulic systems in a HIL environment | The fundamental inefficiency of classic PID controllers due to the nonlinearity of the fluid has been experimentally proven. Optimal control, methods of active disturbance suppression and tracking differentiators have been implemented |
| School of Mechanical Engineering, University of Jinan [14] | Preventing wheel slip of agricultural machinery using valve equipment | Field test platform with laser measurement of actual distance traveled and wheel speed | Forced steering has been proven to reduce the slip coefficient from 6.17% to a stable 3.79% at an operating speed of 6 km/h, increasing the required stability |
| Faculty of Mechanical Engineering, Military University of Technology [4] | Mobility of unmanned platforms on rough terrain. Development of high traction forces on unstable soils | Computer simulation modeling followed by bench validation of hydraulic motor traction forces | It has been proven mathematically and practically that external electro-hydraulic braking outperforms flow dividers in terms of energy efficiency |
| College of Engineering, Nanjing Agricultural University [18] | Grey-box modelling of electro-hydraulic lifting mechanisms and intelligent algorithms with anti-slip device | Experimental test bench with proportional solenoid control valves | Using Whale Optimization Algorithm to identify hidden parameters. Extreme control accuracy achieved (RMSE of errors was only 0.33 mm) |
| Poclain / Danfoss firm innovations [9, 16] | Development of commercial systems CreepDrive, H1 traction control, Twin Lock | Certified Application Development Centers with truck dynamometers | esting of independent electronic control of engine displacement. Successful testing on gravel slopes, avoiding engine stall effects |
| College of Mechanical and Electronic Engineering, Shandong Agricultural University [19] | Analysis of the shifting quality of hydrodynamic continuously variable transmissions during critical hydraulic system failures | A full-fledged dynamometer for testing hydrodynamic continuously variable transmissions without starting the internal combustion engine | A safe methodology for testing hydraulic system failures on a bench without destroying a real, expensive tractor transmission has been created |
| AVIC The First Aircraft Institute [20] | Creation of miniature electrohydrostatic braking systems for aircraft with anti-slip algorithms | Inertial test bench with semi-real-life simulation of aircraft aerodynamics | Implementation of backstepping surfaces and on/off valves to increase reliability in mineral oil contamination conditions |

Modern developers are trying to rigidly separate the hydraulic power unit and software logic, transferring the lion's share of algorithm testing to a virtual environment with hardware locking. This will allow a real axial piston pump and motors to be physically rotated on the experimental test bench, while the inertia of a multi-ton machine, dynamic soil resistance and the percentage of tire wheel slip are calculated and simulated in real time by a powerful computer. At the same time, it applies the appropriate physical load to the hydraulic motor shafts through high-speed loading devices.

## Research Methodology.

The main goal of the article is to substantiate and develop the concept of an experimental test bench for a comprehensive study of working processes in the hydraulic drive of a mobile machine with an anti-slip device.

The experimental test bench is designed according to the modular principle, which allows to study both individual elements (pump, hydraulic motors, valve equipment) and the entire system as a whole. The primary power source of the test bench is a power-and-drive module that simulates the internal combustion engine of the vehicle. The use of real diesel engines in laboratories is associated with environmental problems and the complexity of control. Therefore, modern stands use powerful industrial asynchronous AC electric motors (with a power of 5 to 90 kW, depending on the scale of the transmission), which are controlled by high-precision Variable Frequency Drives. This allows you to programmatically create various dynamic torque characteristics, simulating, for example, turbocharger lag or a reduction in diesel-engine speed under sudden hydraulic overload.

For full testing of the anti-slip device, it is critical to be able to independently and extremely quickly change the load on each output hydraulic motor, physically simulating sharp spatial changes in the tire–road adhesion coefficient [18]. To do this, the output shafts of the hydraulic motors are rigidly connected to the loading devices.

A stand for testing highly dynamic fast-moving processes, such as the transition from normal operation to transient wheel slip, must record changes in indicators with a sampling frequency of at least 1 kHz, and ideally up to 5 kHz. The basic list of necessary precision sensors must include: pressure measurement, flow measurement, speed and position sensor, and torque measurement.

The study of modern high-speed proportional valves, which are widely used in anti-slip device, requires perfectly clean oil. Servo valves are extremely sensitive to micro-contamination, which can cause spool jamming [21, 22]. Strict industry standards categorically require the use of stands capable of maintaining oil cleanliness two ISO code levels higher than in a conventional working machine in the field. This is technologically achieved by installing special Hydrostatic Filter Groups (e.g. 9U-5899) with duplex filters (10 μm and 5 μm filtration) in the pressure and drain lines with visual and electrical clogging indication. In addition, since throttling during anti-slip device operation generates a huge amount of waste heat, the stand must have a main cooling system. It consists of water-oil heat exchangers or air radiators controlled by a PID thermostat, which guarantees the absolute maintenance of the liquid temperature within 50±2 ° C. Only under such conditions is the constancy of the kinematic viscosity of mineral oil ensured during experiments lasting many hours.

A modern experimental test bench is not just a set of drives, but a complex cyber-physical complex controlled by programmable logic controllers. To test the anti-slip algorithm, a real commercial control unit is usually installed on the stand. In this case, the Real-Time Target Machine calculates the full multi-body dynamics of the mass of the tractor or loader, reads the hydraulic motor speeds with microsecond-level timing resolution from the stand, mathematically calculates the virtual movement of the chassis and the tire–ground contact conditions. After that, the HIL system generates a control command for the dynamometers, instantly increasing or decreasing the physical resistance on the shaft, realistically

reproducing the transition to a low-adhesion surface in laboratory conditions [23]. Next, the measuring system monitors how the anti-slip device controller reacts to this sudden event.

Based on the analysis of the research methodology, the main recommendations for systems and subsystems for the configuration of the experimental test bench were formulated (Table 2).

**Table 2. Recommended systems and subsystems for the implementation of the experimental test bench**

| Main subsystems of the experimental test bench | Recommended specifications | Purpose in the experiment |
|---|---|---|
| Power and Drive Module | Electric motor, 5-90 kW, with variable-frequency drive control, 0-3000 rpm | Simulation of a car's internal combustion engine taking into account the nonlinear torque curve and speed drops |
| Dynamic Load Unit | Electromechanical servomotors with dynamometers | Highly dynamic simulation of ground resistance, instantaneous changes in tire–road adhesion coefficient |
| DAQ Module | Sampling frequency from 1 kHz, 16-bit analog-to-digital converter, digital buses CAN-bus, EtherCAT | Reliable synchronization of data collection of pressure, speed and micro-displacements of the main pump swash plate |
| Hydraulic Station | Working pressure 250-400 bar, flow up to 200-380 l/min, ultrafiltration ISO 16/13 | Ensuring stable physical, chemical and temperature conditions for the operation of the hydrostatic transmission. |

To implement the control of the experimental test bench processes on a programmable logic controller, the following basic structure of the anti-slip device control algorithm was developed:

1. System initialization (sensor polling, operating pressure check);
2. Main measurement cycle (with a period of 10 ms);
2.1. Reading the speeds of the hydraulic motors;
2.2. Calculation of the average theoretical speed;
2.3. Determination of the slip coefficient for each wheel;
3. Conditions for turning on the anti-slip device: IF the permissible slip is exceeded, THEN we generate a control signal for the valves of the anti-slip device of the corresponding wheel and correct the supply of the adjustable pump to minimize pressure losses, OTHERWISE we support the nominal flow distribution mode.
4. Return to step 2.

Furthermore, the modular architecture of the experimental test bench provides hydraulic ports and software interfaces for the direct integration of energy recovery systems. To fully explore energy recuperation within hydraulic drives, hydropneumatic accumulators and advanced directional control valves can be connected to the main circuit. This hardware flexibility allows for the physical simulation of regenerative braking, where the kinetic energy of the virtual vehicle, calculated by the HIL system, is converted back into hydraulic pressure and stored.

Thus, based on the analysis, complex requirements for the hardware and software components of the experimental test bench have been formed. The use of precision measuring equipment in combination with high-speed servo valves and dynamometers enables accurate reproduction of complex off-road operating conditions in laboratory conditions. The described control algorithm provides flexibility of settings for testing various strategies for redistribution of traction force.

The practical implementation of the proposed methodology will allow not only to investigate the effectiveness of commercial anti-slip devices, but also to develop and validate our own, adapted to domestic operating conditions, hydrostatic transmission control algorithms. The next step is to develop a scheme of an experimental test bench and analyze the required accuracy of the hydraulic drive characteristics in wheel slip simulation modes.

## Results.

After completing the stage of theoretical justification of the experimental test bench configuration, its scheme was developed. The general view of the experimental test bench scheme during test execution and recording of operating parameters is shown in Fig. 1. This allows you to visualize the layout of key hydrostatic transmission lines, loading devices and an array of measuring sensors involved in the study.

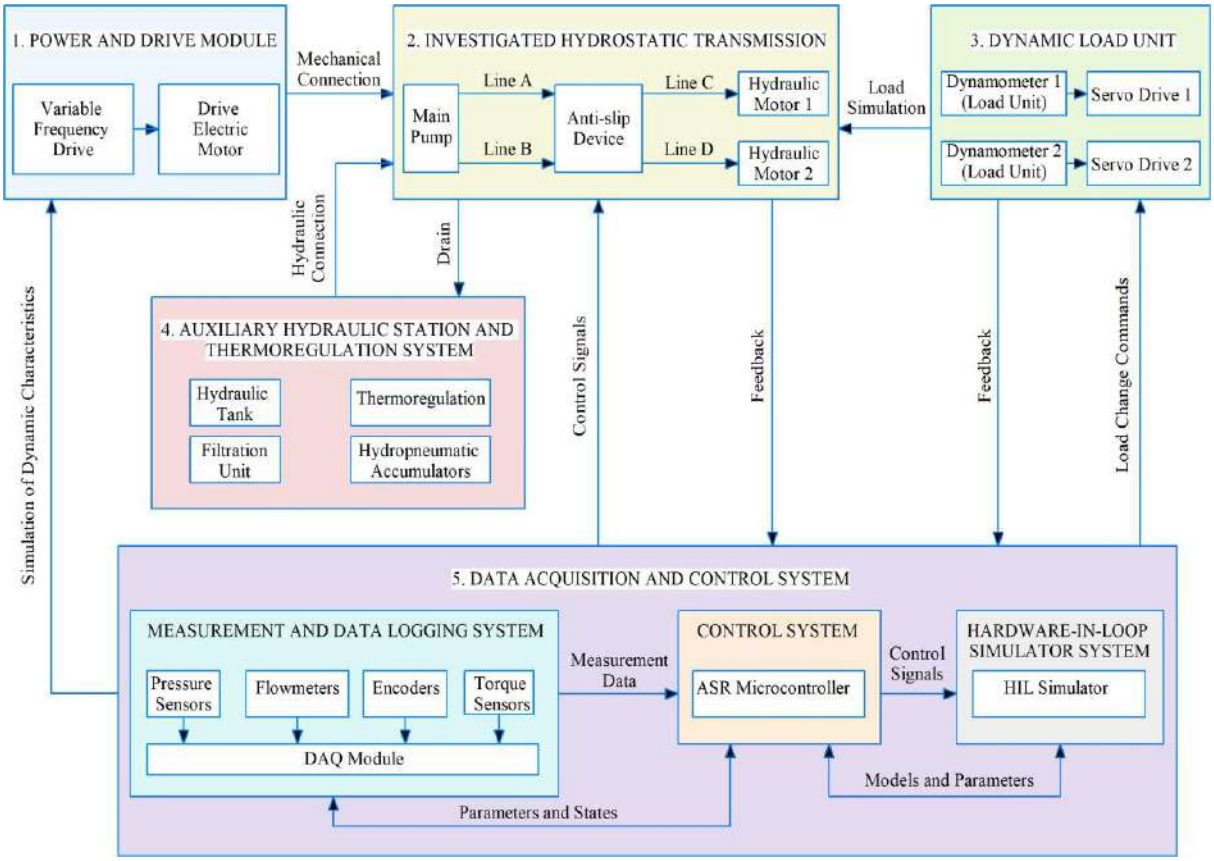



**Fig. 1. Scheme of the experimental test bench for studying the characteristics of a hydraulic drive with an anti-slip device.**

To ensure high accuracy of verification of nonlinear mathematical models, the use of modern high-speed analog-to-digital converters and precision sensors is envisaged. Fast transient processes that occur during sudden wheel slip and at the moment of anti-slip device activation are recorded.

Table 3 summarizes the key parameters studied on the experimental test bench, provided by the measuring equipment under different loading conditions and simulated tire–road adhesion coefficient. These results serve as an empirical basis for assessing the effectiveness of the proposed control algorithms.

The main experimental procedures include stall testing, transient-response testing, simulated wheel-slip testing, efficiency mapping, and energy-recovery testing. Stall test is a classic, but extremely important procedure for verifying the maximum traction capacity of hydraulic and mechanical systems without actual vehicle movement. On the bench, the hydraulic motors are forcibly blocked, the pump displacement is brought to maximum, and

the drive electric motor is accelerated to maximum speed. During the study, the maximum pressure achieved in the system is recorded, the correct operation of the pressure relief valves is checked, and the case drain is measured. To ensure the reliability of the results and prevent mineral oil degradation, the temperature of the working fluid during the test is strictly controlled by bench automation (maintained at about 50°C). This test will be used to verify whether the system can withstand the critical peak loads that occur when the traction control device redistributes 100% of the traction force to one wheel with a high tire–road adhesion coefficient to the ground.

**Table 3. Investigated parameters on the experimental test bench**

| Measured parameter | Sensor type | Measurement range | Accuracy |
|---|---|---|---|
| Pressure in the pressure and return lines | Strain gauge pressure transducer | 0...40 MPa | ±0,5% |
| Hydraulic fluid flow rate | High-pressure turbine flow meter | 5...150 l/min | ±1,0% |
| Hydraulic motor speed | Incremental encoder | 0...3000 rpm | ±2 rpm |
| Hydraulic fluid temperature | Thermal resistance | -20...+100 °C | ±0,5 °C |

Transient response testing and slip simulation involves operating the stand in the basic and most informative mode for studying Traction Control systems. The complex test protocol involves bringing the hydrostatic transmission to a stationary cruising mode with high symmetrical resistance, after which the HIL system instantly (10–50 ms) minimizes the load on one of the hydraulic motors, simulating a sudden loss of traction. The provoked uncontrolled slip causes a sharp drop in pressure and stops the support motor. Having identified a kinematic mismatch in the form of a critical increase in differential speed, the anti-slip drive instantly initiates countermeasures - reduces the displacement of the hydraulic motor. The stand equipment at high speed records the time of restoration of traction and the dangerous amplitude of pressure pulsations, which, thanks to the use of modern control algorithms, is damped 2.5-5 times more effectively compared to classic proportional regulators.

The experimental test bench additionally provides automated construction of multidimensional efficiency maps by testing the object in the entire matrix of pressures and speeds by recording the balance between input and useful output power. Highly accurate assessment of energy losses of the anti-slip device itself is critical for the latest electric forklifts and hybrid equipment. Given the specific balance of power, each joule of stored hydraulic energy directly extends the duration of autonomous operation of such machines from the battery. To comprehensively investigate this process, a dedicated energy recuperation testing protocol will be implemented. During simulated braking or downhill movement, the dynamic load units will operate in a driving mode, transferring mechanical energy back to the hydraulic motors, forcing them to act as pumps. The measuring system will evaluate the efficiency of capturing this reverse fluid flow into hydropneumatic accumulators and record the transient responses of the mechatronic valves during the rapid switch between traction and recuperation modes.

As a result, the data obtained after experimental studies will be used to develop and refine nonlinear mathematical models of the hydraulic drive of a mobile machine in simulation environments.

## Conclusions.

The creation of a specialized experimental test bench for studying the characteristics of a hydraulic drive with an integrated anti-slip device is an extremely complex multidisciplinary engineering task. This task combines the laws of ultra-high-pressure hydraulics, the applied theory of complex nonlinear spatial control of multi-mass systems, and the most modern information cyber-physical technologies. An analysis of scientific and technical sources over the past decade has been conducted, noting a clear transition from hydromechanical compensators (such as passive flow dividers) to intelligent high-speed systems for the individual electronic control of the working volume of each hydraulic motor.

It should be emphasized that this article primarily focuses on the methodological development, architectural design, and hardware validation of the experimental test bench itself. The developed hardware and software complex proves its suitability and readiness for a comprehensive assessment of such intelligent systems. The proposed control algorithms are expected to provide more effective damping of critical pressure pulsations than classical proportional controllers. Executing the proposed stall test and transient response protocols will provide extensive empirical data sets to evaluate the dynamic damping of critical pressure pulsations under simulated loss of traction.

In addition to assessing traction characteristics, the created stand opens up wide opportunities for automated efficiency mapping and the accurate measurement of measurement of small energy losses within the system. This creates a reliable scientific and technical basis for the further improvement of energy recovery systems in modern hydraulic drives, which is a critically important stage in the design of energy-efficient hybrid technologies and modern mobile machines. Ultimately, the developed test rig forms a robust experimental foundation for future comprehensive studies on energy recuperation in mechatronic hydraulic drives, enabling the practical validation of intelligent control strategies for regenerative braking.

## References


1. Mishra S.K., Wrat G., Ranjan P., Jose J.T., Das J. Precision and Stability in Hydrostatic Transmissions with Robust H∞ Control Under Parametric Uncertainties. *Journal of Experimental and Theoretical Analyses*, 2025. 3(2). 14. https://doi.org/10.3390/jeta3020014
2. Березюк О. В. Огляд конструкцій машин для збирання та первинної переробки твердих побутових відходів. *Вісник машинобудування та транспорту*. 2015. №1. С. 3–8.
3. Трегубов В. О., Піонткевич О. В. Огляд обладнання для гідравлічних трансмісій мобільних робочих машин. *Наукові праці Вінницького національного технічного університету*, 2025. Вип. 4. С. 198-208. https://doi.org/10.31649/2307-5376-2025-4-198-208
4. Łopatka MJ, Cieślik K, Krogul P, Muszyński T, Przybysz M, Rubiec A, Spadło K. Research on Terrain Mobility of UGV with Hydrostatic Wheel Drive and Slip Control Systems. *Energies*, 2023. 16(19). 6938. https://doi.org/10.3390/en16196938
5. Wang L., Fu W., Wang H., Meng Z., et al. Autonomous driving system for single hydrostatic transmission crawler tractor based on multi-modal steering control. *Frontiers in Plant Science*, 2026. 17. 1887292. https://doi.org/10.3389/fpls.2026.1887292
6. Xu, L., Wang, J., Zhao, S., Wu, Y., Li, X., Li, Y. Prediction of Tractor Traction Performance and Traction Efficiency in Hilly and Mountainous Terrain. *International Conference on Mechanical Design and Simulation*. Singapore: Springer Nature Singapore, 2026. 195–211 https://doi.org/10.1007/978-981-92-2440-1_17
7. Li Yu., Ding L., Zheng Z., Yang Q., et al. A multi-mode real-time terrain parameter estimation method for wheeled motion control of mobile robots. *Mechanical Systems and Signal Processing*, 2018. 104 P. 758–775. https://doi.org/10.1016/j.ymssp.2017.11.038
8. Li R, Yuan W, Ding X, Xu J, Sun Q, Zhang Y. Review of Research and Development of Hydraulic Synchronous Control System. *Processes*, 2023. 11 (4). 981. https://doi.org/10.3390/pr11040981
9. Веб сайт фірми Poclain Hydraulics. URL: https://poclain.com/ (Дата звернення: 06.07.2026)

10. Аврунін Г. А., Подригало М. А., Єременко А. В., Мороз І. І. Аналіз можливості застосування гідромотор-колес в трансмісіях швидкісних тракторів. *Вісник Національного технічного університету "ХПІ"*. Серія: "Гідравлічні машини та гідроагрегати", 2023. (2). С. 24–32. https://doi.org/10.20998/2411-3441.2023.2.03

11. Mahato A. C., Ghoshal S. K. An Overview of Energy Savings Approaches on Hydraulic Drive Systems. *International Journal Fluid Power*, 2020. 21 (1). 81–118. https://doi.org/10.13052/ijfp1439-9776.2114

12. Vieira D., Orjuela R., Spisser M., Basset M. Longitudinal vehicle control based on off-road tire model for soft soil applications. *IFAC-PapersOnLine*, 2021. 54 (10). 304–309. https://doi.org/10.1016/j.ifacol.2021.10.180

13. Xiong S., Wilfong G., Lumkes J. Jr. Components Sizing and Performance Analysis of Hydro-Mechanical Power Split Transmission Appliedto a Wheel Loader. *Energies*, 2019. 12 (9), 1613. https://doi.org/10.3390/en12091613

14. Zhang C., Li C., Zhao C., Li L., Gao G., Chen X. Design of hydrostatic chassis drive system for large plant protection machine. *Agriculture*, 2022. 12 (8). 1118. https://doi.org/10.3390/agriculture12081118

15. Нестеренко О. Г., Кунченко Т. Ю. Модульна імітаційна модель електромобіля з протибуксувальним керуванням. *Вісник Приазовського державного технічного університету*. Серія: Технічні науки, 2026. 2 (53). С. 46–55. https://doi.org/10.31498/2225-6733.53.2.2026.359912

16. Веб сайт фірми Danfoss. URL: https://www.danfoss.com/en/industries/mobile-hydraulics/dps/propel/traction-control/ (Дата звернення: 06.07.2026)

17. Dang N. D. Advanced control designs for output tracking of hydrostatic transmissions Doctoral dissertation, Dissertation, Rostock, Universität Rostock, 2022. 118 p. https://doi.org/10.18453/rosdok_id00003429

18. Sun X., Pan S., Song Y., Jiang C., Lu Z. A Distributed Parameter Identification Method for Tractor Electro-Hydraulic Hitch Systems Based on Dual-Mode Grey-Box Modelling. *Processes*, 2025. 13 (11). 3608. https://doi.org/10.3390/pr13113608

19. Study on the shifting quality of the CVT tractor under hydraulic system failure / Wang G. et al. *Applied Sciences*, 2020. 10 (2), 681. https://doi.org/10.3390/app10020681

20. Zhao J., Chang K., Ru F., Xie Y., Li W. Design and Verification of an Electro Hydrostatic Brake System. *Journal of Physics: Conference Series*, IOP Publishing, 2022. 2228 (1). 012020. https://doi.org/10.1088/1742-6596/2228/1/012020

21. Лозінський Д. О., Сиротін О. А. Експериментальний стенд для дослідження характеристик електрогідравлічних систем для роботи з пасивним навантаженням. *Наукові праці Вінницького національного технічного університету*, 2025. № 4. 8 с. https://doi.org/10.31649/2307-5376-2025-4-164-171

22. Лозінський Д. О., Піонткевич О. В., Сиротін О. А. Інноваційні підходи до підвищення енергоефективності електрогідравлічних систем. *Наукові праці Вінницького національного технічного університету*, 2025. Вип. 2. С. 1–8. https://doi.org/10.31649/2307-5376-2025-2-214-221.

23. Wu Z., Kang C., Li B., Ruan J., Zheng X. Dynamic modeling, simulation, and optimization of vehicle electronic stability program algorithm based on back propagation neural network and PID algorithm. *Actuators*, MDPI. 2024. Vol. 13, No. 3, p. 100. https://doi.org/10.3390/act13030100

*Дата першого надходження статті до видання 11.09.2026*
*Дата прийняття статті до друку після рецензування 14.10.2026*
*Дата публікації (оприлюднення) статті 04.11.2026*
*Стаття поширюється на умовах ліцензії відкритого доступу(CC BY 4.0)*

# ЕКСПЕРИМЕНТАЛЬНИЙ ВИПРОБУВАЛЬНИЙ СТЕНД ДЛЯ ДОСЛІДЖЕННЯ ХАРАКТЕРИСТИК ГІДРОПРИВОДУ З АНТИБУКСУВАЛЬНИМ ПРИСТРОЄМ

**В. О. Трегубов[1], О. В. Піонткевич[1]**
[1]*Вінницький національний технічний університет*

***Анотація***

Робота присвячена вирішенню складної мультидисциплінарної інженерної задачі – розробці та дослідженню спеціалізованого апаратно-програмного експериментального випробувального стенда для тестування гідростатичних трансмісій з інтегрованими антибуксувальним пристроєм. Головною метою є обґрунтування та розробка концепції експериментального випробувального стенду для комплексного дослідження робочих процесів у гідроприводі мобільної машини з антибуксувальним пристроєм. У процесі дослідження застосовано комплексний підхід, що поєднує закони гідравліки, теорію просторового керування багатомасовими системами та сучасні кіберфізичні HIL-технології. В процесі дослідження також проаналізовано продукцію інноваційних фірм Poclain та Danfoss, зокрема, їхні розробки: CreepDrive, H1 traction control, Twin Lock. Для верифікації параметрів реалізовано специфічні протоколи: тести на утримання з жорстким температурним контролем для оцінки внутрішніх витоків; випробування на перехідний відгук, які імітують раптову втрату зчеплення колеса з ґрунтом шляхом миттєвого скидання опору навантажувального пристрою; а також алгоритми побудови багатовимірних карт ефективності. Проведено ґрунтовний аналіз тенденції переходу від класичних пасивних гідромеханічних компенсаторів до швидкодійних систем індивідуального електронного керування робочим об’ємом гідромоторів. Наведені рекомендації систем із технічними характеристиками для комплектації експериментального випробувального стенду, а також діапазони та точність досліджуваних параметрів. Отримані результати створюють міцне науково-технічне підґрунтя для вдосконалення систем рекуперації енергії в гідравлічних приводах. Точний облік енергетичного балансу є критично важливим для розробки новітньої мобільної машини, де кожен збережений джоуль гідравлічної енергії прямо пропорційно продовжує час автономної роботи машини від акумуляторних батарей.

***Ключові слова:*** гідропривод, антибуксувальний пристрій, експериментальний випробувальний стенд, алгоритм керування, гідромотор.

**DOI https://doi.org/10.32782/1994-4691-2026-1-77-10**
UDK 621.225.001.4

# SUBSTANTIATION OF THE METHOD FOR INCREASING THE EFFICIENCY AND RELIABILITY OF FLUID COUPLINGS IN MINE CONVEYOR DRIVES WHEN USING WATER EMULSIONS AS A OPERATING FLUID

# ОБГРУНТУВАННЯ МЕТОДУ ПІДВИЩЕННЯ ЕФЕКТИВНОСТІ ТА НАДІЙНОСТІ ГІДРОМУФТ ПРИВОДІВ ШАХТНИХ КОНВЕЄРІВ ПРИ ЗАСТОСУВАННІ В ЯКОСТІ РОБОЧОЇ РІДИНИ ВОДНИХ ЕМУЛЬСІЙ

S. Voronin[1,2], PhD, Associate Professor ORCID: 0000-0001-8443-3222
V. Poletaev[1*], ORCID: 0009-0004-1544-4250

[1] *Ukrainian State University of Railway Transport, Kharkov, Ukraine,*
[2] *Dmytro Motornyi Tavria State Agrotechnological University, Ukraine,*
*e-mail: poletaev.vpolet@gmail.com

**Abstract**. The article addresses the urgent problem of increasing the reliability and efficiency of constant-fill safety-start fluid couplings in the drives of underground scraper chain conveyors. An analysis of the use of various types of operating fluids is conducted in terms of ensuring fire safety and optimizing key operational characteristics. The study aims to establish regularities between the mechanical characteristics of fluid couplings and the concentration and properties of operating fluids—specifically, water-oil emulsions of the HFA-E type. The research was carried out through bench testing of a serial GPE345U fluid coupling at various fill volumes and concentrations of Solcenic Pl Plus emulsol. It has been experimentally proven that increasing the emulsol concentration in the operating fluid significantly improves mechanical characteristics during transient operating modes of the fluid coupling, while minimizing heat generation and excessive energy losses. The scientific novelty lies in identifying the deviations in the behavior of water-oil emulsions from the laws of classic Newtonian fluids within the flow passage of fluid couplings. The practical value of the results consists in justifying the feasibility of using a 10% HFA-E type emulsion as the operating fluid of a fluid coupling to significantly improve efficiency and durability indicators.

**Keywords**: hydrodynamic drive, constant-fill fluid coupling, mine scraper chain conveyor, mechanical characteristic, oil-in-water emulsion, HFA-E, operating fluid, concentration.

## Introduction.

Hydrodynamic power transmissions have become widely used in the drives of belt and scraper mine conveyors [1]. During operation, the fluid coupling is a critical component that ensures their reliable performance.

In scraper conveyor drives (Fig. 1) with a power rating of 30–250 kW, it is technically viable to use constant-fill safety-start fluid couplings (closed-loop system), which provide the following functions:

– facilitated starting of conveyor electric motors under no-load and loaded conditions;

– maximum utilization of the electric motor's traction characteristics to start the conveyor in a loaded state;

– protection of the drive and the conveyor traction element against overloads by limiting the torque;

– load equalization between drives in multi-drive conveyors.

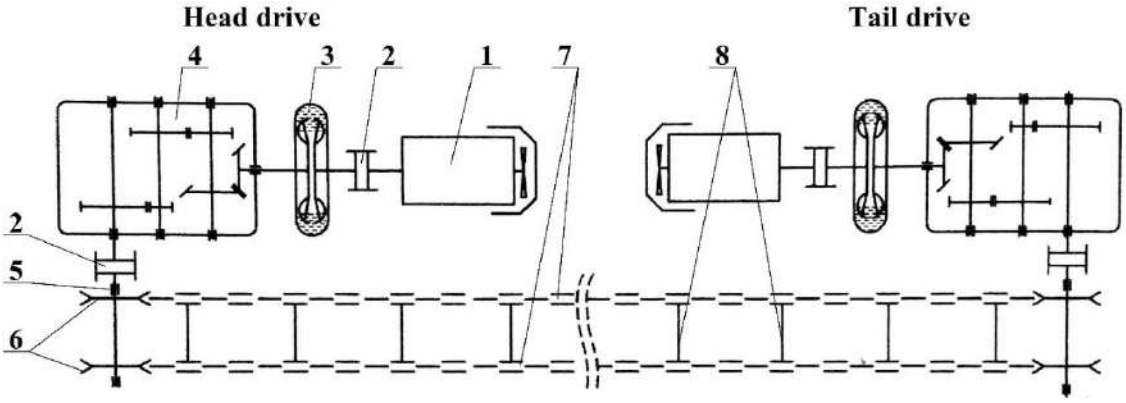



**Fig. 1 Kinematic diagram of a scraper conveyor equipped with fluid couplings in the drives: 1 – electric motor; 2 – connecting coupling; 3 – fluid coupling; 4 – gear reducer; 5 – drive shaft; 6 – sprockets; 7 – drag chains; 8 – scrapers.**

This type of fluid coupling features a relatively simple design, with only an internal operating fluid circulation loop and air cooling. In drives with a power output exceeding 250 kW, there arises a need for additional cooling of the operating fluid. This is achieved either by introducing an external circulation loop or by using fluid couplings with auxiliary chambers that increase the volume of the operating fluid, expand the cooling surface, and can provide a smoother, slower start. Both approaches lead to a more complex design and reduce the viability of using fluid couplings. In high-power drives, competing technical solutions are more frequently utilized, such as controlled drives with electromagnetic brakes [2], two-speed electric motors with flexible couplings, thyristor soft starters, variable frequency drives [3], and others [4].

Thus, along with their advantages and beneficial functions, fluid couplings also possess a number of fundamental drawbacks, such as high heat generation and energy losses, and therefore require improvement.

## Literature Review.

The conducted analysis identified the following directions for improving the performance of hydrodynamic transmissions:

**Increasing energy capacity.**

This is aimed at reducing the mass and dimensions of the hydrodynamic transmission and the drive as a whole, which intends to lower equipment costs, reduce installation expenses, and expand the feasibility of using compact drives when mining thin coal seams. This can be achieved through:

Using high-density operating fluids (ρ). The torque that a hydrodynamic drive can transmit has a direct linear dependence on ρ [5, 15]. This follows from the formula for determining torque derived from the general similarity theory of turbomachines:

$$M = \lambda \cdot \rho \cdot D^5 \cdot \omega^2, \quad (1)$$

where λ is the torque coefficient, which accounts for the shape of the fluid coupling's flow passage and the viscosity of the operating fluid; ρ is the density; D is the active diameter (in the case of fluid couplings, the outer blades diameter); ω is the rotational speed.

Optimizing the viscosity-temperature parameters of operating fluids. This reduces friction losses during the circulation of the operating fluid during operation, increases transmission efficiency, lowers heat generation, and consequently enables the use of more compact transmissions for a given power and rotational speed.

Enhancing the heat dissipation capability and heat capacity of the fluid. This is aimed at maintaining operation within a specified temperature range (without overheating) due to the properties of the operating fluid, the design and materials of the main components, and the

presence of a cooling circuit.

Optimizing the geometry of the flow passage. This includes reducing the thickness of the impeller blades and the surface roughness of the flow passage.

**Increasing reliability.**

This is aimed at improving the operational performance indicators of both the fluid coupling itself and the drive as a whole, while maintaining all functional properties. This can be achieved through:

Reducing thermal stress during operation by means of the operations [5, 15].

Using operating fluids with high anti-corrosion and anti-friction properties to prevent the failure of transmission components.

Simplifying the design of hydrodynamic systems and reducing the mass and dimensions of rotating parts to lower dynamic loads.

Using operating fluids with a high boiling point and low saturated vapor pressure, which is crucially important for closed-circuit fluid couplings to prevent additional loads on the housing. Concurrently, preference should be given to fluids with a high flash point, and in the conditions of underground coal mines – to non-flammable, non-toxic, and environmentally safe fluids.

**Reducing energy consumption in steady-state and transient conditions**

It is technically expedient to bring the transmission efficiency as close to 100% as possible in steady-state (nominal) operating modes that do not require impeller slippage. Generally, these modes account for about 90% of the drive operation time. Therefore, increasing efficiency by even 1–3% yields significant energy savings, reduces the thermal load on all transmission elements, and enhances drive reliability.

However, the hydrodynamic method of torque transmission requires operating fluid circulation, which is only possible when slip occurs S>0. This means that using purely hydrodynamic methods, we can only approach an efficiency of 100%. Currently, the best-performing fluid couplings achieve an efficiency of 97–98% in nominal mode (with a nominal slip of S = 2…3%).

The efficiency of a fluid coupling can be increased by optimizing its design (the shape of the flow passage, the number and tilt angle of the blades, etc.), by altering the parameters of the operating fluid, or by a combination of both methods.

As an example, transitioning from the use of I-20A industrial oil to a water-oil emulsion (3% oil, 97% water) as the operating fluid increases the nominal efficiency from 96.1% to 97.7% without modifying the design of the 1GPE400U fluid coupling [2]. Given the nominal power of 55 kW transmitted by this fluid coupling, power losses under nominal load in this specific case decreased from 2.12 kW to 1.25 kW, while the heat flux causing the coupling to heat up was reduced by 40%.

A transmission efficiency of 100% can be achieved by mechanically locking the impellers during operation [6, 7]. This possibility derives from the friction torque component $M_{FRIC}$ in the torque equation for a fluid coupling:

$$M = M_{HD} + M_{FRIC} + M_D - M_W \quad (2)$$

where M is the total torque transmitted by the fluid coupling; $M_{HD}$ is the hydrodynamic component (torque transmission via the energy of operating fluid flows); $M_{FRIC}$ is the torque transmitted by friction in bearings and seals, via internal fluid friction, or through locking elements (for couplings featuring a lockup system); $M_D$ is the dynamic component during non-steady-state (transient) conditions due to the acceleration of the fluid coupling's driven rotating masses and the operating fluid (equals 0 under steady-state conditions without acceleration); $M_W$ is the windage torque caused by the friction between the housing and the surrounding medium (air).

In practice, implementing a mechanical lockup requires a more complex fluid coupling

design and the integration of a control system. In most cases, this is impractical in terms of reliability, ease of maintenance, and manufacturing cost. Furthermore, during lockup, the fluid coupling loses several beneficial functions, such as protection against static and dynamic overloads, and load balancing between drives in multi-drive conveyors. Consequently, the use of impeller lockups in fluid coupling drives requires a cautious approach.

Locking the impellers or reducing slip can also be achieved by controlling the viscosity of the operating fluid—specifically, by transitioning from the "fluid coupling" mode (low viscosity, high circulation) to the "viscous coupling" mode (high viscosity, low or no circulation). The latter method remains under-researched but holds promise for the development and efficiency enhancement of hydrodynamic drives.

During transient operating modes (drive startup, overload operation), when slip can reach values from 5 to 100%, a large amount of energy is lost, converting into heat that warms up the operating fluid and the fluid coupling itself. Although such modes account for only about 10% of the drive operation time, their behavior significantly affects the operational reliability of both the fluid coupling itself and the drive as a whole.

Most scraper conveyor failures occur precisely during startup (especially when buried under coal), static overload, and dynamic overload during flight bar chain jamming. As a result, the temperature of the fluid coupling operating fluid rises, and under critical load and long duration, the thermal protection of the fluid coupling trips. According to data [2], in scraper conveyors equipped with fluid coupling drives, thermal protection tripping accounts for 14% of failures and 7.55% of downtime.

Recent studies on the failure distribution among main components during the operation of the TR-7A conveyor [8] are shown in Fig. 2.

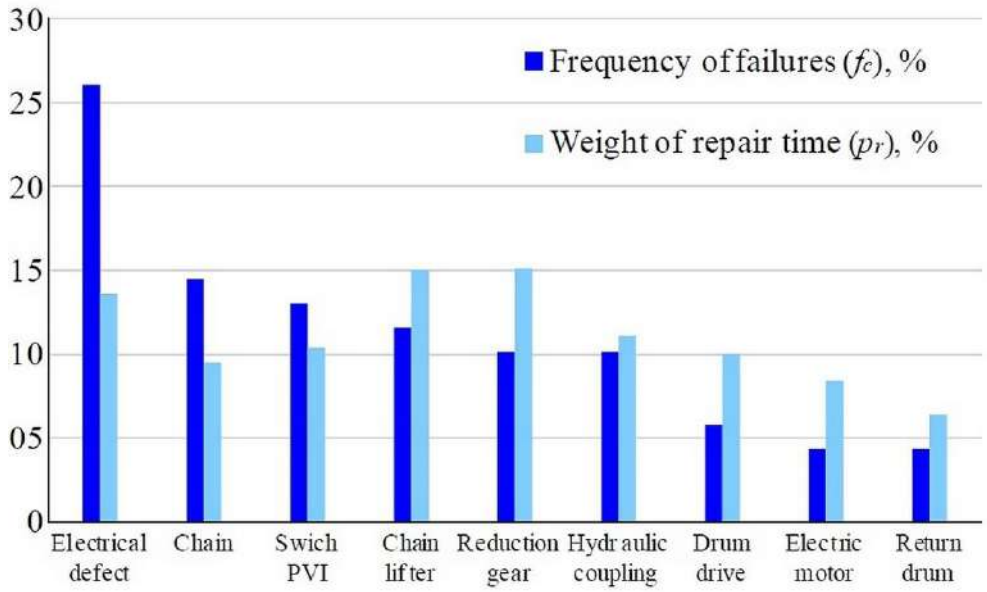



**Fig. 2 Failure distribution for main components during the operation of the TR-7A conveyor.**

The nature of the conveyor failure distribution indicates that fluid couplings account for approximately 10% of failures and 11% of time spent on restoration and repairs. Indirectly, the operation of the fluid coupling also influences the reliability of all listed components, including electrical equipment. Due to the cushioned motor startup, the cables and the electromagnetic starter experience high startup currents for a shorter duration, thanks to the starting and safety properties of the fluid coupling. That is, the correct operation of the fluid coupling can significantly increase the reliability of all conveyor components and reduce repair costs, both in terms of material and time.

Therefore, it is important to optimize the starting, acceleration, and static characteristics of fluid couplings. On one hand, this reduces wasted energy; on the other hand, it increases

the reliability and operational efficiency of the fluid coupling, electric motor, drive, and the machine (conveyor) as a whole. In the drive of a mine scraper conveyor, the joint operation of the fluid coupling and the induction motor must be considered. Figure 3 shows the superposition of their mechanical characteristics. The slip S is plotted along the abscissa axis (x-axis), and the torque M transmitted by the fluid coupling and the motor is plotted along the ordinate axis (y-axis).

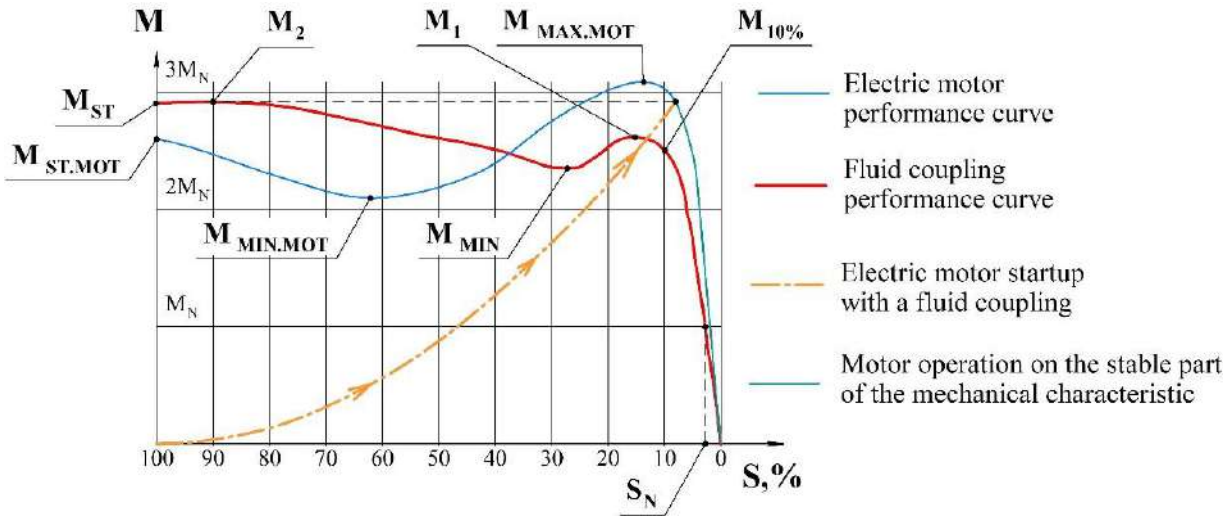



**Fig. 3 Mechanical characteristics of the electric motor, fluid coupling, and their joint operation in the scraper conveyor drive.**

Under a static load of an operating drive, the torque transmitted by the drive is determined by the fluid coupling, while the electric motor operates on the stable part of its mechanical characteristic, thereby being protected from overloads. This occurs due to the absence of a rigid connection between the driving shaft of the electric motor and the driven shaft of the gearbox – the fluid coupling separates the electric motor and the output part of the drive via a hydrodynamic method of torque transmission.

As the load increases, the slip S of the fluid coupling increases from the nominal value up to 100%, at which point the output shaft is braked (stalled condition). In this case, the electric motor operates under overload, but there is no stalling (drop-off) into the unstable part of its mechanical characteristic. Under these conditions, the motor's traction capabilities are fully utilized: the torque reaches values of 2…3 $M_N$ ($M_N$ is the nominal torque), and the current reaches values of 3…4 $I_N$ ($I_N$ is the nominal current).

At the moment of the drive startup, due to the slip S decreasing from 100% to the nominal value, the fluid coupling allows the motor to accelerate rapidly (up to 1 s) and pass the unstable part of the mechanical characteristic, where the currents reach 5.5…8.5 $I_N$. This provides protection for the electric motor during the starting mode.

To ensure protection of the electric motor and the drive against overloads on one hand, and to maximize the utilization of the motor's traction capabilities on the other, the mechanical characteristics of fluid couplings in scraper conveyor drives must meet the following requirements:

– The fluid coupling slip at nominal load, $S_N$ , must be as low as possible and should not exceed 3%, which ensures minimum efficiency $\eta \geq 97\%$:

$$S_N \leq 3\ \%; \tag{3}$$

– The maximum torque values that the fluid coupling can transmit must range from 0.85 to 0.95 of the maximum torque $M_{MAX.MOT}$ that the electric motor can develop on the stable part of its mechanical characteristic:

$$M_{ST}, M_1 , M_2 = 0{,}85…0{,}95\ M_{MAX.MOT;} \tag{4}$$

– The starting torque of the fluid coupling, $M_{ST}$, must be equal to or higher than the maximum torques $M_1$ and $M_2$ of the fluid coupling's static characteristic. This is a necessary condition for damping self-excited oscillations during chain jamming, which was experimentally proven by A.V. Leusenko [2]:

$$M_{ST} \geq M_1 , M_2; \quad (5)$$

– To ensure the required rigidity of the stable section of the mechanical characteristic of the fluid coupling, the minimum values of the maximum torque $M_1$ and the torque $M_{10\%}$ at a slip S = 10% are standardized as follows:

$$M_1 \geq 2\ M_N; \quad (6)$$

$$M_{10\%} \geq 1{,}7\ M_N; \quad (7)$$

– To ensure uniform and efficient drive acceleration and to prevent long-term operation of the fluid coupling with high slip values during overload, the minimum torque $M_{MIN}$ (the torque "dip") should be absent or is standardized by the following expression:

$$M_{MIN} \geq 2\ M_N; \quad (8)$$

– To protect the drive and the conveyor's flight bar chain assembly from dynamic loads (for example, during chain jamming), the maximum dynamic torque \(M_{dyn.c}\) transmitted by the fluid coupling during emergency stalling of its driven part must not exceed 3.5 $M_N$ within a braking time of t = 0.5 s [3]:

$$M_{DYN} \leq 3.5\ M_N. \quad (9)$$

Summarizing all the considered aspects, three main directions for regulating and improving the characteristics of fluid couplings can be distinguished:

– Changes in the design and geometry of the flow passage;
– Selection of the optimal fluid coupling filling volume;
– Optimization of the operating fluid parameters.

The first direction (**design-based**) can be applied at the stages of development, manufacturing, and bench testing. This direction has been foundational for fundamental research ever since the inventor of hydrodynamic transmissions, Prof. Föttinger. Currently, the largest amount of research in this field is conducted by Voith (Germany). The general optimization of the modern design of safety-starting fluid couplings for mine scraper conveyors produced in Ukraine by the "Svitlo Shakhtarya" plant was carried out in the 1980s and 1990s, based on research from the Skochinsky Institute of Mining and the works of engineers from their own research laboratory: A.V. Leusenko, V.K. Gavrilenko, and V.Y. Kapshtyk. The general dependencies of mechanical characteristics on the number of blades, flow passage parameters, and other design variables are provided in [9].

The second direction (**filling volume optimization**) is used during the testing and fine-tuning phases to match the characteristics to specific operating conditions once the design and operating fluid type have been finalized. As a rule, safety-starting fluid couplings are filled with operating fluid to 65...90% of the total internal cavity volume. Higher filling values correspond to higher values of transmitted torque M and power N. The optimal filling volume, which maximizes the traction, safety, and starting capabilities of the fluid coupling, is approximately 88% of the internal cavity volume. By reducing the filling volume, the torque can be regulated from $M_{MAX}$ down to $0{,}6M_{MAX}$. This method of selecting the optimal filling volume is used as an auxiliary tool during the final phase of pre-operational testing.

In our research, we examined the third path – **optimizing the composition of the operating fluid**, as it can improve the performance efficiency of both newly designed equipment and machinery already in operation. Design changes always require significant material costs, which are much higher than the cost of replacing the operating fluid. Practical experience with safety-starting fluid couplings has revealed that operating fluids significantly

affect both the mechanical characteristics of the couplings and their operational reliability. In our opinion, insufficient attention has been paid to this issue in previous studies. Therefore, it is crucial to establish the dependencies that will aid in selecting the optimal characteristics of the operating fluid.

We will examine the key requirements for operating fluids used in fluid couplings of coal mine conveyor drives.

Modern coal mine safety regulations [10, 11] require **the use of fire-resistant fluids only.** This requirement is due to the periodic discharge of overheated operating fluid when the thermal protection of fluid couplings is tripped. The tripping temperature of the protection system in modern fluid couplings ranges between +120...+150 °C, which is determined by the thermal stability of seal and bearing materials, as well as the allowable casing temperatures of +165...+170 °C upon contact with coal dust [12]. To prevent fires and explosions in Ukrainian mines, the use of mineral oils as operating fluids in hydraulic drives was discontinued in the 1970s. They were replaced by HFA-type oil-in-water emulsions consisting of water and emulsol in concentrations up to 20% (oil in water), which are completely non-flammable fluids (classified according to ISO 12922:2020 [13]). The transition to HFA-type fluids provided many advantages regarding their application in fluid couplings, but it also introduced certain technical difficulties compared to mineral oils. Below, we examine the criteria by comparing these two types of operating fluids.

HFA-type emulsions **must contain a package of anti-friction and anti-corrosion additives to compensate for the aggressive properties of water** toward metal parts and friction pairs. For the same purpose, in fluid couplings operating with emulsions, the bearings are lubricated with grease instead of the operating fluid and are equipped with additional seals. That is, bearing units in fluid couplings using mineral oils as operating fluids have a somewhat simpler design than those operating with HFA emulsions. The fluid couplings manufactured by the "Svitlo Shakhtarya" plant, which were used in this study, are adapted for operation with water emulsions; they feature two levels of protection (against overheating and overpressure) and are equipped with bearing units isolated from the operating fluid.

When selecting an operating fluid, it is necessary to ensure **compatibility with seal materials (elastomers).**

Operating fluids must have **low viscosity to reduce internal friction losses** and increase hydrodynamic efficiency during fluid coupling operation in the steady-state mode. In terms of this parameter, HFA-type emulsions have a major advantage over oils because they possess significantly lower viscosity and show less dependence of viscosity on temperature. It is worth noting that choosing the optimal viscosity of the operating fluid is a critical issue. As a result of our research, we obtained findings indicating more complex dependencies than those considered in classical sources (see below in the text).

In order to increase energy capacity, preference is given to fluids with **higher density**. HFA emulsions have a density 15...20% higher than mineral oils, which provides a corresponding gain in the torque and power that the fluid coupling can transmit.

During the operation of hydrodynamic transmissions in starting modes and during overloads under steady-state modes, a significant amount of heat is generated, which goes toward heating the operating fluid. To ensure the proper operation of the drive in these modes (without overheating), the operating fluid must effectively store thermal energy and dissipate it to the environment. It is most expedient to **use fluids with a higher specific heat capacity** (the ability to heat up less with the same amount of supplied heat) **and a higher thermal conductivity coefficient** (the ability to transfer heat within the fluid). HFA emulsions are twice as effective as oils in terms of specific heat capacity, and 4...5 times more effective in terms of heat transfer [14].

Operating fluids **must comply with environmental and sanitary standards and have the lowest possible cost**. Since HFA-type emulsions consist of more than 80% water, they have an advantage in these indicators not only over mineral oils but also over water-glycols

(HFC) and synthetic operating fluids (HFD), which can also be used in fluid couplings.

Table 1 presents a comparison of the performance indicators of various types of operating fluids for fluid couplings [5, 14, 15].

**Table 1. Characteristics of operating fluids for fluid couplings**

| Parameter / fluid type (ISO 6743-4) | Mineral oils | HFA (oil in water) | HFB (water in oil) | HFC (water-glycol) | HFD-U (synthetic fluid) |
|---|---|---|---|---|---|
| Water content, % | — | ≈ 95 (80 min) | 40…60 | 35…45 (18–20 for HFC-E) | — |
| Fire resistance (minimum ignition temperature), °C | flam-mable | non-flammable | +650 | +600 | +400 |
| Compliance with Section 3.1.1 of the 7th Luxembourg Report [11] | - | + | - | + | - |
| Fire resistance class according to Section 3.1.3 of the 7th Luxembourg Report [11] | H | A | E | B-C | G-H |
| Lubricating capacity | +++ | + | + | ++ | +++ |
| Kinematic viscosity at +60 °C, cSt | 6…18 | 0,5…3 | 18…25 | 10…25 | 14…25 |
| Density, kg/dm³ | 0,85…0,9 | 0,99…1 for HFA-E, 1…1,15 for HFA-S | 0,92…1,05 | 1,07…1,14 | 0,91…0,93 |
| Specific heat capacity relative to mineral oil | 1 | 2,3 | 1,8 | 1,8 | 0,7 |
| Thermal conductivity relative to mineral oil | 1 | 4 | 5 | 2,5 | 0,9 |
| Relative cost | 1 | 0,5 | 0,5 | 3 | 6 |

As can be seen from the table, only HFA and HFC-type fluids fully comply with fire safety regulations. One of the leading manufacturers of hydrodynamic transmissions, "Voith Turbo" (Germany), recommends HFD-U class fluid as fire-resistant, considering it one of the primary options alongside HFA fluids [5, 16]. In essence, HFD-U fluid is a synthetic substitute for mineral oil [17] and can be used as a fire-resistant fluid in industrial gearboxes of mining equipment and in metallurgy. However, for fluid couplings operating in mines hazardous due to gas and coal dust, which are typical for Ukraine, the use of HFD-U fluid is impossible due to its non-compliance with safety regulations.

Based on an aggregate assessment of all factors, it is evident that HFA-type emulsions are the most expedient choice for hydrodynamic couplings under coal mine conditions. In the mines of Ukraine and Eastern European countries, the most widespread practice is the use of emulsions based on the Solcenic Pl Plus concentrate (manufactured by FUCHS Petrolub SE, Germany). The data were obtained from surveys of technical departments at mines in the Donets Coal Basin (Donbas) and from open internet sources (tender procurement, Prozorro) for the period from 2009 to 2025. In our research, we selected this operating fluid as the primary subject for analysis.

## Research Methodology.

In the vast majority of studies focusing on the performance characteristics of fluid couplings, homogeneous liquids—such as mineral and synthetic oils, water, and even vegetable oils, which are considered an environmentally friendly alternative to petroleum-based oils [18]—have been used as operating fluids. However, the operating fluids currently used in the fluid couplings of coal mine scraper conveyor drives are emulsions, i.e., two-component liquids. Therefore, establishing relationships between fluid coupling characteristics and the composition and properties of HFA-type operating fluids represents an urgent contemporary problem addressed in this study.

In this work, a pilot study was conducted to trace the dependence of the torque transmitted by the fluid coupling on the concentration of the water emulsion. Water emulsions of the HFA-E type based on Solcenic Pl Plus concentrate (a mineral oil-based concentrate) were investigated. The concentration recommended by the manufacturer has changed over time. In the 2000s and 2010s, it was recommended to use a 0.5–2% emulsion; currently, Fuchs Lubricants Ukraine recommends using a 1.3–5% emulsion [19]. Practical experience demonstrates that saving on concentration compromises the operational reliability of mine hydraulics, and it is recommended to increase the concentration up to 5% [20]. In 2009, a survey of mechanical engineers at SE Sverdlovantratsit (Luhansk Oblast) revealed that increasing the emulsion concentration from 1.5% to 10% led to a 3.5-fold increase in the service life of fluid coupling seals. Consequently, it was decided to test the fluid couplings using operating fluids with the following volumetric content of concentrate in water: 1.5, 3, 5, and 10%.

The tests were performed on a GPE345U safety-start constant-filling fluid coupling using an STG110M test bench at the "Svitlo Shakhtarya" plant. The GPE345U fluid coupling has the following main technical specifications:

- Active diameter D = 345 мм;
- Internal cavity volume V = 6.26 $dm^3$ (l),
- Weight without motor half-coupling and flexible insert m = 32 kg;
- Total weight (including motor half-coupling and flexible insert) M = 46.5 kg;
- Rated power $N_n$ = 22…30 kW at a motor rotational speed $n_1$ = 1480 rpm.

The design and operating principle of safety-start fluid couplings manufactured by the "Svitlo Shakhtarya" plant are discussed in detail in [2]. The installation layout of the GPE345U fluid coupling in conveyor drives and other machinery is shown in Fig. 4.

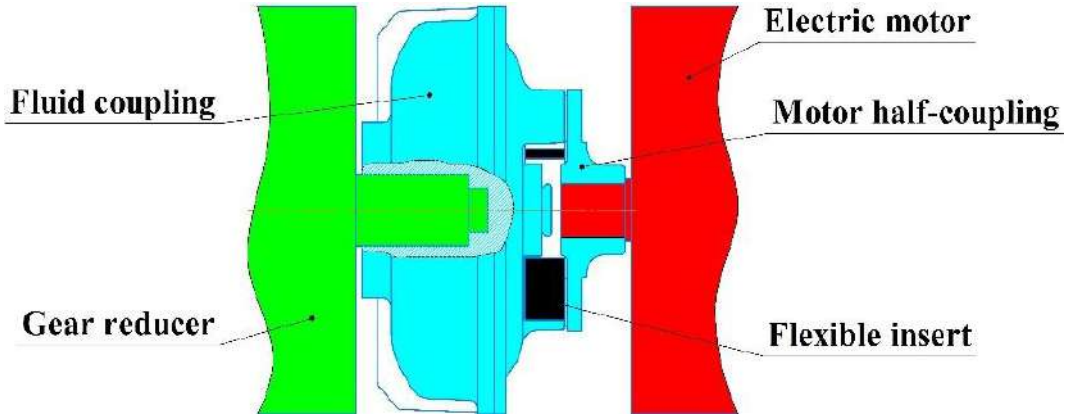



**Fig. 4. Installation diagram of a fluid coupling in machine drives.**

The mechanical characteristics were recorded at two different operating fluid fillings:

– 4.9 $dm^3$ (l), which constitutes 78% of the internal cavity volume and is used for operation with electric motors rated at $N_n$ = 22 kW;

– 5.3 dm³ (l), which constitutes 85% of the internal cavity volume and is used for operation with electric motors rated at $N_n$ = 30 kW.

Figures 5, 6, and 7 show the test bench for fluid couplings. The technical capabilities of the test bench allow for testing fluid couplings and electric motors with power ratings ranging from 11 to 500 kW. On the test bench, fluid coupling 4 is installed identically to its operational layout in machine drives (Fig. 4). The STG110M test bench measures the torque M and power N transmitted by the fluid coupling, as well as the rotational speeds of the driving part $n_1$ and the driven part $n_2$ (the pump and turbine impellers). The rotational speeds are measured by tachometers 10, which are mounted on the rear end of electric motor 1 (driving part) and on the shaft of mechanical brake 7 (driven part). Torque is measured using torque transducer shaft 5. One side of this shaft connects to the driven part of the fluid coupling, while the other side connects to transfer gearbox 6, which distributes the torque between brakes 7 and 8. The fluid coupling receives rotation from electric motor 1, which is mounted on support 2. Brakes apply the load while recording mechanical characteristics. Powder electromagnetic brakes 8 generate the load when recording static and start-up characteristics, as well as when determining slip S at fixed loads. Mechanical drum brake 7 applies emergency loads to simulate conveyor chain jamming within a braking time of $t \leq 0.5$ s [3]. Bench control (starting, setting the load level), speed monitoring, and load control are managed via control panel 9.

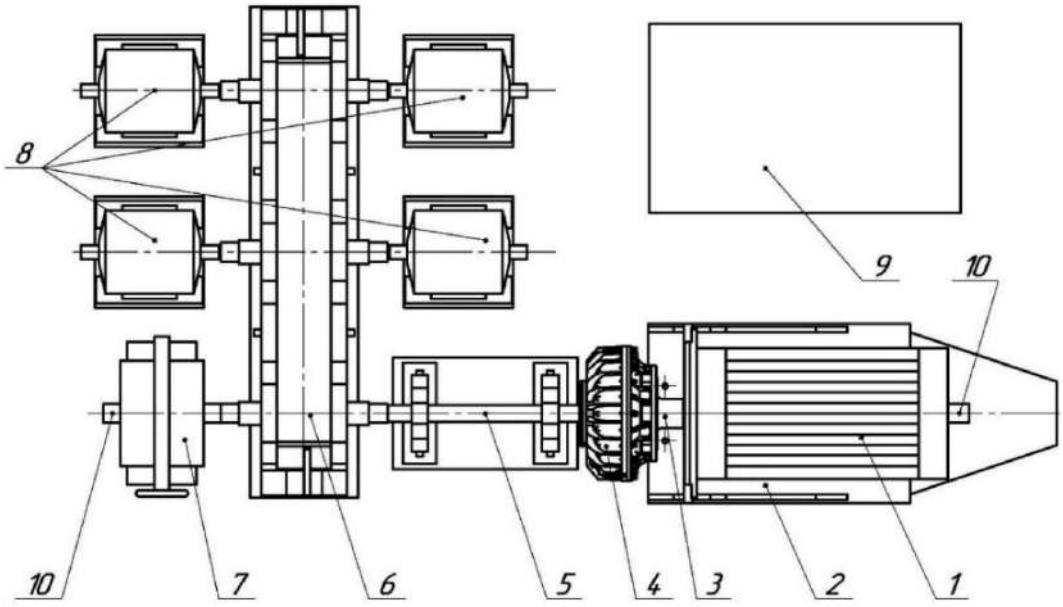



**Fig. 5. Schematic diagram of the STG110M test bench for fluid coupling testing: 1 – electric motor, 2 – electric motor support (base); 3 – motor half-coupling (connecting coupling); 4 – fluid coupling under test; 5 – torque transducer shaft; 6 – transfer gearbox; 7 – mechanical drum brake; 8 – powder electromagnetic brakes; 9 – control panel; 10 – tachometers.**

Rotational speeds are measured by two optical sensors (tachometers), which ensure a high response speed with an accuracy of ± 1 rpm. Their signals are sent to a computer to be recorded while capturing static, start-up (acceleration), locked-rotor (starting), and dynamic characteristics. They are also sent to the control panel to visualize rotational speeds under steady loads.

The torque measurement accuracy is at least ± 5 N·m. The torque transducer shaft transmits the signal to the computer for recording via Bluetooth wireless technology. Compared to the previously used contact-based data transmission via brushes, wireless technology reduces noise by an order of magnitude and improves measurement accuracy.

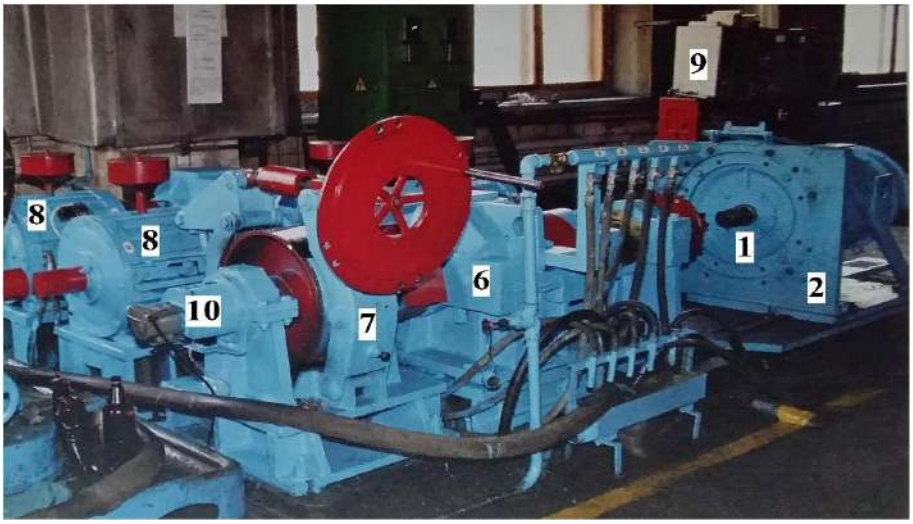



**Fig. 6. General view of the STG110M test bench for fluid coupling testing.**




**Fig. 7. Mounting location of fluid couplings for testing on the STG110M test bench.**

Load monitoring and visualization during the tests are performed using a wattmeter installed in the control panel. The wattmeter measures the active electrical power $N_A$ consumed by the electric motor with an accuracy of ± 0.5 kW. When creating the required mechanical load level, the value of the active electrical power was determined based on the electric motor efficiency using the formula:

$$N_A = N_M / \eta, \quad (10)$$

where $N_A$ is the active electrical power indicated by the wattmeter; $N_M$ is the mechanical power developed by the electric motor; $\eta$ is the electric motor efficiency.

During the tests, the following characteristics were recorded:

**a) Start-up (acceleration) characteristics.** The torque M, as well as the rotational speeds of the driving part $n_1$ and the driven part $n_2$, were recorded from the moment of start-up until the driven part reached its maximum speed under a specified load. The load was defined by the idle resistance torque of the powder brake with no voltage applied to it. The resistance torque in this case was 100…120 N·m, which accounted for approximately 80% of the nominal load at 22 kW and 60% at 30 kW.

**b) Static characteristics.** The driven part of the fluid coupling was gradually loaded from a minimum torque of 0,6…0,8 $M_N$ up to the locked-shaft state, where the speed of the driven shaft $n_2 = 0$ (slip S = 100 %), while recording the rotational speeds and torque. The nominal rotational speed of the driving shaft was $n_1 = 1495$ rpm. To eliminate the influence of

the inertia of rotating masses on the torque readings, the load was increased smoothly, ensuring a braking time of 15...20 s. To construct the torque M versus slip S characteristic curve, the speed readings $n_1$ and $n_2$ were converted using formula (11):

$$S = \frac{\omega_1 - \omega_2}{\omega_1} \cdot 100\% = \frac{n_1 - n_2}{n_1} \cdot 100\%, \quad (11)$$

where $\omega_1$ is the angular velocity of the fluid coupling driving part, rad/s; $\omega_2$ is the angular velocity of the fluid coupling driven part, rad/s; $n_1$ is the rotational speed of the driving part, rpm; $n_2$ is the rotational speed of the driven part, rpm.

**c) Locked-rotor (starting) characteristics.** The test was performed by starting the system with a completely locked (braked) driven shaft while recording the starting (stall) torque $M_{ST}$ – simulating the start-up of a conveyor drive under a coal blockage.

**d) Dynamic characteristics.** From the nominal rotational speed of the driven shaft, emergency braking was applied to bring it to a complete stop within 0.5 s, while recording the torque and rotational speeds. The maximum torque value is standardized and represents the dynamic torque $M_{DYN}$, which is used in structural strength calculations for drive components, the traction element, and conveyor housing parts.

**e) Measurement of slip $S_N$ at nominal load.** The required load level was set using the powder brake: $M_N$ = 142.5 N·m at $N_N$ = 22 kW and $M_N$ = 194 N·m at $N_N$ = 30 kW. The speeds $n_1$ and $n_2$ were recorded. Slip $S_N$ was calculated using formula (11). Oscillograms were recorded for all filling levels and concentrations. For static loading, they were converted into static characteristics, the general view and symbols of which are shown in Fig. 8.

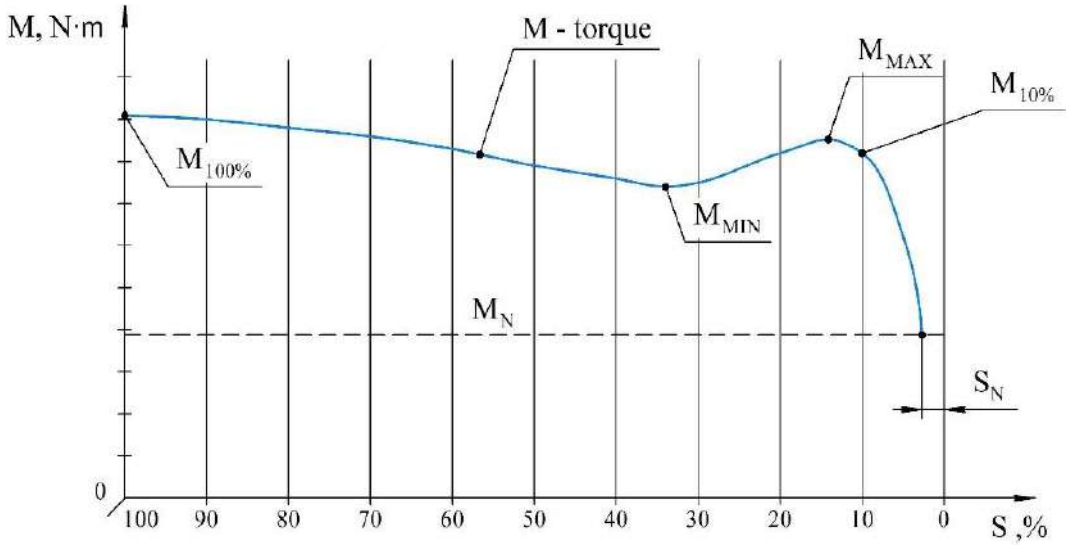



**Fig. 8. Parameters of static characteristics and accepted notation.**

Accepted notation in tables and figures:
$S_N$ – nominal slip,
$M_N$ – nominal torque,
$M_{10\%}$ – torque at S = 10 % slip,
$M_{MAX}$ – maximum torque on the stable part of the mechanical (static) characteristic curve,
$M_{MIN}$ – minimum torque on the unstable part of the mechanical (static) characteristic curve,
$M_{100\%}$ – torque at S = 100 % slip (with the driven part locked),
$T_{ST}$ – run-up (acceleration) time of the driven part after switching on the electric motor,
$M_{ST}$ – starting torque at S = 100 % slip (starting with a locked driven shaft),
$M_{DYN}$ – maximum torque during emergency braking within 0.5 s.

## Results.

For comparison, Fig. 9 shows the acceleration characteristics and static load at the same fluid filling of 5.3 dm³ under different emulsol concentrations: 1.5% (Fig. 9a) and 10% (Fig.9b).

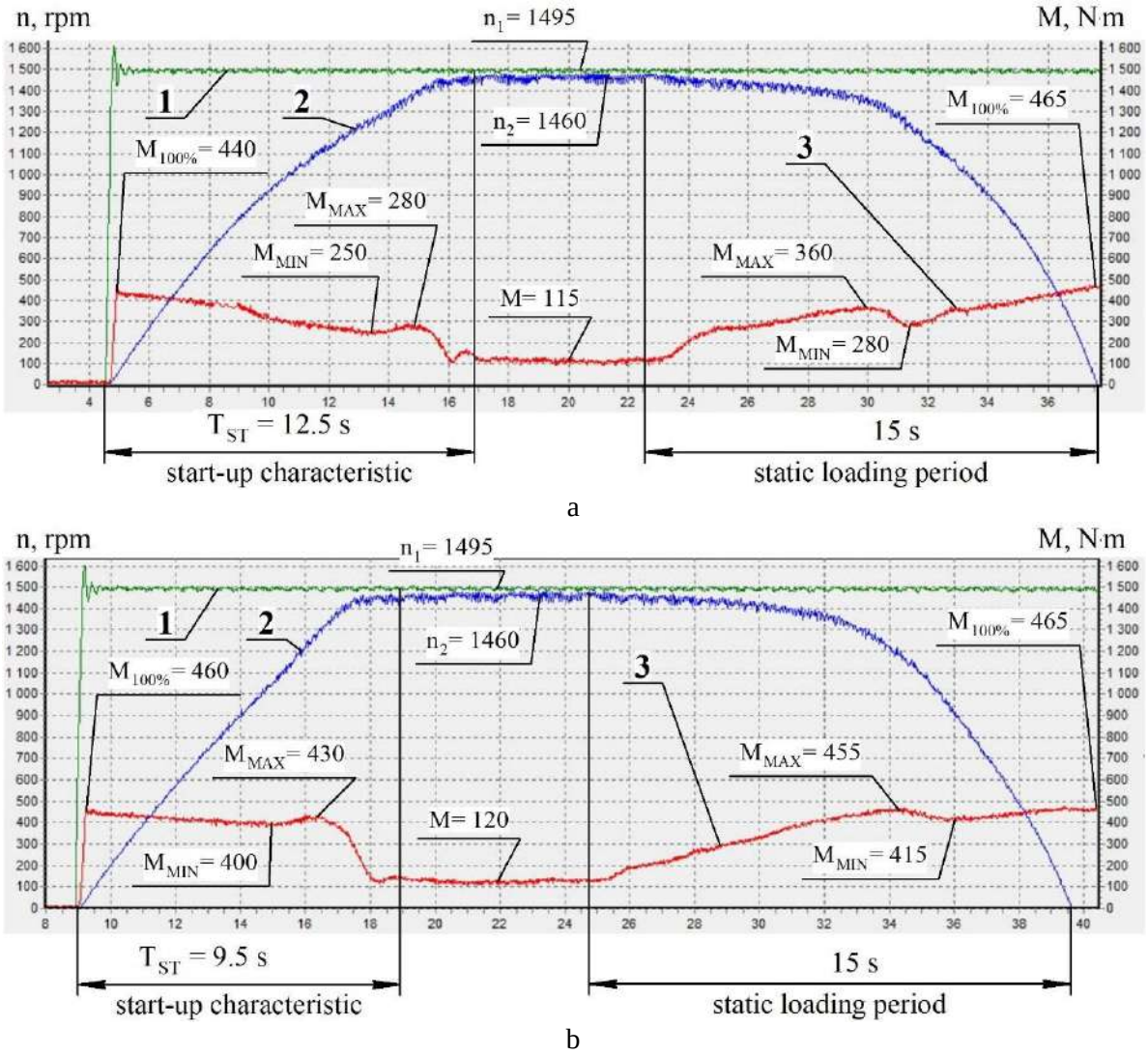



**Fig. 9. Start-up characteristics and static loading of the fluid coupling GPE345U with a 5.3 dm³ (l) fluid fill at different emulsol concentrations: a – 1.5%; b – 10%: 1 – speed curve of the driving part $n_1$ (electric motor); 2 – speed curve of the driven part $n_2$ (gear reducer); 3 – torque curve M.**

A lower emulsol concentration (Fig. 8a) corresponds to lower torque values. There is a noticeably large "dip" on the unstable part of the mechanical characteristic, along with a prolonged, inefficient run-up featuring a large torque drop and excessive fluid coupling operation time at high slip values (S). This can lead to increased heating of the operating fluid and the inability to start the conveyor under a coal overload. In contrast, at a 10% concentration (Fig. 8b), the start-up and static load curves exhibit no large drops or "dips" and meet the performance requirements for scraper conveyors.

A similar pattern is observed for both fluid fills (4.9 and 5.3 dm³) — as the concentration increases, the characteristics gradually approach more acceptable levels. For convenience of result analysis, all obtained data were plotted as overlaid static characteristics (Figs. 10, 11) and summarized in reference Tables 2 and 3.

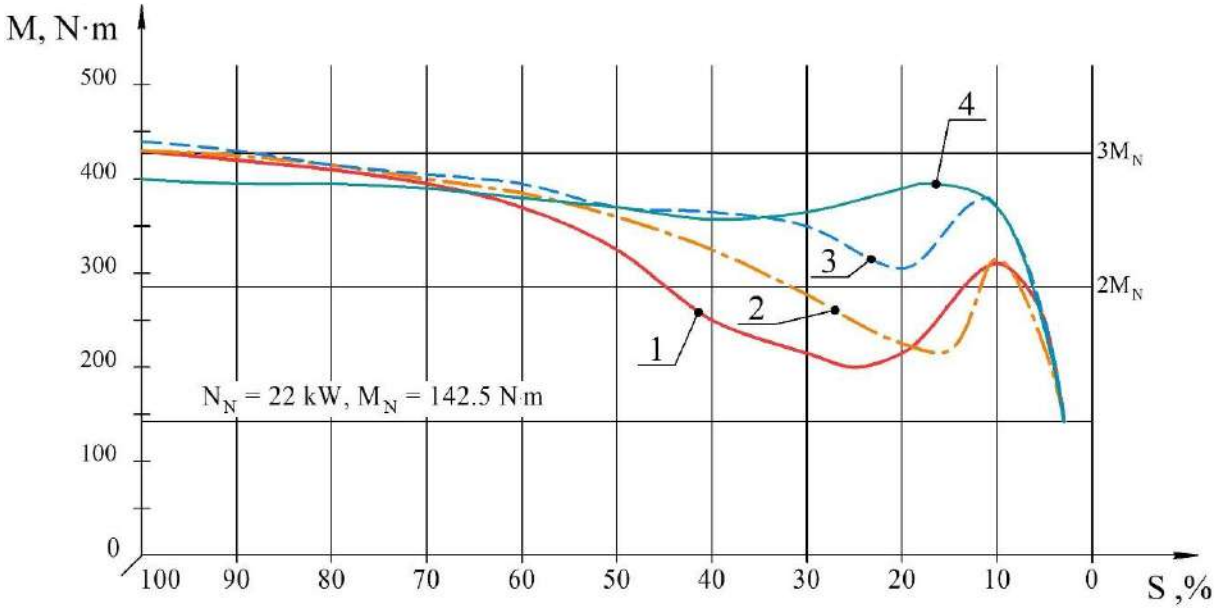



**Fig. 10. Static characteristics of the fluid coupling GPE345U with a 4.9 dm³ (l) fluid fill at different emulsol concentrations: 1 – torque curve at 1.5% concentration; 2 – torque curve at 3% concentration; 3 – torque curve at 5% concentration; 4 – torque curve at 10% concentration.**

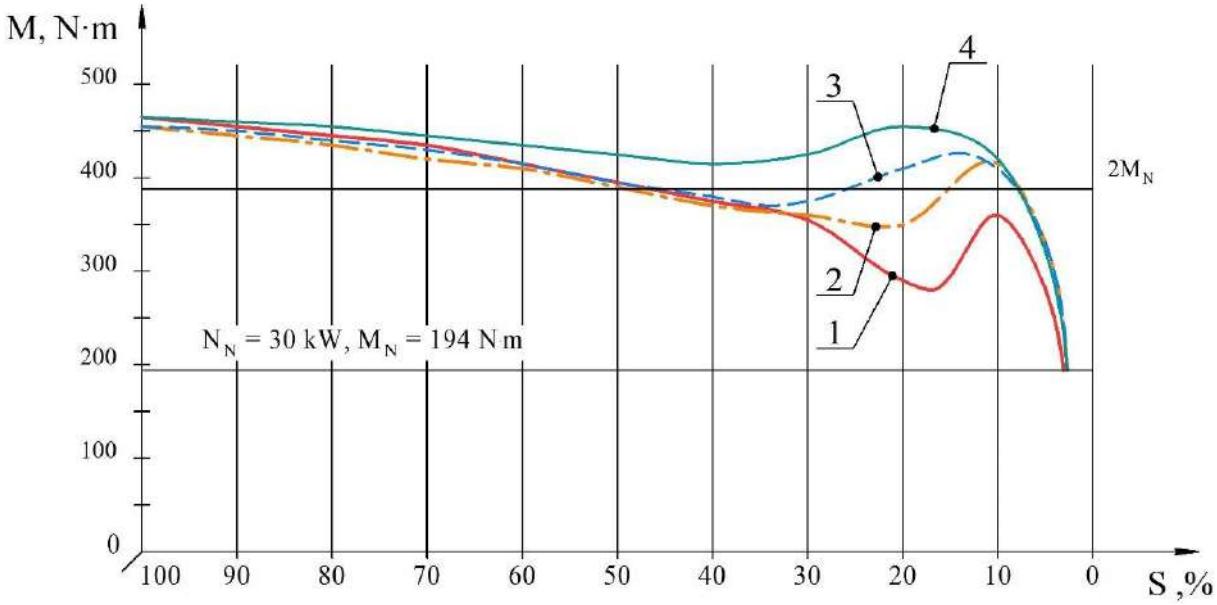



**Fig. 11. Static characteristics of the fluid coupling GPE345U with a 5.3 dm³ (l) fluid fill at different emulsol concentrations: 1 – torque curve at 1.5% concentration; 2 – torque curve at 3% concentration; 3 – torque curve at 5% concentration; 4 – torque curve at 10% concentration.**

In Tables 2 and 3, parameters that do not meet the performance requirements for scraper conveyor drives are highlighted in red. It is evident that operating fluid couplings with emulsions of 1.5...3% concentration fails to satisfy several criteria—see formulas (6), (7), and (8). Therefore, fluid coupling operation can be recommended with emulsions containing a Solcenic PL PLUS emulsol concentration of 5...10%.

The greatest deviations in the mechanical characteristics at low emulsol concentrations are associated with the occurrence of a "dip" on the unstable part of the mechanical characteristic at a slip of 10...40%. This is a negative phenomenon that leads to inefficient performance during transient modes–drive startup (especially under a coal overload) and operation with overloads.

**Table 2. Mechanical characteristics of the fluid coupling GPE345U. Operating fluid: Solcenic PL PLUS water emulsion at concentrations of 1.5, 3, 5, and 10%. Fluid coupling fill volume: 4.9 dm³ (l). Nominal load: $N_N$ = 22 kW, $M_N$ = 142.5 N·m.**

| Concentration | $S_N$, % | $M_{10\%}$, N·m | $M_{MAX}$, N·m | $M_{MIN}$, N·m | $M_{100\%}$, N·m | $T_{ST}$, s | $M_{ST}$, N·m | $M_{DYN}$, N·m |
|---|---|---|---|---|---|---|---|---|
| 1,5% | 2,9 | 310 (2,18$M_N$) | 310 (2,18$M_N$) | 200 (1,4$M_N$) | 430 (3,02$M_N$) | 17 | 385 (2,7$M_N$) | 490 (3,44$M_N$) |
| 3% | 2,9 | 250 (1,75$M_N$) | 315 (2,21$M_N$) | 215 (1,51$M_N$) | 425 (2,98$M_N$) | 16 | 385 (2,7$M_N$) | 498 (3,5$M_N$) |
| 5% | 2,9 | 370 (2,6$M_N$) | 380 (2,67$M_N$) | 305 (2,14$M_N$) | 440 (3,09$M_N$) | 11 | 396 (2,78$M_N$) | 500 (3,5$M_N$) |
| 10% | 3,0 | 370 (2,6$M_N$) | 395 (2,77$M_N$) | 357 (2,51$M_N$) | 400 (2,81$M_N$) | 11 | 390 (2,74$M_N$) | 470 (3,3$M_N$) |

**Table 3. Mechanical characteristics of the fluid coupling GPE345U. Operating fluid: Solcenic PL PLUS water emulsion at concentrations of 1.5, 3, 5, and 10%. Fluid coupling fill volume: 5.3 dm³ (l). Nominal load: $N_N$ = 30 kW, $M_N$ = 194 N·m.**

| Concentration | $S_N$, % | $M_{10\%}$, N·m | $M_{MAX}$, N·m | $M_{MIN}$, N·m | $M_{100\%}$, N·m | $T_{ST}$, s | $M_{ST}$, N·m | $M_{DYN}$, N·m |
|---|---|---|---|---|---|---|---|---|
| 1,5% | 3,1 | 360 (1,86$M_N$) | 360 (1,86$M_N$) | 280 (1,44$M_N$) | 465 (2,4$M_N$) | 12,5 | 445 (2,29$M_N$) | 538 (2,77$M_N$) |
| 3% | 2,7 | 415 (2,14$M_N$) | 415 (2,14$M_N$) | 347 (1,79$M_N$) | 455 (2,35$M_N$) | 11 | 435 (2,24$M_N$) | 510 (2,63$M_N$) |
| 5% | 2,8 | 410 (2,11$M_N$) | 425 (2,19$M_N$) | 370 (1,91$M_N$) | 455 (2,35$M_N$) | 10,5 | 435 (2,24$M_N$) | 528 (2,72$M_N$) |
| 10% | 2,7 | 425 (2,19$M_N$) | 455 (2,35$M_N$) | 415 (2,14$M_N$) | 465 (2,4$M_N$) | 9,5 | 450 (2,32$M_N$) | 528 (2,72$M_N$) |

The shape of the "dip" and the minimum torque $M_{MIN}$ clearly depend on the emulsol concentration. At the same time, the highest quality mechanical characteristics, featuring small drops in torque M at a slip S = 10...100 %, were observed at high concentrations (curves 3 and 4). Run-up efficiency is indicated by the parameter $T_{ST}$ (start-up time to nominal speed). Increasing the emulsion concentration from 1.5% to 10% reduces the start-up time by 25...35%. As noted previously, the startup was performed under a load of 0.6...0.8 $M_N$. Under real operating conditions with a nominal load, and even more so when starting a conveyor under overload, the start-up time, excess energy losses, and fluid coupling overheating will differ significantly across concentrations. This will crucially affect the conveyor's tractive characteristics and drive reliability. The parameter $M_{MIN}$ serves as an indicator of the conveyor's capability to start under an overload. As the emulsol concentration in the operating fluid increases, it rises:

- with a 4.9 dm³ fill volume and $N_N$ = 22 kW from 1,4$M_N$ to 2,5$M_N$
- with a 5.3 dm³ fill volume and $N_N$ = 30 kW from 1,44$M_N$ to 2,14$M_N$

Based on the obtained data, the relationships between the mechanical characteristics and the operating fluid concentration have been plotted.

Fig. 12 shows that the torque values, especially during transient operating modes of the fluid coupling, are a function of both emulsion concentration and viscosity. A rather

unexpected result was that higher torque is achieved with emulsions of high concentration and viscosity. In classical sources, lower viscosity values should correspond to higher torque values due to lower internal friction losses. However, during our research, we obtained the opposite result.

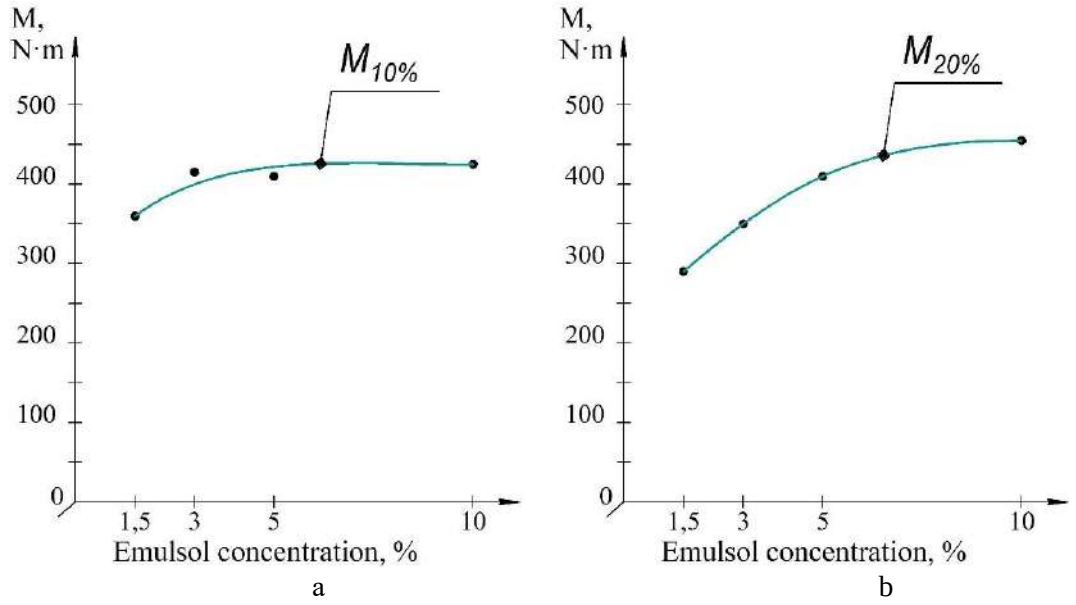



**Fig. 12. Dependence of the torque transmitted by the fluid coupling (5.3 dm³ fluid fill) on the emulsol concentration: a – at 10% slip; b – at 20% slip.**

This may be caused by several factors:

– easier discharge of the low-viscosity fluid into additional chambers, which are designed into the fluid coupling to limit torque [2, p. 187], at lower emulsol concentrations;

– deviation of HFA-E type emulsion properties from the classical properties of Newtonian fluids (according to [21], oil-in-water emulsions exhibit non-Newtonian properties at oil concentrations of 5...80%);

– the Toms effect [22], which states that polymer substances added to water reduce fluid friction against the walls, smooth out surface defects, and dampen turbulent pulsations in the fluid flow. These facts require verification and further research to develop a more accurate physical model of the processes occurring during fluid coupling operation with HFA-E type operating fluids.

## Conclusions.

An analysis of prior research into improving power drives for mine conveyors indicates that the most promising and relevant approach to enhancing fluid coupling efficiency and reliability is the use of HFA-E type water emulsions as an operating fluid. This area remains insufficiently explored and requires a comprehensive set of studies aimed at investigating fluid coupling characteristics depending on the percentage composition of water emulsions.

Based on the mechanical characteristics of the GPE345U fluid coupling obtained during exploratory bench testing, it can be asserted that at an emulsion concentration of 10%, the fluid coupling operates with maximum efficiency according to the following parameters:

– maximum utilization of the electric motor's traction characteristics due to a high torque value $M_{MAX}$ on the operating section of the mechanical characteristic;

– smooth acceleration of the conveyor chain, without oscillations, including startup under maximum load of the transported material;

– minimum heating of the operating fluid during startup due to the absence of a "dip" in the mechanical characteristic, which ultimately increases the operational reliability of the fluid coupling and reduces power consumption.

These findings show that using Solcenic PL PLUS emulsion as the operating fluid improves conveyor efficiency. Increasing the emulsol concentration from 1.5–5% (the standard for hydraulic roof supports) to 10% significantly boosts scraper conveyor performance and reliability.

Further research should focus on how viscosity, which depends on emulsol concentration, affects torque and slip across operating modes. Additionally, developing physical models and calculation methods for fluid coupling traction characteristics using HFA-E emulsions holds both scientific and practical value.

## References


1. Tabachenko, M. M., Dychkovskyi, R. O., Falshtynskyi, V. S., Medianyk, V. Yu., & Ruskykh, V. V. (2012). Dovidnyk z hirnychoho obladnannia dilnyts vuhilnykh i slantsevykh shakht: navch. posibnyk [Handbook of mining equipment for coal and shale mine sections: A textbook]. Dnipropetrovsk: NGU, 2012
2. Ulianovskyi, O. Z. (Ed.).. Shakhtni skrebkovi konveiery. Konstruktsiia ta perspektyvy. Proektuvannia. Vyhotovlennia. Ekspluatatsiia: monohrafiia [Mine scraper conveyors. Design and prospects. Engineering. Manufacturing. Operation: A monograph]. Kharkiv: Zoloti Storinky, 2012
3. Tkachenko, A. O. Znyzhennia dynamichnykh navantazhen v asynkhronnykh elektropryvodakh skrebkovykh konveieriv u robochykh ta avariinykh rezhymakh [Reduction of dynamic loads in asynchronous electric drives of scraper conveyors under operating and emergency modes] (Extended abstract of Candidate's thesis). National Technical University "Kharkiv Polytechnic Institute", Kharkiv, 2013.
4. Filipowicz, K., Kuczaj, M., Kwaśny, M., & Twardoch, K. Safety of mining machinery drives – selected issues. Mining – Informatics, *Automation and Electrical Engineering*, 2017. 3(531). 93–102. http://dx.doi.org/10.7494/miag.2017.3.531.93
5. Voith Turbo GmbH & Co. KG. Hydrodynamic Couplings. Principles | Features | Benefits: technical brochure. Crailsheim: Voith Turbo, 2017
6. Vysotskyi, H. V., Havrylenko, V. K., Kapshtyk, V. Ya., Leusenko, A. V., & Poletaev, V. V. Blokovana hidromufta [Locked fluid coupling] (Ukrainian Patent No. 78407). State Register of Patents of Ukraine, 2007
7. Hoffeld, H. Hydrodynamische Kupplung [Hydrodynamic coupling] (European Patent No. EP 1 127 231 B1). European Patent Office, 2003
8. Florea, V. A., Pasculescu, D., & Pasculescu, V. M. Reliability and maintainability of scraper conveyor used in coal mining in the Jiu Valley. *Mining of Mineral Deposits*, 2021. 15(3). 16–21. https://doi.org/10.33271/mining15.03.016
9. Sun, Z., Chew, J., Fomison, N., & Edwards, D. Analysis of fluid flow and heat transfer in industrial fluid couplings. *Proceedings of the Institution of Mechanical Engineers, Part C: Journal of Mechanical Engineering Science*, 2009. 223(9). 2049–2062. https://doi.org/10.1243/09544062JMES1478
10. Ministry of Economy of Ukraine. Pro zatverdzhennia Pravyl bezpeky vedennia hirnychykh robit u vuhilnykh shakhtakh: Nakaz Ministerstva ekonomiky Ukrainy vid 04 chervnia 2025 r. No. 2585 [On approval of Safety Rules for Coal Mine Operations: Order of the Ministry of Economy of Ukraine dated June 04, 2025 No. 2585]. Ofitsiinyi Visnyk Ukrainy, 2025
11. Safety and Health Commission for the Mining and Other Extractive Industries. 7th Luxembourg Report: Requirements and tests applicable to fire-resistant hydraulic fluids used for power transmission and control (hydrostatic and hydrokinetic) (Doc. No. 4746/10/91 EN). Luxembourg: European Commission, 1994
12. Voith Turbo GmbH & Co. KG. Safe Drive Solutions with Fluid Couplings in Potentially Explosive Atmospheres: technical brochure. Crailsheim: Voith Turbo, 2014
13. State Standard of Ukraine. DSTU EN ISO 12922:2022 Mastyla, industrialni olyvy ta suputni produkty (klas L). Simeistvo H (hidravlichni systemy). Spetsyfikatsii dlia hidravlichnykh rydyn u katehoriiakh HFAE, HFAS, HFB, HFC, HFDR i HFDU (EN ISO 12922:2020, IDT; ISO 12922:2020, IDT) [Lubricants, industrial oils and related products (class L). Family H (Hydraulic systems). Specifications for hydraulic fluids in categories HFAE, HFAS, HFB, HFC, HFDR and HFDU]. Kyiv: DP "UkrNDNTS", 2022

14. Avrunin, H. A., & Moroz, I. I. (2018). Analiz zastosuvannia robochykh rydyn v obiemnykh hidropryvodakh mobilnykh mashyn [Analysis of working fluids application in displacement hydraulic drives of mobile machines]. *Bulletin of the National Technical University "KhPI". Series: Hydraulic Machines and Hydraulic Units*, 2018. (46). 73–80.

15. Bosch Rexroth AG. Fire-resistant hydraulic fluids – water-containing (HFAE, HFAS, HFB, HFC): application notes and requirements for Rexroth hydraulic components: instruction manual RE 90223. Elchingen: Bosch Rexroth, 2015

16. Voith Turbo GmbH & Co. KG. Operating Fluids for Voith Turbo Couplings: Directive D-0503.1: Version 1/2024-01-30 (T. Pilz, Comp.; Document ID No. 91601312610). Heidenheim: Voith Turbo, 2024

17. Jagger, S. Fire safety: hydraulic systems used in underground work: research report RR1206 (Prepared by the Health and Safety Executive). Harpur Hill: HSE, 2024. https://doi.org/10.69730/hse.24rr1206

18. Olszak, A., Osowski, K., Musiałek, I., Rogoś, E., Kęsy, A., & Kęsy, Z. Application of Plant Oils as Ecologically Friendly Hydraulic Fluids. *Applied Sciences*, 2020. 10(24). 9086. https://doi.org/10.3390/app10249086

19. FUCHS Mastyla Ukraina LLC. SOLCENIC: official website. Lviv: Fuchs, 2026. Retrieved July 24, 2026, from https://www.fuchs.com/ua/uk/brendi/s-z/solcenic/

20. [20] Czerwiński, S., & Kania, J. Sieć wysokiego ciśnienia mediów hydraulicznych w podziemnych zakładach górniczych [High-pressure network of hydraulic media in underground mining operations]. Systemy Wspomagania w Inżynierii Produkcji. Energia i Górnictwo – perspektywy zrównoważonego rozwoju, 9(2), 133–148, 2020

21. Shevchenko, N. H., Drankovskyi, V. E., Koval, O. S., & Kosorukov, O. V. Do pytannia vyznachennia vtrat potuzhnosti na dyskove tertia dlia niutonivskoi i neniutonivskoi rydyny pohruzhnykh nasosiv [On the problem of determination of power losses on disc friction for Newtonian and non-Newtonian fluid of submersible pumps]. Bulletin of the National Technical University "KhPI". Series: Hydraulic Machines and Hydraulic Units, (46), 41–48, 2018

22. Mahliovana, T., Nyzhnyk, T., Strikalenko, T., Kolesnikov, D., Zemlianskyi, O., Stas, S., & Kopytin, D. Hidrodynamichna efektyvnist polimernykh reahentiv u systemakh transportuvannia vody: laboratorne modeliuvannia [Hydrodynamic efficiency of polymer reagents in water transportation systems: Laboratory modeling]. Visnyk KrNU imeni Mykhaila Ostrohradskoho, 1(156), part 2, 53–62, 2026. https://doi.org/10.32782/1995-0519.2026.1.2.6

*Дата першого надходження статті до видання 01.10.2026*
*Дата прийняття статті до друку після рецензування 27.10.2026*
*Дата публікації (оприлюднення) статті 04.11.2026*
*Стаття поширюється на умовах ліцензії відкритого доступу(CC BY 4.0)*

# ОБГРУНТУВАННЯ МЕТОДУ ПІДВИЩЕННЯ ЕФЕКТИВНОСТІ ТА НАДІЙНОСТІ ГІДРОМУФТ ПРИВОДІВ ШАХТНИХ КОНВЕЄРІВ ПРИ ЗАСТОСУВАННІ В ЯКОСТІ РОБОЧОЇ РІДИНИ ВОДНИХ ЕМУЛЬСІЙ

**С. В. Воронін[1], В. В. Полєтаєв[1]**

[1] *Український державний університет залізничного транспорту*
[2] *Таврійський державний агротехнологічний університет імені Дмитра Моторного*

***Анотація***

Статтю присвячено актуальній інженерній проблемі підвищення надійності та експлуатаційної ефективності запобіжно-пускових гідромуфт з постійним заповненням, які використовуються у приводах шахтних скребкових конвеєрів. Проведено комплексний порівняльний аналіз різних робочих рідин для забезпечення вимог пожежної безпеки та оптимізації ключових експлуатаційних параметрів в умовах шахт, небезпечних за газом та вугільним пилом. Головною метою цього дослідження є встановлення закономірностей між механічними характеристиками гідромуфт та властивостями (концентрацією) водомасляних

емульсій класу HFA-E.

Експериментальні дослідження виконано на лабораторному випробувальному стенді з використанням серійної гідромуфти ГПЕ345У виробництва заводу «Світло шахтаря» (Україна). Методика випробувань передбачала оцінку роботи гідромуфти для двох різних об'ємів заповнення рідиною (78% та 85% від повного об'єму внутрішньої порожнини), що відповідає роботі у приводах з асинхронними електродвигунами потужністю 22 кВт та 30 кВт. Склад рідини варіювався за об'ємною концентрацією емульсолу Solcenic Pl Plus (виробництва FUCHS Petrolub SE, Німеччина) – 1,5%, 3%, 5% та 10%.

Експериментальні дані показали, що збільшення концентрації емульсолу суттєво покращує механічні характеристики під час критичних та перехідних режимів роботи, таких як запуск конвеєра та режимів перевантаження. Визначено, що вища концентрація емульсолу усуває падіння («провал») крутного моменту в цих режимах роботи, що призводить до мінімізації нагрівання рідини та марних втрат енергії, тим самим знижуючи ризик спрацьовування теплового захисту. Кількісно, перехід від 1,5% до 10% концентрації емульсії підвищує перевантажувальну здатність привода з 1,4...1,5$M_H$ до 2,1...2,5$M_H$, що відповідає вимогам для приводів забійних скребкових конвеєрів.

Наукова новизна отриманих результатів полягає у виявленні реологічних відхилень від класичних законів ньютонівських рідин у поведінці водомасляних емульсій в проточній частині гідромуфти. Практична цінність результатів полягає в технічному обґрунтуванні використання 10%-ї емульсії типу HFA-E як оптимальної робочої рідини. Впровадження такої концентрації рідини економічно доцільне та забезпечує суттєве підвищення енергоефективності й довговічності як самої гідромуфти, так і всієї приводної системи шахтного скребкового конвеєра.

**Ключові слова:** гідродинамічний привід, гідромуфта постійного заповнення, шахтний скреперний ланцюговий конвеєр, механічна характеристика, масловодна емульсія, HFA-E, робоча рідина, концентрація.

**DOI https://doi.org/10.32782/1994-4691-2026-1-77-11**
УДК 621.225.001.4

# ДИНАМІКА ГІДРОПРИВОДА ВСЮДИХОДА НА РЕЖИМАХ ТЯГОВО-ШВИДКІСНОЇ ХАРАКТЕРИСТИКИ

# DYNAMICS OF THE HYDRAULIC FLUID POWER OF ALL-WHEEL VEHICLES IN THE MODES OF TRACTION-SPEED CHARACTERISTICS

Г. А. Аврунін[1*], канд. техн. наук, доцент ORCID: 0000-0002-0191-3149
І. В. Лебедик[2], Ph.D., головний конструктор ORCID: 0009-0001-2223-7901
М. В. Підгорний[2], інженер ORCID: 0009-0004-6001-2078
І. В. Білан[1], аспірант ORCID: 0009-0005-5585-1317
І. І. Мороз[1], старший викладач ORCID: 0000-0001-5950-2089

[1] *Харківський національний автомобільно-дорожній університет, Харків, Україна*
[2] *ТОВ «Завод всюдиходів Торнадо»*
*e-mail: griavrunin@ukr.net

**Анотація**. Розглянуті можливості створення гідроприводної бортової трансмісії вітчизняного колісного всюдихода «Tornado» шляхом проведення статичних і динамічних розрахунків з моделюванням параметрів тягово-швидкісної характеристики за допомогою пакету прикладних програм VisSim при рішенні нелінійних диференціальних рівнянь щодо визначення швидкості навантажувача і тиску в гідроприводі від часу. Проведений аналіз показав, що за допомогою моделювання варіювання витрати насоса і зміни робочого об'єму аксіально-поршневих гідромоторів можливо виявлення екстремальних режимів, які приводять до коливань тиску в гідроприводі і швидкості всюдихода. Зокрема, визначено, що при гальмуванні всюдихода з максимальної швидкості шляхом зменшення подачі насоса для забезпечення безкавітаційної роботи гідроприводу необхідно одночасно зберігати постійним встановлено значення робочого об'єму гідромоторів.

**Ключові слова**: динаміка об'ємного гідроприводу, аксіально-поршневі гідромашини, крутний момент, швидкість, потужність, перепад тисків.

## Вступ.

Створення колісних всюдиходів потребує рішення задач, пов'язаних з виконанням вимог швидкісно-тягових характеристик на режимах зрушування, подолання підйомів, транспортної швидкості, а також запобігання буксуванню. Тому слід вважати актуальним проведення розрахунків трансмісії всюдихода як одного з найважливіших етапів його проектування. Об'єктом роботи обрана трансмісія дослідного зразка вітчизняного всюдихода (ВХ) «Tornado» з бортовим об'ємним гідроприводом. Застосування гідромотор-коліс замість механічних трансмісій дає можливість забезпечення безступінчастого регулювання швидкості всюдиходів і прискорити їх виготовлення блоковим методом при застосуванні покупних комплектуючих вузлів, зокрема насосів, гідромоторів, гідроапаратів та систем кондиціювання робочої рідини. Особливу увагу приділено розрахункам динамічних характеристик, які дають можливість визначити коливальні процеси, суттєво впливаючи на довговічність трансмісії ВХ. До наукової новизни роботи слід віднести отримання динамічних характеристик гідроприводної трансмісії ВХ за результатами математичного моделювання параметрів тягово-швидкісної характеристики при використанні пакету прикладних про-грам VisSim для рішення нелінійних диференціальних рівнянь щодо

визначення швидкості навантажувача, тиску в гідроприводі і його корисної потужності від часу.

## Огляд літератури.

Розглянемо технічні характеристики, розрахунки і дослідження гідроприводних трансмісій всюдиходів для потреб вітчизняних галузей промисловості, зокрема нафтогазової, сільськогосподарському виробництві, рятувальних роботах при надзвичайних ситуаціях і для допомоги військовим при бойових діях [1]. В роботі [2] розглянуті характеристики ВХ «Tornado» з гідроприводною бортовою трансмісією. В дослідженні [3] розглянуті способи машинного керування гідравлічними трансмісіями із замкненим ланцюгом циркуляції робочої рідини (РР), математичні моделі гідроприводів та алгоритми управління окремими гідромашинами. Керування базується на децентралізованій схемі, де гідромотор та насос керуються окремо відносно структури керування, але синхронізовано відносно дорожніх умов пересування транспортного засобу. Слід відмітити науковий теоретичний підхід до алгоритмів керування гідроприводом і отримані практичні результати.

Трансмісія з системою контролю тяги, яка складається з регульованих насоса та двох гідромоторів, які працюють паралельно, приведена в роботі [4]. Паралельна робота гідромоторів можлива на кожну вісь транспортного засобу або як альтернативна тільки на одну вісь у вигляді мотор-коліс обертання безпосередньо маточин. Аналізується трансмісія транспортного засобу масою 5000 кг і потужністю 60 кВт при тяговому зусиллі до 25 кН та максимальній швидкості до 30 км/год.

Питання керування об'ємною гідравлічною трансмісією з невизначеною динамікою виконавчого механізму розглянуто в роботі [5]. Трансмісія з насосом і гідромотором з регульованими робочими об'ємами функціонує по замкненому ланцюгу циркуляції РР. Математична модель гідропривода дала можливість побудувати значення перепаду тисків і частоти обертання гідромотора. В електронний блок (ECU) надсилаються сигнали зворотного зв'язку роботи трансмісії, зокрема частоти обертання ДВЗ, насоса та гідромотора, значення тисків в основних магістралях. Регулятори зміни робочих об'ємів насоса і гідромотора керуються пропорційними електромагнітами. Регулювання подачі палива до ДВЗ та реверсування трансмісії також здійснюється через електронний блок.

Велику увагу приділяють проблемам гальмування транспортних засобів, що пов'язано з тим, що при найбільш простому способі гальмування переведенням насоса на мінімальне значення робочого об'єму можливі суттєві коливання тиску в гідросистемі і спрацьовування запобіжних клапанів. Такі режими (робота на «клапан») приводять к перегріву гідропривода і зменшенню його довговічності. Тому фахівці пропонують більш м'які способи гальмування для тих випадків, коли воно не є екстреним, Так в патентах [6;7] та дослідженні [8] розглянуті способи гальмування трансмісій з об'ємним гідроприводом (ОГП) «насос-гідромотор» шляхом дросельного навантаження додаткового насосу, об'єднання основних магістралей гідросистеми або повідомлення однієї магістралі з лінією підживлення, а також примусового розвантажування запобіжного клапану.

Гідравлічні принципові схеми трансмісій з декількома гідромотор-колесами фірми «Poclain Hydraulics» за допомогою дільників потоку розглянуті в роботі [9]. В мобільних позашляхових транспортних засобах великою проблемою є боротьба з буксуванням. Тому фірма «Poclain Hydraulics» запропонувала комплексне рішення за допомогою спеціального блоку «SD-CT OFF-Road System» [4; 10-12], який має дроселі з електрогідравлічним пропорціональним управлінням. Спрацьовування цих дроселів виконується згідно з аналізом швидкості обертання кожного з гідромотор-коліс, для чого встановленні відповідні перетворювачі (Speed Sensor). Встановлений також перетворювач (Turn Detector) положення рульового колеса. Сигнали перетворювачів

поступають в бортовий комп'ютер (Regulating Computer), аналізуються і запобігають буксуванню гідромотор-коліс шляхом зупинки подання до них витрати РР від насосу. Система повністю автоматизована, що відповідає сучасним вимогам до трансмісій позашляхових транспортних засобів.

Розрахунковий аналіз можливості застосування гідравлічної трансмісії з мотор-колесами для ВХ «NOMAD ATV», зокрема з високомоментними радіально-поршневими багатоцикловими гідромоторами, виконаний в роботі [13].

## Методологія дослідження.

Методологія дослідження передбачає побудову тягово-швидкісної характеристики, структурної і розрахункової схем динаміки гідроприводної трансмісії ВХ «Tornado» та виконання таких етапів:

1. Проведення статичних розрахунків ОГП з метою визначення крутних моментів та частот обертання гідромотор-коліс на всіх етапах тягово-швидкісної характеристики.
2. Адаптація математичної моделі динаміки ОГП обертального руху [16] для умов роботи трансмісії всюдихода, зокрема підготовка до моделювання шляхом завданням параметрів зовнішнього навантаження, подачі насосів, об'ємного і гідромеханічного ККД насосів і гідромоторів за допомогою відповідних чисельних значень в блоках пакетів map-VisSim.
3. Отримання осцилограм динамічних розрахунків щодо перепаду тисків в ОГП, частоти обертання гідромотор-коліс, швидкості ВХ та його корисної потужності від часу в повному діапазоні транспортного руху до 40 км/год. При цьому повний режим руху ВХ умовно укладався на осцилограмах в 36 с.
4. Аналіз отриманих динамічних навантажень на ОГП ВХ і виявлення критичних режимів щодо максимальних тисків при зрушуванні ВХ і мінімальних кавітаційних значень тиску на режимах гальмування, аналіз впливу на динамічні характеристики зменшення модулю пружності РР.
5. Моделювання режимів, що запобігають отриманню критичних зон роботи гідроприводної трансмісії ВХ.

## Результати.

ВХ типа «Tornado» має повний ОГП з колісною формулою 4х4 і призначений для використання в нафтогазовій галузі, сільськогосподарському виробництві та надзвичайних ситуаціях, а також може оснащуватись причепом. ВХ «Tornado» долає бруд, воду, завали дерев та каміння заввишки до 1 м. ВХ оснащений дизельним двигуном моделі «Doosan» (виробництва південної Кореї), який має робочий об'єм в 2,4 дм$^3$. На ВХ максимальна швидкість досягає 40 км/год при витратах пального до 5 л/год. Паливний бак ємністю в 160 дм$^3$ сприяє отриманню запасу ходу. Завдяки мінімальному радіусу розвороту ВХ «Tornado» чудово маневрує між деревами. За допомогою бортової схеми повороту ВХ розвертається майже на місці. ВХ оснащений колесами з низьким тиском, які мають висоту 1,65 м і ширину 0,57 м, протектор має висоту 35 мм. ВХ достатньо легко виходить на лід з води, має гарну прохідність та плавучість. Колеса в зборі з диском мають водотонажність в 933 дм$^3$. За рахунок протектора в 35 мм на шинах ВХ рухається на воді зі швидкістю до 6 км/год. Централізована система живлення дає можливість накачування всіх коліс ВХ одночасно не більш ніж за 40 с. ВХ має кліренс 600 мм і є невразливим для будь-яких доріг. Повна вантажопідйомність ВХ досягає 1000 кг з можливістю перевезення 8 осіб з водієм та додатково 500 кг вантажу. Кабіна ВХ оснащена також трьома спальними місцями.

На рис. 1 представлена компоновка силової установки і гідравлічних агрегатів бортової трансмісії з аксіально-поршневими гідромоторами ВХ «Tornado».

Підсумковий максимальний крутний момент 4-х провідних коліс досягає 25420 Н.м, а швидкість ВХ досягає 40 км/год.




**Рис. 1. Всюдихід «Tornado» та розташування його силової установки і гідравлічних машин бортової трансмісії з аксіальнопоршневими гідромоторами.**

Аксіально-поршневі гідромотором з похилим диском мають регульований робочий об'єм з електрогідравлічним управлінням. Гідромотори кожного з бортів мають живлення від окремого насоса. Бортове керування поворотом забезпечує електричний джойстик шляхом зміни живлення на пропорційних електромагнітах в відповідних регуляторах насосів і гідромоторів. Такі системи бортового керування з постійним аналізом швидкості провідних коліс кожного з бортів, як зворотних зв'язків в електронних блоках керування трансмісії, використовується, наприклад, в гусеничних тракторах ХТЗ моделі ТС-10 з використанням насосів і гідромоторів компанії «Rexroth Bosch Group» і також розроблені компанією «Sauer-Danfoss» [14; 15].

Структурна схема бортового об'ємного ОГП трансмісії ВХ представлена на рис. 2. Тандем-насоси аксіально-поршневого типу Нл і Нпр обертаються від приводного ДВЗ через проміжний редуктор Ред з підвищеним передавальним відношенням (мультиплікатор) для адаптації частоти обертання насоса до його номінальної технічної характеристики. Кожний з насосів подає РР до відповідних гідромоторів: Насос Нл до гідромоторів-коліс правого борту МПр1 і МПр2; насос Нл до гідромоторів-коліс лівого борту МЛ1 і МЛ2. Гідромотори обертають ведучі колеса через бортові редуктори БР, відповідно. Всі насоси і гідромотори мають регульований робочий об'єм з системами електрогідравлічного пропорційного керування. Пропорційні електромагніти керування насосами позначені як Y1 і Y2, гідромоторами як Y3…Y6.

Система керування подачі палива до ДВЗ позначена Y7. Система контролю параметрів ОГП побудована на перетворювачах: частоти обертання гідромоторів ДЧОпр1 і ДЧОпр2, ДЧОл1 і ДЧОл2, а також частоти обертання валу двигуна ДЧОдвз; тиску в основних магістралях гідропривода ПТ1…ПТ4. Електронний блок управління здійснює зміну параметрів ОГП щодо частоти обертання насосів і робочого об'єму насосів і гідромоторів за допомогою керуючих сигналів Y1…Y7. Водій всюдихода має важіль управління (джойстик) РКР для здійснення прямолінійного ходу (F - вперед, R - назад) і бортового повороту шляхом зміни швидкості коліс.

Розрахункова схема для створення математичної моделі і визначення статичних та динамічних параметрів ОГП ВХ приведена на рис. 3. Розглядається тільки один гідромотор М1, до якого підводиться подача РР від насоса значенням в половину від підсумкової. На схемі показані потоки РР щодо течії від насосу до гідромотора, а також витоки, пов'язані з її втратами по зазорах поршневих пар і розподільного вузла, а також втрати, пов'язані зі стисливістю РР. Параметри ОГП контролюються перетворювачами

частоти обертання насоса ДЧОн і гідромотора ДЧОбр (вихідного валу бортового редуктора), а також аналоговими перетворювачами тиску ПТ1 і ПТ2.

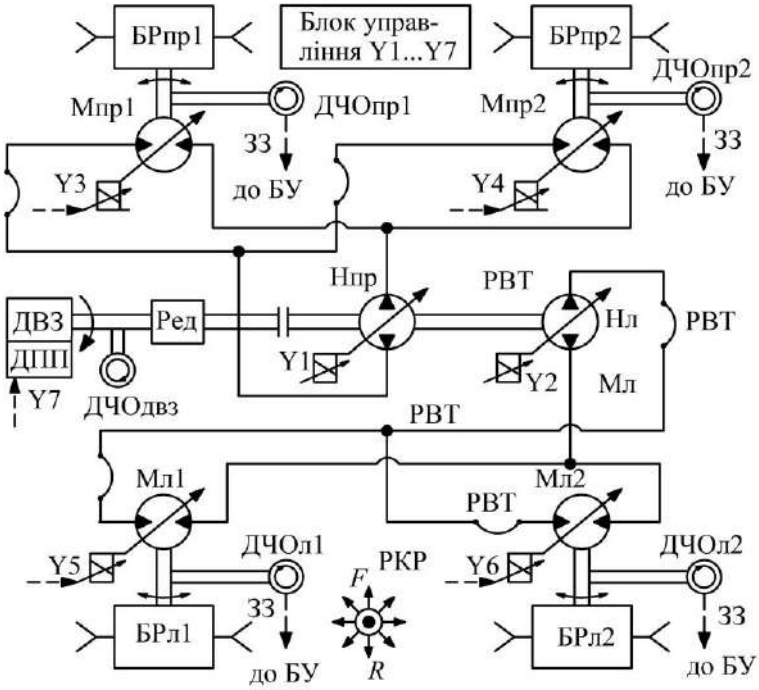



**Рис. 2. Структурна схема бортового гідропривода трансмісії всюдихода.**

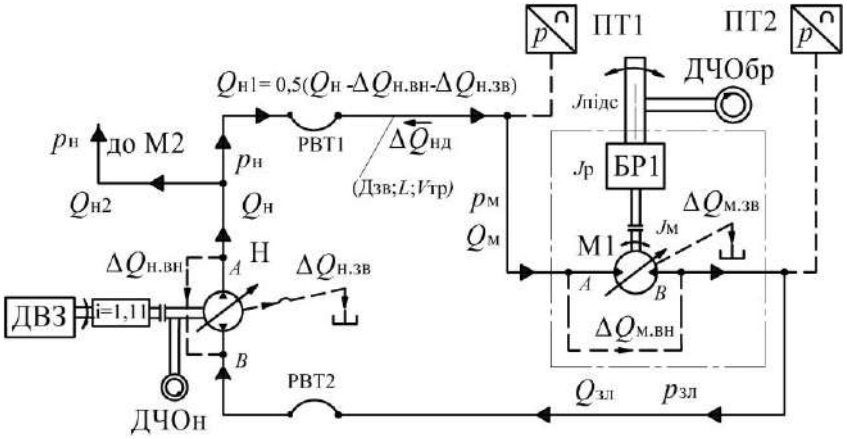



**Рис. 3. Розрахункова схема гідроприводної трансмісії всюдихода.**

На рис. 4 приведена тягово-швидкісна характеристика (ТШХ) ВХ, побудована з максимальними значенням тягового зусилля 32,8 кН і швидкості в 40 км/год.

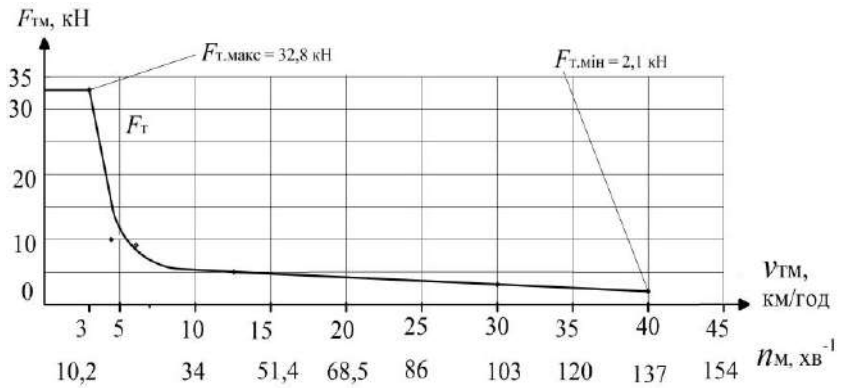



**Рис. 4. Тягово-швидкісна характеристика всюдихода.**

Результати моделювання ТШХ і розрахунку ОГП приведені в табл. 1.

**Таблиця 1. Транспортні режими прямолінійного руху всюдихода**

| Параметри, розмірність | Режим руху всюдихода: | | | | | |
|---|---|---|---|---|---|---|
| | 1 | 2 | 3 | 4 | 5 | 6 |
| Час зміни режиму згідно моделюванню в пакеті VisSim, с | 0-7 | 9 | 10-13 | 16-19 | 2326 | 29-36 |
| Тягове зус., $F_{тм}$, кН (F ВХ)* | 32,8 | 9,78 | 8,87 | 5 | 3,1 | 2,17 |
| Швидк., $v_{тм}$, км/год (V ВХ)* | 0-2,5 | 3,6 | 4,2-6,2 | 8,7-12,8 | 30,6 | 36-40 |
| Вихідна потужність ВХ, кВт | 22,8 | 9,79 | 15,0 | 17,8 | 26,4 | 24,1 |
| Вих. потужн. ОГП ВХ, кВт | 25,33 | 10,9 | 16,7 | 19,8 | 29,3 | 26,8 |
| Крут. момент ВХ $M_{тм}$, Н.м | 25420 | 7580 | 6874 | 3875 | 2403 | 1682 |
| Крут. мом. колеса $M_к$, Н.м | 6355 | 1895 | 1719 | 969 | 601 | 421 |
| Крут. мом. мотора $M_м$, Н.м | 642 | 172,3 | 174 | 97,9 | 60,7 | 42,5 |
| Частота оберт. колеса $n_к$, хв$^{-1}$ | 8,57 | 12,33 | 21,2 | 43,6 | 105 | 137 |
| Част. оберт. М, $n_м$, хв$^{-1}$ (i=11) | 94,3 | 135,6 | 233 | 480 | 1155 | 1507 |
| Робочий об'єм М, $V_{м,i}$, см$^3$ * | 115,6 | 115,6 | 115,6 | 101-85 | 65-50 | 48 |
| Подача насоса $Q_{нт}$, л/хв.** | 13,9 | 17,6 | 20-28 | 34-42 | 52-59 | 73,3 |
| Роб. об'єм насоса Vнт, см$^3$ | 0-5,7 | 7,2 | 11,5 | 60 | 60 | 60 |
| Переп. в ОГП, $\Delta p_{м,i}$, МПа ** | 39-35 | 10,4 | 9,5 | 6,2-7,6 | 6,8-10 | 7,2 |
| ККД ОГП ** | 0,7 | 0,7 | 0,73-0,8 | 0,77 | 0,68 | 0,61 |
| Спож. потужн. ОГП, кВт ** | 37 | 16,2 | 16,2-23,4 | 16-26 | 29-45 | 43 |
| Втрати потужн. ОГП, кВТ ** | 11,4 | 4,8 | 4,4 | 6 | 9-15,5 | 17,5 |
| Об'ємний ККД Н * | 0,65-0,89 | 0,98 | 0,99 | 0,99 | 0,99 | 0,99 |
| Гідромех. ККД Н * | 0,95 | 0,95 | 0,95 | 0,97 | 0,92 | 0,90 |
| Об'ємний ККД М * | 0,5-0,82 | 0,89 | 0,92-0,98 | 0,99 | 0,99 | 0,99 |
| Гідромех. ККД М * | 0,85-0,99 | 0,99 | 0,99 | 0,97-0,92 | 0,86 | 0,75 |

Примітка: 1. *) Задані дані; 2. **) Дані з осцилограм на плотерах VisSim; 3. Всі інші параметри є розрахунковими.

Вихідна (корисна) потужність ВХ знаходиться за формулою:

$$P_{вх} = F_{т.вх} \cdot v_{вх} = 10^{-3} \frac{10^3}{3600} F_{т.вх} \cdot v_{вх} = 0,000278 \cdot F_{т.вх} \cdot v_{вх}, \text{ кВт}, \quad (1)$$

де $F_{т.вх}$ – тягове зусилля трансмісії ВХ, Н; $v_{вх}$ – швидкість ВХ, км/год.

Вихідна (корисна) потужність ОГП трансмісії ВХ повинна бути збільшена за рахунок використання ККД планетарного редуктора в маточині:

$$P_{м.вх} = P_{вх} / \eta_{ред}, \text{ кВт}, \quad (2)$$

де $\eta_{ред}$ – ККД редуктора маточини, $\eta_{ред}$ = 0,9.

ВХ розвиває крутний момент 4-ма провідними колесами:

$$M_{вх} = F_{т.вх} \frac{d_в}{2}, \text{ Н.м}, \quad (3)$$

де $d_в$ – зовнішній діаметр провідного колеса (за шиною), $d_в$ = 1,55 м.

Тоді крутний момент одного провідного колеса всюдихода:

$$M_{\text{вед.вх}} = \frac{M_{\text{вх}}}{4}, \text{ Н·м}, \quad (4)$$

Запишемо формулу для крутного моменту одного гідромотора ВХ при заданому тяговому зусиллі $F_{\text{т.вх}}$:

$$M_{\text{м}} = 10^3 F_{\text{т.вх}} \frac{d_{\text{в}}}{2 \cdot z \cdot i_{\text{ред}} \cdot \eta_{\text{ред}}}, \text{ Н·м}, \quad (5)$$

де $z$ – кількість бортових провідних гідромоторів в трансмісії ВХ, $z$ = 4; $i_{\text{ред}}$ – передавальне відношення планетарного редуктора, $i_{\text{ред}}$ = 11.

Частота обертання провідних коліс трансмісії ВХ знаходиться за формулою:

$$n_{\text{вед.вх}} = \frac{10^3}{60} \frac{v_{\text{вх}}}{\pi \cdot d_{\text{в}}} = 5,31 \frac{v_{\text{вх}}}{d_{\text{в}}}, \text{ хв}^{-1}, \quad (6)$$

де $v_{\text{вх}}$ – швидкість ВХ, км/год.

Частота обертання одного гідромотора трансмісії ВХ:

$$n_{\text{м}} = n_{\text{вед.вх}} \cdot i_{\text{ред}}, \text{ хв}^{-1}, \quad (7)$$

Робочий об’єм гідромотора для створення необхідного крутного моменту:

$$V_{\text{м},i} = \frac{M_{\text{м},i}}{0,159 \cdot \Delta p_{\text{м},i} \cdot \eta_{\text{мгм}}}, \text{ см}^3, \quad (8)$$

де $\Delta p_{\text{м},i}$ – перепад тисків на гідромоторі як різниця значень на вході і виході, МПа; $\eta_{\text{мгм}}$ – гідромеханічний ККД аксіально-поршневого гідромотора.

ККД об’ємного гідроприводу розраховуємо за формулою:

$$\eta_{\text{огп}} = P_{\text{вх.огп}} / P_{\text{спож.огп}}, \quad (9)$$

де вхідна потужність ОГП:

$$P_{\text{вх.огп}} = z \frac{M_{\text{м}} \cdot n_{\text{м}}}{9550}, \text{ кВт}, \quad (10)$$

де $z$ = 4 – кількість провідних гідромоторів трансмісії ВХ;

Споживана потужність одного основного насосу дорівнює:

$$P_{\text{спож.осн}} = \frac{Q_{\text{н}} \cdot \Delta p_{\text{н}}}{60 \cdot \eta_{\text{н}}} = \frac{Q_{\text{нт}} \cdot \Delta p_{\text{н}}}{60 \cdot \eta_{\text{нгм}}}, \text{ кВт}, \quad (11)$$

де $\Delta p_{\text{н}}$ – перепад тисків на насосі, МПа; $Q_{\text{н}}$ – дійсна подача основного насоса з урахуванням його об’ємного ККД, л/хв; $Q_{\text{нг}}$ – теоретична подача (витрата РР) основного насоса, л/хв; $\eta_{\text{н}}$ – загальний (повний) ККД основного (аксіально-поршневого) насоса; $\eta_{\text{нгм}}$ – гідромеханічний ККД основного насоса.

Перепад тисків на насосі, який потрібен для створення необхідного крутного моменту гідромотора в ОГП із замкненим ланцюгом циркуляції РР:

$$\Delta p_{\text{н}} = \Delta p_{\text{м}} + 2\Delta p_{\text{втрат}}, \text{ МПа}, \quad (12)$$

де $\Delta p_{\text{втрат}}$ – втрати тиску по довжині в трубопроводі між насосом і гідромотором, МПа.

В першому наближенні враховуємо тільки втрати тиску за довжиною трубопроводів [14]:

$$2\Delta p_{\text{втрат}} \approx \Delta p_{\text{тр.}L} = 2 \cdot 0,584 \cdot \frac{L}{d_{\text{тр}}^4} \cdot Q_{\text{нт}} \cdot \nu_{\text{в'язк}}, \text{ МПа}, \quad (13)$$

де 2 – коефіцієнт, який враховує подвійну довжину трубопроводів між насосом і гідромотором в замкненому ланцюгу циркуляції РР; $L$ – довжина трубопроводу від

насоса до гідромотора, м; $d_{тр}$ – внутрішній (зведений) діаметр трубопроводу, мм; $\nu_{в'язк}$ – значення коефіцієнту кінематичної в'язкості РР, мм $^2$/с (сСт).

Знаходимо споживану шестеренним насосом підживлення потужність:

$$P_{нп} = \frac{10^{-3} \cdot V_{нп} \cdot n_{дв} \cdot p_{нп}}{60 \cdot \eta_{нпгм}} = \frac{Q_{нпт} \cdot p_{нп}}{60 \cdot \eta_{нпгм}}, \text{ кВт}, \quad (14)$$

де $V_{нп}$ – робочий об'єм насоса підживлення за каталогом виробника, см$^3$; $n_{дв}$ – номінальна частота обертання насоса підживлення на основному насосі, хв$^{-1}$; $p_{нп}$ – тиск, що розвиває насос підживлення за допомогою налаштування вмонтованого клапану тиску, який зазвичай не перевищує 2,4 МПа; $\eta_{нпгм}$ – орієнтовне значення гідромеханічного ККД насоса підживлення, $\eta_{нпгм}$ = 0,7; $Q_{нпт}$ – теоретична подача (витрата) насоса підживлення, яка дорівнює:

$$Q_{нпт} = 10^{-3} V_{нп} \cdot n_{дв}, \text{ л/хв}. \quad (15)$$

Підсумкова споживана потужність насосів одного борту дорівнює:

$$P_{\sum спож} = P_{спож.осн} + P_{нп}, \text{ кВт}. \quad (16)$$

Всі приведені формули дають можливість виконати статичний розрахунок ОГП [14].

Задані значення ККД насоса і гідромотора трансмісії ВХ в блоках пакетів map-VisSim приведені в табл. 2.

**Таблиця 2. ККД насосів і гідромоторів трансмісії всюдихода**

| Час руху ВХ, с | ККД $Н_{об}$ | ККД $Н_{гм}$ | ККД $М_{об}$ | ККД $М_{гм}$ |
|---|---|---|---|---|
| 0,01 | 0,65 | 0,95 | 0,5 | 0,85 |
| 1 | 0,68* | 0,95* | 0,6* | 0,9 |
| 3 | 0,75 | 0,95* | 0,68* | 0,94* |
| 5 | 0,82* | 0,95 | 0,76 | 0,99 |
| 10 | 0,99 | 0,95* | 0,92 | 0,99* |
| 14 | 0,99* | 0,95* | 0,99 | 0,98 |
| 16 | 0,99* | 0,95 | 0,99* | 0,97 |
| 30 | 0,99 | 0,9 | 0,99 | 0.75 |
| 36 | 0,99 | 0,9 | 0,99 | 0,75 |

Примітка: *) – отримані з графічних залежностей в блоках map-VisSim.

При розгляді математичної нелінійної моделі динаміки ОГП ВХ приймаємо допущення [16] щодо постійності моменту інерції ВХ і значень модуля об'ємної пружності, температури, щільності та в'язкісті РР. Крім того, завдяки використанню досить коротких трубопроводів між насосами і гідромоторами хвильові процеси в трубопроводах не враховуємо.

Запишемо формули для визначення перепаду тисків $\Delta p_м$ [МПа] і частоти обертання гідромоторів $n_м$ [хв$^{-1}$]:

$$\Delta p_м = \int_0^t \left[ Q_{нт,e}(t) - 10^{-3} V_{м,i}(t) \cdot n_м(t) - C_{(н+м).вит} \cdot p_м(t) \right] \frac{E}{V_{тр}} dt, \quad (17)$$

$$n_м = \int_0^t \frac{3,6 \cdot 10^3}{J_п} \left[ \frac{1}{2\pi} V_{м,i}(t) \cdot (p_н - p_{зл}) \cdot \eta_{м.гм} - M_с \right] dt, \quad (18)$$

де $Q_{нт,e}$ – витрата (подача) аксіально-поршневого насосу при відносному значенні кута зміщення похилого диску, $Q_{нт,e} = Q_{нт} \cdot e$, $e = 0 \ldots \pm 1$, л/хв; $Q_{нт}$ – теоретичне значення

подачі насоса при його максимальному робочому об'ємі $V_н$ [см$^3$] та частоті обертання валу $n_н$ [хв$^{-1}$] без урахування зовнішніх та внутрішніх витоків РР по зазорах поршнів, гідростатичних підп'ятників поршнів і торцевого розподільного вузла, л/хв, $Q_{нт} = 10^{-3} \cdot V_н \cdot n_н$; $V_{м,i}$ – поточний робочий об'єм гідромотора, який є пропорційним максимальному його значенню $V_м$ і залежить від відносного параметра $i$, см$^3$, $V_{м,i} = V_м \cdot i$; $C_{(н+м).вит}$ – загальний коефіцієнт витоків РР (підсумкових значень зовнішніх та внутрішніх витоків РР насоса $\Delta Q_{н.вит}$ і гідромотора $\Delta Q_{м.вит}$ по зазорах прецизійних пар поршнів та розподільного вузла, л/(хв.МПа); $V_{тр}$ – об'єм стиснення РР в трубопроводі діаметром $D_{зв}$ [мм] та довжиною $L$ [м] між насосом та гідромотором, дм$^3$; $E$ – модуль пружності РР, від значення якого залежить деформаційна витрата $\Delta Q_{нд}$ в ОГП, пропорційна стисливості та об'єму трубопроводу $V_{тр}$, МПа; $J_п$ – підсумкове значення моменту інерції, приведеного до вихідного валу гідромотора зі складовими моментами інерції: аксіально-поршневого гідромотора $J_м$, редуктора $J_р$, частини ВХ, яка позначена як $J_{р0}$, кг.м$^2$, $J_п = J_м + J_р + J_{р0}$; $p_н$ і $p_{зл}$ – значення тисків в магістралях нагнітання насоса і зливу РР до гідромотора в замкненому ланцюзі циркуляції ОГП, МПа; $\eta_{м.гм}$ – значення гідромеханічного ККД гідромотора; $M_с$ – момент зовнішнього навантаження (опору) на гідромоторі, Н.м.

При оцінці динамічних характеристик і моделювання ОГП ВХ змінними від часу задаємо такі параметри: крутний момент зовнішнього навантаження на гідромотор $M_с$; подача (витрата) насоса $Q_{нт,e}$; значення робочого об'єму аксіально-поршневого гідромотора $V_{м,i}$ та гідромеханічні і об'ємні ККД насосів і гідромоторів.

Для рішення диференціальних рівнянь в пакеті VisSim [17] обираємо метод інтеграції Рунге-Кутта четвертого порядку з дискретністю $\Delta = 0{,}001$ с.

Значення коефіцієнтів витоків РР по зазорах прецизійних пар знайдемо через об'ємний ККД (коефіцієнт подачі) насоса:

$$\eta_{но} = \frac{Q_н}{Q_{нт}} = \frac{Q_{нт} - \Delta Q_{н.вит}}{Q_{нт}} = 1 - \frac{\Delta Q_{н.вит}}{Q_{нт}};\ \Delta Q_{н.вит} = Q_{нт}(1 - \eta_{но});$$
$$C_{н.вит} = \frac{\Delta Q_{н.вит}}{p_н + p_{зл}} = \frac{Q_{нт}(1 - \eta_{но})}{p_н + p_{зл}}. \qquad (19)$$

і гідромотора:

$$\eta_{мо} = \frac{Q_{мт}}{Q_{мт} + \Delta Q_{м.вит}};\ \eta_{мо} \cdot Q_{мт} + \eta_{мо} \cdot \Delta Q_{м.вит} = Q_{мт};$$
$$\Delta Q_{м.вит} = Q_{мт}\left(\frac{1}{\eta_{мо}} - 1\right);\ C_{м.вит} = \frac{\Delta Q_{м.вит}}{p_н + p_{зл}} = \frac{Q_{мт}}{p_н + p_{зл}}\left(\frac{1}{\eta_{мо}} - 1\right), \qquad (20)$$

де $Q_{мт}$ – теоретична витрата аксіальнопоршневого гідромотора, яка пропорційна його робочому об'єму $V_{м,i}$ [см$^3$] і частоті обертання $n_м$ [хв$^{-1}$], л/хв, $Q_{мт} = 10^{-3} \cdot V_{м,i} \cdot n_м$.

Підсумкове значення коефіцієнту витоків РР насоса і гідромотора запишемо у такому вигляді:

$$C_{(н+м).вит} = C_{н.вит} + C_{м.вит} = \frac{Q_{нт}(1 - \eta_{мо}) + Q_{мт}\left(\frac{1}{\eta_{мо}} - 1\right)}{p_н + p_{зл}}. \qquad (21)$$

Розглянемо отримані осцилограми динамічних розрахунків (рис. 5–8) при моделюванні роботи ОГП трансмісії ВХ в повному діапазоні транспортного руху до 40 км/год, де повний режим руху ВХ умовно укладений на плотерах в 36 с.

При цьому задавали постійні значення параметрів:

1. Частота обертання ДВЗ приймалась постійною в 2200 хв$^{-1}$, частота обертання

тандем-насосів встановлена підвищеною з урахуванням мультиплікатора значенням 1,11.

2. Передавальне число редуктора між гідромотором і маточиною колеса – 11.
3. Діаметр колеса за шиною 1,55 мм;
4. Момент інерції на одному колесі 70 кг.м$^2$;
5. Модуль пружності РР 1500 МПа;
6. Об'єм РР в трубопроводі діаметром 16 мм і довжиною 2,5 м між насосом і гідромотором складає 5 дм$^3$;
7. Коефіцієнт кінематичної в'язкості РР прийнятий 30 сСт при розрахунку гідравлічних втрат за довжиною трубопроводу.

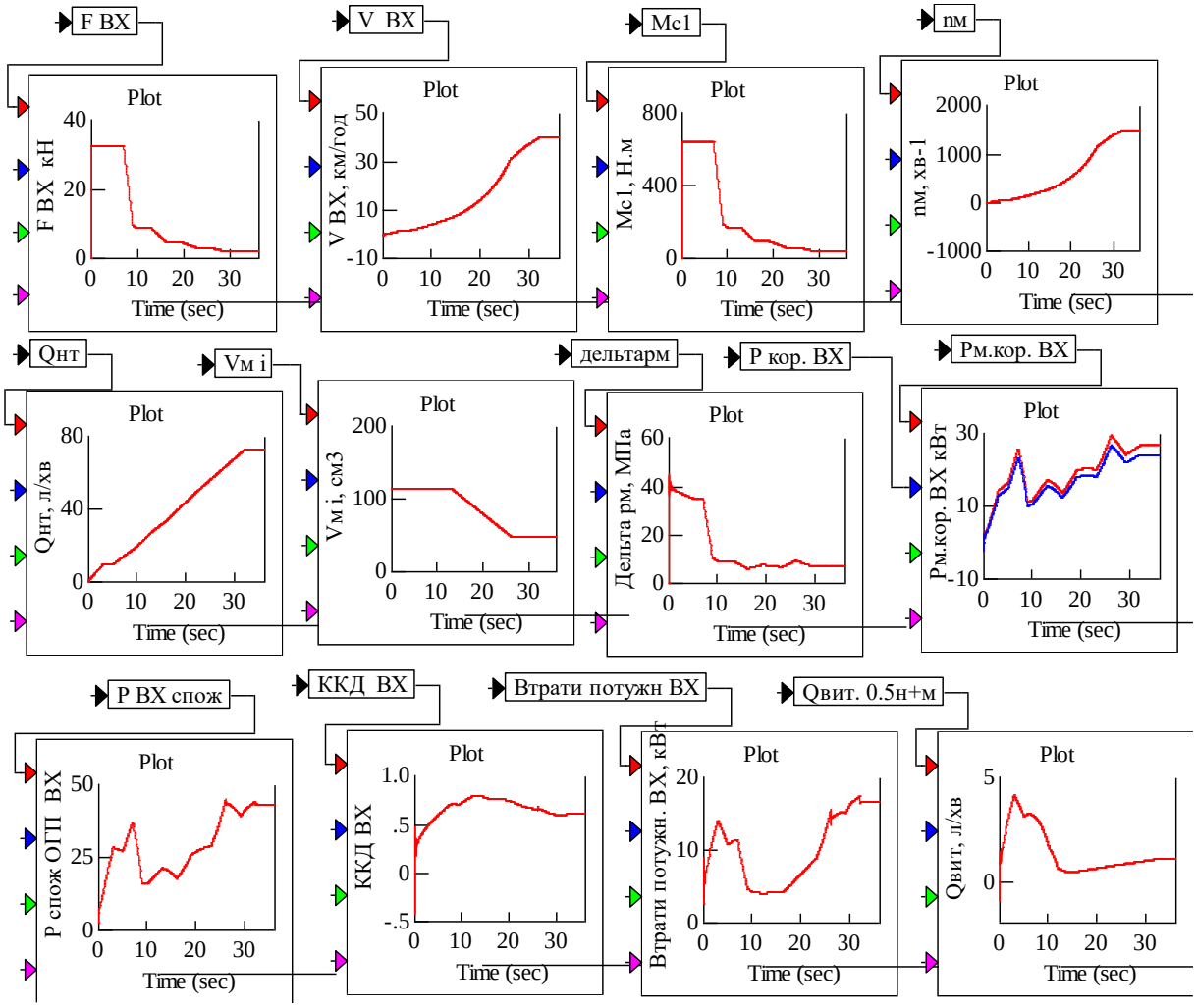



**Рис. 5. Характеристики гідроприводу всюдихода в повному діапазоні швидкості**

На плотерах представлені:

1. F ВХ – тягова характеристика ВХ.
2. V ВХ – швидкісна характеристика ВХ.
3. Mc1 – крутний момент одного гідромотора.
4. пм – частота обертання одного гідромотора.
5. Qнт – теоретична подача насоса до одного гідромотора. Закон зміни подачі дозволяє мати потрібну швидкість ВХ при максимальному постійному робочому об'ємі гідромотора.
6. Vм,і – характеристика зміни робочого об'єму гідромотора.
7. Дельта Рм – перепад тисків на гідромоторі.
8. Рм кор. ВХ – корисна потужність 4-х гідромоторів (червона лінія).

9. Р кор. ВХ – корисна потужність на маточинах ВХ (синя лінія).
10. Р ВХ спож – споживана потужність ОГП (трансмісії);
11. ККД ВХ – ККД всюдихода.
12. Втрати потужності ВХ для вибору оливаохолоджувача.
13. Q вит. 0,5н+м – витоки РР з насоса (приймаємо 0,5 від повних одного насосу) і гідромотора.

14-17. Завдання ККД насоса та гідромотора.

Примітка: результати за пп. 4 і 7 отримані при рішенні диференціальних рівнянь математичної моделі чисельним методом в пакеті VisSim.

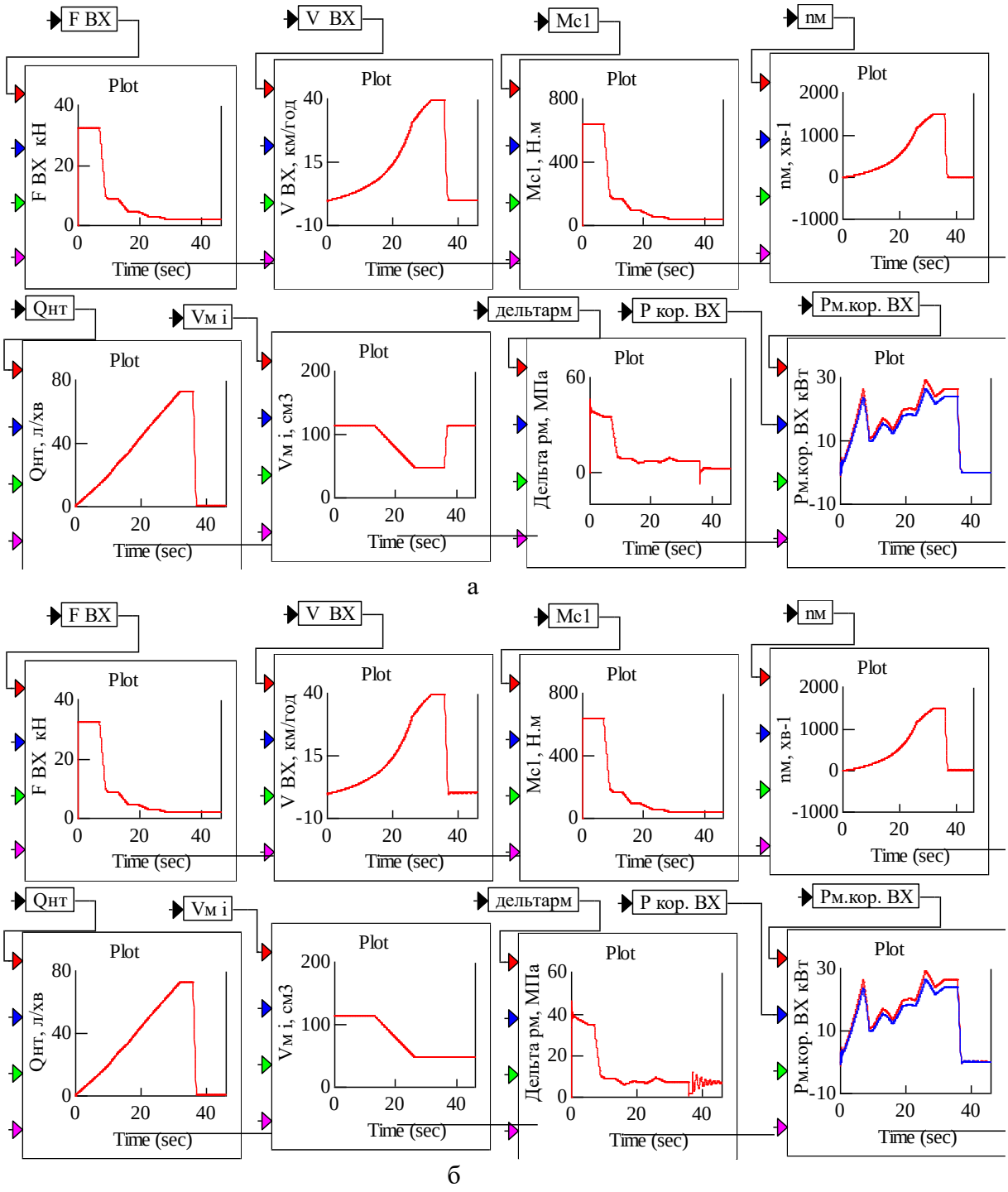



**Рис. 6. Режими роботи ВХ при гальмуванні зі швидкості 40 км/год: а – при одночасному збільшенні робочого об'єму гідромотора до максимального значення; б – без підвищення робочого об'єму гідромотора (див. осцилограму «дельта рм» в нижньому рядку).**

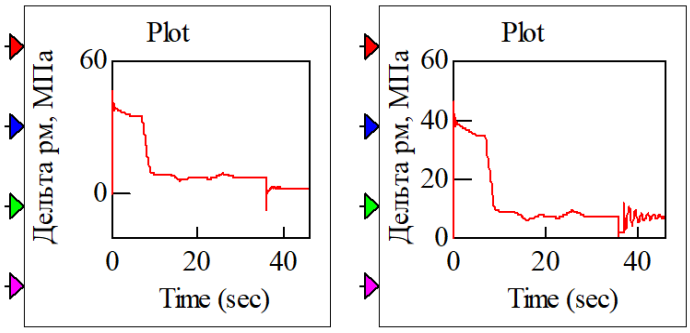
На рис. 5 представлені осцилограми при транспортному русі ВХ, починаючи зі зрушування до максимальної швидкості в 40 км/год.

На основі цих осцилограм можна зробити такі попередні висновки:

1. ОГП трансмісії виконує вимоги тягово-швидкісної характеристики в її повному діапазоні.
2. Тиск в ОГП коливається від 52 МПа при зрушуванні ВХ і знижується до 10 МПа при швидкості більше ніж 10 км/год.
3. Максимальна швидкість ВХ в 40 км/год може бути досягнута при робочому об'ємі гідромотора в 48 см$^3$.
4. ККД ОГП змінюється від максимального значення в 80 % при швидкості ВХ в 13 км/год і зменшується до 61 % на максимальній швидкості в 40 км/год.
5. Втрати потужності не перевищують 17,5 кВт (тобто, оливаохолоджувач повинен мати таку максимальну характеристику або вищу).
6. На підвищених швидкостях пересування ВХ споживана потужність досягає 45 кВт, в діапазоні швидкості до 25 км/год не перевищує 37 кВт.
7. Побудована математична модель ОГП ВХ дозволяє варіювати деякими параметрами для аналізу їх впливу на вихідні характеристики. До таких параметрів слід віднести частоту обертання ДВЗ, момент інерції ВХ, модуль пружності і коефіцієнт кінематичної в'язкості РР, значення ККД насоса і гідромотора.

На рис. 6 показані режими переміщення ВХ з гальмуванням наприкінці. Якщо встановити регулятор насоса в нульове положення і одночасне підняти робочий об'єм гідромотора до максимального значення (рис. 6,а), то має місце зниження тиску нижче нульового значення на 36-й секунді руху, тобто до кавітаційного становища в ОГП. Якщо при гальмуванні не збільшувати робочий об'єм гідромотора (рис. 6,б), то тиск в ОГП не знижується до нульового значення.

На рис. 7 приведені окремі осцилограми тиску в ОГП, де в першому випадку (а) тиск короткочасно зменшився до значення вакууму в 7 МПа, а при утриманні значення робочого об'єму гідромотора на рівні 48 см$^3$, що відповідало швидкості всюдихода в 40 км/год, тиск не зменшується до значення нижче атмосферного (б).




а б

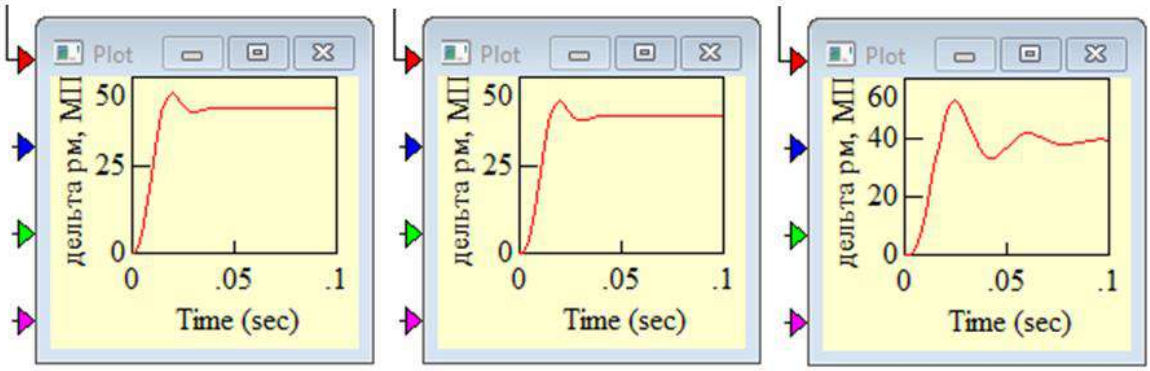
**Рис. 7. Зміна тиску в лінії нагнітання насоса ОГП при гальмуванні шляхом зміни робочого об'єму насоса: а – при одночасному збільшенні робочого об'єму гідромотора до максимального значення 115,6 см$^3$; б – при збереженні робочого об'єму гідромотора на рівні 48 см$^3$, що відповідало швидкості всюдихода в 40 км/год.**

Далі розглянуті режими зрушування ВХ при таких вихідних даних:
Максимальна маса машини – 3500 кг;
Мінімальна швидкість при зрушуванні – 3 км/год;
Зовнішній діаметр шини $d_в$ = 1,55 м;
Кількість ведучих гідромотор-коліс $z$ = 4;
Максимальний крутний момент одного гідромотора 642 Нм;
Момент інерції на одне колесо 70 кг.м$^2$.

У першому наближенні розглянуті лінійні режими навантаження на гідромотор до крутного моменту Мс = 642 Н.м за 0,015 с і різний час підвищення подачі насосу щодо одного гідромотора до $Q_{нт1}$ = 50 л/хв. При рішенні диференціальних рівнянь за допомогою пакету VisSim отримані значення частоти обертання гідромотора і тиску в ОГП, швидкості і корисної потужності ВХ. Швидкість ВХ зростала до 3 км/год, а корисна потужність не перевищувала 33,5 кВт.

Для більшої наочності на рис. 8 приведені отримані осцилограми тільки для перепаду тисків «дельта рм» від часу.

Час підвищення зовнішнього навантаження до значення $M_c$ = 642 Н·м встановлювався постійним за 0,015 с для всіх 3-х режимів.




а б в

**Рис. 8. Осцилограми зміну перепаду тисків в ОГП ВХ залежно від часу зростання подачі насоса до 50 л/хв і модуля пружності робочої рідини.**

На рис. 8, а час зростання подачі насоса встановлений в 0,1 с. Тиск зрушування досягає 45 МПа і зменшується до статичного значення в 39 МПа.

На рис. 8, б час зростання подачі насоса збільшений на порядок до 1,0 с, завдяки чому тиск зрушування зменшився до 43 МПа. Для досягнення такого ефекту в лініях управління регуляторами насосів встановлюють дроселі (зазвичай, є декілька типорозмірів щілин дроселів при замовленні насосів).

При зменшенні модуля пружності РР з 1500 МПа до 500 МПа згідно рис. 8,в (таке можливо при насіченні РР нерозчиненим повітрям) маємо підвищення коливань тиску з 43 МПа до 52 МПа.

Таким чином, під час підготовки ВХ до експлуатації необхідно налаштувати систему регулювання з запізненням щодо підвищення часу подачі насоса і очистити РР від нерозчиненого повітря (бульбашок).

## Висновки.

За допомогою математичної моделі динаміки бортового об'ємного гідроприводу всюдихода проведено моделювання зміни подачі насоса і навантаження гідромоторів, ККД гідромашин та модуля пружності робочої рідини на їх вплив на динамічні характеристики.

Гідропривод трансмісії виконує вимоги тягово-швидкісної характеристики в її повному діапазоні, при цьому тиск коливається від 52 МПа при зрушуванні всюдихода і знижується до 10 МПа при швидкості більше ніж 10 км/год.

При гальмуванні всюдихода з максимальної швидкості шляхом зменшення подачі насоса для забезпечення безкавітаційної роботи гідроприводу треба зберігати постійним мінімальне значення робочого об'єму гідромотора.

Зниження модуля пружності робочої рідини при її насиченості нерозчиненим повітрям приводить к підвищенню тиску при зрушування всюдихода.

Під час підготовки гідроприводної трансмісії всюдихода до експериментальних

випробувань необхідно налаштувати систему регулювання з запізненням часу подачі насоса.

Представляється корисним подальше проведення аналізу динамічних характеристик при поворотах всюдихода, а також застосування високомоментних безредукторних гідромотор-коліс замість аксіально-поршневих.

## Література


1. Аврунін Г.А., Білан І.В., Мороз І.І., Підгорний М.В., Надобко Є.В. Огляд і аналіз технічних характеристик вітчизняних всюдиходів. *Polish journal of science*, 2026. 94. 00-033. 56–70. https://doi.org/10.5281/zenodo.18331058
2. https://auto.24tv.ua/u_poltavi_nalahodyly_vyrobnytstvo_vsiudykhodiv_tornado_n41275 (завод всюдиходів «TORMADO», м. Полтава, дата звернення 30.07.2026)
3. Ngoc Danh Dang. Advanced Control Designs for Output Tracking of Hydrostatic Transmissions. DISSERTATION. University of Rostock. Faculty of Mechanical Engineering and Marine Technology Chair of Mechatronics. Rostock, 19, November 2021. 118 p. https://doi.org/10.18453/rosdok_id00003429
4. Massimo Martelli, Luca G. Zarotti. Hydrostatic Transmission with a Traction Control. 22nd International Symposium on Automation and Robotics in Construction ISARC 2005. September 11-14, 2005, Ferrara (Italy). 115–121.
5. Hao Sun, Harald Aschemann. Sliding-Mode Control of a Hydrostatic Drive Train with Uncertain Actuator Dynamics. 2013 European Control Conference (ECC). July 17-19, 2013, Zürich, Switzerland. 3216–3221.
6. PATENTANMELDUNG EP 2 975 304 A1. VERFAHREN ZUM ABBREMSEN EINES HYDROSTATISCHEN ANTRIEBS UND HYDROSTATISCHER ANTRIEB. Erfinder: Behm, Martin. Anmelder: ROBERT BOSCH GMBH. Vertreter: Thьrer, Andreas. Bosch Rexroth AG. 13 p. Prioritдt: 17.07.2014 DE 102014213905
7. Hydrostatically Driven Vehicle with Retarder Valve. Lloyd Taylor, Wilhelm Collner. US patent 6,202,783, B1. Mar. 20, 2001.
8. Antonino Bonanno, Luca G. Zarotti HYDROSTATIC BRAKING REVISITED. 16th International Conference of the International Society for Terrain-Vehicle Systems. ISTVS 2008. Turin, November 25-28, 2008, 362–370.
9. Traction Control Methods by Poclain Hydraulics. RCS397 566 860-pointvrqle.fr-03 44 23 48 48. 24 p.
10 .SD-CT OFF-Road System. Electronic Traction Control. Technical Catalog Poclain Hydraulics. Bo9244W. 24/11/2020. 44 p.
11. Smart Drive Premier System. Electronic Traction and Hydrostatic Transmission Control. Technical Catalog Poclain Hydraulics. Poclain Driving Values for Future. A06615Q. 15/01/2014. 52p.
12. Power Transmission Valves. Technical Catalog Poclain Hydraulics. B33971Z. 05/10/2021. 88p.
13. Аврунін, Г., Подригало, М., Подригало, Н., Мороз, І., & Поторока, А. Аналіз можливості застосування гідравлічної трансмісії з мотор-колесами для всюдихода NOMAD ATV. *Автомобільний транспорт*, 2024. (54). 15–24. https://doi.org/10.30977/AT.2219-8342.2024.54.0.02
14. Самородов В. Б., Аврунін Г. А., Кириченко І. Г., Бондаренко А. І., Пелипенко Є. С. Гідро-та пневмосистеми в автотракторобудуванні: навчальний посібник: за ред. В. Б. Самородова; НТУ «ХПІ», Харків : ФОП Панов А. М., 2020, 524 с.
15. https://www.yumpu.com/en/document/view/4906552/generic-dual-path-subsystem-application-system-sauer-danfoss (Система «generic-dual-path», дата звернення 30.07.2026)
16. Лур'є З.Я., Самородов В.Б., Аврунін Г.А., Цента Є.М. Метод поліпшення динамічних характеристик процесу пуску об'ємного гідропривода з замкненим ланцюгом циркуляції робочої рідини. Вісник Національного технічного університету «ХПІ». Серія: Гідравлічні машини та гідроагрегати: Х : НТУ «ХПІ». 2019. № 2 (2019). С. 68-76.
17. https://pro-mobility.org/instruction/instruktsiia-z-vstanovlennia-studentskoi-versii-ptv-vissim/ (Інструкція з встановлення студентської версії PTV Vissim, дата звернення 30.07.2026)

*Дата першого надходження статті до видання 05.08.2026*
*Дата прийняття статті до друку після рецензування 03.09.2026*
*Дата публікації (оприлюднення) статті 04.11.2026*
*Стаття поширюється на умовах ліцензії відкритого доступу(CC BY 4.0)*

# DYNAMICS OF THE HYDRAULIC FLUID POWER OF ALL-WHEEL VEHICLES IN THE MODES OF TRACTION-SPEED CHARACTERISTICS

**G. Avrunin[1], I. Lebedyk[2], M. Podgorny[2], I. Bilan[1], I. Moroz[1],**
[1] *Kharkiv National Automobile and Road University*
[2] *Ceo LLC «Tornado» All-Terrain Vehicle Factory*

## Abstract

**Goal.** Creation of a domestic all-terrain vehicle «Tornado», equipped with a transmission with a hydraulic fluid power based on axial-piston hydraulic motor-wheels with adjustable working volume and end-gears. **Scientific novelty.** Obtaining dynamic characteristics of the all-terrain vehicle's hydraulic drive transmission based on the results of mathematical modeling of the parameters of the traction-speed characteristic using the VisSim application software package for solving nonlinear differential equations for determining the speed of the loader, the pressure in the hydraulic fluid power and its useful power over time. **Practical value.** Conclusions were obtained regarding the loading algorithms of the all-terrain vehicle's hydraulic fluid power transmission, which provide pressure limitations at all stages of its traction-speed characteristic. **Main results.** The analysis of oscillograms of dynamic processes in the hydraulic fluid powerof the all-terrain vehicle showed that by modeling the pump supply modes and changing the working volume of axial-piston hydraulic motors, it is possible to detect extreme modes that lead to fluctuations in the speed of the all-terrain vehicle and the pressure in the hydraulic fluid power. In particular, it was determined that when braking the all-terrain vehicle from maximum speed by reducing the pump supply to ensure cavitation-free operation of the hydraulic fluid power, it is necessary to simultaneously maintain the set value of the working volume of the hydraulic motors constant. **Conclusions.** According to the results of the research, limiting modes of loads of the hydraulic fluid power transmission were established at the stage of experimental research of the all-terrain vehicle «Tornado».

**Keywords:** dynamics of a hydraulic fluid power, axial piston hydraulic machines, torque, speed, power, pressure drop.

**DOI https://doi.org/10.32782/1994-4691-2026-1-77-12**
УДК 631.372:629.114.2

# АНАЛІЗ РОБОТИ ГІДРОМЕХАНІЧНИХ ТРАНСМІСІЙ FENDT VARIO ТА JOHN DEERE AUTOPOWR ТА ПОРІВНЯННЯ ЇХ ЕФЕКТИВНОСТІ

# ANALYSIS OF THE OPERATION OF FENDT VARIO AND JOHN DEERE AUTOPOWR HYDROMECHANICAL TRANSMISSIONS AND COMPAR-ISON OF THEIR EFFICIENCY

М. С. Волянський[1], доцент ORCID 0000-0002-3595-9365
О.Т. Лавріненко[1], канд. техн. наук ORCID 0000-0003-1347-6668
Ю.О. Гуменюк[1], канд. техн. наук, доцент ORCID 0000-0003-2463-1950
Ю.О. Росамаха[1], канд. техн. наук, доцент ORCID 0000-0001-9818-0246

[1] *Національний університет біоресурсів і природокористування України, Київ, Україна*
*e-mail: mvolyanskij@ukr.net

**Анотація**. У статті проведено порівняльний аналіз ефективності безступінчастих гідромеханічних сило-роздільних трансмісій Fendt Vario та John Deere AutoPowr. Метою є визначення впливу розподілу потужності між механічною та гідрооб'ємною гілками на ККД трансмісії залежно від швидкості руху. Методи включають теоретичний аналіз енергетичного балансу, математичне моделювання, застосування рівняння Вілліса та оцінювання втрат. Наукова новизна полягає у встановленні зв'язку між часткою гідрооб'ємної потужності та сумарним ККД. Встановлено, що збільшення гідрооб'ємної частки знижує сумарний ККД. Для швидкостей 4–12 км/год середній розрахунковий ККД становить 0,875 для Fendt Vario та 0,947 для John Deere AutoPowr. Значення отримано за авторською моделлю, а не експериментально. Практична цінність полягає у використанні підходу для попереднього інженерного оцінювання енергетичної ефективності трансмісій.

.**Ключові слова**: гідромеханічна трансмісія, безступінчаста трансмісія, силорозділення потужності, power-split, гідрооб'ємна гілка, планетарний механізм

## Вступ.

Сучасний трактор працює у широкому діапазоні тягових навантажень і швидкостей. За таких умов ступінчаста трансмісія змушує двигун періодично відхилятися від оптимальної робочої точки. Силороздільна безступінчаста гідромеханічна трансмісія поєднує механічну та гідрооб'ємну гілки, що дає змогу реалізувати безступінчасте регулювання швидкості при високій частці механічного передавання потужності [1, 2].

## Огляд літератури.

Сучасні дослідження гідромеханічних трансмісій сільськогосподарських тракторів зосереджені на підвищенні енергетичної ефективності силороздільних CVT, оптимізації розподілу потужності та вдосконаленні алгоритмів керування. У працях Ahn та ін. розглянуто інтегроване керування двигуном і гідромеханічною трансмісією та алгоритми перемикання діапазонів [4, 5]. Дослідження Wang та ін. присвячені якості пуску і перемикання, роботі CVT при відмовах гідравлічної системи та оптимізації паливної економічності [6–8]. Zhao та ін. досліджували енергетичні витрати і паливну економічність нових концепцій гідромеханічних трансмісій [3, 9], а Xia, Sun і Qin - комплексну стратегію керування перемиканням [10]. Сучасні роботи 2023–2026 рр.

також охоплюють нові конфігурації силороздільних систем та оцінювання їх тягових характеристик [11–14].

Разом із тим у наведених дослідженнях основна увага приділяється окремим аспектам конструкції, енергетичного аналізу або керування. Невирішеною частиною проблеми залишається узгоджене порівняльне оцінювання Fendt Vario та John Deere AutoPowr на основі єдиного розрахункового підходу до частки потужності, що проходить через гідрооб'ємну гілку, з чітким розмежуванням модельних розрахунків і комплексних показників DLG PowerMix. Саме цьому питанню присвячено дане дослідження.

Для Fendt Vario та споріднених конструкцій у літературі описано гідрооб'ємно-механічне силорозділення. Для ZF ECCOM, який застосовувався в системах AutoPowr відповідних поколінь John Deere, описано планетарну передачу, де реалізуються автоматично чотири швидкісні діапазони, гідрооб'ємний модуль і реверсивну передачу [6, 20].

## Методологія дослідження.

Методологія дослідження передбачає вирішення наступних завдань:

– формалізувати розподіл вхідної потужності між механічною та гідрооб'ємною гілками;

– запропонувати теоретичний апарат вихідного матеріалу та подати формули у класичному вигляді;

– проаналізувати кінематику планетарного механізму за рівнянням Вілліса;

– оцінити вплив частки гідрооб'ємної потужності на сумарний ККД;

– порівняти розрахункову характеристику $\eta(v)$ для заданого у вихідному матеріалі набору точок;

– сформулювати коректні межі застосування DLG PowerMix як показника всієї машини, а не ізольовано трансмісії.

**Теоретичні основи функціонування гідромеханічної трансмісії.**

У першому наближенні вхідна потужність двигуна розгалужується на механічну та гідрооб'ємну складові. Для кутової швидкості $\omega_{in}$ та моменту $M_{in}$ маємо:

$$P = P_{mech} + P_{hydr} \tag{1}$$

Частку потужності, що проходить через гідрооб'ємний контур, введемо як:

$$\gamma = \frac{P_{hydr}}{P} \tag{2}$$

Тоді первинна інженерна оцінка сумарного ККД має вигляд [14]

$$\eta_{total} = (1-\gamma)\eta_{mech} + \gamma\eta_{hydr} \tag{3}$$

Це рівняння є моделлю першого порядку. Воно не враховує окремо циркуляцію потужності, втрати в муфтах, підшипниках, зубчастих передачах, ущільненнях та паразитні потоки, тому при чисельній ідентифікації конкретної трансмісії його слід розглядати як інженерну апроксимацію.

Для гідрооб'ємної гілки, якщо втрати насоса і мотора подаються добутком об'ємних, гідравлічних та механічних складових, маємо:

$$\eta_{hydr} = \eta_v^p \eta_h^p \eta_m^p \eta_v^m \eta_h^m \eta_m^m \tag{4}$$

де індекси $p$ та $m$ відповідають насосу і гідромотору. Звідси очевидно, що навіть за високого механічного ККД загальний ККД системи знижується зі зростанням $\gamma$, якщо $\eta_{hydr} < \eta_{mech}$. Принцип мінімізації частки потужності, яка проходить через гідрооб'ємний контур, є одним із ключових чинників ефективного проєктування power-split трансмісії [1, 2].

**Кінематика планетарного механізму та розширені теоретичні викладки.**

Для планетарного механізму із сонячною шестернею *a*, коронною шестернею *b* та водилом *h* використовується рівняння Вілліса (15):

$$\omega_a - k\omega_b + (k-1)\omega_h = 0 \quad (5)$$

де $\omega_a$ – кутова швидкість сонячної шестерні; $\omega_b$ – кутова швидкість коронної (зовнішньої) шестерні; $\omega_h$ – кутова швидкість водила; $k$ – передаточне відношення, яке визначається числом зубців коронної та сонячної шестерень, $k = -(z_b / z_a)$.

Це рівняння описує кінематичний зв'язок між трьома основними елементами планетарного механізму. За геометричними параметрами, прийнятими у вихідному матеріалі, $z_a = 31$, $z_b = 67$:

$$k = -\frac{67}{31} = -2{,}161 \quad (6)$$

За номінальної частоти обертання двигуна 2100 об/хв, тобто приблизно 220 рад/с, та $\omega_h = \omega_{in}$:

$$\omega_a + 2{,}161\omega_b - 3{,}161\omega = 0 \quad (7)$$

$$\omega_a = 695{,}42 - 2{,}161\omega_b \quad (8)$$

Для прийнятої у вихідному матеріалі ідеалізованої моделі пропорційний розподіл моменту записується [15]:

$$M_a = \frac{M}{(1-k)} = \frac{M}{3{,}161} \approx 0{,}316M \quad (9)$$

де $M$ – сумарний момент, що передається через механізм; $M_a$ – частка моменту, яка припадає на сонячну шестерню; 1 – k – знаменник, що враховує геометричні параметри (відношення зубців).

Ця залежність є спрощеною і використовується лише для ідеалізованої моделі. У реальних трансмісіях розподіл моментів залежить від топології планетарних рядів та балансу потужності. Для серійної трансмісії точні знаки моментів і величини потоків визначаються конкретною топологією планетарних рядів та балансом потужності; тому числові коефіцієнти вихідного матеріалу не слід трактувати як паспортні дані конкретної серійної коробки.

Зв'язок швидкостей насоса і мотора в замкненому гідрооб'ємному контурі у спрощеному вигляді [18]:

$$\frac{\omega_m}{\omega_p} = \frac{(V_p \eta_v^p \eta_v^m)}{V_m} \quad (10)$$

де $\omega_m$ – кутова швидкість гідромотора; $\omega_p$ – кутова швидкість гідронасоса; $V_p$ – робочий об'єм насоса (см³/об); $V_m$ – робочий об'єм мотора (см³/об); $\eta_v^p$ – об'ємний коефіцієнт корисної дії насоса (враховує внутрішні витоки); $\eta_v^m$ – об'ємний коефіцієнт корисної дії мотора.

Ця формула показує, що швидкість мотора пропорційна швидкості насоса, але з поправкою на робочі об'єми та втрати від витоків. Якщо об'єми насоса і мотора однакові, а ККД близькі до 1, то швидкості будуть майже рівні. Отже, зміна $V_p$ та $V_m$ змінює $\omega_p$ і $\omega_m$, а через планетарний механізм - вихідну швидкість. У реальній системі необхідно додатково враховувати напрямок потоку, знак кутової швидкості, тиск, об'ємні втрати та механічний ККД гідромашин.

**Енергетичний баланс і втрати.**

За заданої частки гідрооб'ємної потужності енергетичний ККД можна подати через еквівалентний баланс [18]:

$$P_{out} = (1-\gamma)\eta_{mech} P + \gamma \eta_{hydr} P \quad (11)$$

де $P_{out}$ – корисна вихідна потужність системи; $P$ – загальна вхідна потужність системи; $\gamma$ – частка гідрооб'ємної потужності у загальному балансі; $\eta_{mech}$ – механічний ККД (ефективність механічної гілки); $\eta_{hydr}$ – гідравлічний ККД (ефективність гідрооб'ємної гілки).

Дтрати енергії у системі

$$P_{loss} = P - P_{out} = P\left[(1-\gamma)(1-\eta_{mech}) + \gamma\left(1-\eta_{hydr}\right)\right] \quad (12)$$

Формула (12) показує, що втрати складаються з двох частин: $(1-\gamma)(1-\eta_{mech})$ – втрати у механічній гілці і $\gamma\,(1-\eta_{hydr})$ – втрати у гідравлічній гілці.

Диференціюючи рівняння (3) за $\gamma$ при сталих $\eta_{mech}$ та $\eta_{hyd}$, одержуємо:

$$\frac{d}{d\gamma}\eta_{total} = \eta_{hydr} - \eta_{mech} \quad (13)$$

де $\eta_{total}$ – сумарний ККД системи.

Похідна показує, як змінюється загальний ККД при зміні частки гідрооб'ємної потужності. Якщо $\eta_{hydr} < \eta_{mech}$, то збільшення γ знижує сумарний ККД.

Оскільки для типових робочих режимів $\eta_{hydr}$ нижчий за $\eta_{mech}$, збільшення частки гідрооб'ємної потужності в першому наближенні знижує сумарний ККД. Це не означає, що максимізація механічної частки завжди оптимальна: необхідно одночасно враховувати робочу точку двигуна, тяговий режим та динаміку керування.

**Інтегральний ККД на інтервалі швидкостей.**

Для безперервної характеристики середній ККД на інтервалі $[v_{min},\ v_{max}]$ визначається [17]:

$$\bar{\eta} = \frac{1}{(v_{max} - v_{min})}\int_{v_{min}}^{v_{max}} \eta_v\, dv \quad (14)$$

де $\overline{\eta}$ – середній ККД, обчислений як інтеграл по інтервалу швидкостей, нормований на його довжину; $[v_{min},\ v_{max}]$ – інтервал швидкостей руху; $\eta_v$ – миттєвий ККД при швидкості $v$.

Для дискретних експериментальних або розрахункових точок доцільне трапецієподібне інтегрування:

$$\bar{\eta} \approx \frac{\Sigma}{(v_n - v_1)}\frac{(\eta_i + \eta_i^{+1})}{2}(v_{i+1} - v_i) \quad (15)$$

де $v_1$, $v_n$ – крайні значення швидкості у вибірці; $\eta_i$, $\eta_i^{+1}$ – значення ККД у сусідніх точках.

Формула реалізує чисельне інтегрування методом трапецій, що дозволяє оцінити середній ККД за експериментальними або розрахунковими даними.

**Динамічна модель керування.**

Розширений теоретичний апарат включає PID-регулятор швидкості. Для похибки $e_v(t) = v_{target}(t) - v_{actual}(t)$ [17]:

$$u_{hydro}(t) = K_{p,h}e_v(t) + K_{i,h}\int_0^t \left(e_v(t)\right) + K_{d,h}\frac{d}{dt}e_v(t) \quad (16)$$

де $u_{hydro}(t)$ – керуючий сигнал на гідравлічний сервопривід (наприклад, положення золотника чи клапана); $K_{p.h}$ – коефіцієнт пропорційної складової (реакція на миттєву похибку); $e_v(t) = v_{target}(t) - v_{actual}(t)$ – похибка швидкості (різниця між бажаною та реальною); $K_{i.h}$ – коефіцієнт інтегральної складової (накопичення похибки у часі, усуває сталу помилку); $K_{d.h}$ – коефіцієнт диференціальної складової (реакція на швидкість зміни похибки, демпфування).

$$\frac{d}{dt}V_p(t) = \frac{\left(C_{valve}\,u_{hydro}(t) - V_p(t)\right)}{T_{servo}} \quad (17)$$

де $V_p(t)$ – положення або об'ємна подача насоса (керований параметр); $C_{valve}$ – коефіцієнт підсилення клапана (перетворює сигнал у фізичний вплив); $u_{hydro}(t)$ – сигнал від PID-регулятора; $T_{servo}$ – постійна часу сервоприводу (визначає інерційність системи).

Формула описує, як реальне положення $V_p(t)$ наближається до бажаного значення під дією керуючого сигналу [17].

$$J_{eng}\frac{d}{dt}\omega(t) = M_{ind}\left(q_{fuel},\omega\right) - M_{mech_{loss}}(\omega) - M(t) \quad (18)$$

де $l_{eng}$ – момент інерції двигуна; $\omega(t)$ – кутова швидкість колінчастого вала; $M_{ing}(qfuel,\omega)$ – індикаторний момент двигуна, що залежить від подачі палива $q_{fuel}$ та швидкості $\omega$; $M_{mechloss}(\omega)$ – механічні втрати (тертя, допоміжні агрегати); $M(t)$ – момент навантаження від трансмісії.

Рівняння описує баланс моментів: прискорення двигуна визначається різницею між корисним моментом і втратами. Узгодження керування трансмісією і двигуном можна сформулювати як задачу мінімізації інтегрального критерію:

$$L(q_{fuel},V_p) = \int_0^T \left(g_e(\omega,M_{ind})P + \lambda e_v(t)\right)dt \to min \quad (19)$$

де $L(q_{fuel},V_p)$ – функціонал (критерій оптимізації); $g_e(\omega,M_{ind})$ – питома витрата палива (г/кВт·год), залежить від режиму двигуна; $P$ – потужність двигуна; $\lambda e_v(t)$ – штраф за відхилення швидкості (вага $\lambda$ визначає важливість точності). Інтеграл береться за час роботи $T$.

Завдання: знайти таке керування подачею палива $q_{fuel}$ та положенням насоса $V_p$, щоб мінімізувати сумарну витрату палива та похибку швидкості.

Така постановка показує, що паливна економічність не є виключно властивістю кінематичної схеми, вона залежить від того, наскільки система керування здатна утримувати двигун і гідромеханічну гілку у сприятливій області режимів. Дослідження інтегрованого керування двигуном і гідромеханічною трансмісією підтверджують важливість спільного вибору передатного відношення та режиму двигуна [4].

## Результати.

Принципові схеми гідромеханічної трансмісії розподілу потужності тракторів Fendt Vario і John Deere AutoPowr / ZF ECCOM наведені на рис. 1.

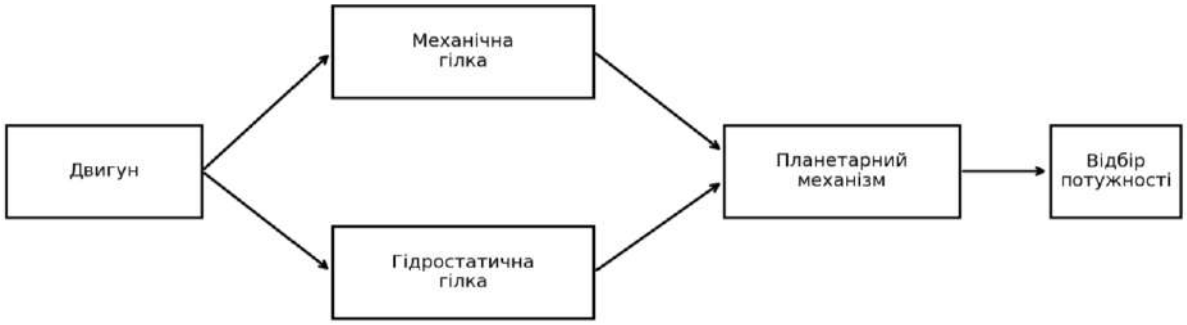



**Рис. 1. Принципова схема гідромеханічної трансмісії розподілу потужності тракторів Fendt Vario і John Deere AutoPowr/ZF ECCOM**

### Fendt Vario: конструктивно-кінематичні особливості.

Fendt Vario є класичним прикладом гідрооб'ємно-механічної силороздільної трансмісії. Технічна публікація Brenninger описує концепцію Fendt Vario CVT та її застосування у сільськогосподарських тракторах [15, 17].

Для аналізу Vario у науковій літературі використовується силороздільна схема з планетарним механізмом та гідрооб'ємною гілкою. У конкретних серійних модифікаціях розташування елементів і напрямки потоків можуть відрізнятися, тому наведена у статті схема має статус узагальненої принципової моделі [3, 5].

Для Vario характерна зміна співвідношення механічної та гідрооб'ємної складових залежно від швидкості; це є фундаментальною властивістю power-split CVT [1, 3, 15].

**John Deere AutoPowr/ZF ECCOM: конструктивно-кінематичні особливості.**

У науковій і технічній літературі AutoPowr відповідних поколінь John Deere пов'язується з гідрооб'ємно-механічними трансмісіями ZF ECCOM. ZF ECCOM характеризується як безступінчаста силороздільна передача з планетарною частиною, гідрооб'ємним модулем та реверсивною передачею. У повному діапазоні швидкостей є чотири швидкісні діапазони які автоматично перемикаються [6, 20].

Для John Deere принципово важливо не переносити параметри одного покоління AutoPowr на всі інші моделі. Технічні джерела показують різні реалізації ECCOM залежно від потужності та покоління трактора. Тому в цій статті чотиридіапазонну концепцію наведено як характеристику відповідних ECCOM/AutoPowr реалізацій, а не як універсальну властивість кожного трактора John Deere [22].

У кожному діапазоні безступінчаста зміна швидкості забезпечується регулюванням гідрооб'ємної гілки; структура power-split дає змогу зменшувати гідрооб'ємну частку та підвищувати ефективність у сприятливих робочих зонах [1, 2, 6].

**Розрахункова оцінка ККД $\eta(v)$.**

Для кількісного порівняння ефективності гідромеханічних трансмісій Fendt Vario та John Deere AutoPowr використано дискретний набір розрахункових значень коефіцієнта корисної дії залежно від швидкості руху трактора. Наведені значення не є результатами стендових випробувань конкретних трансмісій або офіційними показниками DLG і тому розглядаються виключно як дані авторської розрахункової моделі. Загальний коефіцієнт корисної дії трансмісії визначається відношенням потужності на її виході до потужності, що підводиться до трансмісії:

$$\eta_{тр} = \frac{P_{вих}}{P_{вх}} \tag{20}$$

де $\eta_{тр}$ – загальний коефіцієнт корисної дії трансмісії; $P_{вих}$ – потужність на виході трансмісії, кВт; $P_{вх}$ – потужність на вході трансмісії, кВт.

Для силороздільної гідромеханічної трансмісії вхідний потік потужності розподіляється між механічною та гідрооб'ємною гілками. У першому інженерному наближенні сумарний ККД може бути представлений як зважена сума ККД цих гілок:

$$\eta_{тр} = (1 - \gamma)\eta_{мех} + \gamma\eta_{гідр} \tag{21}$$

де $\gamma$ – частка вхідної потужності, що передається через гідрооб'ємну гілку; $\eta_{мех}$ – ККД механічної гілки; $\eta_{гідр}$ – ККД гідрооб'ємної гілки.

Частка потужності, що передається через гідрооб'ємну гілку, визначається співвідношенням:

$$\gamma = \frac{P_{гідр}}{P_{вх}} \tag{22}$$

де $P_{гідр}$ – потужність, що передається через гідрооб'ємну гілку, кВт. Відповідно, механічна частка потужності дорівнює:

$$\gamma_{мех} = 1 - \gamma \tag{23}$$

Якщо $\eta_{мех} > \eta_{гідр}$, то збільшення механічної частки потужності сприяє підвищенню сумарного ККД. Цю умову можна записати як:

$$\eta_{\text{мех}} > \eta_{\text{гідр}} \quad (24)$$

Рівняння (21) є моделлю першого порядку. Воно не враховує окремо втрати в планетарних механізмах, зубчастих передачах, підшипниках, муфтах, ущільненнях, гідравлічних магістралях, а також циркуляційні та паразитні потоки потужності. Тому його слід використовувати для первинної інженерної оцінки, а не як повну модель енергетичного балансу конкретної серійної трансмісії.

Для узгодження розрахунку з конструктивно-кінематичними особливостями силороздільних трансмісій у таблиці 1 виконано розрахунок за рівнянням (21). Значення $\eta(v)$ визначаються через частку потужності гідрооб'ємної гілки $\gamma(v)$.

**Таблиця 1. Розрахункові значення частки гідрооб'ємної потужності та ККД трансмісій Fendt Vario і John Deere AutoPowr**

| $v$, км/год | Fendt Vario | | John Deere AutoPowr | |
|---|---|---|---|---|
| | $\gamma F$ | $\eta F$ | $\gamma JD$ | $\eta JD$ |
| 2 | 0,941 | 0,857 | 0,180 | 0,948 |
| 4 | 0,892 | 0,863 | 0,360 | 0,927 |
| 6 | 0,843 | 0,869 | 0,360 | 0,927 |
| 8 | 0,794 | 0,875 | 0,180 | 0,948 |
| 10 | 0,745 | 0,881 | 0,000 | 0,970 |
| 12 | 0,696 | 0,886 | 0,063 | 0,963 |
| 14 | 0,647 | 0,892 | 0,125 | 0,955 |
| 16 | 0,598 | 0,898 | 0,188 | 0,948 |
| 18 | 0,549 | 0,904 | 0,250 | 0,940 |
| 20 | 0,500 | 0,910 | 0,179 | 0,949 |
| 25 | 0,375 | 0,925 | 0,000 | 0,970 |
| 30 | 0.250 | 0,940 | 0,096 | 0,958 |
| 40 | 0.000 | 0,970 | 0,208 | 0,945 |

У розрахунку прийнято $\eta_{\text{мех}} = 0{,}97$ та $\eta_{\text{гідр}} = 0{,}85$ як інженерні модельні параметри першого порядку, а не як паспортні або експериментально визначені значення. Для Fendt Vario $\gamma F(v)$ апроксимовано за документованою тенденцією зменшення гідрооб'ємної частки зі зростанням швидкості; для John Deere AutoPowr $\gamma JD(v)$ визначено за опублікованою характеристикою механічної частки потужності 55–100 % для 7R AutoPowr [21, 22].

Для оцінювання середнього ККД на заданому інтервалі швидкостей використано трапецієподібне інтегрування дискретних значень:

$$\eta_{\text{тр}} = \frac{1}{v_{max} - v_{min}} \sum_{i=1}^{n-1} \frac{\eta_i + \eta_i + 1}{2} (v_i + 1 - v_i) \quad (25)$$

де $\eta_{\text{тр}}$ – середній ККД трансмісії на заданому інтервалі швидкостей; $v_{min}$ і $v_{max}$ – мінімальна та максимальна швидкості досліджуваного інтервалу, км/год; $v_i$ та $v_i + 1$ – сусідні значення швидкості; $\eta_i$, $\eta_i$ +1 – відповідні значення ККД; $n$ – кількість дискретних точок.

У таблиці 1 $v$ – швидкість руху трактора, км/год; $\gamma F$ – частка вхідної потужності, що передається через гідрооб'ємну гілку Fendt Vario; $\eta F$ – розрахунковий ККД Fendt; $\gamma JD$ – частка гідрооб'ємної потужності John Deere AutoPowr; $\eta JD$ – розрахунковий ККД John Deere; $\eta_{мех} = 0{,}97$ та $\eta_{гідр} = 0{,}85$ – прийняті модельні параметри.

Застосування рівняння (25) до інтервалу швидкостей 4–12 км/год дає середній розрахунковий ККД 0,875 для Fendt Vario та 0,947 для John Deere AutoPowr. Це підтверджує, що збільшення частки гідрооб'ємної потужності знижує сумарний ККД, а оптимізація power-split трансмісії полягає у мінімізації γ [14, 15]. Це інтегральна оцінка розрахункової моделі, а не експериментальний показник конкретної серійної трансмісії.

У загальному випадку реальний ККД трансмісії залежить не лише від швидкості руху, а й від розподілу потужності, навантажувального моменту, робочого тиску, частоти обертання двигуна та температури робочої оливи. Тому багатофакторну залежність можна подати у вигляді:

$$\eta_{тр} = \eta_{тр}(v, \gamma, M_н, p, \omega_д, T_{ол}) \quad (26)$$

де $M_н$ – навантажувальний крутний момент, Н·м; $p$ – робочий тиск у гідрооб'ємному контурі, МПа; $\omega_д$ – кутова швидкість колінчастого вала двигуна, рад/с; $T_{ол}$ – температура робочої оливи, °С.

Рівняння (26) підкреслює, що швидкість руху сама по собі не є достатньою змінною для повного опису реального ККД.

Розрахункова залежність ККД від швидкості руху тракторів Fendt Vario і John Deere AutoPowr наведені на рис. 2.

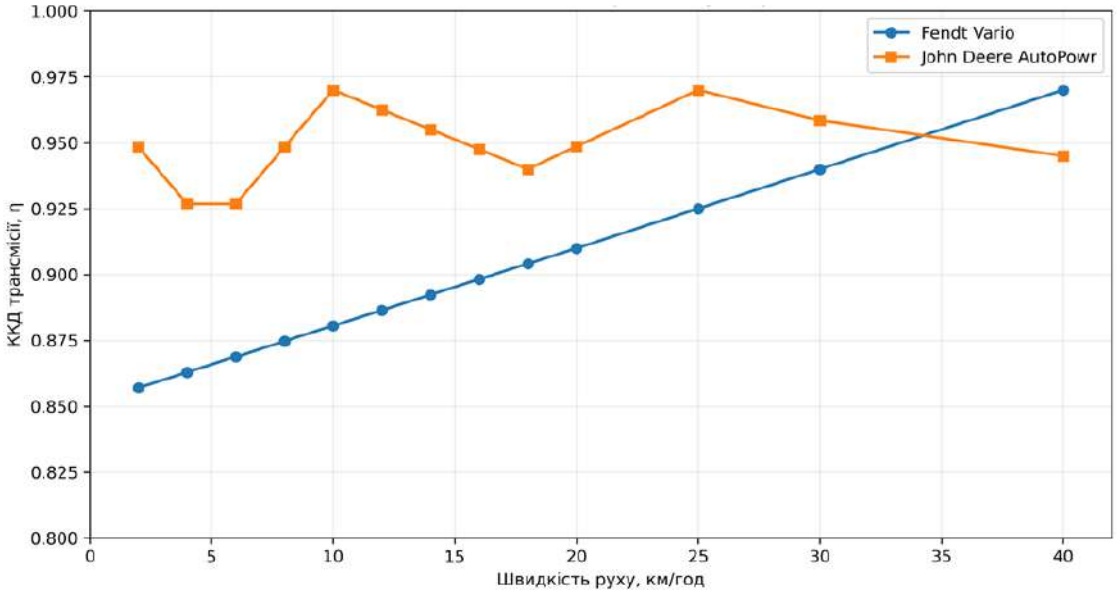



**Рис. 2. Розрахункова залежність ККД від швидкості руху тракторів Fendt Vario і John Deere AutoPowr**

Отримані результати слід трактувати як інженерну оцінку першого порядку. Вона відображає вплив документованого характеру розподілу потужності між механічною та гідрооб'ємною гілками, але не замінює повної моделі power-flow з урахуванням циркуляційних, паразитних та інших локальних втрат.

**DLG PowerMix: методологічне розмежування.**

DLG PowerMix є стандартизованою методикою комплексного оцінювання паливної та експлуатаційної ефективності трактора. Результат формується під впливом роботи двигуна, трансмісії, гідравлічної системи, шин, маси машини, навантаження та налаштувань. Тому показник PowerMix не можна безпосередньо ототожнювати з ККД трансмісії $\eta_{тр}$, визначеним рівнянням (20). У цій роботі числовий розрахунок $\eta(v)$ виконано окремо на основі моделі розподілу потужності $\gamma(v)$, тоді як DLG PowerMix розглядається лише як незалежне комплексне джерело для методологічної перевірки.

Методологічно необхідно розмежовувати два рівні оцінювання: ККД самої трансмісії, який характеризує співвідношення вихідної та вхідної потужності відповідно до рівняння (20), та комплексну паливну й експлуатаційну ефективність трактора, яку характеризує DLG PowerMix.

У межах цієї роботи результати PowerMix використовуються лише як джерело комплексної оцінки трактора і не переносяться безпосередньо на характеристики гідромеханічної трансмісії.

Коректне порівняння Fendt Vario та John Deere AutoPowr має виконуватися за даними конкретних моделей і поколінь трансмісій, для яких документально підтверджено відповідну конструктивну схему. Для повного кількісного порівняння необхідні кінематична схема, передатні числа, характеристики гідромашин, карти об'ємного та механічного ККД, робочий тиск, навантаження, частота обертання двигуна, температура оливи та результати незалежних стендових або польових випробувань.

Отже, розрахункова характеристика $\eta(v)$, побудована за таблицею 1 та усереднена за рівнянням (25), і результати DLG PowerMix повинні розглядатися як доповнювальні, але методологічно різні показники: перша характеризує розрахункову енергетичну ефективність трансмісії, друга - комплексну ефективність трактора в заданих умовах випробування.

**Керування трансмісією та двигуном.**

Електронна система керування координує частоту обертання двигуна, положення регульованих гідромашин, передатне відношення та, у багатодіапазонних трансмісіях, моменти перемикання. AutoPowr має автоматизовані режими керування, а сучасні системи Fendt реалізують узгоджене керування двигуном і трансмісією. Однак конкретні алгоритми, коефіцієнти PID та внутрішні фільтри виробники не розкривають повністю, тому числові параметри з вихідного матеріалу не слід подавати як заводські.

З теоретичної точки зору цільовою є така траєкторія керування, за якої задана швидкість підтримується з мінімальною витратою палива та без перевищення допустимих тисків, частот обертання і моментів.

Отже Fendt Vario демонструє характерну для power-split CVT залежність між механічною та гідрооб'ємною гілками. ZF ECCOM/AutoPowr використовує багатодіапазонну архітектуру, яка дає змогу формувати сприятливий розподіл потужності у різних діапазонах [1, 3, 6].

Водночас за наведеними у вихідному матеріалі значеннями не можна робити висновок про універсальну перевагу одного виробника. Таблиця $\eta(v)$ є модельною; реальний ККД залежить від навантаження, тиску, частоти обертання, передатних чисел, температури оливи, стану гідромашин та алгоритму керування.

## Висновки.

Сформований теоретичний апарат вихідної статті — енергетичний баланс, коефіцієнт розгалужування $\gamma$, гідростатичний ККД, рівняння Вілліса, кінематичні залежності гідромашин, баланс втрат та динамічна модель керування.

Силороздільна гідромеханічна трансмісія може мати вищу ефективність за чисто гідрооб'ємну передачу завдяки проходженню значної частини потужності механічною гілкою [1, 2].

Рівняння (21) придатне для первинної інженерної оцінки впливу розподілу потужності, але не замінює повної моделі power-flow з циркуляційними та паразитними втратами.

Fendt Vario є гідрооб'ємно-механічною power-split концепцією; у наукових і технічних джерелах описано зростання механічної частки у відповідних режимах зі збільшенням швидкості [3, 15].

John Deere AutoPowr у відповідних поколіннях пов'язаний із гідромеханічними трансмісіями ZF ECCOM; чотиридіапазонна концепція документована для ECCOM і не повинна автоматично переноситися на всі моделі AutoPowr [6, 20].

Наведені значення $\eta(v)$ мають статус розрахункових і не є результатами стендових випробувань DLG.

Для остаточного кількісного порівняння конкретних тракторів необхідні узгоджені за моделлю трансмісії та умовами випробування дані: передатні числа, характеристики

гідромашин, карти ККД, навантаження, частота обертання двигуна та результати незалежних стендових або польових випробувань.

Для підвищення точності та відтворюваності результатів доцільно виконати параметричну ідентифікацію конкретних трансмісій із використанням повної кінематичної матриці планетарних механізмів, характеристик гідронасоса і гідромотора, карт об'ємного та механічного ККД, моментів інерції, втрат у підшипниках і муфтах. Це дасть можливість перейти від інженерної апроксимації до відтворюваної моделі $\eta(v,\ M,\ \omega)$.

## Література


1. Macor, A., Rossetti, A. Optimization of hydro-mechanical power split transmissions. *Mechanism and Machine Theory*. 2011, 46(12), 1901–1919. https://doi.org/10.1016/j.mechmachtheory.2011.07.007
2. Rossetti, A., Macor, A. Multi-objective optimization of hydro-mechanical power split transmissions. *Mechanism and Machine Theory*, 2013. 62. 112–128. https://doi.org/10.1016/j.mechmachtheory.2012.11.009
3. Farkas, Z., Kerényi, G. Power flows and efficiency analysis of out- and input coupled IVT. *Periodica Polytechnica Mechanical Engineering*, 2009/ 53(2)/ 61–68. https://doi.org/10.3311/pp.me.2009-2.02
4. Ahn, S., Choi, J., Kim, S., Lee, J., Choi, C., Kim, H. Development of an integrated engine-hydro-mechanical transmission control algorithm for a tractor. *Advances in Mechanical Engineering*, 2015. 7. https://doi.org/10.1177/1687814015593870
5. Ahn, S., Choi, J., Kim, S., Lee, J., Kim, H. Development of a sub-shift control algorithm for an agricultural tractor with hydro-mechanical transmission. *Advances in Mechanical Engineering*, 2016. https://doi.org/10.1177/1687814016676943
6. Wang, G., Song, Y., Wang, J., Xiao, M., Cao, Y., Chen, W., Wang, J. Shift quality of tractors fitted with hydrostatic power split CVT during starting. *Biosystems Engineering*, 2020. 196. 183–201. https://doi.org/10.1016/j.biosystemseng.2020.06.001
7. Wang, G., Song, Y., Wang, J., Xiao, M., Chen, W., Cao, Y., Wang, J. Study on the shifting quality of the CVT tractor under hydraulic system failure. *Applied Sciences*, 2020. 10(2). 681. https://doi.org/10.3390/app10020681
8. Wang, G., Zhao, Y., Song, Y., et al. Optimizing the fuel economy of hydrostatic power-split system in continuously variable tractor transmission. *Heliyon*, 2023. 9(5). e15915. https://doi.org/10.1016/j.heliyon.2023.e15915
9. Zhao, Y., Chen, X., Song, Y., Wang, G., Zhai, Z. Energy and fuel consumption of a new concept of hydro-mechanical tractor transmission. *Sustainability*, 2023. 15(14). 10809. https://doi.org/10.3390/su151410809
10. Xia, Y., Sun, D., Qin, D. Designing comprehensive shifting control strategy of hydro-mechanical continuously variable transmission. *Applied Sciences*, 2022. 12(11). 5716. https://doi.org/10.3390/app12115716
11. Wang, J., Sun, D., Wang, J., Liao, G. Configuration of the power reflux hydro-mechanical transmission system. *Actuators*, 2024. 13(4). 120. https://doi.org/10.3390/act13040120
12. Cao, Y., Zhao, Y., Yang, Y., Yu, Z., Zhang, T., Wang, G. Design of series hydrostatic power split tractor transmission. *Journal of Agricultural Mechanization Research*, 2023. 45(1). 250–255. https://doi.org/10.13427/j.cnki.njyi.2023.01.008
13. Zhao, Y., et al. Energy consumption analysis of 2Z-X(B) planetary input-coupled hydro-mechanical tractor transmission. *Applied Sciences*, 2025. 15(23). 12576. https://doi.org/10.3390/app152312576
14. Song, Y., Jin, Y., Kong, Y., Zhao, Y., Yin, T., Wang, G. Analysis of traction performance for 180 HP continuously variable transmission tractor. *Applied Sciences*, 2026. 16(14). 6979. https://doi.org/10.3390/app16146979
15. Marani, P., Chiarabelli, D., Gessi, S., Martelli, M. Design of power-split hydrostatic CVT agricultural transmission for enhanced control and efficiency. *JFPS Int. Journal of Fluid Power System*, 2025. 18(1). 29–36. https://doi.org/10.5739/jfpsij.18.29
16. Bi-level iterative-driven dynamic matching design for power reflux hydro-mechanical transmission system. *Energy*, 2026. 360. 141779. https://doi.org/10.1016/j.energy.2026.141779

17. Coordinated dual-rolling control of shifting in HMCVT based on KF-MPC algorithm. *Computers and Electronics in Agriculture*, 2024. 227. 109561. https://doi.org/10.1016/j.compag.2024.109561

18. Energy-efficient path tracking control for autonomous tractors equipped with hydro-mechanical CVT. *Computers and Electronics in Agriculture*, 2026/ 252/ 112115. https://doi.org/10.1016/j.compag.2026.112115

19. Brenninger, M. M. Fendt Vario CVT in agricultural tractors. *SAE Technical Paper* 2007-01-4205, 2007. https://doi.org/10.4271/2007-01-4205

20. Pohlenz, J., Gruhle, W.-D. The ECCOM continuously variable hydrostatic-variable power-split transmission for use in tractors. *VDI-Berichte*, 2001/ 1592, 451–468.

21. Fendt. *The Fendt 300 Vario* [Product brochure]. URL: https://www.fendt.com/au/geneva-assets/article/49092/185174-fendt300vario-1901-en-v2.pdf

John Deere. *7R Series tractor* [Product brochure]. URL: https://www.deere.ro/assets/pdfs/region-2/products/tractors/yy2314125-7r-series-tractor-brochure.pdf

*Дата першого надходження статті до видання 03.09.2026*
*Дата прийняття статті до друку після рецензування 01.10.2026*
*Дата публікації (оприлюднення) статті 04.11.2026*
*Стаття поширюється на умовах ліцензії відкритого доступу(CC BY 4.0)*

## ANALYSIS OF THE OPERATION OF FENDT VARIO AND JOHN DEERE AUTOPOWR HYDROMECHANICAL TRANSMISSIONS AND COMPAR-ISON OF THEIR EFFICIENCY

**M. Volianskyi[1], A. Lavrinenko[1], Y. Humeniuk[1], Y. Rosamakha[1]**
[1] *National University of Life and Environmental Sciences of Ukraine*

**Abstract**

The paper presents a comparative analysis of the operating principles and energy efficiency of continuously variable hydro-mechanical power-split transmissions Fendt Vario and John Deere AutoPowr used in modern agricultural tractors. The relevance of the study is determined by the increasing requirements for energy efficiency, fuel economy, operational adaptability, and rational utilization of engine power under different operating conditions. The objective of the research is to establish the relationship between power distribution between the mechanical and hydro-volume branches of the transmission and its calculated overall efficiency depending on tractor travel speed.

The research is based on theoretical analysis of power flow in power-split continuously variable transmissions, consideration of the kinematic characteristics of planetary mechanisms, and mathematical modeling of the transmission energy balance. The Willis equation is used to describe kinematic relationships in planetary gear mechanisms. A combined efficiency model is applied to account for losses in the mechanical and hydro-volume branches. The comparative assessment is performed using common methodological assumptions, which makes it possible to evaluate the influence of transmission architecture and power distribution on calculated efficiency. Particular attention is given to distinguishing calculated model values from experimental or certified test results.

The results indicate that the proportion of power transmitted through the hydro-volume branch is an important factor affecting overall transmission efficiency. Increasing the hydro-volume component increases hydraulic losses and, under the adopted assumptions, reduces calculated total efficiency. For the investigated travel-speed interval of 4–12 km/h, the average calculated transmission efficiency is approximately 0,875 for Fendt Vario and 0,947 for John Deere AutoPowr. These values are obtained from the calculation model and should not be interpreted as direct experimental measurements or official manufacturer performance indicators. The practical significance of the research is the possibility of applying the proposed approach for preliminary engineering assessment, comparative evaluation of tractor transmissions, and selection of rational operating modes. Further research should include identification of actual hydraulic-unit and planetary-mechanism parameters and experimental validation under standardized operating conditions.

**Keywords:** hydro-mechanical transmission, continuously variable transmission, power-split transmission, power distribution, hydro-volume branch, mechanical branch, planetary gear mechanism.

**DOI https://doi.org/10.32782/1994-4691-2026-1-77-13**
УДК 681.533.56

# ОБЧИСЛЮВАЛЬНИЙ ФАКТОРНИЙ ЕКСПЕРИМЕНТ ДОСЛІДЖЕННЯ ДИНАМІЧНИХ ХАРАКТЕРИСТИК РЕГУЛЯТОРА ТИСКУ ПНЕВМОСИСТЕМИ

# COMPUTATIONAL FACTORIAL EXPERIMENT FOR INVESTIGATING THE DYNAMIC CHARACTERISTICS OF A PNEUMATIC SYSTEM PRESSURE REGULATOR

В. Т. Дмитрів[1*], д-р техн. наук, проф. ORCID: 0000-0001-9361-6418
Н.-Т. Великий[1], аспірант ORCID: 0009-0001-8550-4974

[1] *Національний університет «Львівська політехніка», Львів, Україна*
*e-mail: vasyl.t.dmytriv@lpnu.ua

**Анотація**. Метою досліджень є визначення динамічних характеристик регулятора тиску з електромагнітним клапаном для трьох форм затвора за різних параметрів пневмосистеми та перевірка адекватності математичної моделі. Отримано кореляційні залежності часових характеристик роботи клапанної системи регулятора тиску пневмосистеми в залежності від тиску в системі, форми затвора клапана, задана параметром еквівалентного клина, ефективної площі дроселя, що уможливлює обґрунтування ефективності клапанної системи за часовими параметрами закриття-відкриття клапана регулятора. Розраховано критерії узгодженості за невизначеністю вимірювань і точністю вихідних даних моделі. За критерієм Стьюдента систематичної похибки моделі не виявлено, розрахункові значення становлять $t$ = 0,29–1,90. За критерієм Фішера ($F$ = 14,6) модель адекватна. Практичне значення отриманих залежностей полягає в можливості адаптивного вибору конструкції затвора клапана і налаштування пневмосистеми. Якщо пріоритетом є швидке закривання (швидке підвищення тиску в лінії) і стабільність цього часу за змінних тиску живлення і опору лінії, доцільно застосовувати конічний затвор.

.**Ключові слова**: тиск, пневмосистема, клапанна система, критерій Фішера, критерій Стьюдента, рівняння регресії, час відкриття, клин, математична модель, напруга живлення.

## Вступ.

Питання функціонування регулятора тиску пневмосистеми полягає в тому щоб унеможливити інерційність керування зміни тиску в системі. Часові характеристики зміни параметрів тиску повинні відповідати заданими часовим інтервалам, які відповідають перехідним характеристикам зміни тиску конкретного об’єкту регулювання. Геометрія поверхні клапана впливає на силові параметри закривання/відкривання регулятора. Тенденція розроблення регуляторів тиску є напрямку зменшення конструкції, зниження маси клапанної системи, що уможливлює зниження потужності приводу й підвищення динаміки перемикання клапана та зменшує інерційність клапанної системи. Факторний експеримент уможливлює експериментально дослідити динамічні характеристики регулятора тиску за різної геометрії поверхні клапана. Тому, з огляду на практичні потреби експериментів, пов'язаних із регулюванням тиску, необхідно обґрунтовувати робочі характеристики пневматичних регуляторів, досліджуючи вплив геометричної форми поверхні на часові характеристики запирання-відпирання клапанної системи.

## Огляд літератури.

Пневматичні регулятори тиску широко використовуються для керування подачею в пневмосистемах високого тиску для технологічного й виробничого обладнання, що передбачають створення заданого тиску в пневмосистемах технічних об'єктів [1].

Для покращення робочих характеристик регулятора тиску пневмосистеми ряд дослідників зосереджуються на оптимізації алгоритму керування таким регулятором. Зокрема, є розроблений метод нелінійної компенсації для пневматичної системи на основі пропорційного регулятора потоку; цей метод дозволив компенсувати нелінійність характеристики «вхід–вихід» регулятора та зменшити його загальну нелінійність, що сприяло покращенню характеристик системи [2]. Також було розроблено пневматичний пропорційний регулятор тиску (скидання тиску) для роботи в умовах надвисокого тиску [3]. Для досягнення вищої точності регулювання в ньому було застосовано ПІ-регулятор із коефіцієнтом пропорційності, що змінюється залежно від заданого вихідного тиску; діапазон регулювання тиску становить від 8 до 25 МПа. Зміна конструкції затвора впливає часові параметри регулятора. Так регулятор тиску конічного пневматичного пропорційного регулятора, що базується на системі подвійного замкненого контуру зворотного зв’язку (контур струму та контур тиску) уможливлює здійснювати плавне регулювання вихідного тиску в діапазоні 0–0,6 МПа з похибкою регулювання в межах 1 кПа [4]. Дослідники вважають, що математичну модель необхідно перевірити експериментально. За допомогою експериментів, в яких регулювалися тиск подачі повітря, критичний тиск та об'єм газового балона, було отримано характеристики [5]. Пневматичний регулювальний клапан виконує функцію регулювання потоку системи або рівня в ключовому резервуарі, і його продуктивність має бути гарантована. Тому моделювання й аналіз витікання повітря в лінії подачі повітря, зміни сили ущільнення клапана та помилкові коригування нуля та діапазону позиціювання є важливим елементом експериментальних досліджень [6]. Пневматичний пропорційний регулятор є ключовим компонентом системи з пневматичним навантаженням і відіграє важливу роль у вирішенні проблеми надмірного підвищення тиску (перевантаження). Для забезпечення параметрів регулювання тиску з врахуванням механічних параметрів клапана, застосовується метод нечіткого адаптивного регулятора [7]. Відповідно похибка вихідного тиску регулятора становить 1,24%, що є незначним показником. Діапазон регулювання тиску становить 0,2–0,6 МПа, а максимальне відхилення – 0,012 МПа. Лінійність характеристики становить 1,34% від діапазону вимірювань.

Для отримання поведінки клапанної системи регулятора високого тиску застосовують динамічне моделювання на основі рівняння руху внутрішніх частин, рівняння нерозривності для різноманітних камер та рівняння для масової витрати. Через нелінійність та зв'язок ці рівняння розв'язують за допомогою чисельних методів [8, 9]. Вирішальним для перевірки результатів моделювання залишається експериментальна перевірка факторним планованим експериментом [10]. дослідження динамічних характеристик клапанної системи регулятора тиску, зокрема механізмів керування роботою, динамічних параметрів роботи клапана є одним з основних методів дослідження є незамінним допоміжним засобом у процесі проєктування структури клапанів, вибору типу внутрішніх компонентів та розробки продукції [11–13]

## Методологія дослідження.

Визначення динамічних характеристик регулятора тиску з електромагнітним клапаном для трьох форм затвора за різних параметрів пневмосистеми та перевірка адекватності математичної моделі проводиться методом планованого факторного експерименту.

Фактори та рівні їх варіювання вибрано з огляду на модельні результати і обмеження обладнання (табл. 1). Перший фактор – форма затвора клапана $X_1$. За своєю природою він якісний, проте форму робочої поверхні затвора можна охарактеризувати кількісною ознакою – параметром еквівалентного клина $\beta$ з моделі пограничного шару (табл. 2). Він пов'язаний з кутом $\Theta$, на який затвор відхиляє струмінь від осі отвору сідла, співвідношенням $\beta = \Theta / 90°$. Кут $\Theta$ визначає коефіцієнт сили струменя $k_{стр} = 1 - \cos\Theta$, а параметр $\beta$ – градієнт тиску в пограничному шарі. Для конічного затвора з кутом при вершині 60° $\Theta = 30°$ і $\beta = 1 / 3$, для сферичного діаметром 4,6 мм $\Theta = 71°$ (кут між дотичною до сфери в точці контакту і віссю клапана) і $\beta = 0{,}789$, для плоского $\Theta = 90°$ і $\beta = 1$. Другий фактор – тиск живлення $X_2 = p_c$. Його рівні 0,2; 0,4 і 0,6 МПа лежать у межах робочого тиску клапана (0,15–0,8 МПа) і діапазону налаштування регулятора AR2000 (0,05–0,85 МПа). Третій фактор – ефективна площа дроселя $X_3 = \mu A_{др}$, задають положенням регулювального гвинта, а відповідні значення визначають калібруванням. Цільові рівні 0,5, 1 і 2 мм² відповідають розрахунковим режимам табл. 2.7 і з огляду на ефективну площу відкритого клапана (близько 1,4 мм² за $d_0 = 1{,}5$ мм) забезпечують помітно різні рівні тиску в лінії відкритого клапана.

**Таблиця 1. Фактори і рівні їх варіювання**

| Фактор | Позначення | Рівень −1 | Рівень 0 | Рівень +1 | Кодування |
|---|---|---|---|---|---|
| Форма затвора (параметр еквівалентного клина $\beta$) | $X_1 = \beta$ | конічний (0,333) | сферичний (0,789) | плоский (1) | $x_1 = (\beta - 2/3)/(1/3)$ |
| Тиск живлення, МПа | $X_2 = p_c$ | 0,2 | 0,4 | 0,6 | $x_2 = (p_c - 0{,}4)/0{,}2$ |
| Ефективна площа дроселя, мм² | $X_3 = \mu A_{др}$ | 0,5 | 1 | 2 | $x_3 = \log_2 \mu A_{др}$ ($\mu A_{др}$, мм²) |

Функціями відгуку є показники динамічної характеристики, визначені в підрозділі 2.2: час закривання $t_{закр}$, часи зростання тиску $t_{10}$ і $t_{90}$, час встановлення $t_{вст}$, усталений тиск відкритого клапана $p_{л.вст}$, час відкривання $t_{відкр}$ і час спадання тиску $t_{90}'$.

Загальний вигляд лабораторної установки приведено на рис. 1. Для реєстрації перехідних процесів застосовано двоканальну схему вимірювання (рис. 2). Канал 1 осцилографа реєструє сигнал датчика тиску ДТ, встановленого через трійник у лінії між вентилем і клапаном. Канал 2 реєструє напругу на котушці і використовується для запуску (синхронізації) запису. За наявності шунта $R_ш$ у колі котушки канал 2 можна перемикати на вимірювання струму. Провал струму, зумовлений ЕРС руху, дає незалежну оцінку моментів початку і завершення руху якоря.

Необхідна точність вимірювань визначається очікуваними відмінностями між досліджуваними варіантами. За змодельованими результатами для $p_c = 0{,}6$ МПа і $\mu A_{др} = 1$ мм² час закривання становить 13,3 мс для конічного, 15,3 мс для сферичного і 15,8 мс для плоского затвора клапана. Найменша різниця є між сферичним і плоским затворами, становить 0,5 мс. Час відкривання становить 74,1, 81,5 і 107,4 мс. Для вимірювання тривалості закривання сферичного і плоского затворів, розширена невизначеність середнього значення не перевищувати 0,2–0,3 мс; для тривалості

відкривання достатньо 1–2 мс. Відмінності в усталеному тиску відкритого клапана між затворами, за результатами моделювання, не перевищують 0,006 МПа.

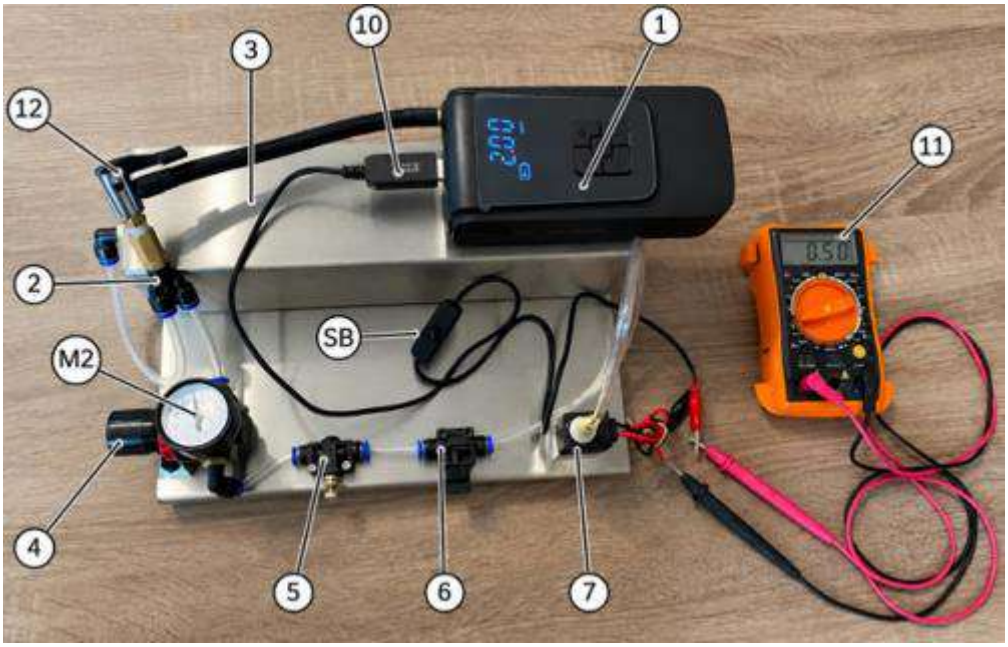



**Рис. 1. Загальний вигляд лабораторної установки: 1 – компресор; 2 – трійник; 3 – ресивер; 4 – регулятор тиску; 5 – дросель; 6 – вентиль; 7 – електромагнітний клапан; 10 – кабель живлення компресора; 11 – мультиметр для вимірювання струму котушки; 12 – шланг компресора із затискачем; M2 – манометр; SB – вимикач**

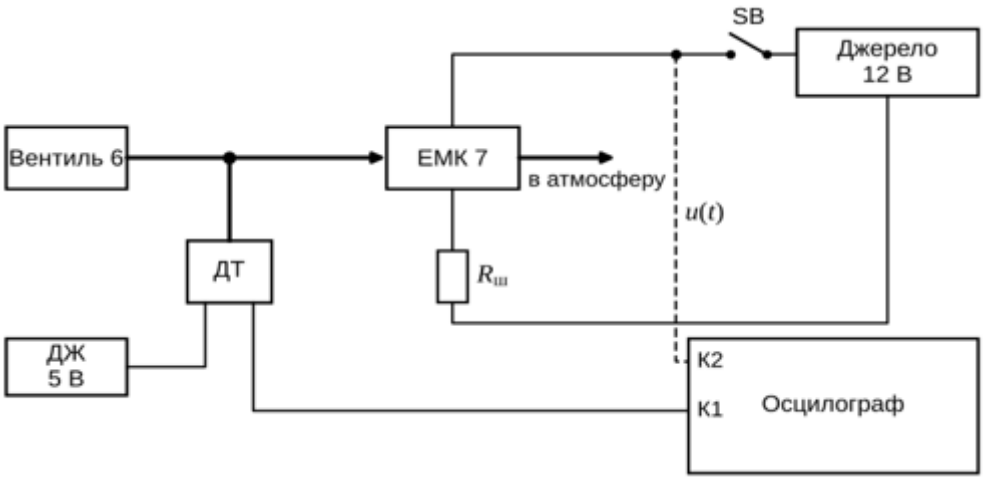



**Рис. 2. Схема вимірювання: ДТ – датчик тиску; ДЖ – джерело живлення датчика; SB – кнопковий вимикач; ЕМК – котушка електромагнітного клапана; $R_ш$ – шунт для вимірювання струму (за потреби); К1, К2 – канали осцилографа**

Характерні тривалості: тривалість зростання тиску після посадки затвора клапана (1,5 - 22 мс) згідно результатів моделювання); тривалість руху якоря (мілісекунди).

Похибка дискретизації за рівномірного розподілу в межах інтервалу дискретизації $\Delta t_д$ має стандартну невизначеність [14]

$$u_д = \frac{\Delta t_д}{\sqrt{12}}. \quad (1)$$

За частоти дискретизації 10 кГц ($\Delta t_д = 0{,}1$ мс) $u_д \approx 0{,}03$ мс, що значно менше за вимогу. Отже, частота дискретизації не нижче 10 кГц є достатньою. Тривалість запису має охоплювати повний цикл, тобто 0,1 с до подачі сигналу, час утримання кнопки і 0,2

с після її відпускання. За утримання 0,3–0,5 с це становить близько 1 с, тому довжина пам'яті осцилографа має бути не меншою за $10^4$ точок на канал.

Вимоги до датчика тиску. Похибка визначення моменту перетину порогового рівня тиску пов'язана з похибкою тиску $u_p$ і швидкістю зміни тиску [14]:

$$u_{t,p} = \frac{u_p}{|dp_п/dt|}. \qquad (2)$$

За моделлю, під час зростання тиску після закриття клапана найбільша швидкість зміни тиску становить 0,01–0,05 МПа/мс. Для датчика з діапазоном 0–1 МПа і зведеною похибкою 0,5 % ($u_p \approx 0{,}005/\sqrt{3} \approx 0{,}003$ МПа) похибка становить $u_{t,p} = 0{,}06$–0,3 мс. Найбільше значення відповідає найменшій провідності дроселя, коли тиск зростає повільно; для визначення моменту закриття, коли крутизна фронту найбільша, похибка не перевищує 0,1 мс. Час відгуку датчика має бути щонайменше на порядок меншим за час зростання тиску, тобто не більше 1 мс. Цим вимогам відповідають п'єзорезистивні датчики тиску з аналоговим вихідним сигналом (наприклад, 0,5–4,5 В) і часом відгуку близько 1 мс.

Оцінювання невизначеності виконується відповідно до настанови JCGM 100 (GUM) [14].

Калібрувальні досліди проводимо наступним чином. Ефективну площу дроселя для кожного положення гвинта визначають за усталеним тиском у лінії відкритого клапана. Якщо течія через дросель і клапан надкритична, з рівності витрат (2.48) випливає

$$\mu A_{\text{др}}\, p_{\text{с}}^{\text{абс}} = \mu A_{\text{к}}\, p_{\text{л.вст}}^{\text{абс}}, \qquad \mu A_{\text{др}} = \mu A_{\text{к}}\, \frac{p_{\text{л.вст}}^{\text{абс}}}{p_{\text{с}}^{\text{абс}}}, \qquad (3)$$

де індекс «абс» позначає абсолютні тиски.

Умова надкритичності для дроселя – $p_{\text{л.вст}}^{\text{абс}}/p_{\text{с}}^{\text{абс}} \le 0{,}528$, для клапана - $p_a/p_{\text{л.вст}}^{\text{абс}} \le 0{,}528$ [15]. Ефективну площу відкритого клапана $\mu A_{\text{к}}$ визначають методом спорожнення ємності [16]. Для цього заповнюють ресивер до 0,6–0,8 МПа, вимикають компресор, повністю відкривають дросель і регулятор, а датчик тиску тимчасово приєднують до ресивера. За надкритичного витікання тиск у ресивері спадає за експонентою, відповідно:

$$\mu A_{\Sigma} = \frac{V_{\text{р}}}{nR_{\text{г}}TC_1\,\Delta t} \ln\frac{p_{\text{р1}}}{p_{\text{р2}}}, \qquad C_1 = \sqrt{\frac{k}{R_{\text{г}}T}}\left(\frac{2}{k+1}\right)^{\frac{k+1}{2(k-1)}}, \qquad (4)$$

де $\mu A_{\Sigma}$ – сумарна ефективна площа послідовно з'єднаних елементів, м²; $p_{\text{р1}}$, $p_{\text{р2}}$ – абсолютні тиски на початку і в кінці інтервалу $\Delta t$, Па.

Інтервал вибирають так, щоб $p_{\text{р2}}$ перевищував $p_a/0{,}528 \approx 0{,}19$ МПа. Для послідовно з'єднаних елементів за надкритичного режиму наближено виконується співвідношення $\mu A_{\Sigma}^{-2} = \sum_i \mu A_i^{-2}$ [17], що дає змогу виділити ефективну площу клапана, якщо площі інших елементів значно більші.

Напругу на котушці контролюють мультиметром під час перемикання клапана. Зниження напруги під навантаженням характеризує внутрішній опір джерела живлення (виходу компресора) і використовується для оцінювання фактичних умов закривання клапана.

## Результати.

Результати основного факторного експерименту для плану $3^3$ у вигляді матриці плану наведено в табл. 2. Значення показників отримано усередненням результатів повторних дослідів у кожному режимі.

**Таблиця 2. Матриця плану експерименту і експериментальні значення функцій відгуку**

| № | Затвор | $\beta$ | $x_1$ | $p_c$, МПа | $x_2$ | $\mu A_{др}$, мм² | $x_3$ | $t_{закр}$, мс | $t_{90}$, мс | $t_{відкр}$, мс | $p_{л.вст}$, МПа |
|---|---|---|---|---|---|---|---|---|---|---|---|
| 1 | конічний | 0,333 | −1 | 0,2 | −1 | 0,5 | −1 | 13,2 | 32,6 | 132,5 | 0,022 |
| 2 | конічний | 0,333 | −1 | 0,4 | 0 | 0,5 | −1 | 13,1 | 34,7 | 124,8 | 0,081 |
| 3 | конічний | 0,333 | −1 | 0,6 | +1 | 0,5 | −1 | 13,3 | 34,1 | 115,2 | 0,158 |
| 4 | сферичний | 0,789 | 0,367 | 0,2 | −1 | 0,5 | −1 | 12,8 | 33,3 | 111,6 | 0,021 |
| 5 | сферичний | 0,789 | 0,367 | 0,4 | 0 | 0,5 | −1 | 13,5 | 35,9 | 95,5 | 0,079 |
| 6 | сферичний | 0,789 | 0,367 | 0,6 | +1 | 0,5 | −1 | 13,3 | 36,2 | 86,5 | 0,152 |
| 7 | плоский | 1 | +1 | 0,2 | −1 | 0,5 | −1 | 12,5 | 33,1 | 102,4 | 0,031 |
| 8 | плоский | 1 | +1 | 0,4 | 0 | 0,5 | −1 | 13,3 | 35,4 | 85,1 | 0,080 |
| 9 | плоский | 1 | +1 | 0,6 | +1 | 0,5 | −1 | 14,0 | 36,2 | 76,1 | 0,152 |
| 10 | конічний | 0,333 | −1 | 0,2 | −1 | 1 | 0 | 12,2 | 18,9 | 125,1 | 0,105 |
| 11 | конічний | 0,333 | −1 | 0,4 | 0 | 1 | 0 | 12,7 | 19,6 | 118,2 | 0,238 |
| 12 | конічний | 0,333 | −1 | 0,6 | +1 | 1 | 0 | 13,6 | 20,0 | 107,2 | 0,375 |
| 13 | сферичний | 0,789 | 0,367 | 0,2 | −1 | 1 | 0 | 14,2 | 20,2 | 105,2 | 0,098 |
| 14 | сферичний | 0,789 | 0,367 | 0,4 | 0 | 1 | 0 | 13,9 | 20,8 | 90,3 | 0,242 |
| 15 | сферичний | 0,789 | 0,367 | 0,6 | +1 | 1 | 0 | 15,6 | 22,2 | 81,1 | 0,368 |
| 16 | плоский | 1 | +1 | 0,2 | −1 | 1 | 0 | 13,2 | 19,9 | 98,6 | 0,115 |
| 17 | плоский | 1 | +1 | 0,4 | 0 | 1 | 0 | 14,4 | 21,2 | 83,1 | 0,246 |
| 18 | плоский | 1 | +1 | 0,6 | +1 | 1 | 0 | 16,0 | 22,9 | 73,8 | 0,361 |
| 19 | конічний | 0,333 | −1 | 0,2 | −1 | 2 | +1 | 12,8 | 14,5 | 120,1 | 0,170 |
| 20 | конічний | 0,333 | −1 | 0,4 | 0 | 2 | +1 | 13,3 | 14,1 | 113,5 | 0,354 |
| 21 | конічний | 0,333 | −1 | 0,6 | +1 | 2 | +1 | 12,9 | 14,9 | 103,3 | 0,531 |
| 22 | сферичний | 0,789 | 0,367 | 0,2 | −1 | 2 | +1 | 14,0 | 15,9 | 101,7 | 0,172 |
| 23 | сферичний | 0,789 | 0,367 | 0,4 | 0 | 2 | +1 | 15,5 | 17,1 | 87,6 | 0,352 |
| 24 | сферичний | 0,789 | 0,367 | 0,6 | +1 | 2 | +1 | 16,4 | 17,9 | 79,1 | 0,530 |
| 25 | плоский | 1 | +1 | 0,2 | −1 | 2 | +1 | 14,2 | 16,0 | 96,6 | 0,172 |
| 26 | плоский | 1 | +1 | 0,4 | 0 | 2 | +1 | 15,7 | 17,5 | 81,6 | 0,342 |
| 27 | плоский | 1 | +1 | 0,6 | +1 | 2 | +1 | 17,4 | 19,1 | 73,3 | 0,531 |

Примітка. $\beta$ – параметр еквівалентного клина, $\beta = \theta/90°$; $x_1 = (\beta - 2/3)/(1/3)$, $x_2 = (p_c - 0{,}4)/0{,}2$, $x_3 = \log_2 \mu A_{др}$; значення функцій відгуку – середні за результатами дослідів.

Час закривання конічного затвора клапана в усіх 27 режимах лежить у вузьких межах 12,2–13,6 мс і майже не залежить ні від тиску живлення, ні від площі дроселя. Для сферичного затвора він становить 12,8–16,4 мс, для плоского — 12,5–17,4 мс. Найбільший час закривання плоского затвора (17,4 мс) отримано за найбільшого тиску в лінії відкритого клапана ($p_c$ = 0,6 МПа, $\mu A_{др}$ = 2 мм², $p_{л.вст}$ = 0,531 МПа). За найменшої площі дроселя (0,5 мм²) тиск у лінії відкритого клапана малий (0,021–0,158 МПа), сила струменя незначна, і час закривання всіх затворів однаковий у межах 1,5 мс. Час відкривання змінюється у зворотному порядку. Найменший він для плоского затвора (73,3–102,4 мс), найбільший — для конічного (103,3–132,5 мс), а сферичний займає

проміжне положення (79,1–111,6 мс). Зі збільшенням тиску живлення і площі дроселя час відкривання всіх затворів зменшується, оскільки зростає тиск, що діє на затвор у напрямку відкривання. Час зростання тиску $t_{90}$ визначається передусім площею дроселя: за 0,5 мм² він становить 32,6–36,2 мс, за 2 мм² — 14,1–19,1 мс. Усталений тиск у лінії відкритого клапана для трьох затворів.

Відповідно до методики експериментальні дані апроксимовано повним рівнянням регресії другого порядку. Фактори наведені в табл. 1, відповідно є такі:

– фактор $X_1$ — форма затвора клапана, задана параметром еквівалентного клина $\beta$: $\beta$ = 0,333 для конічного, 0,789 для сферичного і 1 для плоского затвора; кодоване значення $x_1 = (\beta - 2/3)/(1/3)$ становить відповідно −1; 0,367; +1;

– фактор $X_2$ — тиск живлення $p_c$ = 0,2; 0,4; 0,6 МПа; кодоване значення $x_2 = (p_c - 0{,}4)/0{,}2$ становить −1; 0; +1;

– фактор $X_3$ — ефективна площа дроселя $\mu A_{др}$ = 0,5; 1; 2 мм²; кодоване значення $x_3 = \log_2 \mu A_{др}$ становить −1; 0; +1;

– функції відгуку $y$ — експериментальні час закривання $t_{закр}$, час зростання тиску до 90 % перепаду $t_{90}$, час відкривання $t_{відкр}$ і усталений тиск у лінії відкритого клапана $p_{л.вст}$

Вибір параметра $\beta$ як кількісної характеристики форми затвора клапана має фізичне обґрунтування. Він однозначно пов'язаний з кутом $\theta$, на який затвор відхиляє струмінь від осі отвору сідла: $\pi\beta = 2\theta$, тобто $\beta = \theta/90°$. Цей кут визначає коефіцієнт сили струменя $k_{стр} = 1 - \cos(90°\beta)$ і водночас градієнт тиску в пограничному шарі на поверхні затвора. Показник градієнта тиску $m = \beta/(2 - \beta)$ не є, оскільки однозначно визначається через $\beta$ і характеризує ту саму ознаку. Маса затвора окремим фактором також не є окремим фактором. Кожна форма затвора має власну масу (5,8 г для плоского і по 7,0 г для конічного і сферичного затворів), тому коефіцієнти при $\beta$ відображають сумарний вплив форми і маси реальних затворів. Розділити ці впливи можна лише за дослідами із затворами однакової форми і різної маси або різної форми і однакової маси.

Для переходу до натуральних значень факторів рівняння регресії мають такий вигляд (позначено $\lambda = \log_2 \mu A_{др}$, де $\mu A_{др}$ — в мм²; $\beta$ — безрозмірний; $p_c$ — в МПа):

– для часу закривання, мс:

$$t_{закр} = 11{,}83 + 3{,}794\beta - 2{,}108p_c - 1{,}356\lambda + 6{,}985\beta p_c + 2{,}105\beta\lambda + 1{,}500p_c\lambda - \\ -3{,}241\beta^2 + 1{,}111p_c^2 - 0{,}02222\lambda^2, \quad (5)$$

– для часу зростання тиску до 90 % перепаду, мс:

$$t_{90} = 16{,}06 + 5{,}879\beta + 5{,}115p_c - 9{,}808\lambda + 7{,}651\beta p_c + 1{,}417\beta\lambda - 0{,}8333p_c\lambda - \\ -4{,}467\beta^2 - 6{,}528p_c^2 + 4{,}839\lambda^2, \quad (6)$$

– для часу відкривання, мс:

$$t_{відкр} = 161{,}4 - 72{,}80\beta - 67{,}65p_c - 8{,}972\lambda - 29{,}31\beta p_c + 5{,}544\beta\lambda + 2{,}500p_c\lambda + \\ +27{,}23\beta^2 + 41{,}67p_c^2 + 1{,}183\lambda^2, \quad (7)$$

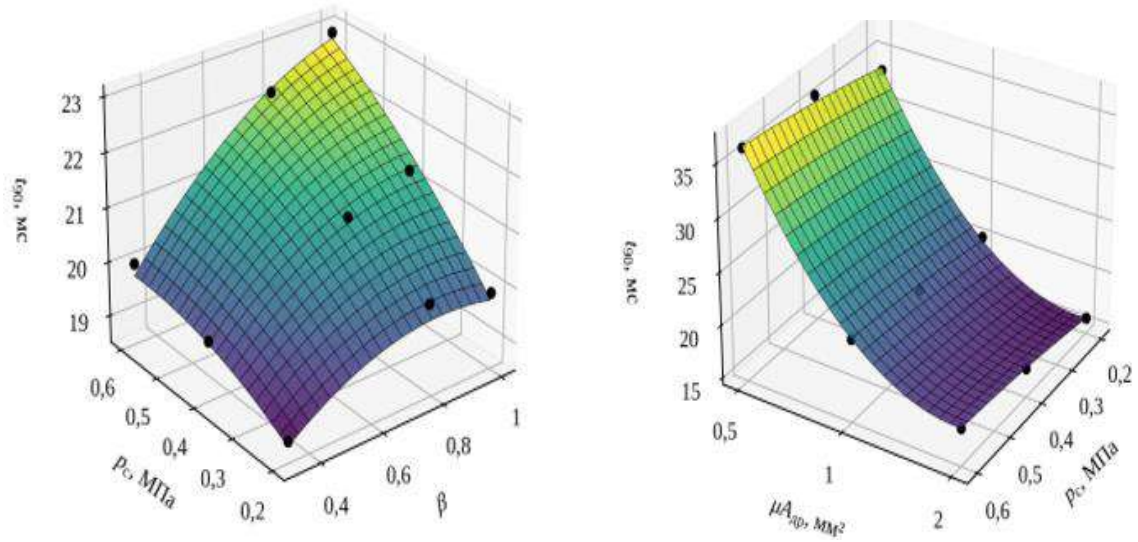
– для усталеного тиску в лінії відкритого клапана, МПа:

$$p_{л.вст} = -0{,}009971 - 0{,}009116\beta + 0{,}6177p_c + 0{,}01856\lambda - 0{,}04539\beta p_c - 0{,}002052\beta\lambda + \\ +0{,}2875p_c\lambda + 0{,}01995\beta^2 + 0{,}05000p_c^2 - 0{,}02033\lambda^2. \quad (8)$$

Рівняння (5–8) справедливі в межах факторного простору $1/3 \le \beta \le 1$, $0{,}2 \le p_c \le 0{,}6$ МПа, $0{,}5 \le \mu A_{др} \le 2$ мм². Коефіцієнти детермінації становлять 0,934–0,999, тобто рівняння пояснюють від 93 до 99,9 % варіації показників. Залишкові середньоквадратичні відхилення (0,42 мс для $t_{закр}$, 0,41 мс для $t_{90}$, 1,55 мс для $t_{відкр}$ і

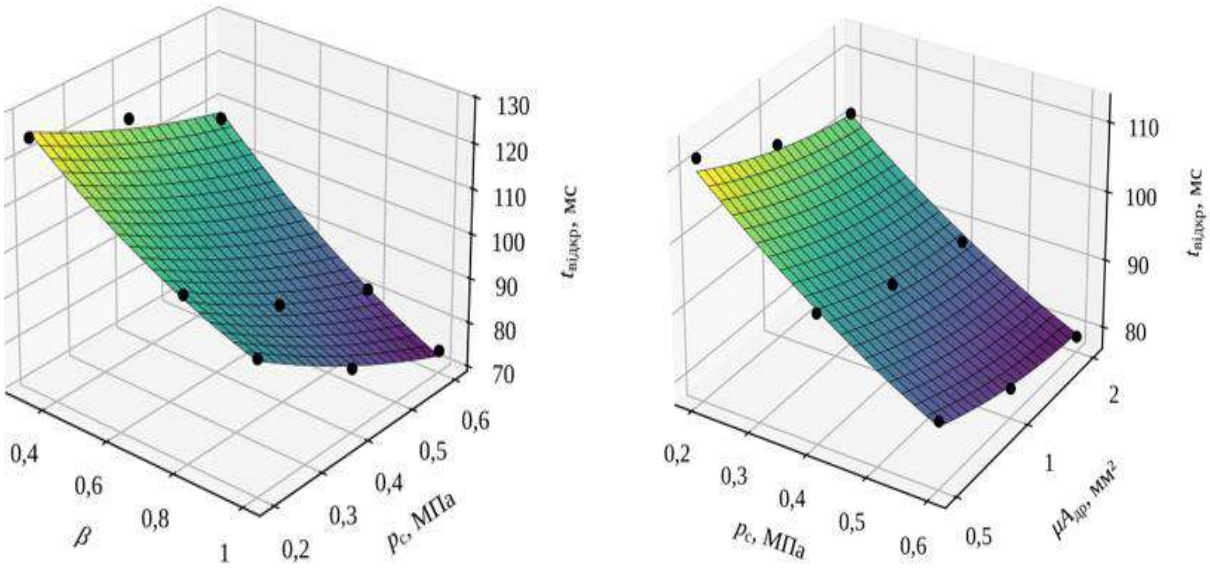
0,0069 МПа для $p_{\text{л.вст}}$) того самого порядку, що й очікувана невизначеність вимірювань (підрозділ 3.3).

Графічне зображення кореляційних залежностей у вигляді поверхонь відгуку наведено на рис. 3, 4.




а б

**Рис. 3. Залежність часу зростання тиску $t_{90}$: а – від параметра форми затвора клапана $\beta$ і тиску живлення $p_c$ за $\mu A_{др}$ = 1 мм²; б – від тиску живлення і ефективної площі дроселя для сферичного затвора ($\beta$ = 0,789); точки – експериментальні усереднені значення**




а б

**Рис. 4. Залежність часу відкривання $t_{\text{відкр}}$: а – від параметра форми затвора клапана $\beta$ і тиску живлення $p_c$ за $\mu A_{др}$ = 1 мм²; б – від тиску живлення і ефективної площі дроселя для сферичного затвора ($\beta$ = 0,789).**

Аналіз результатів дослідження (рис. 3, залежності (5-8)) показує, що час закривання зростає зі збільшенням усіх трьох факторів, причому головні ефекти близькі за значенням ($b_1$ = 0,756, $b_2$ = 0,687 і $b_3$ = 0,648 мс). Найбільшою за модулем серед взаємодій є $b_{13}$ = 0,702 мс: вплив форми затвора клапана посилюється зі збільшенням площі дроселя. Значущою є і взаємодія $b_{12}$ = 0,466 мс, тобто вплив тиску живлення посилюється зі збільшенням $\beta$. Обидві взаємодії мають одну фізичну причину. Збільшення тиску живлення і площі дроселя підвищує тиск у лінії відкритого

клапана, а отже, і силу струменя, яку має подолати електромагніт. Ця сила пропорційна $k_{\text{стр}} = 1 - \cos(90°\beta)$, тому для конічного затвора вона мала, і його час закривання майже не залежить від режиму. Квадратичні коефіцієнти незначущі, тож у межах факторного простору залежність близька до білінійної. Від'ємний коефіцієнт $b_{11}$ відображає те, що за малого тиску в лінії сферичний затвор закривається не швидше за плоский. Причиною є менша маса плоского затвора (5,8 г проти 7,0 г), яка за слабкого струменя переважає

Залежність часу відкривання від факторів (рис. 4) має протилежний характер: час відкривання зменшується зі збільшенням усіх трьох факторів. Вплив форми затвора клапана тут найсильніший: кодований коефіцієнт $b_1 = -16{,}07$ мс перевищує за модулем коефіцієнт тиску $b_2 = -10{,}77$ мс у 1,5 раза, а коефіцієнт площі дроселя $b_3 = -4{,}28$ мс — майже в 4 рази. У межах факторного простору час відкривання змінюється від 73 до 133 мс, тобто у 1,8 раза. Конічний затвор відкривається найповільніше, оскільки сила струменя, що допомагає відкриванню, для нього найменша. Під час відкривання сила струменя сприяє руху затвора, тому плоский затвор, що сприймає найбільшу частку імпульсу, відкривається найшвидше.

Таким чином, отримані дослідження дозволяють встановити що конічний затвор клапана закривається найшвидше, а перевага зростає з тиском: за 0,6 МПа і 2 мм² час закривання плоского затвора в 1,35 рази більший, ніж конічного (модель - 1,27). За 0,5 мм² тиск у лінії малий, і часи закривання трьох затворів відрізняються не більше ніж на 0,7 мс, що відповідає моделі (до 0,9 мс). У діапазоні тиску в лінії відкритого клапана 0,02–0,53 МПа час закривання плоского затвора клапана зростає в середньому на 0,97 мс на кожні 0,1 МПа (модель — 0,91 мс), сферичного — на 0,69 мс (модель — 0,63 мс), а конічного майже не змінюється (0,06 мс; модель — 0,14 мс).

## Висновки.

Експериментально підтверджено, що форма затвора клапана визначально впливає на динамічну характеристику регулятора тиску, коли клапан закривається назустріч потоку. Конічний затвор закривається найшвидше і найстабільніше (12,2–13,6 мс за тиску живлення 0,2–0,6 МПа і ефективної площі дроселя 0,5–2 мм²), але відкривається найповільніше (103,3–132,5 мс). Плоский затвор, навпаки, відкривається найшвидше (73,3–102,4 мс), а його час закривання найсильніше зростає з тиском у лінії (з 12,5 до 17,4 мс). Сферичний затвор займає проміжне положення. Час зростання тиску визначається передусім площею дроселя, а усталений тиск у лінії від форми затвора не залежить.

Отримані регресійні моделі уможливлюють обґрунтування форми затвора клапана і налаштування дроселя та регулятора тиску відповідно до режиму роботи пневмосистеми.

Наступним етапом дослідження пропонується визначити вплив конструктивних розмірів на динаміку роботи клапанної системи.

## Література

1. Pan Z., Yiping D., , Jiangfeng W. Design and thermodynamic analysis of a hybrid energy storage system based on A-CAES (adiabatic compressed air energy storage) and FESS (flywheel energy storage system) for wind power application. *Energy*, 2014. 70(C). 674–684. https://doi.org/10.1016/j.energy.2014.04.055

2. Bai Y., Li X. A nonlinear compensation method for pneumatic positioning system with proportional flow regulator. *Hydr. Trans*., 2007. 7. 52–55

3. Wang X., Chen Y. Design and simulation of pneumatic proportional extra-high pressure regulator. *J Zhejiang Univ* (Eng Sci), 2005. 39. 614–617

4. Ban W., Tao G., Meng D. Design of pneumatic proportional pressure regulator pressure controller with pyramid regulator. *J Zhejiang Univ*, 2015. 5. 873–879

5. Yu Q., Zhai J., Wang Q., Zhang X., Tan X. Experimental Study of a New Pneumatic Actuating System Using Exhaust Recycling. *Sustainability*, 2021. 13. 1645. https://doi.org/10.3390/su13041645

6. Yang-seok K., Dae-woong K., Byoung-oh L., Rae-hyuk J., Seung-ho L. Experimental Study of Operating Parameters for Pneumatic Control Valve in Abnormal Conditions. *Transactions of the Korean Society of Mechanical Engineers A*, 2016. 40(6). 613–619. https://doi.org/10.3795/KSME-A.2016.40.6.613

7. Wang N., Xu L. Y., Xie F., et al. Research on the dynamic characteristics of pneumatic proportional regulator in pneumatic-loading system and design of fuzzy adaptive controller. *Sci China Tech Sci*, 2022. 65. 956–965. https://doi.org/10.1007/s11431-021-1932-1

8. Shahani A. R., Esmaili H., Aryaei A., Mohammadi S., Najar M. Dynamic Simulation of a High Pressure Regulator. *JCARME*, 2011. 1(1). 17–28. https://doi.org/10.22061/JCARME.2011.3

9. Stryzhak M., Hasanov R. Mathematical Modeling of the Dynamic Performance of a Pneumatic Actuator with a Proportional Pressure Regulator. *Bulletin of the National Technical University KhPI Series Hydraulic machines and hydraulic units*, 2026. 19–26. https://doi.org/10.20998/2411-3441.2026.1.03

10. Luo K., Chen K., Yu X., Zang J., Yang L. Numerical Simulation and Experimental Verification on Dynamic Behavior of Pilot-Operated Isolation Valve. *ICCMT '25: Proceedings of the 2025 2nd International Conference on Computer and Multimedia Technology*, 2025. 481–489. https://doi.org/10.1145/3757749.3757831

11. Shen R., Jiao Z., Parker T., et al. Recent application of Computational Fluid Dynamics (CFD) in process safety and loss prevention: *A review[J]. Journal of Loss Prevention in the Process Industries*, 2020. 67. 104252. https://doi.org/10.1016/j.jlp.2020.104252

12. Scuro N. L., Angelo E., Angelo G., et al. A CFD analysis of the flow dynamics of a directly-operated safety relief valve. *Journal Nuclear Engineering and Design*, 2018. 328. 321–332. https://doi.org/10.1016/j.nucengdes.2018.01.024

13. Tiwari G., Kumar J., Prasad V., et al. Utility of CFD in the design and performance analysis of hydraulic turbines. *A review Journal Energy Reports*. 2020. 6. 2410–2429. https://doi.org/10.1016/j.egyr.2020.09.004

14. JCGM 100:2008. Evaluation of measurement data – Guide to the expression of uncertainty in measurement. Sèvres : Joint Committee for Guides in Metrology, 2008.

15. Anderson J. D. Modern Compressible Flow: With Historical Perspective. 3rd ed. New York : McGraw-Hill, 2003. 760 p.

16. ISO 6358-2:2019. Pneumatic fluid power – Determination of flow-rate characteristics of components using compressible fluids – Part 2: Alternative test methods. Geneva : International Organization for Standardization, 2019.

17. Beater P. Pneumatic Drives: System Design, Modelling and Control. Berlin ; Heidelberg : Springer, 2007. https://doi.org/10.1007/978-3-540-69471-7

*Дата першого надходження статті до видання 07.10.2026*
*Дата прийняття статті до друку після рецензування 29.10.2026*
*Дата публікації (оприлюднення) статті 04.11.2026*
*Стаття поширюється на умовах ліцензії відкритого доступу(CC BY 4.0)*

# COMPUTATIONAL FACTORIAL EXPERIMENT FOR INVESTIGATING THE DYNAMIC CHARACTERISTICS OF A PNEUMATIC SYSTEM PRESSURE REGULATOR

**V. Dmytriv[1], S. N.-T. Velykyi [1]**
[1] *Lviv Polytechnic National University*

**Abstract**

The objective of this research is to determine the dynamic characteristics of a pressure regulator equipped with an electromagnetic valve—considering three different valve plug shapes and various pneumatic system parameters—and to verify the adequacy of the mathematical model. Correlation relationships were derived for the temporal operating characteristics of the pressure regulator's valve system. These relationships depend on system pressure, the shape of the valve plug (defined by an "equivalent wedge" parameter), and the effective throttle area. This allows for an assessment of the valve system's efficiency based on the opening and closing time parameters of the regulator. The results of a three-factor experiment are presented. The factors considered were: $X_1$ (valve plug shape, defined by the equivalent wedge parameter $\beta$: $\beta$ = 0,333 for a conical plug, 0.789 for a spherical plug, and 1 for a flat plug); $X_2$ (supply pressure $p_c$ = 0.2, 0.4, 0.6 MPa); and $X_3$ (effective throttle area $\mu A_{thr}$ = 0.5, 1, 2 mm²). The experimental response functions include: closing time $t_{close}$; the time required for pressure to rise to 90% of the differential $t_{90}$; opening time $t_{open}$; and the steady-state pressure in the line downstream of the open valve $p_{line}$. It has been experimentally confirmed that the shape of the valve plug has a decisive influence on the dynamic characteristics of the pressure regulator when the valve closes against the direction of flow. A conical valve element closes the fastest and most consistently (12.2–13.6 ms at a supply pressure of 0.2–0.6 MPa and an effective orifice area of 0.5 - 2 mm², but it opens the slowest (103.3–132.5 ms). Conversely, a flat valve element opens the fastest (73.3–102.4 ms), while its closing time increases most significantly with line pressure (from 12.5 to 17.4 ms). A spherical valve element occupies an intermediate position. The pressure rise time is determined primarily by the orifice area, whereas the steady-state line pressure is independent of the valve element's shape. Consistency criteria were calculated based on measurement uncertainty and the accuracy of the model's input data. According to the Student's criterion, no systematic model error was detected (calculated values: t = 0.29–1.90). Based on the Fisher criterion (F = 14.6), the model is considered adequate. The practical significance of these derived relationships lies in the ability to adaptively select the valve element design and configure the pneumatic system. If the priority is rapid closing (a quick rise in line pressure) and consistency in this timing despite variations in supply pressure and line resistance, a conical valve element is the appropriate choice.

**Keywords:** pressure, pneumatic system, valve system, Fisher criterion, Student's criterion, regression equation, opening time, wedge, mathematical model, supply voltage.

**Промислова гідравліка і пневматика**

*наукове фахове видання категорії Б*

**№ 1 (77)**

*Заснований у 2003 р*
*Виходить два рази на рік*
*Мова розповсюдження – українська, англійська*

Дата оприлюднення 04.11.2026 р.
Дата друку 11.11.2026 р.
Формат 60x84/8. Гарнітура Times New Roman.
Папір офсет. Цифровий друк. Ум. друк. арк. 12,4.
Замов № 1026/873. Наклад 100 прим.

Видавництво і друкарня – Видавничий дім «Гельветика»
65101, м. Одеса, вул. Інглезі, 6/1
Телефони: +38 (095) 934 48 28, +38 (097) 723 06 08
E-mail: mailbox@helvetica.ua
Свідоцтво суб'єкта видавничої справи
ДК № 7623 від 22.06.2022 р.